

Metallurgical optimization of the HFQ[®] process for AA7075-F sheets

A thesis submitted to the University of Manchester for the
degree of
Doctor of Philosophy
in the Faculty of Science and Engineering

2023

Francesco Guarracino
School of Natural Sciences
Department of Materials

Table of Contents

Abstract	6
Declaration of originality	7
Copyright statement	8
Acknowledgements.....	9
Chapter 1: Introduction.....	10
1.1: Background of the research topic.....	11
1.2: Research questions	19
1.3: Research aims and objectives.....	23
1.4: Research scope.....	25
1.5: Significance of the research.....	26
1.6: Outline of the research.....	28
Chapter 2: Literature review	29
2.1: The production of F-tempered 7000 aluminium alloy sheets	30
2.2: Summary of the literature related to the HFQ [®] process.....	33
2.3: The solution heat treatment optimisation at low heating rates	36
2.4: The effect of heating rate on the dissolution process.....	40
2.5: The effect of solution heat treatments on the grain structure of 7000 aluminium alloys.....	43
2.6: Quench sensitivity of 7000 aluminium alloys	46
2.7: The cooling rate optimisation in the HFQ [®] process	50
2.8: Stress corrosion cracking of 7000 aluminium alloys	53
2.9: The link of electrochemical parameters with SCC susceptibility of 7000 aluminium alloys.....	58
2.10: The evolution of GBP microchemistry with heat treatment parameters	60
2.11: Uniaxial tensile tests of 7000 aluminium alloys.....	64
2.12: The effect of cooling rate on the microstructure of 7000 aluminium alloys	69
2.13: Constraints of the HFQ [®] aging step	72
2.14: Basic principles of age hardening	76
2.15: Aging strategies for 7000 aluminium alloys.....	78

Chapter 3: Research Methodology	83
3.1: The experimental plan	84
3.1.1: Solution heat treatment	84
3.1.2: Cooling step	86
3.1.3: Aging step	88
3.2: Starting materials	90
3.3: Layout of the experiments	91
3.3.1: The optimisation of the solution heat treatments at low heating rates	91
3.3.2: The effect of the heating rate	94
3.3.3: The optimisation of the cooling step	98
3.3.4: The design of the RRDA strategy	101
3.3.5: Microstructure and property evolution during RRDA steps	103
3.3.6: The RRDA properties compared to industrially relevant tempers	105
3.3.7: The link of anodic polarisation parameters with SCC susceptibility and the OM observation of the corroded surfaces	107
3.4: Experimental techniques and experimental procedures	108
3.4.1: Cutting operations and precision cutting	108
3.4.2: Heat treatments	109
3.4.3: Dilatometry heat treatments	112
3.4.4: Surface preparation and thickness reduction	113
3.4.5: Vickers hardness measurements	114
3.4.6: Differential scanning calorimetry	115
3.4.7: Etching	116
3.4.8: Optical microscopy	117
3.4.9: Mean linear intercept method	118
3.4.10: Scanning electron microscopy	119
3.4.11: Small-angle x-ray scattering	120
3.4.12: Electropolishing	124
3.4.13: Transmission electron microscopy	125

3.4.14: Distribution of grain boundary precipitate lengths and average precipitate-free zone width	126
3.4.15: Uniaxial tensile tests and Kocks-Mecking plots	128
3.4.16: Stress corrosion cracking experiments	129
3.4.17: Anodic polarisations	132
3.5: CIPHER simulations	134
Chapter 4: Solution heat treatment step	136
4.1: Results	137
4.1.1: Experiments at low heating rate	137
4.1.2: Experiments at high heating rate	143
4.2: Discussion	149
4.2.1: The precipitate dissolution process at high temperatures and low holding times	149
4.2.2: Incipient melting at high solution heat treatment temperatures	152
4.2.3: Optimisation of the HFQ[®] solution heat treatment parameters	155
4.2.4: The heating rate effect on the precipitate dissolution process	158
4.2.5: The effect of accelerated solution heat treatments on the grain structure	165
Chapter 5: Cooling step	168
5.1: Results	169
5.1.1: Microstructural evolution with varying cooling rate	169
5.1.2: Tensile properties with varying cooling rate	177
5.1.3: Corrosion properties with varying cooling rate	180
5.2: Discussion	183
5.2.1: The effect of cooling rate on matrix precipitation	183
5.2.2: The effect of cooling rate on the GB microstructure	186
5.2.3: The effect of cooling rate on tensile properties	188
5.2.4: The cooling rate optimisation for the HFQ[®] process	192
5.2.5: Simulated GBP composition with varying cooling rate	194
5.2.6: The effect of cooling rate on corrosion properties	196

Chapter 6: Aging step	199
6.1: Results	200
6.1.1: The design of the RRDA strategy	200
6.1.2: Microstructural evolution during the RRDA steps	202
6.1.3: Tensile properties of the RRDA Steps	205
6.1.4: Stress corrosion cracking resistance of the RRDA steps	207
6.1.5: Microstructure of RRDA samples compared to relevant industrial tempers	208
6.1.6: Tensile properties of the RRDA strategy compared to relevant industrial tempers	218
6.1.7: The RRDA strategy corrosion properties compared to relevant industrial tempers	220
6.2: Discussion	222
6.2.1: The design of the RRDA strategy	222
6.2.2: The evolution of microstructure and final properties during the RRDA steps	227
6.2.3: Microstructure of RRDA samples compared to relevant industrial tempers	234
6.2.4: The optimisation of the HFQ® aging step	237
6.2.5: Simulated GBP composition with varying aging parameters	240
6.2.6 The effect of aging parameters on corrosion properties	241
6.2.7: Impact of the research findings	243
Chapter 7: Conclusions	245
7.1: Key findings	246
7.2: Optimised heat treatment pathways for the HFQ® process	249
7.3: Future work	252
References	254

Abstract

In the automotive sector, high-strength aluminium alloys have recently been considered a valid alternative to steel for highly stressed car body panels; the use of such alloys might reduce the automobile environmental impact and increase passenger safety. However, as the production of car frames based on high-strength aluminium alloys raises both formability and heat treatment challenges, new technologies are needed to address these manufacturing difficulties.

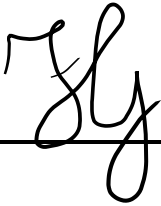
HFQ[®] is an innovative hot stamping process which might solve the described production challenges and promote the diffusion of high-strength aluminium alloys among car manufacturers. To reach the required productivity levels and ensure acceptable final properties in the auto panels, a fine-tuning of the HFQ[®] heat treatment parameters is still needed. Therefore, this study aims to optimise the HFQ[®] heat treatment sequence based on the metallurgy of 7000 aluminium alloys.

Transmission electron microscopy, small-angle x-ray scattering and differential scanning calorimetry are the main techniques used for microstructural characterisations. Meanwhile, uniaxial tensile tests and U-bend stress corrosion cracking (SCC) experiments exemplify the mechanical and corrosion properties of the samples. The HFQ[®] heat treatment sequence consists of solution heat treatment, cooling, and aging steps. During the cooling step, aluminium blanks are simultaneously shaped into the final component.

When AA7075 is used as reference material, it is suggested that the optimal solution heat treatment duration strictly depends on the heating rate used to reach the solution heat treatment temperature. Specifically, the adoption of high heating rates can reduce the required holding time to just 1–2 minutes. This study also confirms that moderately reducing the cooling rate from the maximum achievable can greatly improve the SCC resistance of the workpieces without compromising their hardening potential. Finally, it is suggested that the use of multi-step aging strategies can greatly reduce the required aging duration, delivering improved SCC resistance compared to peak aged samples and similar mechanical properties.

Declaration of originality

I hereby confirm that no portion of the work referred to in the thesis has been submitted in support of an application for another degree or qualification of this or any other university or other institute of learning.

X 

Copyright statement

- I. The author of this thesis (including any appendices and/or schedules to this thesis) owns certain copyright or related rights in it (the “Copyright”) and s/he has given The University of Manchester certain rights to use such Copyright, including for administrative purposes.
- II. Copies of this thesis, either in full or in extracts and whether in hard or electronic copy, may be made only in accordance with the Copyright, Designs and Patents Act 1988 (as amended) and regulations issued under it or, where appropriate, in accordance with licensing agreements which the University has from time to time. This page must form part of any such copies made.
- III. The ownership of certain Copyright, patents, designs, trademarks and other intellectual property (the “Intellectual Property”) and any reproductions of copyright works in the thesis, for example graphs and tables (“Reproductions”), which may be described in this thesis, may not be owned by the author and may be owned by third parties. Such Intellectual Property and Reproductions cannot and must not be made available for use without the prior written permission of the owner(s) of the relevant Intellectual Property and/or Reproductions.
- IV. Further information on the conditions under which disclosure, publication and commercialisation of this thesis, the Copyright and any Intellectual Property and/or Reproductions described in it may take place is available in the University IP Policy (see <http://documents.manchester.ac.uk/DocuInfo.aspx?DocID=24420>) in any relevant Thesis restriction declarations deposited in the University Library, The University Library’s regulations (see <http://www.library.manchester.ac.uk/about/regulations/>) and in The University’s policy on Presentation of Theses.

Acknowledgements

I would like to express my sincere gratitude to EPSRC, Advanced Metallic Systems CDT and Impression Technologies Ltd for the financial support provided.

A special thanks also goes to my academic supervisors, Professor Joseph Robson and Professor Michele Curioni, for their assistance and feedback throughout every stage of my research project.

In addition, I would like to acknowledge my industrial supervisor, Doctor Richard Hunt, for his incredibly useful suggestions and expertise on the HFQ[®] process.

My appreciation extends as well to my colleagues, particularly Ziyu Ma and Yichao Yao, for all the help provided along the way.

Similarly, I would like to express my appreciation for the technical assistance provided from the technicians with whom I was in contact, especially Doctor David Strong and William Asheshov.

Finally, I would like to thank my family and friends for the emotional support they offered throughout the years of my PhD studies.

Chapter 1:

Introduction

Interest is growing among car manufacturers regarding the use of high-strength aluminium alloy sheets for stress-constrained frames in car bodies. However, implementing a cost-effective process for these components is challenging, due to manufacturing difficulties related to the formation and heat treatment of these alloys.

HFQ[®] (Hot Form Quench), a novel hot stamping process patented by Impression Technologies Ltd, is aimed at overcoming these difficulties and expanding the use of high-strength aluminium alloys in the automotive sector. Despite its effectiveness, the HFQ[®] process still needs to be optimised to make it applicable on an industrial scale.

The aim of this research is to develop a metallurgical optimisation of each step in the HFQ[®] process to minimise the manufacturing time while preserving acceptable levels of the material's key properties.

This introductory chapter presents the background of the research topic and defines the research questions. Additionally, the aims, objectives, significance and limitations of the work are discussed.

1.1: Background of the research topic



Figure 1.1: An example of a car body with a monocoque design [1].

In modern car design, the car body (Fig.1.1) is the structural frame that supports all the other vehicle components. In case of an impact, all the parts of the car body act together to avoid injuries to passengers. The portions of the car body that are not in direct contact with the crew, the so-called crumple zones, deform extensively to absorb the highest fraction of the kinetic energy transmitted to the car. At the same time, the components of the car body that are in direct contact with passengers (e.g., pillars, side impact bars, floor and roof frames) exhibit limited deformation to prevent their intrusion into the cabin. This creates a safety cage for the passengers, the so-called roll cage.

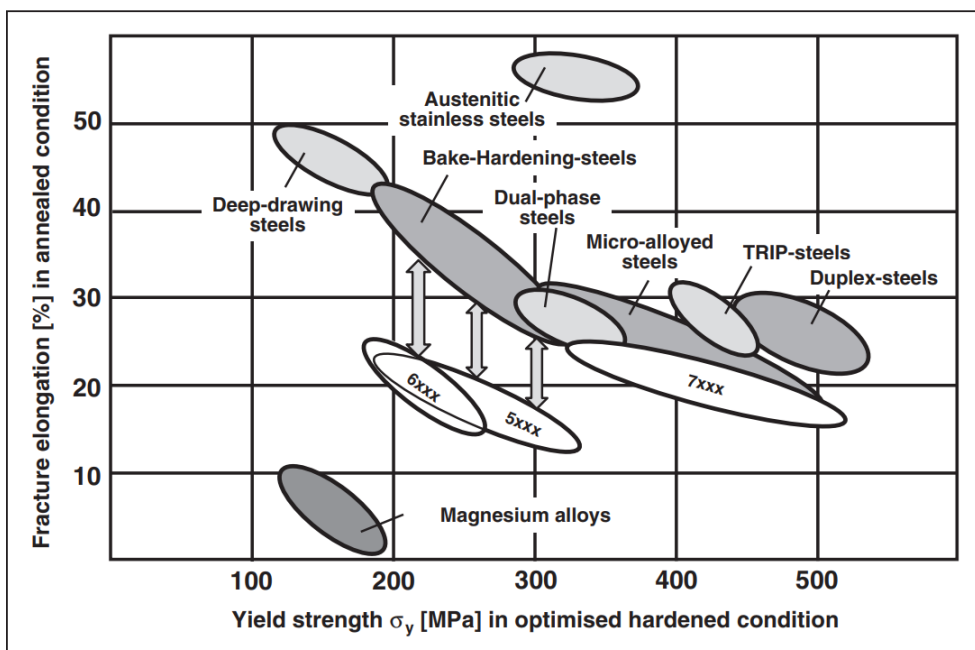


Figure 1.2: An illustration of the ranges of yield strength and fracture elongation for different classes of materials that are relevant for the automotive sector [2].

For such components, a key parameter guiding the choice of material is the yield strength. A structural frame subjected to stress superior to its yield strength will deform plastically, irreversibly losing its original shape and potentially injuring the passengers.

Due to its high yield strength compared with other materials (Fig.1.2), steel has been the most frequent choice among manufacturers for these structural frames. However, the use of 7000 aluminium alloys (with Zn, Mg and Cu as main additions) is becoming an attractive option in the automotive sector, leading to fierce competition between this group of alloys and the latest classes of steel that have been developed.

When considering yield strength, 7000 aluminium alloys exhibit a lower value for this parameter than steel. However, because the aluminium density is approximately just one-third that of steel, a roll cage frame made of a 7000 aluminium alloy can deliver the same strength performance as one made of steel, once it has been ensured that the aluminium frame has a slightly wider section. The strength per unit density of 7000 aluminium alloys is comparable to that of steel, if not superior; therefore, choosing aluminium for safety cage elements could result in a lighter car body.

As the European Commission has announced stricter tailpipe emission limits for 2025 – with similar emission targets being set for all major countries, including China, the United States and India [3] – reducing vehicle mass has become one of automotive manufacturers' main goals. Lightweighting is an effective strategy to reduce fuel consumption and the associated tailpipe emissions. The push to save car weight via careful material selection is even stronger when considering that the average customer prefers larger cars with more accessories, which are inherently heavier [4]. A lighter car body would help counterbalance those design choices that are based on customers' preferences.

In addition to the strength-to-weight-ratio considerations, a relevant parameter guiding material selection for structural frames in car bodies is the elongation to fracture, which dictates how extensively a component can be plastically deformed before fracturing. Usually, 7000 aluminium alloys are characterised by an elongation to fracture comparable to certain classes of steel (Fig.1.2).

Therefore, using aluminium frames instead of steel frames does not increase the fragmentation risk of safety cage components in the event of a car accident [5].

Modern car designs meet safety standards regardless of whether they use aluminium or steel, and steel structural frames are still dominant in the automotive industry [6]. Due to the cost difference between components made of these two materials (aluminium components are at least two to three times more expensive than those made of steel [5,6]), aluminium structural frames are currently used mainly in high-end cars, such as the Audi A8, the Jaguar XJ and the Tesla Model X and Model S [7].

A technological effort is needed to make aluminium car body components more affordable and extend their use to other car market segments. Structural frames can be produced successfully from extrusions, castings or sheet forming, depending on the specific car body design strategy. Nevertheless, in the logic of mass production, manufacturing frames from sheet-formed parts would be the most economically advantageous compared with the other options [9].



Figure 1.3: The Audi A8 is an example of a high-end car with high-strength aluminium structural frames [8].

However, although it would be highly beneficial, the sheet forming of car body parts made of 7000 aluminium alloys is still a challenging process, as the forming of a part with a complex shape has to be coupled with the heat treatment schedule required to achieve the desired final properties. The main targets of the heat treatment schedule are competitive mechanical properties (the importance of which has already been highlighted) and acceptable corrosion properties.

In terms of mechanical properties, 7000 aluminium alloys acquire their strength through several different mechanisms: strain hardening, solution strengthening, grain boundary strengthening and precipitation hardening. Precipitation hardening is currently the most important for 7000 aluminium alloys, as it is the main mechanism technologically exploited to increase the strength of these alloys dramatically.

Due to the presence of alloying elements in the material, secondary phases can nucleate and grow in the aluminium matrix, depending on their thermodynamic stability. Atomic composition, volume fraction, size distribution, shape and coherency with the matrix of these secondary phases are among the factors that influence their ability to hinder dislocation movement, thereby strengthening the material. Among these secondary phases, precipitates – which are artificially generated through a well-defined heat treatment schedule – play a major strengthening role in 7000 aluminium alloys.

The heat treatment schedule to promote precipitation hardening consists of three steps: solution heat treatment, cooling and ageing treatment (Fig.1.4).

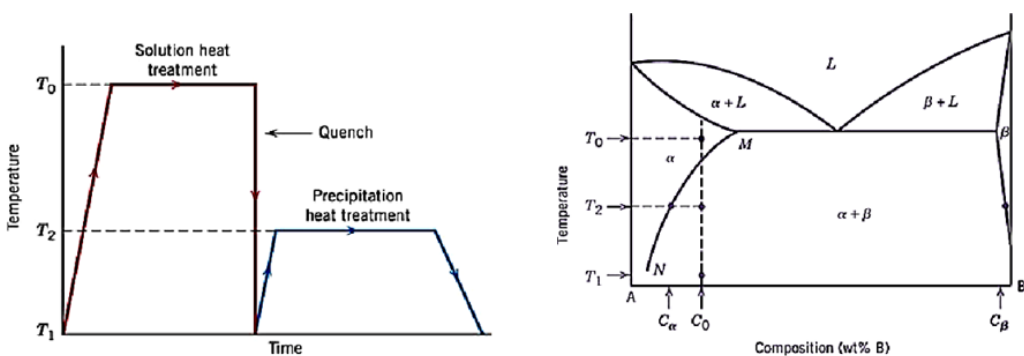


Figure 1.4: The heat treatment sequence represented in a time-temperature diagram (left) and the corresponding schematic phase diagram [11].

Solution heat treatment involves heating samples above the solvus temperature, resulting in a homogeneous distribution of the alloying elements in the aluminium matrix. Subsequently, rapid quenching to room temperature places the samples in a condition of supersaturated solid solution. For 7000 aluminium alloys, it is generally accepted that Guinier-Preston zones (GP zones) are the first type of metastable precipitate to form from a condition of supersaturated solid solution. GP zones transform into metastable η' precipitates, and the thermodynamically stable η phase evolves from η' precipitates.

The supersaturated solid solution is characterised by a high thermodynamic driving force for nucleation and growth of precipitates but a limited velocity of formation, due to a low kinetic driving force.

Therefore, a final ageing treatment at a temperature below the solvus is required to accelerate the formation and growth of these precipitates, which, in turn, are responsible for a considerable strength increase in the material. For example, the

yield strength of aluminium alloy 7075 can improve from 145 MPa to roughly 500 MPa when it is subjected to the precipitation hardening heat treatment sequence [10].

The precipitation hardening heat treatment's thermal path influences not only the mechanical properties of the workpiece but also its corrosion properties. A particularly relevant corrosion property for this class of alloys is stress corrosion cracking (SCC) resistance, which can increase the car component's risk of unexpected failures if not carefully optimised. Maximising the workpiece's corrosion properties via heat treatment generally leads to a worsening of its mechanical properties and vice versa; thus, the first challenge in the manufacturing of 7000 aluminium alloys is selecting the appropriate heat treatment parameters (temperatures, holding times for each step and heating and cooling rates) to balance the mechanical and corrosion properties.

Additionally, sheet forming must be integrated into the heat treatment sequence, which further complicates the manufacturing process. The formability of the workpiece and, consequently, the success of the shaping operation greatly depends on when the forming step is planned regarding the heat treatment schedule, as each thermal step modifies the properties of the sheet. For example, the strength improvement gained from the precipitation hardening sequence is linked to a marked reduction in formability of the sheet; therefore, a post-ageing stamping process performed at room temperature would generally lead to the failure of the component [12]. Additionally, the auto panel might lose its geometrical accuracy when the tools loading is removed due to the springback phenomenon [13], the severity of which is higher for room temperature operations [14].

It is widely accepted in the literature that the formability of 7000 aluminium alloys is generally inadequate at room temperature for correctly shaping the workpiece in its final form. Nevertheless, different approaches to making this operation possible are under investigation.

In the O-temper process, sheet stamping is completed before the workpiece is subjected to the heat treatment schedule. Therefore, research efforts are made to tailor the upstream processes of sheet formation from the as-cast metal to

maximise formability [15]. However, this process has a major disadvantage: When the formed part is subjected to solution heat treatment and quenching, the thermal distortion associated with the cooling stage can affect the geometrical accuracy of the workpiece [16]. A different approach has been tried in the W-temper process, where the forming operation is completed directly after quenching. This process is still under development, and current experiments are focused mainly on understanding its characteristics and comparing it with other available forming operations [13,17].

Samples that have been solution heat treated and are in the condition of supersaturated solid solution need to be formed immediately, as their formability worsens rapidly due to the onset of ageing at room temperature (so-called natural ageing [18]). A second drawback is the possible interaction of solutionised alloying elements with moving dislocations during the forming operation, known as the Portevin-Le Chatelier effect. This phenomenon can lead to surface inhomogeneities in the part and can corrupt the quality of the final product [19].



Figure 1.5: Aluminium auto panels formed at room temperature (left) and at 250°C (right) [20].

When carrying out the forming operation at temperatures above room temperature, aluminium sheets show improved formability and a less severe springback (Fig.1.5). The so-called warm forming processes involve forming steps performed at temperatures below the recrystallization temperature of the aluminium alloy sample, in a temperature range similar to that of ageing treatments. Therefore, warm forming alters the microstructure of the workpiece,

and a careful design must be applied when integrating this step into the precipitation hardening heat treatment sequence.

The two possible approaches under investigation are: locating the warm forming step after the ageing treatment [21,22] or between multiple ageing steps [23,24]. An alternative approach is to conduct the forming operation directly from the solution heat treatment, so that the forming and quenching steps are performed together. With this strategy, the improved formability is exploited during forming, while the rapid quenching eliminates the risk of undesirable microstructural changes.

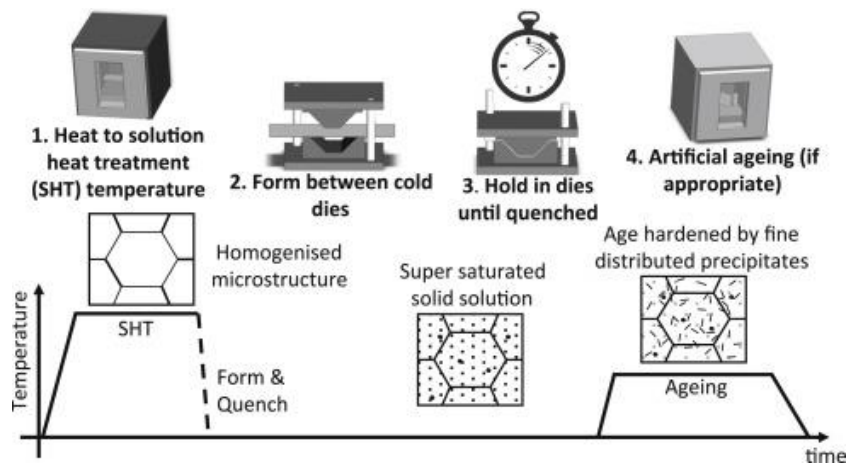


Figure 1.6: A schematic representation of the HFQ® processing sequence (top) and the associated temperature profile experienced by the workpieces [27].

The sequence of solution heat treatment, forming during quenching and ageing is known as the Hot Form Quench (HFQ®) process and has been patented by Impression Technologies Ltd (Fig.1.6). HFQ® offers several advantages in the manufacturing process. For example, overall productivity benefits from the thorough integration of the forming and heat treatment steps. Moreover, as the workpiece is held between the dies during quenching, it undergoes lower levels of thermal distortion and springback, resulting in higher geometrical accuracy [25] The ability to obtain complex shapes also allows for less reliance on joining techniques. The HFQ® process undoubtedly already constitutes a step towards the more affordable production of high-strength aluminium auto panels; however, further research is needed to make the process competitive in terms of cost [26].

The biggest opportunities for cost reduction in the HFQ® process are related to the supply and recycling of the blank material, the improvement of cutting

operations, the lubrication management in the press and better control of the heat treatment schedule [26]. As this work focuses on the metallurgy of 7000 aluminium alloys, optimisation of the heat treatment schedule is the only cost-reduction opportunity explored here. The heat treatment parameters must be tailored to reduce manufacturing time while preserving an acceptable balance of key properties [26]. A simplification strategy is needed to approach this complex problem, even when focusing only on this aspect of HFQ[®] optimisation, due to the large number of variables involved in the heat treatment sequence and their possible interaction.

In the HFQ[®] process sequence (Fig.1.6), the blanks are heated up to solution heat treatment temperature through a circulating air furnace before being automatically transferred to the stamping stage. The press action shapes and cools down the workpiece during the cooling step, and ultimately, the auto panel undergoes the final aging treatment. In this study, each step of the heat treatment sequence (the solution heat treatment, cooling and ageing) is investigated separately; this eliminates the interaction problem in the heat treatment steps, but it affects the completeness of the study.

The interaction among different steps is not considered. For example, the combined effect of the cooling and ageing strategy on the panel's final properties has not been investigated. However, due to its relevance, the problem of the interaction between the various steps is discussed on a theoretical level.

A second limitation relates to the effect of deformation during the cooling step. As most of the samples in this study are not HFQ[®]-processed parts, they have just been cooled instead of being cooled and shaped simultaneously. Therefore, the effect of deformation on the microstructure evolution during HFQ[®] is examined only briefly. Additionally, the experiments are conducted using only one type of 7000 aluminium alloy, thereby excluding the effect of the alloy chemistry from the optimisation process. Excluding the deformation step implies that the tuning of the heat treatment parameters is not aimed at maximising the formability of the panel during the press stage.

1.2: Research questions

The foundation of the optimisation process is understanding the current knowledge regarding each of the heat treatment steps and evaluating the literature gaps that need to be filled. The use of sheets in the HFQ® process has been shown to shorten the solution heat treatment compared with the treatment of thicker components, thereby improving the overall productivity of the process [26,30,31]. The reduction in treatment duration is also known to be larger if the temperature used is higher than the usual values employed to treat thicker workpieces [30,31,32].

However, this temperature raise is subject to boundaries, and it is still not possible to deduce a safe limit for the solution heat treatment temperature from the literature, as the available information is somewhat contradictory [31,32]. Additionally, it is not well documented how both a shorter duration (below 10 minutes) and the range of temperatures discussed influence precipitate dissolution.

The heating rate to reach the solution heat treatment temperature is also an important parameter to tailor. The notion that an increased heating rate accelerates the dissolution of precipitates and influences the sample texture is relatively new in the literature [33,34]. Consequently, the effect of the heating rate on the microstructural evolution and the dissolution process must be consolidated. This is not only important from a theoretical point of view – optimising the heating rate could be exploited to shorten the duration of the solution heat treatment step in the HFQ® process.

Regarding the cooling step, most of the experimental research stresses the importance of applying the maximum possible cooling rate to preserve the material's hardening potential [31,35,36]. However, even if not directly related to the HFQ® process, different studies on the precipitation hardening sequence of 7000 aluminium alloys suggest that a reduction in the cooling rate can improve the SCC resistance of the workpiece [37,38].

The tuning of the cooling rate to balance strength and the SCC resistance of samples subjected to HFQ® is still not well documented and needs to be

consolidated. From a microstructural point of view, it is well known that lowering the cooling rate can lead to an increase in the average size of grain boundary precipitates (GBPs) and their interparticle distance, as well as a widening of the precipitates-free zones (PFZs).

However, these microstructural parameters are reported in the literature mostly as averaged values; a beneficial improvement in this microstructural characterisation would require a statistical approach using the distributions of these parameters [37,39,40].

This approach, which is rare in the literature, would consider the heterogeneity of the grain boundary (GB) microstructures in a more suitable way and would expand the understanding of the linked properties [37,39,40]. Another gap in the literature involves the effect of the cooling rate on the GBP composition and on the segregation of solute elements in GBs [37,38,41]. It is well known that during isothermal holding, the copper content of GBPs increases with increased temperature and treatment duration, which, in turn, improves the SCC resistance of the workpiece [42,43]. However, the relationship between the cooling rate and GB microchemistry is still a subject of debate and remains poorly documented [37,38,41].

Finally, while consensus exists in the literature regarding the strength reduction caused by slow quenching, the influence of this cooling rate on matrix precipitation is still unclear. It is still a matter of debate whether the loss of solute atoms is confined just to the GB regions or whether it also extends to the grain interior [44,45,46,].

As the cooling operation is usually performed at the highest possible rate during the HFQ® process, the target mechanical and corrosion properties of the panel must be achieved in the final ageing step.

However, the optimisation of the ageing step is somewhat constrained, as the body panels produced are always subjected to an additional thermal step during paint baking (the car manufacturing step in which the final coatings and paint are cured). Therefore, the approach used involves applying an isothermal ageing step known as pre-ageing, which, when integrated into paint baking, delivers the final properties in the panel.

It is consolidated in the literature that using the pre-ageing step prior to paint baking can result in similar mechanical properties in the workpiece as peak ageing treatments [47,48], while the evaluation of SCC resistance for samples subjected to this new ageing strategy has not been documented. The time span between pre-ageing and paint baking can influence the sample's final properties due to the effect of natural ageing, and the hardening response triggered during paint baking can be compromised if this effect is too pronounced.

Therefore, a second aim of the pre-ageing step is to stabilise the workpiece and ensure a negligible strength increase during the natural ageing period. Pre-ageing treatments optimised to prevent the onset of natural ageing have been designed for different 7000 aluminium alloys, but this goal has not always been successfully achieved [49,50]. Better coverage in the literature is necessary for both the design process and the understanding of the microstructural evolution linked to the time interval between pre-ageing and paint baking.

An analysis of the literature regarding ageing optimisation not directly related to HFQ® shows it is generally agreed that peak aged samples display the best mechanical properties but are prone to SCC, while overaged samples gain an acceptable SCC through sacrificing some of their strength and toughness.

Additionally, both of these traditional ageing strategies would compromise the productivity of the HFQ® process due to their duration. It has also been documented that for 7000 aluminium alloy sheets, the retrogression and reaging (RRA) strategy can deliver mechanical properties similar to those in samples subjected to peak ageing, as well as SCC resistance comparable to that of overaged samples [51,52]. The duration of this heat treatment is similar to that of the two abovementioned ageing treatments.

RRA also involves a more complex time-temperature ageing profile than the peak or overaging treatments; the trend of increasing the complexity of ageing time-temperature profiles is currently most frequently explored in the literature for the optimisation of this step. Various examples of these strategies (usually referred to as non-isothermal or multi-step strategies) can impart acceptable mechanical and corrosion properties in the final panel, while considerably reducing the duration of the ageing treatment [53,54]. While a description of the

microstructural changes triggered by time-temperature ageing profiles is usually provided in these studies [53,54], it is still necessary to obtain more experience of and control over how these microstructural changes can be determined. Moreover, a multi-step ageing strategy design for HFQ[®], and possible integration with the paint baking step, still has not been reported.

1.3: Research aims and objectives

Historically, 7000 aluminium alloys have been predominantly utilised as materials for stress-constrained components in the aerospace sector.

Consequently, most of the research pertaining to heat treatment optimization has been tailored to components with large cross-sections, such as airplane landing gears, without productivity constraints due to the limited production volumes in this industry.

For example, extensive investigations have already been carried out on the use of prolonged aging treatments or limited heating rates during solution heat treatments. However, the use of 7000 aluminium alloy sheets in the HFQ[®] process, coupled with the productivity constraints of the process, hinders the direct application of most of this specific knowledge regarding heat treatments.

Therefore, it is necessary to explore more unconventional heat treatment regimes in greater detail to optimize the HFQ[®] process. Additionally, this specific area of the literature has not been fully consolidated yet.

The general aim of this study is the metallurgical optimisation of the HFQ[®] heat treatment schedule. More specifically, the main goal is to design solutions for reducing the process manufacturing time while preserving the maximum achievable component strength and ensuring an acceptable level of SCC resistance. The approach focuses on investigating each step separately, while the interaction among all heat treatment steps is discussed theoretically.

Regarding the solution heat treatment step, the aim is to accelerate the dissolution process under different heating rate conditions without negatively altering the sample's microstructure. The effect of short holding times and temperatures above the common industrial practice is explored for the typical convective furnace heating rate; additionally, the effect of short exposures at high temperatures on the sample grain structure is examined. Further experiments are conducted to confirm the advantages of raising the heating rate and to understand this parameter's effect on the dissolution process.

Regarding the cooling step, the main aim is to find an optimum cooling rate that enhances the SCC resistance of the workpiece without reducing its hardening potential. Another aim is to improve the understanding of the cooling rate's effect on the microstructural evolution. Therefore, both the SCC resistance and tensile properties of samples cooled at different rates are examined.

Subsequently, those properties are linked to the microstructural changes in the material – the precipitation at GBs is studied using distributions of the relevant microstructural parameters and modelling approach to characterise the GB microchemistry. Experiments are also conducted to evaluate the effect of the cooling rate on the subsequent matrix precipitation.

The main goal in terms of ageing treatment optimisation is to propose a multi-step ageing strategy that delivers near-peak ageing mechanical properties and satisfactory SCC resistance while reducing the treatment time compared with the duration of traditional ageing strategies. Ideally, this new strategy could be integrated into the paint baking step to boost the overall productivity of the HFQ® process.

A second aim is to characterise the microstructure of samples subjected to the new ageing strategy designed to link the complex time-temperature profile to the microstructural changes imparted. Consequently, a new multi-step ageing strategy is designed, and its effect on tensile properties and SCC resistance are studied. These properties are also compared with those resulting from the use of industrially relevant tempers for 7000 aluminium alloy sheets. Additionally, the same microstructural characterisation methods applied in the cooling rate section are used to understand the link between ageing parameters and the microstructural features that are developed. The effect of natural ageing on the multi-step strategy is studied, and the possible integration into the paint baking step is discussed on a theoretical level.

1.4: Research scope

Identifying and acknowledging limitations is crucial in any research, as it helps expand the understanding of the topic being investigated. In this study, the focus is on optimizing the metallurgical aspects of the HFQ[®] heat treatment schedule. A comprehensive exploration of all the possible improvements of the HFQ[®] process would necessitate a multidisciplinary approach, encompassing various engineering areas. Even within the scope of metallurgical aspects, the study's duration imposes further constraints, requiring a narrower examination. Consequently, the study breaks down the HFQ[®] process into the three sequential steps: solution heat treatment, cooling, and ageing, each analysed and optimized independently. Nevertheless, the study acknowledges the theoretical discussion on the interaction between the steps due to its significance.

Another limitation pertains to the effect of deformation during the cooling step. Since most of the samples used in this study are not HFQ[®]-processed parts, they have only undergone cooling without simultaneous shaping. Therefore, the examination of deformation's influence on microstructure evolution during HFQ[®] is only briefly addressed. Additionally, the experiments conducted solely employ one type of 7000 aluminium alloy, thereby excluding the impact of alloy chemistry from the optimization process. By excluding the deformation step, the tuning of heat treatment parameters does not prioritize maximizing the panel's formability during the press stage.

1.5: Significance of the research

The life cycle assessment (LCA) is a rigorous methodology to assess the environmental impact of an industrial process, and it considers all the inputs, manufacturing steps and outputs related to the process. Different studies applying the LCA methodology to HFQ[®] revealed its potential to benefit the environment. For example, Peppas et al. [55] compared the LCAs of two different vehicles, the first made with a reference amount of steel and aluminium components and the second with an enhanced quantity of aluminium panels produced via HFQ[®]. It emerged that this replacement results in less energy-intensive forming operations, lower fuel consumption and greater recyclability.

As opposed to focusing on the effect of substituting steel components with HFQ[®] aluminium panels, Raugei et al. [56] compared the LCA of two vehicles with the same amount of aluminium panels. In the first car, those panels were produced with conventional manufacturing technology, and in the second they were manufactured using HFQ[®]. The results show that even if HFQ[®] is more energy-intensive than other aluminium manufacturing processes, the enhanced recyclability of the HFQ[®] panels means the environmental impact is lower overall.

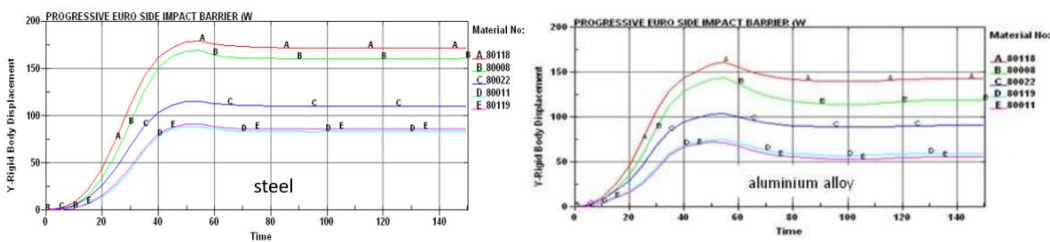


Figure 1.7: B-pillar displacements plotted against the side impact barrier impact time when using (a) steel and (b) a high-strength aluminium alloy [57].

The LCA evaluations in these studies involved an unoptimised HFQ[®] process. Therefore, optimising the process would result in an even greater increase in environmental benefits. As this study is focused on upgrading the HFQ[®] heat treatment schedule, mitigating the environmental impact of the aluminium panel production is industrially relevant. In addition to the environmental benefits mentioned, the HFQ[®] heat treatment optimisation would result in the more

consistent use of aluminium body panels in cars, possibly also leading to improved safety. Several recent studies have pointed out that using high-strength aluminium structural components can enhance vehicles' crashworthiness. For example, the simulation research by Qiao et al. [57] showed that substituting a steel B-pillar with a high-strength aluminium B-pillar improved the overall crashworthiness of the vehicle, with the intruded part of the B-pillar being less prominent during a collision when using an aluminium alloy (Fig.1.7).

Lee et al. [58] found a slight advantage in automobile crashworthiness when using a high-strength aluminium bumper instead of the consolidated steel option. As highlighted in the research questions, studying HFQ® heat treatment parameters is also important from an academic point of view, as it deepens the knowledge of the precipitation hardening sequence of 7000 aluminium alloys, contributing to filling gaps in the existing related literature.

1.6: Outline of the research

In the introductory chapter, the research topic is introduced, providing fundamental background information. The study aims, objectives, and identified literature gaps are also outlined. Additionally, the significance of the research, along with its limitations, is presented.

The literature review chapter provides a comprehensive overview of the existing literature on the research topic. Detailed discussions are conducted to identify research gaps.

Moving to the materials and methods chapter, a complete experimental plan is presented, including the outline of the experimental design and an explanation of the relevant experimental techniques.

The experimental results and discussion are organized based on the specific step of the heat treatment schedule they focus on, which includes solution heat treatment, cooling, or aging. The findings are explained, compared with the existing literature, and their significance and relevance to the research questions are discussed.

Consequently, in the conclusions chapter, the main findings are summarized. Optimized HFQ[®] heat treatment pathways are presented, and a brief discussion is provided on the potential interaction between different heat treatment steps. Additionally, suggestions for future contributions are summarized.

Chapter 2:

Literature review

In this chapter, the relevant studies linked to the metallurgical optimisation of the HFQ® process are reviewed, and the emerging literature gaps are identified. The fundamental knowledge needed to understand the current state of the research is also briefly summarised.

The topics are presented following the order of the heat treatment schedule for the HFQ® process (solution heat treatment, cooling step and aging treatment).

2.1: The production of F-tempered 7000 aluminium alloy sheets

In this work, F-tempered 7000 aluminium alloy sheets are the starting material to which the experimental precipitation hardening heat treatments are applied. The F-tempered sheets develop their characteristic microstructure through the production upstream processes that start with aluminium extraction. The Hall-Heroult process, for example, is a continuous electrochemical separation method to extract aluminium from bauxite. In the electrochemical cell, the pure aluminium is removed as a molten metal. Afterwards, the molten aluminium is alloyed and then casted. In 7000 aluminium alloys – besides the main additions

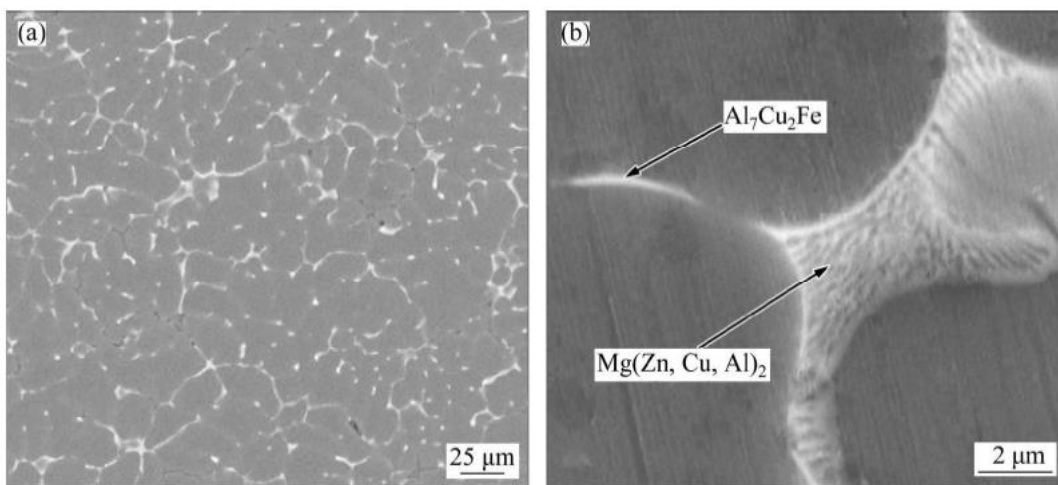


Figure 2.1: (a) Eutectic net surrounding grains in an as-cast AA7075 sample and (b) magnification of the eutectic phase [60].

of Zn, Mg and Cu – Fe, Si, Mn, Cr, Ti and Zr are also present. The casting method is called direct chill (DC) casting: the molten aluminium flows in a case surrounded by a cool water jacket where it experiences a non-equilibrium solidification, which leads to the formation of a ‘cored’ structure. In fact, its alloying elements are distributed with a concentration that decreases when moving from the grain boundaries towards the inner parts of the grains. Each grain is also surrounded by an eutectic layer (Fig.2.1, a) constituted by the η (MgZn₂) phase enriched by dissolved Al and Cu atoms (Fig.2.1, b) [59,60]. Due to having extremely low solubility, the second phases bearing Fe and Si are the first to precipitate during solidification, reaching dimensions in the micrometric range. These second phases are called constituents and persist during the subsequent stages of the sheet production; Al₇Cu₂Fe and Mg₂Si are some of the

most abundant constituents in 7000 aluminium alloys [34,61]. The second phases η , θ (Al_2Cu), T ($\text{Al}_2\text{Mg}_3\text{Zn}_3$) and S (Al_2CuMg), referred to as precipitates, also form

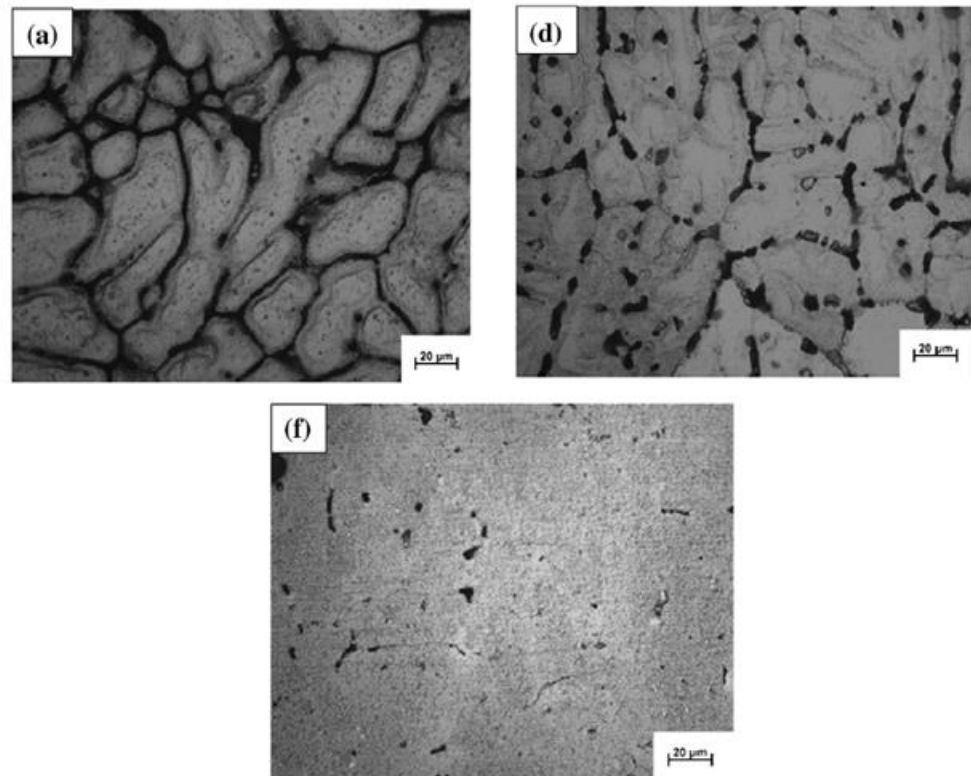


Figure 2.2: Example of an AA7075 sample homogenized at 465 °C for (a) 15 min, (d) 24 h and (f) 96 h [59].

during solidification, but their high solubility in the aluminium matrix means their distributions are highly affected by the downstream manufacturing stages [59]. To eliminate the eutectic layer and the alloying elements gradient concentration, the material is subjected to a long homogenisation treatment (Fig.2.2). The precipitates dissolve during this step, and because the material becomes supersaturated in Cr, Zr and Mn, another class of second phases, called dispersoids, precipitate in the workpiece. In terms of size range, dispersoids usually measure hundreds of nanometres in length: because the solidification gradient concentration of alloying elements and the deformation steps that follow homogenisation, dispersoids are mostly distributed in bands or layers in the microstructure [34,61]. After the homogenisation treatment, different stages of hot and cold rolling impart the final sheet thickness to the workpiece and help the grains develop their final characteristic texture: a ‘pancake-shaped’ structure. They are elongated in the rolling direction of the sheet and equiaxed toward the other two axes (Fig.2.3). During these deformation steps, precipitates

form again and continue to grow even after the manufacturing process is finished due to natural aging.

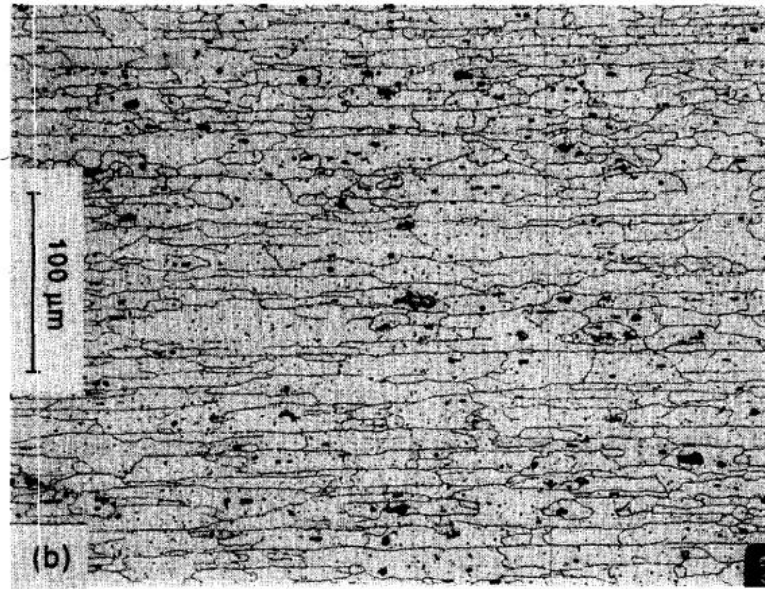


Figure 2.3: Typical grain structure of AA7075 sheets (RDxST) plane [61].

2.2: Summary of the literature related to the HFQ® process

HFQ® is an innovative hot stamping process designed for metallic sheets and successfully applied to high-strength aluminium alloys. This technology combines the cooling step typical of the precipitation hardening sequence with the forming operation (Fig.2.4).

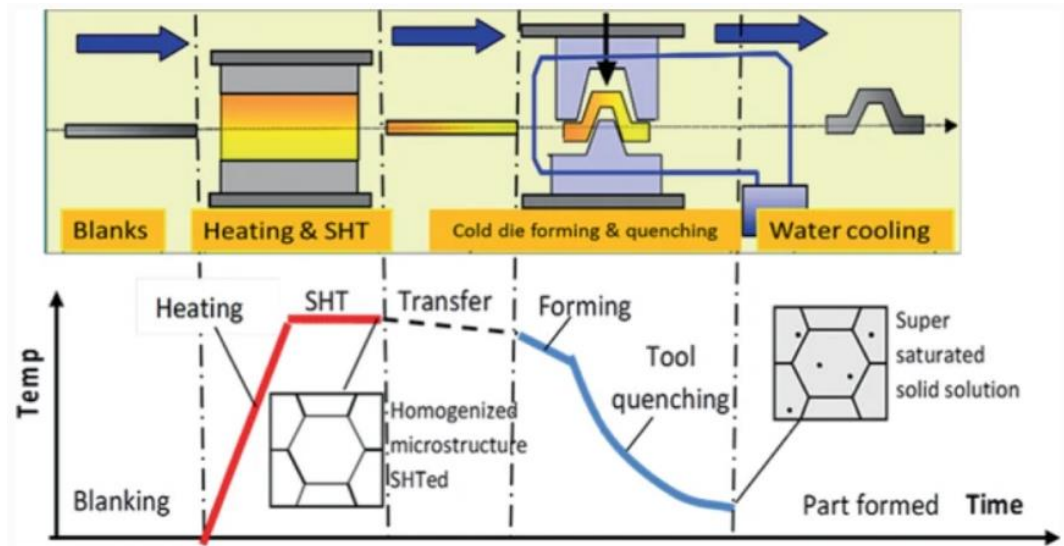


Figure 2.4: Schematic representation of the core part of the HFQ® process (top) and associated time-temperature profile (bottom), where cooling and forming steps are combined [62].

In fact, the aluminium blanks are first heated to solution heat treatment temperature and then immediately transferred to the press, where the cooling and shaping steps occur simultaneously. The high temperature imparted allows the solute elements to be evenly distributed in alloy and to exploit the superior formability associated with hot flow behaviour. During the forming step, the workpiece is also rapidly cooled to room temperature while held between the dies: this process allows for preserving the maximum concentration of alloying elements in the solid solution and reaching an optimal final geometrical accuracy of the formed auto panel. The precipitation hardening sequence is completed and the properties of the components are adjusted with the final aging treatment.

Studies potentially related to the optimisation of HFQ® are a broad section of the scientific literature. Indubitably, the core of the process and the most challenging

step is the shaping and quenching under the action of cold dies, to which a good share of the literature about HFQ® is related.

In this share of works, a first group of studies presents the following typical structure: the cooling path after solution heat treatment is varied experimentally to study how the formability under the press is thereby influenced and which microstructural changes in the workpiece are triggered. Lastly, the post-process mechanical properties are evaluated [35,36,63,64,65]. Modifying the time to transfer to the dies [36], changing the temperature of the dies [35] and dividing the cooling step in a sequence of more steps with precooling [63] are all examples of cooling rate path variation.

Regarding the cooling and shaping step, a second topic investigated in the literature relates to the technological characteristics of the forming step that allow the best outcomes in terms of geometrical accuracy, uniformity of thickness and surface quality of the workpiece [66,67,68,69]. This category includes works that study friction and lubrication between the dies and the workpiece [67], the mitigation and compensation of the springback phenomenon [70], and the tribology of the workpiece [69]. Effort has also been made to predict the forming behaviour and final geometrical characteristics of the aluminium auto panels via a modelling approach (Fig.2.5) [64,71].

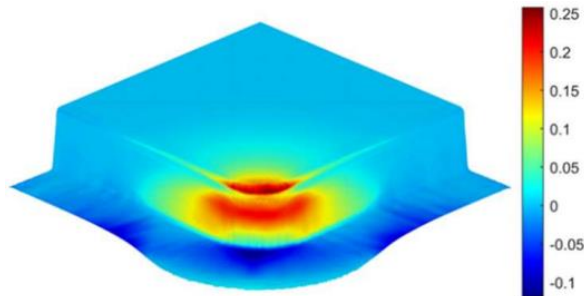


Figure 2.5: Example of finite elements simulation predicting the thickness reduction of the workpiece after the forming step [71].

To support the studies that simulate the deformation and cooling step, another group of contributions focuses on modelling the interfacial heat transfer coefficient between the tool and the alloy [31,32] since this parameter is critical for most of the simulation-based works.

While most of the studies examined are linked to the forming and cooling step, a smaller share of works focuses on either the solution heat treatment step or the aging step. Some studies also aimed to boost the overall productivity by focusing

on the optimisation of solution heat treatment parameters when using the heating rates typical of air-circulating furnaces [31,32].

Other studies instead aimed to accelerate the solution heat treatment experiments in more efficient ways to heat up the material and raise the heating rate [33,72]. Regarding the aging step, a few investigations focused on the design of a compact aging strategy that can maximise the final auto-panel properties after the paint-baking step [73,74]. Finally, the effect of the HFQ® process on the weldability of high-strength aluminium alloys [75] and the environmental benefits of HFQ® [55] are additional topics that have been investigated in the literature.

2.3: The solution heat treatment optimisation at low heating rates

The role of the solution heat treatment is to dissolve the precipitates derived from the previous thermal history of the material and then uniformly distribute the alloying elements in the aluminium matrix.

In the aircraft industry, where thicker plates are typically used (Fig.2.6) and the production volume is limited, solution heat treatments last multiple hours. Like many other studies focused on the metallurgy of 7000 aluminium alloy thick plates, Robinson et al. [30] heat treated the 82 mm AA7075 blocks for 2 hours at 470 °C. Across the literature, consensus exists



Figure 2.6: Example of a gear manufactured from an AA7075 thick plate [77].

around the solution heat treatment duration when processing high-strength aluminium sheets: the solution heat treatment duration can already be



Figure 2.7: Example of a circulating air furnace used for industrial solution heat treatments of aluminium [78].

consistently reduced, usually in less than 1 hour, due to the limited thickness compared to the thick plates.

A typical example is reported in the work of Moon et al. [76], where the 1 mm thick AA7075 sheets are solution heat treated for 30 minutes at 470 °C.

Because the transfer to the dies and the cooling/forming step last less than one minute in the HFQ® process [28],

even the reduced solution heat treatment step typical of sheet materials would constitute a rate-determining step, hindering the overall productivity of the process [28,29]. For this reason, the use of an accelerated solution heat treatment is a technologically important step. The heating rate to the solution heat treatment temperature (HR), the solution heat treatment temperature (T_{SHT}) and holding time (t_{SHT}) are the parameters that univocally define the solution heat treatment. As circulating air furnaces are commonly used to heat up aluminium blanks [34], the characteristic heating rate for this operation lies

below 10 °C/s [33,34,79]. In this work, heating rates below 10 °C/s are defined as low heating rates, while heating rates above 10 °C/s are defined as high heating rates. For a fixed heating rate HR, the increase of the solution heat treatment temperature T_{SHT} is the only option to reduce the solution heat treatment time t_{SHT} because the thermal stability of the second phases decreases with increasing temperature [81] and the dissolution rate of the second phases is controlled by the diffusion rate of the alloying elements [80].

Regardless of the technological relevance, few authors have dealt with the solution heat treatment acceleration when adopting low heating rates. Therefore, the strategy to raise the solution heat treatment temperature has rarely been adopted and studied. A reason for this gap could be hidden in the fact that homogenisation treatments, which commonly induce incipient melting in the workpiece if the temperature used is higher than the characteristic of the eutectic point, are sometimes also referred to as solution heat treatments in the literature [60,82]. A typical example of a 7000 aluminium alloy microstructure showing incipient melting is shown in Figure 2.8.

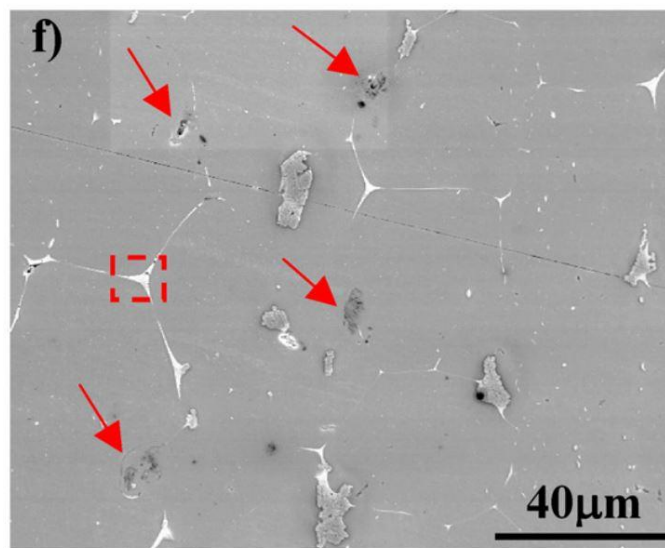


Figure 2.8: Example of scanning electron microscopy micrograph of an AA7150 sample showing signs of incipient melting after solution heat treatment at 515 °C for 1 hour [84].

For example, Zou et al. [60] studied how the homogenisation treatment parameters affect the AA7075 as-cast microstructures but framed the study as an optimisation of the solution heat treatment parameters. Aligning with other papers focused on homogenisation treatments, the researchers proposed an

optimised homogenisation treatment lasting 5 hours at 460 °C, which is safely below the eutectic temperature for AA7075 (475 °C).

The safe practice of choosing a temperature below the eutectic temperature is usually retained when performing solution heat treatments as well, even if workpieces in such cases have already been homogenised. Using calorimetric experiments, various studies assessed the incipient melting onset for homogenised 7000 aluminium alloy microstructures in a temperature range between 475 °C and 500 °C [81]. Yet neither how severe incipient melting should be to degrade the alloy's mechanical properties or how the solution heat treatment temperature affects the extent of this phenomenon is well-documented. In fact, to shorten the solution heat treatment duration, different studies surpassed the safe temperature limit previously discussed and still achieved optimal mechanical properties.

For example, Milkereit et al. [31] carried out solution heat treatment optimisation for AA7075 with low heating rates, exploring temperatures above the eutectic temperature and setting 490 °C as upper-limit temperature. In this range, the researchers did not report degradation of the sample's mechanical properties and selected as optimum solution heat treatment adopting a 15-minute hold at 480 °C.

Instead, in a similar AA7075 solution heat treatment optimisation study performed by Liu et al. [32], the optimum solution heat treatment was established at 510 °C for 30 minutes, while degradation of the mechanical properties and consistent onset of incipient melting were identified only at temperatures as high as 550 °C. While exploring a wide range of temperatures (between 430 °C and 550 °C), the researchers investigated the effect of holding times just equal to or above 10 minutes. These parameters are not completely relatable to the HFQ® process, which would require a further duration reduction. Other studies reported that very short holding times in the 1- to 10-minute range can determine acceptable mechanical properties in the samples, even without increasing the solution heat treatment temperature above the eutectic temperature.

For example, Tanaka et al. [83] used as solution heat treatment parameters of 5 minutes at 480 °C for AA7475, while Xu et al. [84] used 5 minutes at 475 °C for AA7150. In sum, the solution heat treatment step needs to be shortened in the HFQ® process to both boost productivity and improve the synchronisation with the forming/quenching step. However, the necessary temperature increase needed to realise this aim might induce incipient melting in the workpiece and possibly degrade its mechanical properties. Currently, the literature has not yet reached a consensus on how the solution heat treatment should be optimised using a short holding time, nor on how relevant the incipient melting phenomenon is when using temperatures higher than the eutectic one.

2.4: The effect of heating rate on the dissolution process

In this work, solution heat treatments are categorised depending on the value of the heating rate to the solution heat treatment temperature. Heating rates below $10\text{ }^{\circ}\text{C}/\text{s}$, which are typical of circulating air furnaces, are defined as low heating rates, while heating rates above $10\text{ }^{\circ}\text{C}/\text{s}$, which can be achieved with the use of different heating technologies, are defined as high heating rates. The importance of how the heating rate affects in the second phase dissolution process has been confirmed in several studies [33,85]. For example, Zhang et al. [33] compared the mechanical properties of samples after aging that were subjected to solution heat treatment with different heating rates. The samples exposed to the low heating rate ($0.4\text{ }^{\circ}\text{C}/\text{s}$) and traditionally heated for 20 minutes at $475\text{ }^{\circ}\text{C}$ achieved very similar strength levels as samples fast heated ($15.8\text{ }^{\circ}\text{C}/\text{s}$) to $475\text{ }^{\circ}\text{C}$ in just one minute.

In another example, Liu et al. [85] used a radiant heating furnace combined with high emissivity coatings to ensure a high heating rate during the solution heat treatments of aluminium sheets. Because of the rapid heating rate achieved, the coated sheets required only half the duration of the solution heat treatment compared to bare aluminium sheets, which experienced a slower heating rate, in order to attain similar mechanical properties (Fig.2.9).

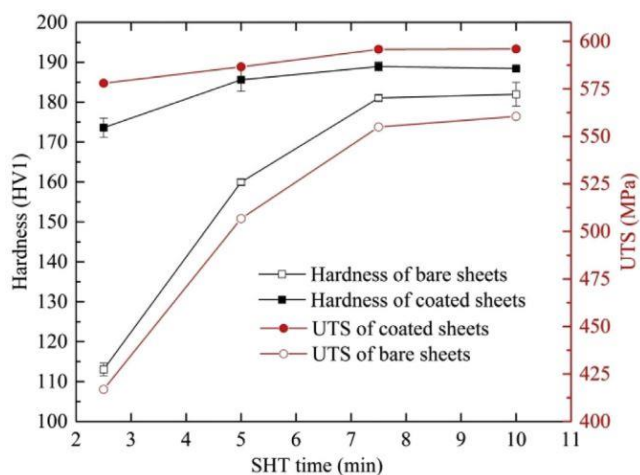


Figure 2.9: Mechanical properties of AA7075-T6 sheets heat treated undergoing various solution heat treatment durations and different heating rates [85].

The noticeable advantage means different technologies are flourishing to allow the adoption of fast heating rates at an industrial level. In the two studies cited

above, the high heating rate was realized through the contact of the aluminium sheet with two hot contact bodies [33] or through exploiting the combination of high emissivity coatings and a radiant heating furnace [85].

Apart from these two methods, other examples include the use of electrical resistance heating [86] or direct exposure to flames [72]. Consensus in the literature already exists around the advantage of using high heating rates in solution heat treatments, but how the dissolution of the second phases is affected by this parameter remains under debate. In the studies of both Zhang et al. [33] and Choi et al. [87], the researchers stated that the dissolution of the second phases during a high heating rate ramp is greater when compared with a low heating rate ramp. This deduction stems from the observation of an increased number density and reduced inter-distance of nanometric precipitates in fast heated samples. However, the final mechanical properties when adopting different heating rates are almost identical in both studies.

Huo et al. [79] instead affirmed that the dissolution of the second phases during the heating ramp is unaffected by the heating rate since they detect indistinguishable precipitate distributions after aging when comparing samples subjected to different heating rates. Finally, Wang et al. [34] deduced that the higher the heating rate during the heating ramp, the lower the dissolution during this step. Such a conclusion arises from the fact that the longer heating time during the slow heating ramp contributes more to the dissolution of precipitates than does the steep temperature increase realized in the high heating rate ramp.

The discrepancies found in the literature might be related to the fact that the comparison of samples heated at different rates presents intrinsic difficulties. In fact, once the solution heat treatment temperature is fixed T_{SHT} , the variation of the heating rate determines a change of the heating time $t_{heating}$, and in turn, this parameter modifies the total holding time of the solution heat treatment t_{SHT} (Fig.2.10). Consequently, comparisons

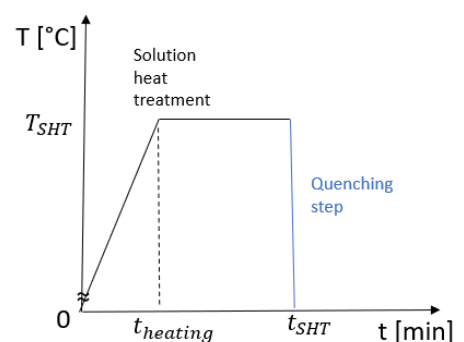


Figure 2.10: Schematic diagram showing a solution heat treatment and the relationship between $t_{heating}$ and t_{SHT} .

among samples heated at different rates must be designed carefully. For example, a close examination of the works of Zhang et al. [33] and Huo et al. [79] reveals that their respective comparisons between samples with low and high heating rates are undertaken in different ways (Fig.2.11). While Zhang et al. strictly compared the effects of two heating ramps at different rates, Huo et al.

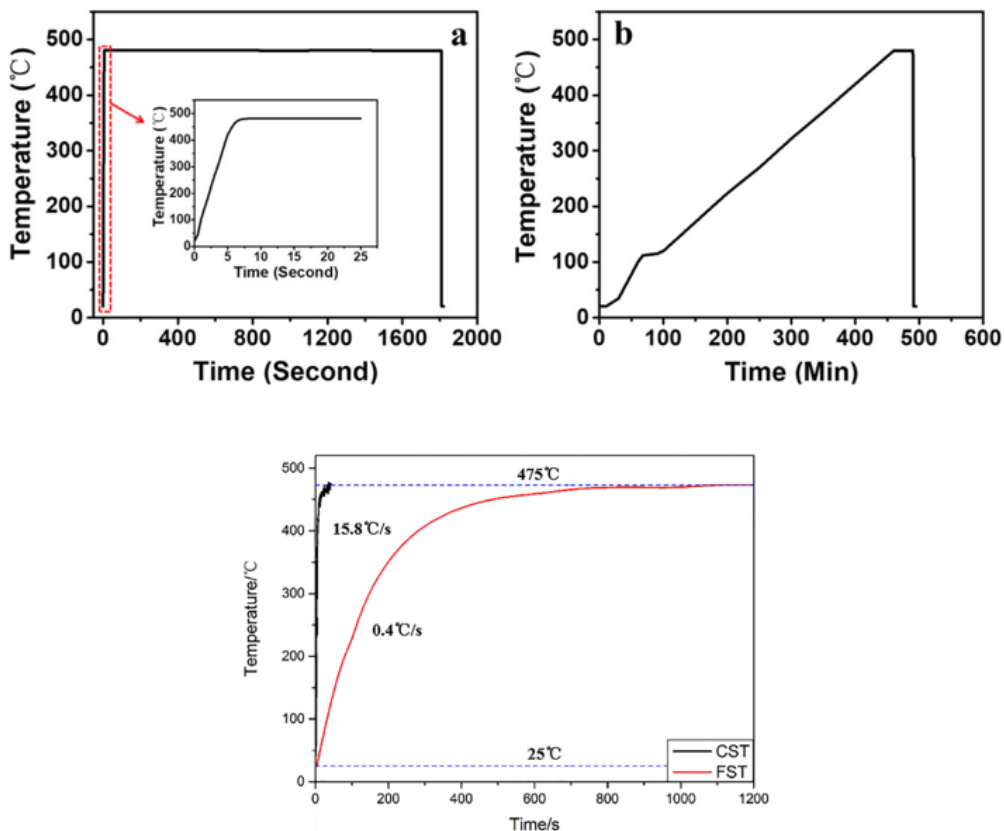


Figure 2.11: Heating rate profile comparisons during solution heat treatment in the studies of Huo et al. (top) [79] and Zhang et al. (bottom) [33].

also included in the comparison a prolonged isothermal holding. Therefore, the differences in the total holding time between studies can make it difficult to distinguish between the effect of the heating ramp itself and the effect of the total duration of the treatment. The magnitude of the heating rates compared could also make a difference in the results. In the two studies already cited, Zhang et al. [33] compared 0.4 °C/s with 15.8 C°/s, while Huo et al. [79] compared 60 °C/s with 0.01 C°/s. Therefore, more work is necessary to clarify how the heating rate influences the dissolution process during solution heat treatment. More experiments are also needed to decouple the effect of the heating ramp from the effect of the total holding time on the dissolution of the second phases.

2.5: The effect of solution heat treatments on the grain structure of 7000 aluminium alloys

Solution heat treatments mainly aim to promote dissolution in the second phases, but can also alter the workpiece grain structure. During the heating up process to reach the solution heat treatment temperature, three different phenomena occur depending on the thermal energy stored.

Recovery is the first process during the heating up phase and needs the least amount of thermal energy to be activated compared to the other phenomena. During recovery, dislocations and vacancies annihilate and rearrange in the material, therefore reducing their concentration. Secondly, recrystallization occurs at higher temperatures during the heating ramp, becoming dominant when a higher thermal energy is available. This process consists in the nucleation of new equiaxed grains at the expense of the pre-existing grains in the matrix. An indicative temperature for the start of

recrystallization for aluminium alloys is 300 °C, but this temperature is strongly influenced by the specific alloy chemistry and sample microstructure heated up. For example, depending on the specific thermo-mechanical history of the sample, the recrystallisation of 7000 aluminium alloy grain structures can be strongly hindered by the dispersoid distribution even at solution heat treatment temperatures since these

second phases can pin the grain boundary (GB) migration [34]. Partially overlapping with recrystallization, grain growth requires even higher thermal energy than the other processes abovementioned and is the last step of the sequence. The dislocation density continues to diminish during this step as dislocations annihilate at the GBs of the enlarging grains.

While diffusing the alloying elements in the matrix, the modification of the grain structure described also modifies the dissolution process during solution heat

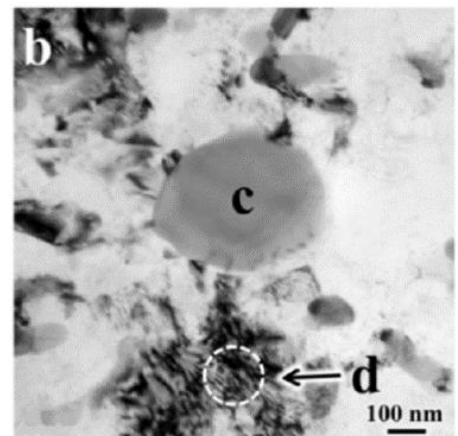


Figure 2.12: Example of a $MgZn_2$ precipitate (c) surrounded by dislocation fields (b,d) in an AA7075 sheet [79].

treatment. Conversely, the distribution of the second phases in the starting material interacts with the dislocation field and alters the characteristics of recrystallization and grain growth. Because the precipitate dissolution and variation of the grain structure are strongly linked, the description of the microstructure evolution during solution heat treatment become more complex.

When focusing on how the solution heat treatment affects the grain structure of 7000 aluminium alloy sheets, provided that F-tempered sheets are used as the starting material, the aluminium blanks processed via HFQ[®] are highly driven to recrystallization and grain growth due to the upstream processes of the sheet production. In fact, during the hot and cold rolling steps necessary to achieve the required final thickness, the matrix deformation dramatically increases the sheet dislocation density and vacancy concentration, and the grains reach an elongated shape in the working direction. In particular, the dislocation fields are located mostly around constituents and large precipitates not deformed during the rolling stages (Fig.2.12) [34,79].

As recently highlighted in the literature, the grain structure of the processed aluminium sheet is modified differently depending on the heating rate required to reach the solution heat treatment temperature [33,34,79]. At low heating rates, the transition through the temperatures where recovery serves as the predominant process is slow enough to considerably lower the dislocation density in the sample. For this reason, the decrease of stored energy then reduces the drive for recrystallization and grain growth during the higher temperature range of the heating ramp [34,79]. Therefore, throughout solution heat treatments of 7000 aluminium alloys at low heating rates, a modest change of the grain structure is expected [84].

Xu et al. [84] focused on the characteristics of solution heat treatments for 7000 aluminium alloys and reported that, in the 470 °C–500 °C range, recrystallization and grain growth become relevant for holding times of multiple hours, thus both processes are expected to be negligible during the accelerated solution heat treatments designed for HFQ[®]. However, the researchers also stated that the holding time required for the onset of these phenomena is highly sensitive to

temperature: more than 24 hours are needed for recrystallization to start at 475 °C and roughly 8 hours at 495 °C.

Interestingly, the rate at which recrystallization and grain growth develop at temperatures above the eutectic temperature (needed to accelerate the solution heat treatment) are not well-documented in the literature and require further investigation.

In contrast, a few studies have already dealt with how high heating rates affect the grain structure of workpieces subjected to solution heat treatment. At high heating rates, the transition through the temperatures where recovery is the predominant process happens quickly, almost preserving the original dislocation density developed in the sheet. The intact stored energy in the sample therefore causes a bigger drive for recrystallization and grain growth during the higher temperature range of the heating ramp [34,79].

For example, Zhang et al. [33] decreased the average grain size of AA7075 sheets from 57 μm to 44 μm when raising the heating rate from 0.4 °C/s to 15.8 °C/s to reach the final solution heat treatment temperature. Although the effect of a high heating rate on the grain structure of aluminium alloy sheets is somehow consolidated, more work is needed to better define the link between the magnitude of the heating rate applied during solution heat treatment and the resultant refinement of the sample grain structure. Such work should also account for the thermo-mechanical history of the starting material.

2.6: Quench sensitivity of 7000 aluminium alloys

During the cooling step, aluminium alloy samples experience a range of temperatures that can induce precipitation of the secondary phases at GBs and on dispersoids (heterogeneous precipitation), therefore greatly influencing the final properties of the component. The extent of these precipitation events is a function of many factors. First, the rate at which the workpieces experience the temperature variation plays a fundamental role. In fact, the dwell time at each one of the temperatures included in the cooling profile determines how kinetically relevant the precipitation reactions become. The thickness of the sample processed is therefore also crucial because, the greater the thickness, the larger the range of cooling rates across the thickness of the material.

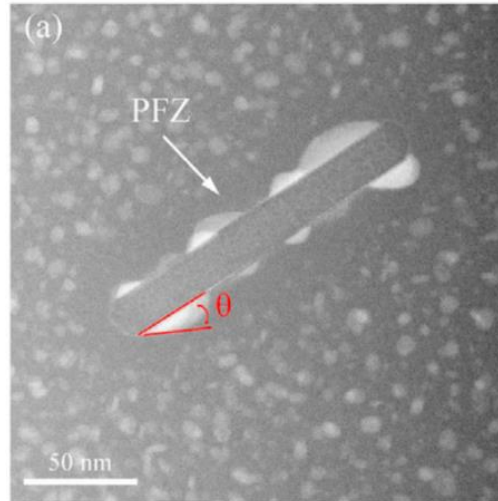


Figure 2.13: *η phase (white) nucleated heterogeneously on a dispersoid (grey) during cooling [88].*

For aluminium alloy sheets, the cooling rate can be assumed to be homogeneous due to their limited thickness. The solute element concentration in the alloy is the second important factor to consider. A greater concentration of alloying elements increases the driving force for precipitation reactions to occur. Finally, the dispersoid distribution, the grain size and the specific sample microstructure affect the extent of precipitation during the cooling step. When attention is focused on 7000 aluminium alloys, a higher sum of Zn, Mg and Cu concentrations and a higher Zn/Mg ratio contribute to raise the quench sensitivity of the material [89,90]. The substitution of Cr with Zr instead decreases the quench sensitivity of 7000 aluminium alloys [89,91]. While dispersoids bearing Cr are larger and incoherent with the aluminium matrix, dispersoids containing Zr are smaller and coherent. Consequently, Cr-dispersoids constitute a better nucleation site for precipitation in the secondary phases [89].

Compared to the other members of the 7000 aluminium alloy family, AA7075 is characterised by a low Zn/Mg ratio and only Cr-rich dispersoids; therefore, AA7075 is usually classified as a high quench sensitive material [89].

A consolidated way to assess the quench sensitivity of a specific aluminium alloy is via the study of its time-temperature-property (TTP) diagrams. If the alloy under study from the solution heat treatment temperature is instantly quenched to a selected temperature that is then maintained for a certain period before the sample is instantaneously quenched to room temperature, a decrease of the property of interest might occur. This specific cooling path is defined as isothermal holding.

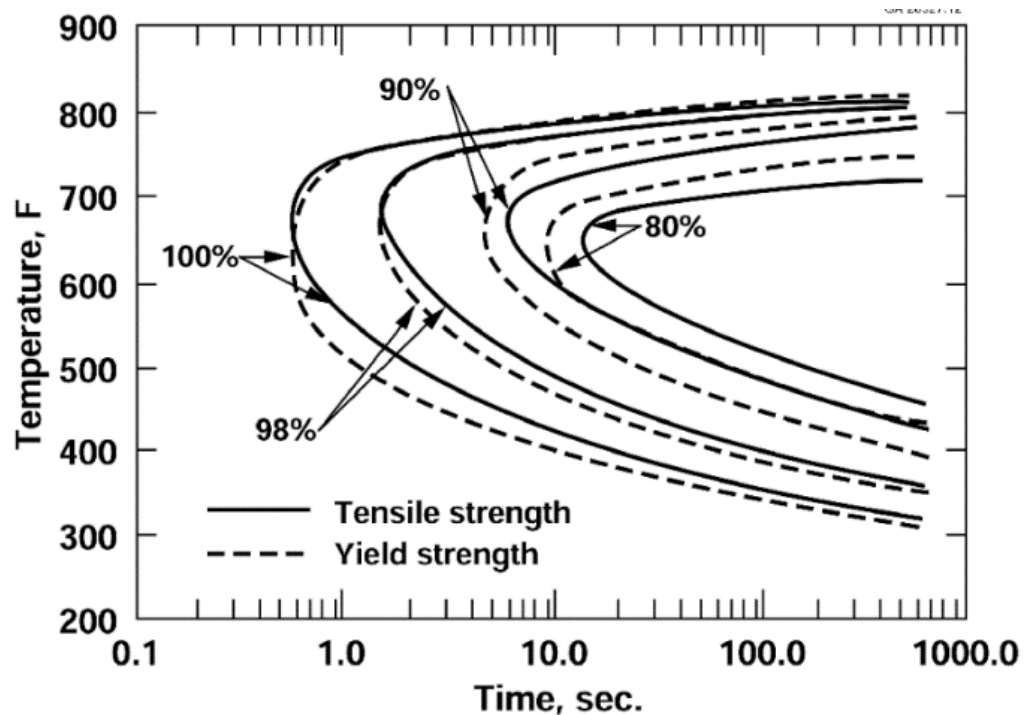


Figure 2.14: Example of time-temperature-property diagram for AA7075-T6 [92].

In a TTP diagram, the time-temperature plane is subdivided into regions that lead to the same loss of the property investigated when applying an isothermal holding. The subdivision of these regions is done using a group of curves: each curve highlights all the time and temperature pairs of the isothermal holding path that would cause an identical property reduction in the material (Fig.2.14). TTP curves for 7000 aluminium alloys usually have a 'C shape', which can be easily explained by referring to classic nucleation theory [93]. At high temperatures (close to solution heat treatment temperatures), the undercooling and the thermodynamic drive for the heterogeneous nucleation of secondary

phases are low. An isothermal holding time in this range of temperatures would require long holding times to induce appreciable precipitation. Similarly, at temperatures close to room temperature, precipitation reactions are kinetically hindered. Instead, intermediate temperatures satisfy both kinetic and thermodynamic needs for achieving a fast nucleation: isothermal holdings in this temperature range need short durations to promote precipitation. Therefore, iso-property curves of TTP diagrams are naturally C-shaped.

The C-curves characteristics can be used to generally evaluate the quench sensitivity of an alloy. For example, a measure of quench sensitivity is the position of the 'nose' of the C-curve, namely the shortest isothermal holding time that causes precipitation. As one of many examples in the literature, Liu et al. [89] ranked the quench sensitivity of different members of the 7000 aluminium alloy family via a study of the position of the C-curves noses. These curves can also be useful to roughly understand the temperature range in which heterogeneous nucleation occurs: this understanding is deduced by identifying the edges of the C-curve. As industrially relevant cooling paths are quite dissimilar than isothermal holdings, the prediction of property reductions with more realistic cooling paths requires using the TTP diagram in conjunction with a specific methodology called quench factor analysis (QFA) [89,92,93].

In QFA, the cooling path is treated as a stairway made of small instantaneous coolings and isothermal holdings that mimic the original cooling path. Each step of the stairway contributes to the final property depending on its relative position to the C-curve. The final property loss achieved via the overall cooling path is obtained by adding together the contributions of each step. As this methodology is usually performed via automated integration, the experimental C-curves must also be transformed into mathematical expressions. An exponential function with five different constants is commonly used to represent C-curves, and the constants derived can also be directly used as a measure of quench sensitivity. Dolan et al. [94], for example, successfully applied the QFA to predict the hardness loss with varying cooling rate in the heat treatments of AA7175 plates. A second way to assess the quench sensitivity of high strength aluminium alloys is through continuous cooling precipitation (CCP) diagrams. In these diagrams, experimental curves in the time-temperature plane quantify the

reduction of the property of interest when intersected with an industrial cooling profile (Fig.2.15).

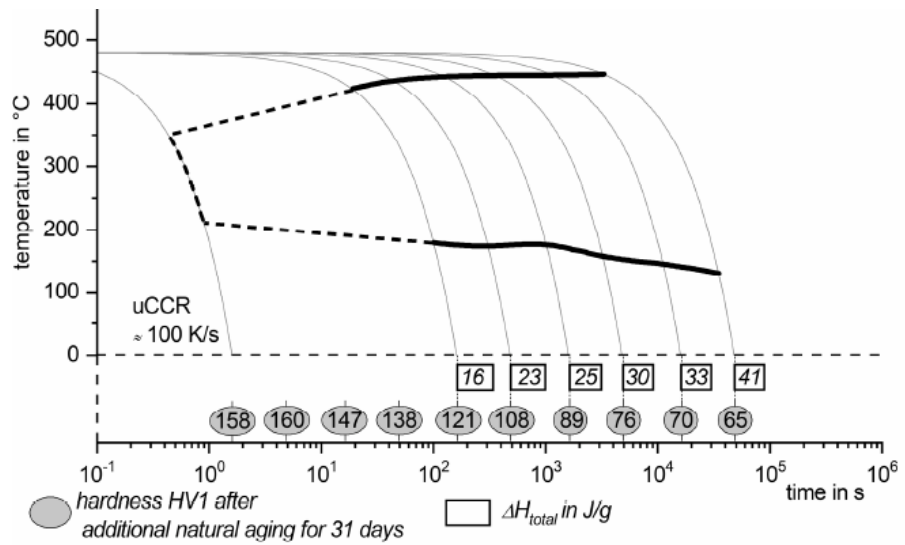


Figure 2.15: Example of continuous cooling precipitation diagram based on hardness measurements for AA7075 [31]

The quench sensitivity of the alloy can be assessed through defining which critical cooling rate must be exceeded to produce a negligible reduction of a property [31,95]. For example, Zhang et al. [95] obtained CCP diagrams for both AA7150 and AA7020 using hardness measurements, microstructural observations and differential scanning calorimetry (DSC) traces evaluation. The researchers also concluded that the critical cooling rate for AA7150 is 300 °C/s, but only 3 °C/s for AA7020.

2.7: The cooling rate optimisation in the HFQ® process

The forming and quenching step is undoubtedly the core of the whole HFQ® process and the subject of many studies. When dealing with the optimisation of the cooling rate from the solution heat treatment temperature, a fundamental principle arose in most related literature: keep the cooling rate as high as possible to avoid quench-induced precipitation and decrease the hardening potential of the workpiece.

For example, Milkereit et al. [31] identified the critical cooling rate for two members of the 7000 aluminium alloy family and recommended performing the cooling step with a rate higher than that threshold value. Scharifi et al. [35] made the same recommendation when analysing how the tool temperature modifies the cooling rate and the mechanical properties of the processed blank. Similarly, Zheng et al. [36] encouraged cooling as fast as possible to avoid quench-induced precipitation when studying how the cooling rate is affected by the transfer step from the solution heat treatment furnace to the press.

Following this principle preserves the highest concentration of solute elements and vacancies in the matrix, promoting the maximum hardening response possible in the material. However, this strategy relies entirely on the aging step to achieve an acceptable level of stress corrosion cracking (SCC) resistance and requires adding a time-consuming overaging step. Besides the coarsening of matrix precipitates, aging increases the size and interparticle distances among the grain boundary precipitates (GBPs) and the width of the precipitate-free zones (PFZs); aging also modifies the chemistry of the GB regions [40].

Interestingly, different studies suggested that similar microstructural changes associated with overaging can be realized by adopting a slower cooling rate rather than the fastest one achievable; in turn, this process enhances the SCC resistance of the workpiece. [37,38]. While this alternative approach to the cooling step could greatly benefit the HFQ® process, the approach would also eliminate the need for the overaging procedure. However, the cooling rate should be tuned to simultaneously improve SCC resistance and preserve the

hardening potential of the workpiece. Both studies mentioned agreed that a feasible range of cooling rates to complete this operation exists [37,38].

For example, Yuan et al. [38] observed that the crack growth of notched low Cu content 7000 aluminium alloys during SCC experiments decreases almost one order of magnitude when lowering the cooling rate from 150 °C/s to 8 °C/s. However, this alternative strategy has not yet been attempted for HFQ®, so related contributions to the literature are strongly needed.

Conversely, increasingly more effort has already been devoted to optimising the cooling path towards achieving better formability under the press. Recent studies suggest that higher formability can be achieved by conducting the deformation step at slightly lower temperatures than the solution heat treatment one [63]. Notably, though, the change of the dies' temperature or the modification of the time transfer from the solution heat treatment furnace are two usual strategies used to control the cooling path in the HFQ® process [35,36,62].

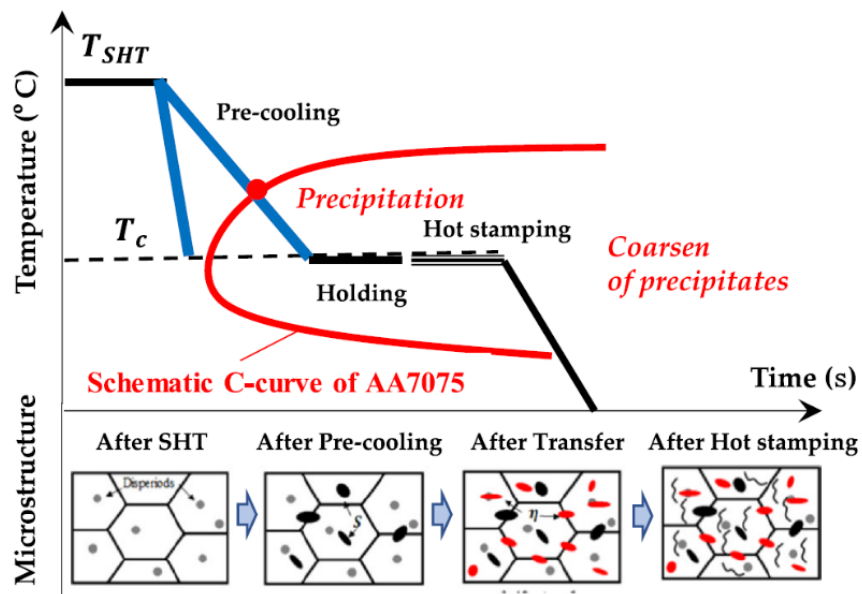


Figure 2.16: Example of a time-temperature profile showing the precooling and isothermal holding strategy in the HFQ® process. The cooling path is superimposed with a time-temperature-property diagram for AA7075 to show the possible formation of quench-induced precipitates [64].

To help realize that higher formability, a new cooling strategy that uses a precooling step followed by an isothermal holding (Fig.2.16) has already been tried [36,64]. In fact, the forming operation is carried out during the isothermal holding at a temperature lower than the solution heat treatment one and this

might improve the overall formability of the workpiece [63,34]. However, as highlighted in the literature, this type of cooling path must be controlled very carefully when processing 7000 aluminium alloys since both uncalibrated precooling and isothermal holding can determine excessive quench-induced precipitation and deteriorate the workpiece strength [64].

For example, Li et al. [64] developed and validated a constitutive model to predict formability, microstructure evolution and final strength of AA7075 sheets subjected to the precooling and isothermal holding strategy. The researchers also found a significant strength loss occurring when precooling the samples at 50 °C/s to a temperature lower than 350 °C, or when precooling that samples at 5 °C/s to a temperature lower than 335 °C. Besides formability, more contributions are needed to study how the precooling and isothermal holding strategy affect other relevant properties in 7000 aluminium alloys.

2.8: Stress corrosion cracking of 7000 aluminium alloys

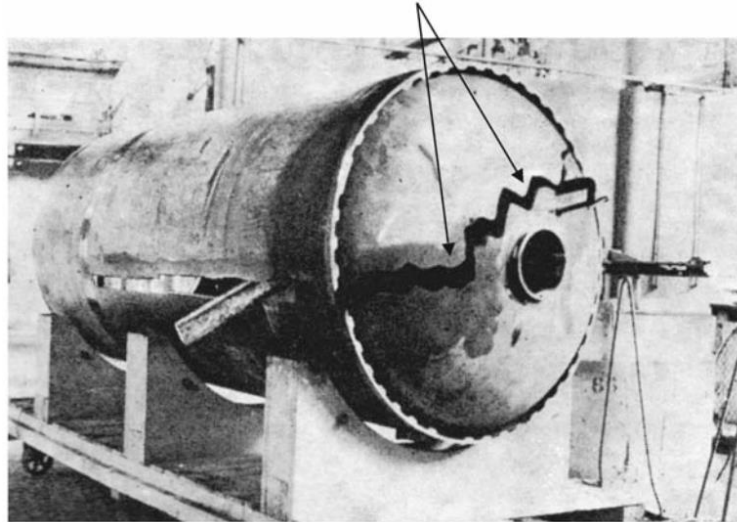


Figure 2.17: In-service failure of a rocket due to stress corrosion cracking (SCC) [96].

Stress corrosion cracking (SCC) is a form of localized corrosion which affects many metallic systems, including 7000 aluminium alloys. This form of localized corrosion develops when a susceptible material comes in contact with specific corrosive environments and simultaneously experiences a stress above a certain threshold.

For some tempers of the 7000 aluminium alloy family, the presence of water vapour in air already constitutes an aggressive environment for this type of localized attack to evolve, and that environment can be further aggravated by the presence of Cl^- , a very common ion in marine environments. The stress level needed to develop SCC falls far below the yield strength of the susceptible alloy and can be caused by an applied external stress or a residual stress; the latter is usually generated during previous heat treatment of the component or machining.

SCC can initiate from a wide range of surface defects of the alloy (e.g., notches, scratches or damage caused by corrosion). This type of localized attack is characterized by the formation of barely detectable cracks that can cause premature failure in service of stressed components (Fig.2.17) when the crack reaches a critical length. Due to having all the characteristics listed above, SCC of aluminium alloys is a dangerous phenomenon that must be limited and successfully controlled. The stress field around a defect or a growing crack tip is

amplified compared to the average stress to which the sample is subjected, and this stress field influences the propagation velocity of the crack itself.

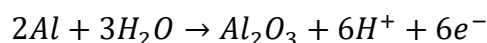
A successful approach to studying the propagation of SCC is to determine the relationship between the amplified stress caused by the crack tip and the crack growth velocity. The stress intensity factor K is defined as the ratio between the local stress and the previously mentioned average stress. Experimental plots that represent the relationship between K and the crack growth rate of pre-notched specimens are commonly used to investigate how the applied stress affects the SCC phenomenon, but also to rank different alloys based on their resistance to this type of corrosion. These plots (Fig.2.18) are also used to study the effect of different environments and to evaluate the time to failure of components where stress corrosion cracks are already formed [97].



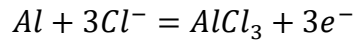
Figure 2.18: Schematic diagram showing the typical relationship between the stress intensity factor at the crack tip and the growth rate of the stress corrosion cracks for an aluminium alloy [97].

Fundamental to understanding the current state of the research on 7000 aluminium alloy SCC mechanisms is illustrating the chemical reactions that occur at the crack tip when an aggressive environment is present. For this illustration, an aqueous solution containing NaCl is used as a reference environment. During service, when environmental moist air comes in contact with the alloy, a thin water layer is developed at the surface; all the corrosion events are related to the existence of this layer. Transport and concentration variations of all the chemical species involved differ whether considering a saline bulk solution or a thin water layer, so the characteristics of the corrosion processes developed.

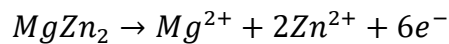
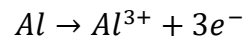
When the bare aluminium alloy surface comes into contact with water, the oxide layer Al_2O_3 forms with the following reaction:



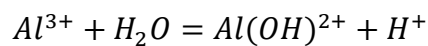
Alternatively, the hydroxide layer $AlCl_3 \cdot H_2O$ can form under the action of Cl^- ions via the reaction below:



Neither of the above forms of passivation protect the alloy from corrosion since the protective layers can be locally damaged when interacting with the environment, exposing the metal underneath. When the saline solution stays in contact with the matrix for a sufficient time, the main local anodic dissolution reactions promoted involve both the aluminium matrix and precipitates:



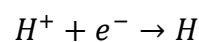
The Al^{3+} cations promote the acidification of the surrounding environment via hydrolysis:



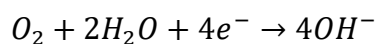
This process enhances the severity of corrosion because, at a lower pH, the oxide layer is less stable.

The interaction of the aluminium ions with the different species in the solution can follow various pathways; for simplicity, these pathways are not described in the current section.

Among the cathodic reactions, the fundamental atomic hydrogen generation occurs through the following reaction:



The hydrogen formed can then be recombined into molecular hydrogen or potentially adsorbed on the alloy surface. Lastly, hydrogen atoms can also be absorbed in the aluminium matrix. A second cathodic reaction also occurs at the Fe and Cu bearing intermetallics and involves oxygen reduction:



The anodic and cathodic reactions described above characterise the evolution of SCC: the local oxidation, hydrogen generation and acidification occur at the advancing crack tip, while the oxygen reduction occurs far from the tip.

Besides the discussed chemical reactions and transport phenomena at the crack tip, the interplay of stress, metallurgical conditions and environmental factors

make the development of a mechanism for SCC quite complex. A valid mechanism for SCC should be able to predict how stress corrosion cracks initiate and their propagation velocity for a selected alloy/environment combination. For 7000 aluminium alloys, a universal mechanism that explains all the experimental observations made has not yet been identified. In fact, each one of the mechanisms proposed fails to give reasonable predictions under certain experimental conditions.

Most of the SCC fractures in 7000 aluminium alloys are intergranular, and a consistent body of experimental observations suggests that the anodic dissolution process happening at GBs is an important factor to consider. In the anodic

dissolution mechanism, preferential dissolution of the GB regions occurs because grain boundary precipitates (GBPs) and atoms segregated at GBs are anodic compared to the surrounding matrix [98].

The crack remains sharp because the removal of atoms is more severe at the crack

tip than behind it. This difference occurs because the oxide film more efficiently protects the crack walls than it does the tip, where a more aggressive chemical environment and a more pronounced stress field are present [99]. At the tip, the slip band intersection determines the rupture of the oxide film; the crack then further grows because of the dissolution process. The slip process also helps with dissolution because the process enhances the diffusion processes at the crack tip [99].

In the discussion about SCC mechanisms for 7000 aluminium alloys, a second predominant role is held by the mechanisms that focus on the interaction of the developed atomic hydrogen with the alloy at the crack tip. In the adsorption induced dislocation emission (AIDE) mechanism (Fig.2.19), adsorbed or absorbed hydrogen at the tip helps the generation of dislocations under the effect of the stress field. This process occurs because the atomic hydrogen in the lattice can weaken the substrate bonds. Meanwhile, the generation of dislocations aids the formations of voids; the subsequent coalescence of voids then causes the crack

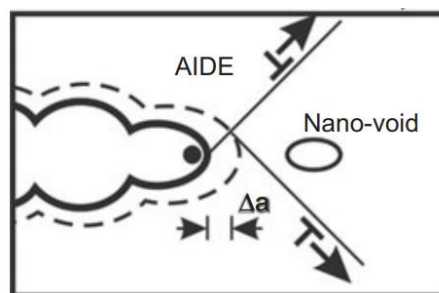


Figure 2.19: Schematic representation of a stress corrosion crack growing via the adsorption induced dislocation emission mechanism [99].

to grow [99,100]. In the hydrogen enhanced decohesion (HEDE) mechanism, atomic hydrogen concentrates at particle/matrix interfaces, at GBs or in regions where the lattice is distorted. The hydrogen accumulation leads to progressive decohesion and crack growth [99].

Finally, in the hydrogen enhanced localized plasticity (HELP) mechanism, the hydrogen accumulation interacts with dislocations and increases plasticity only in localized areas ahead the crack, therefore helping the crack propagation.

Dislocations also play a helping role in hydrogen diffusion [99]. The film induced cleavage (FIC) mechanism

(Fig.2.20) is usually used to justify the rare occasions where the aluminium alloy fails with a transgranular fracture, but the

mechanism can also be used to explain brittle

intergranular fractures. In this mechanism, the oxide film formed on the crack walls undergoes a rapid brittle fracture that extends ahead of the crack in the matrix region. The crack stops and blunts upon encountering obstacles (e.g., slip bands). When the crack is arrested, the formation of the brittle oxide resumes, and the crack then grows in a discontinuous way with cycles of ruptures and film formations [99]. Other less common mechanisms for SCC of aluminium alloys are present, but are not discussed in this study. In general, a combination and interplay of more mechanisms is possible, which makes the study of the SCC phenomenon a challenging topic.

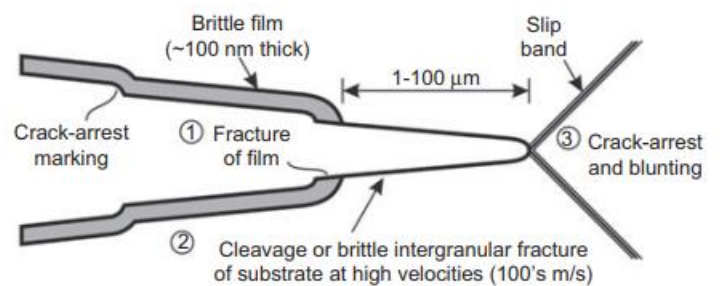


Figure 2.20: Schematic representation of a stress corrosion crack growing via the film induced cleavage mechanism [99].

2.9: The link of electrochemical parameters with SCC susceptibility of 7000 aluminium alloys

Depending on the specific metallurgical condition imparted by heat treatment, 7000 aluminium alloys can be susceptible to SCC when exposed to aggressive environments, such as humid air combined with chloride ions. The majority of the available testing techniques to assess the SCC susceptibility of this type of alloy involve cutting appropriate flat sections from the original samples and exposing them to a standardized corrosive environment after applying a certain level of stress [101].

Because the auto panels produced by HFQ® are often characterised by complex shapes, finding and cutting representative flat coupons from these specimens for a SCC resistance evaluation are extremely challenging. In addition, the evaluation of the SCC resistance is a time-consuming process since conclusions can be made after multiple days of sample exposure. The detection of electrochemical parameters that could be linked with the SCC performance of the alloy is therefore a useful topic to investigate. In fact, samples intended for electrochemical measurements are much smaller than the ones required for a SCC susceptibility evaluation and can thus be easily derived from auto panels. Electrochemical tests are also usually less time-consuming than SCC resistance tests.

Current decay measurements [102] are an example of the electrochemical techniques that could be used to predict SCC susceptibility. Because the advance of a stress-corrosion crack requires the activity at the crack tip to be considerably higher than the activity at the crack sides, all the surfaces exposed besides the crack tip must undergo an active-to-inactive transition [102]. For this reason, measuring the characteristics of current decay at a set potential difference when a bare aluminium surface is exposed to an aggressive environment can be linked to the tendency of the alloy to be susceptible to SCC [102].

Anodic polarisations are a straightforward technique to derive electrochemical parameters strictly linked with the specific metallurgical condition tested. Each sample produces a unique 'signature' that can be coupled with the SCC

resistance evaluation. Then, correlations between the electrochemical parameters obtained and the SCC susceptibility can be attempted.

A schematic anodic polarisation curve of an aluminium alloy immersed in a sodium chloride solution is shown in Fig.2.21.

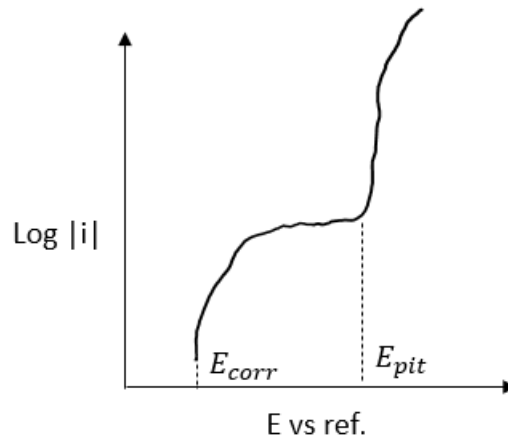


Figure 2.21: Schematic anodic polarisation curve of an aluminium alloy immersed in sodium chloride solution.

Before imposing an increasingly anodic potential difference, the system places itself at a characteristic potential in a condition of no current flowing: this potential is called the open-circuit potential E_{corr} . With an increasing anodic potential difference, the polarisation curve usually displays a less than linear increase of the current density up to the breakdown potential E_{pit} . When the breakdown potential E_{pit} is surpassed, the current density increases sharply, and both the damages to the oxide layer and the corrosion reactions are then more severe and widespread (Fig.2.22).

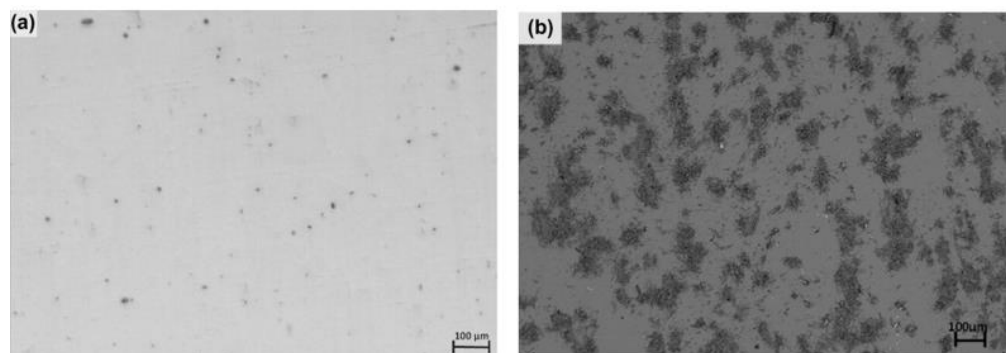


Figure 2.22: AA7475-T7351 scanning electron microscope micrographs showing the corrosion attacks developed during the polarisation experiment: (a) before polarisation test and (b) after polarisation test [103].

2.10: The evolution of GBP microchemistry with heat treatment parameters

In 7000 aluminium alloys, most of the SCC failures are intergranular (Fig.2.23), so both the microstructure and microchemistry at GBs are the main features under investigation when studying this type of corrosion attack [104]. Although GBP sizes and distribution characteristics play an important role in determining the SCC resistance of the alloy, the microchemistry at GBs is regarded as the crucial factor in dictating the SCC susceptibility of the alloy [43].

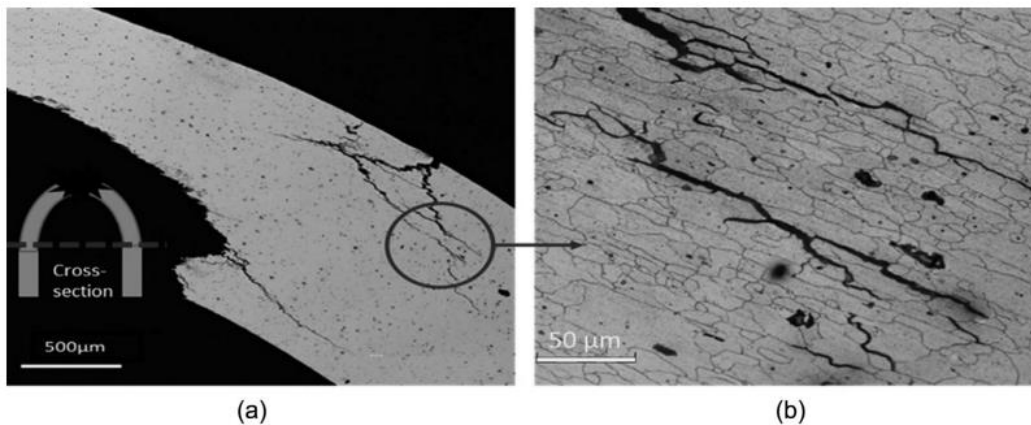


Figure 2.23: Example of an underaged AA7075 sample failed via intergranular stress corrosion cracking [101].

Among the different elements that describe the GB microchemistry, the composition of GBPs has received the most attention in the literature. During heat treatment, η phase ($MgZn_2$) is the most abundant precipitate that forms at GBs, and its composition varies because Al and Cu can replace Zn (Fig.2.24) in its lattice sites [105]. When considering a temperature range where η is stable, the higher the temperature of the heat treatment, the greater the substitution of Zn with Al and Cu atoms (Fig.2.25) [41,42].

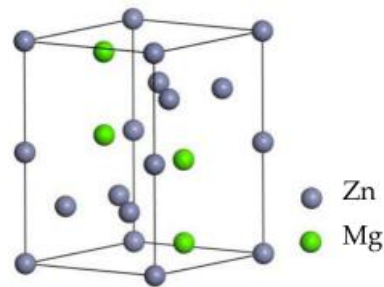


Figure 2.24: Schematic hexagonal structure of $MgZn_2$. Zn atoms can be substituted by Al and Cu atoms [107].

During electrochemical reactions at GBs, $MgZn_2$ is anodic compared to the matrix. Therefore, the higher the Cu content of the η phase, the higher its nobility and the lower its electrochemical activity with the matrix. The increase of Cu content in η precipitates does not hinder only anodic dissolution; in fact, a

lower electrochemical activity results in less hydrogen released and a less pronounced hydrogen embrittlement of the material [106].

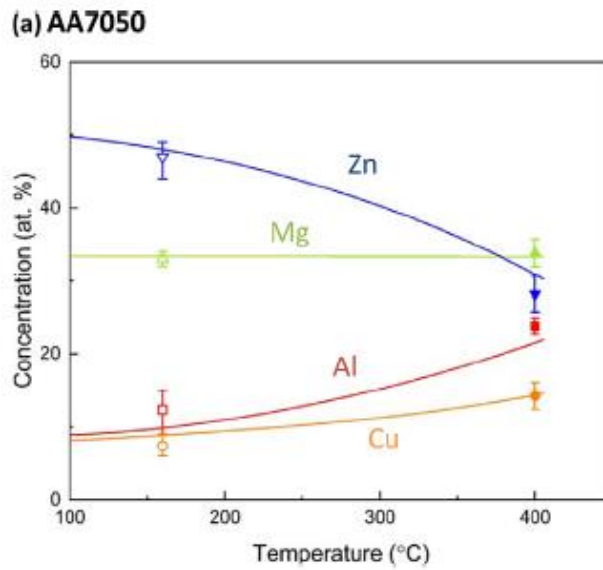


Figure 2.25: Equilibrium concentrations of Al, Cu, Zn and Mg in MgZn₂ precipitates for AA7050 calculated via JMatPro software [41].

Overall, the literature has sufficiently established that the increase of Cu content in GBPs decreases the SCC susceptibility of the samples under study. Despite the well-established link, however, studies that connect SCC resistance to precipitation hardening heat treatment parameters and GBP composition remain rare in the literature and sometimes have contradictory findings. For example, how the cooling rate affects GBP composition remains unclear and under debate: some contributions report a decrease of copper content when decreasing the cooling rate [37], while other studies suggest exactly the opposite trend [108].

Chen et al. [37] outlined that the SCC resistance of 7085 samples reaches a maximum with decreasing cooling rate, being this maximum caused by the superimposition of two effects: the beneficial enlargement and disconnection of GBPs occurring at lower cooling rates, and the detrimental reduction of the GBPs Cu content. Regarding the aging step, more knowledge is already available in the literature.

Overaging practices or retrogression and reaging (RRA) strategies are well-known to enrich GBPs with copper when compared to peak-aging strategies [43,109].

Goswami et al. [43] measured how the copper content of GBPs in overaged AA7075 samples increased from 15% at to 20% at when going from a peak-aged

state to an overaged condition. Instead, the link between GBP copper content, SCC susceptibility, and more complex and performant aging strategies has not yet been explored and would require further investigation [53,104].

In general, although the effect of some specific heat treatment schedules on the elemental composition of GBPs has already been established, studies that more deeply analyse the sensitivity of heat treatment parameters on GBP microchemistry are still missing. The discrepancies found and the lack of information available might be related to the intrinsic experimental difficulties in trying to measure GBP elemental content.

In fact, the compositional information of GB regions is commonly obtained via energy dispersive x-ray spectroscopy, and the use of an inadequate electron probe size can dramatically affect the precision of the elemental profiles measured [110].

Isolating the contribution of the aluminium background from the measurements can also be challenging [41]. Although atom-probe tomography can be used to accurately acquire GB compositional data, the technique is laborious if statistical relevance is needed [41]. Lastly, due to being commonly used as a sample preparation technique prior to analytical electron microscopy, electropolishing might affect the local chemistry at GBs [41].

For this reason, studying the effect of heat treatment schedules on the GBP composition via a modelling approach might be necessary to overcome the related experimental challenges and to increase the number of parameter combinations explored. Among the different possible simulation strategies, phase-field modelling approaches can be successfully used to study the microstructure and microchemistry evolution of GBs during precipitation hardening heat treatment schedules [111].

For example, Liu et al. [111] modelled the microchemistry of AA7050 GBs with varying aging parameters using a CALPHAD-informed phase-field model (CIPHER). The researchers also compared the simulated compositional profiles with their experimental counterpart, reaching excellent agreement between the two methods.

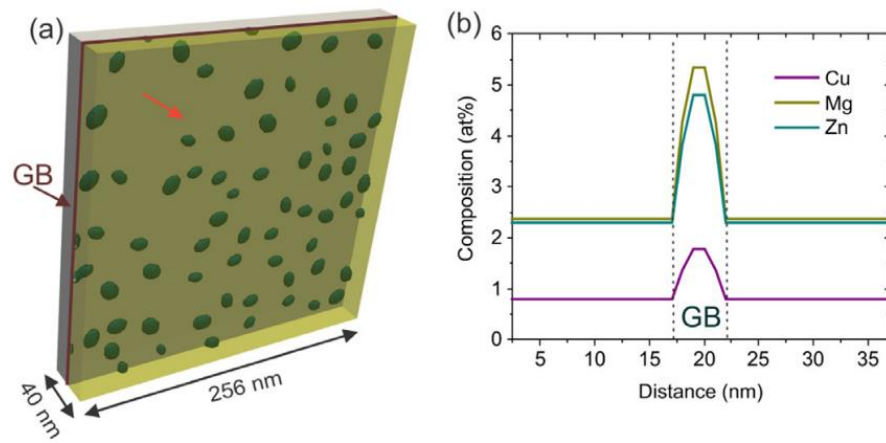


Figure 2.26: Example of the simulation setup of a phase-field model: (a) simulation box containing precipitate nuclei and (b) initial solute composition profiles [59].

In phase-field models, each phase of the system is identified by the value of a unique order parameter ϕ , which generates a field extended in space and time. The evolution of the order parameter ϕ in the field is also dictated by a selected relevant set of kinetic and thermodynamic equations [112]. Consequently, the use of a phase-field modelling approach to predict GBP composition with varying cooling rates or aging steps during the processing of AA7075 sheets would be a useful contribution to the literature. This piece of knowledge would help to clarify the link between precipitation hardening heat treatment parameters and the compositional evolution of GBPs. In addition, such knowledge can help justify the experimental SCC resistance results obtained with varying heat treatment parameters.

2.11: Uniaxial tensile tests of 7000 aluminium alloys

The development of optimal mechanical properties is another crucial aspect in the 7000 aluminium alloys metallurgy. With heat treated samples, understanding their tensile behaviour is an especially fundamental characterisation when assessing the strength level of the alloy.

In a uniaxial tensile test, the specimen is clamped onto a device that gradually elongates it, causing the material to undergo an escalating load and tensile stress on its sections. Stress-strain curves are created recording the functionality

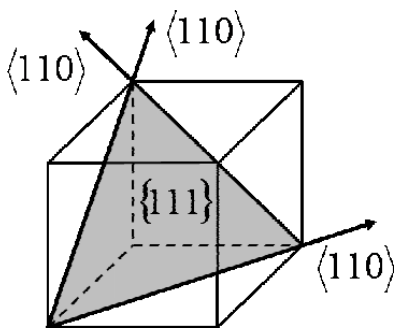


Figure 2.27: Schematic representation of the face-centred cubic lattice, where one $\{111\}$ plane and some $\langle 110 \rangle$ directions are highlighted [113].

between stress and displacement relative to the initial length during tensile tests.

If the stress calculation considers the original cross-section during the tensile test, the stress registered is defined as engineering stress.

Instead, if the stress is calculated considering the progressive restriction of section during the stretching, the stress is defined as true stress. True stress is plotted against true strain, which is a logarithmic function proportional to strain.

The yield stress (YS) defines the threshold between elastic and plastic deformation. When tensile stresses below the yield stress are applied, the atoms in the material stretch, increasing the distance of all the atomic bonds.

Macroscopically, the sample stretches and then reversibly reassumes its original shape once the load is removed. Tensile stresses above the yield stress will determine a permanent and irreversible elongation of the specimen, called plastic deformation. In stress-strain curves, the elastic region is characterised by a linear relationship between stress and displacement.

Deformation in aluminium alloys is commonly accepted as happening via the slip mechanism. The planes and directions in the lattice with the highest number of atoms intersected (close-packed planes and directions) are the ones where slip occurs preferentially as the movement is linked with a lower energy

consumption. Aluminium is characterized by a face-centred cubic (FCC) lattice. Its close-packed planes are in the {111} family, while the close-packed directions are the in the (110) family (Fig.2.27). Slip occurs on combinations of slip planes with slip directions. In aluminium, 12 possible combinations of 111 planes with 110 directions, called slip systems, exist.

On the slip plane, the sliding of a portion of the crystal happens due to the movement of dislocations as the resulting voids in the lattice make the sliding more energetically favourable. The sliding process causes the dislocation line to move in the same direction of the slipping direction (Fig.2.28)

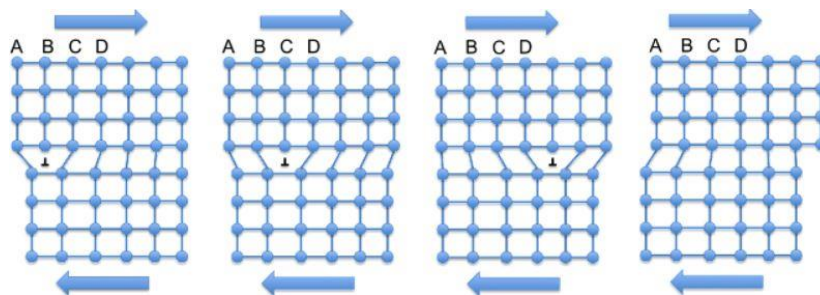


Figure 2.28: The sliding of a crystal portion is associated with the movement of the dislocation line in the same direction (dislocation line perpendicular to the page) [114].

When dislocations are hindered in their movements, a higher stress needs to be macroscopically applied to induce plastic deformation, and the alloy then benefits from a strengthening effect.

The presence of precipitates in the alloy is one of the main sources of impediment for dislocation motion. Therefore, the understanding of the mechanisms by which dislocations can overcome precipitates is of fundamental importance in metallurgy. Such knowledge helps fuel the design of effective microstructures that can maximise the hindering of dislocation passages and thus maximise the strengthening effect.

A moving dislocation can pass through precipitates via the shearing or bowing mechanism where the mechanism selected each time is the least energy-consuming to overcome a specific distribution of precipitates. When encountering precipitates coherent with the matrix on the slip plane, the moving dislocation can cut the precipitates during passage (shearing mechanism), creating two new precipitate-matrix interfaces linked to the cut (Fig.2.29). The

wider the two interfaces to generate, the higher the energetic toll that this mechanism needs. For this reason, the larger the size of the precipitates to cut, the higher the energetic expense of the shearing mechanism.

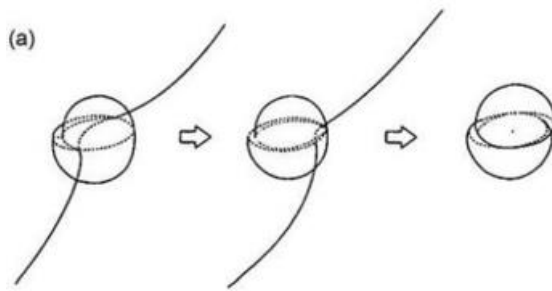


Figure 2.29: Schematic representation of the cutting mechanism [115].

When encountering precipitates incoherent with the matrix on the slip plane, the moving dislocation's passage is realised through the bending of the dislocation line and the creation of dislocation loops around the surpassed precipitates (see Fig.2.30). This process is called the bowing or Orowan mechanism.

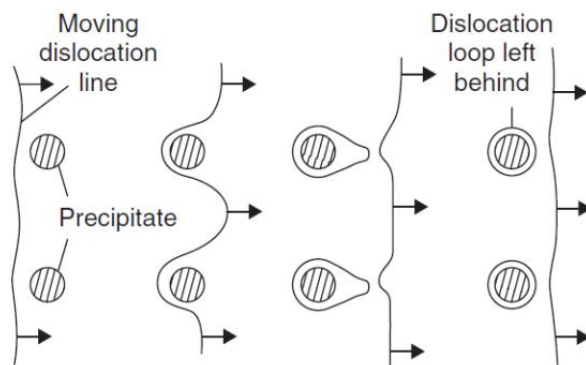


Figure 2.30: Schematic representation of the bowing mechanism [116].

The energy required to perform this mechanism is directly proportional to the distortion imparted to the dislocation line during its passage. Therefore, the lower the interdistance between the precipitates to overcome, the higher the energy requirement associated with the bowing mechanism.

In 7000 aluminium alloys, precipitates in the nanometric scale constitute the main source of impediment for dislocation movement. The precipitates' volume fraction, distribution of sizes and shapes, type and orientation with the matrix

are the major contribution in the observed yield stress of the specimen and in the general deformation behaviour during tensile testing.

As occurs during heat treatment, the nanometric precipitates gradually lose coherency with the matrix and enlarge, the predominant precipitate-dislocation interaction mechanism gradually changes from shearing to bowing.

In the plastic deformation strain range, the generation of new dislocations in the alloy and their mutual interactions determines that an increasing load must be applied to sustain the tensile displacement. This process is called strain hardening.

The formation, annihilation and interaction of dislocations with the typical microstructural features of 7000 alloys control the shape and features of the stress-strain curve during plastic deformation. To quantify and analyse the effect of strain hardening on the stress-strain relationship, Kocks-Mecking plots (Fig.2.31) are commonly used [35,117].

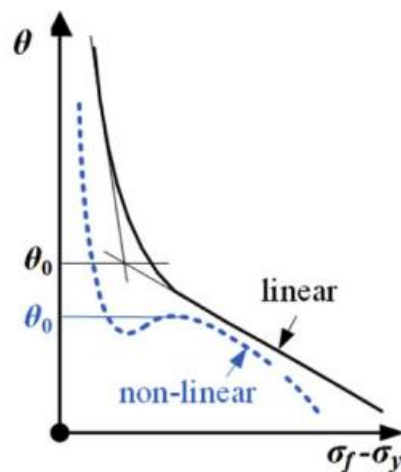


Figure 2.31: Example of Kocks-Mecking plot showing different functionalities of θ with increasing true stress [118].

These types of diagrams display the variation of true stress with true strain (the work-hardening rate θ) as a function of true stress in the plastic deformation range. For aluminium alloys, the elasto-plastic transition during yielding occurs in 'Stage 1'. The range of plastic strains where θ assumes a stable functionality is called 'Stage 3'.

Chen et al. [117] reported that two possible behaviours are possible in this stage: a linear decrease of θ with increasing true stress, or a constant value of θ with

increasing true stress. The middle stage, 'Stage 2', is the range of plastic strains where the functionality of θ adjusts from the one of the elasto-plastic transitions to the one characteristic of 'Stage 3'.

In stress-strain curves based on engineering stress and strain, the stress calculation considers the initial section of the material that remains fixed throughout the entire tensile test. As a result, the recorded engineering stress attains a peak and then diminishes when necking takes place.

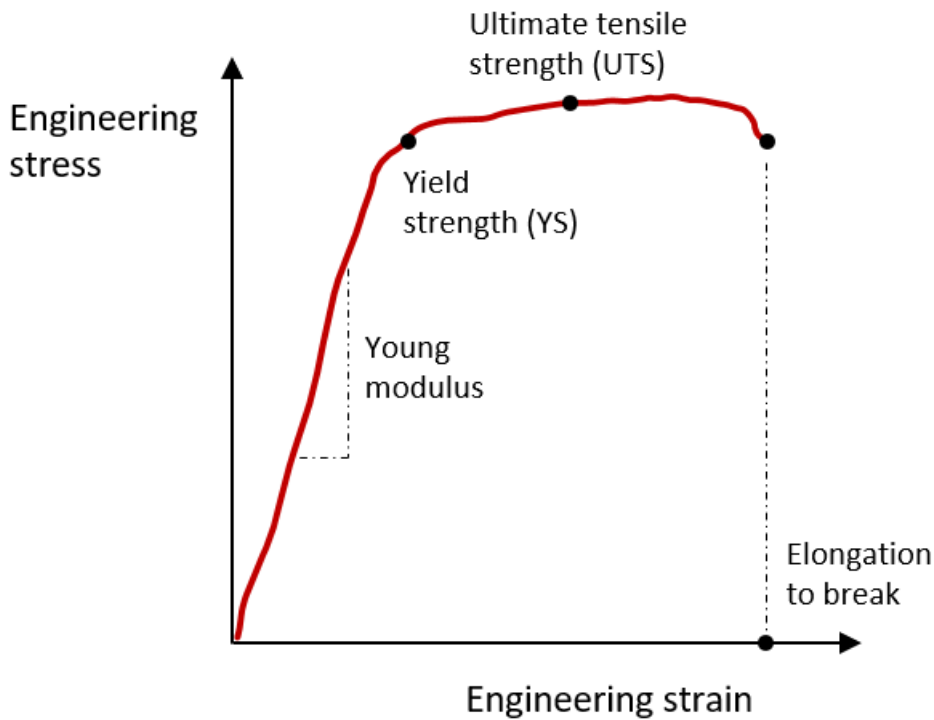


Figure 2.32: Schematic stress-strain curve reported as relationship between engineering stress and engineering strain.

When considering stress-strain curves based on engineering stress and strain, because the section considered for the stress calculation is the initial one and is fixed during the whole tensile test, the engineering stress recorded reaches a maximum and then decreases when necking occurs.

The stress level correspondent to the maximum described is defined as ultimate tensile strength (UTS). The progressive section reduction of the sample and the coalescence of microvoids/cracks causes the specimen to finally fail. The strain at which fracture occurred is defined as the elongation to break (Fig.2.32).

2.12: The effect of cooling rate on the microstructure of 7000 aluminium alloys

The extent of quench-induced precipitation when considering 7000 aluminium alloys is determined by the quench sensitivity of the specific alloy considered and the cooling rate applied (Fig.2.33). Once the alloy system and therefore its quench sensitivity are fixed, the magnitude of heterogeneous precipitation occurring increases as the cooling rate decreases.

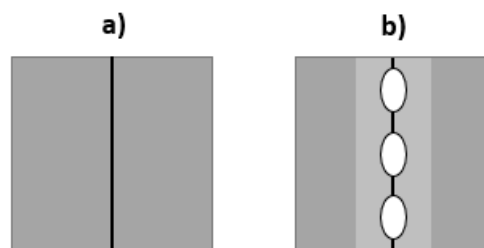


Figure 2.33: Schematic grain boundaries microstructure after cooling from solution heat treatment temperature: (a) high cooling rate and (b) low cooling rate [45,46].

Dispersoids and GBs are preferential sites for heterogeneous precipitation. On dispersoids, precipitation reactions are energetically favoured and are already activated at high temperatures during cooling [44]. The size of η phase on dispersoids easily reaches 200 nm for most cooling rates and leaves a PFZ at the precipitate's surroundings [44,45,119].

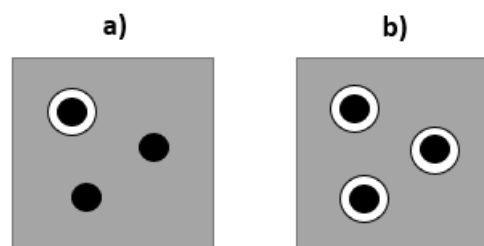


Figure 2.34: Schematic matrix microstructure showing dispersoids after cooling from solution heat treatment: (a) high cooling rate and (b) low cooling rate [45].

Dumont et al. [45] studied how precipitation on dispersoids vary for two cooling rates of different magnitudes. The researchers concluded that, while MgZn_2 dimensions on dispersoids are stable at around 100–200 nm for the two opposite cooling rates studied, the volume fraction of these precipitates dramatically increases when using the lowest of the two cooling rates (Fig.2.34).

GBs are the second preferential site for heterogeneous nucleation of the second phases during cooling. Recent investigations show that not just η phase but also S (Al_2CuMg), T ($\text{Al}_2\text{Mg}_2\text{Zn}_3$) and Mg_2Si can nucleate and grow at GBs during cooling [95,120]. For example, Zhang et al. [95] identified both the η and S phases at the GBs of AA7150 and characterised those reactions via DSC traces.

Due to the intrinsic heterogeneity of GBPs, the studies that focus on how GBP features change with the cooling rate do not completely align. A consistent group of studies suggests that the average size of GBPs increases when lowering the cooling rate [45,46]. For example, Dumont et al. [45] used transmission electron microscopy (TEM) micrographs to measure the average largest GBP dimension cooling rates between 850 K/s and 7 K/s. For AA7050 aged after cooling, this dimension varies from 40 nm to 80 nm when considering the highest and then the lowest cooling rate of the range. In other studies, the average size of GBPs shows small changes with varying cooling rates, even when considering wide ranges of this parameter. A consistent increase in the heterogeneity of dimensions was also reported with lowered cooling rates [44,46].

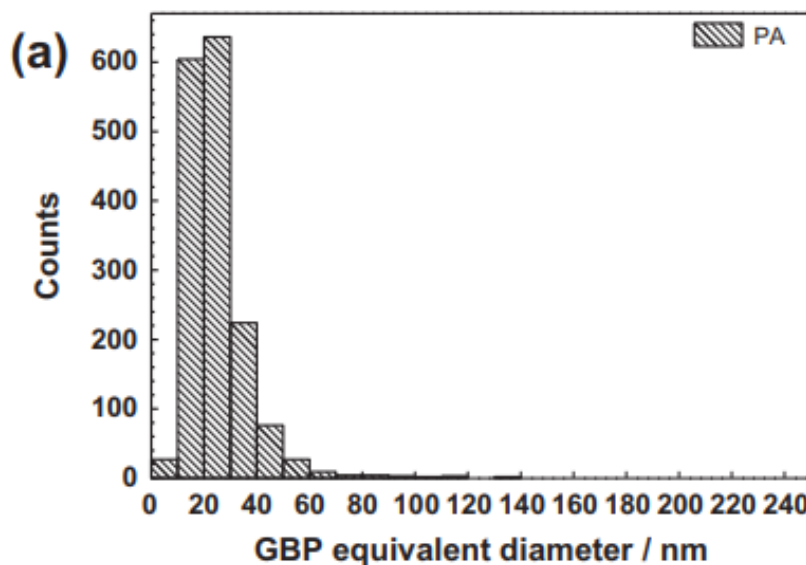


Figure 2.35: Example of distribution of grain boundary precipitate lengths for a peak-aged Al-Zn-Mg-Cu industrial alloy [40].

In general, more detailed data should be collected to rationalize the GBP microstructural variations linked to the cooling rate effect. A record of GBP length distributions with varying cooling rates would add a valuable piece of information in the literature by better highlighting the heterogeneity of GBPs.

Examples of GBP size distributions as a function of aging parameters are present in the literature (Fig.2.35) [40,121], but this type of data is rare as a function of the cooling rate. Finally, many studies agree that the coverage of GBs and the width of PFZs in the second phases increase with a decreasing cooling rate [44,46,95]. Studies have also commonly reported that the inter-particle distance on GBs increases with a decreasing cooling rate [37,122].

Regarding the grain interior microstructure, how the cooling rate affects the development of the fine-scale precipitates remains a topic under discussion. A consistent body of evidence shows that quench-induced precipitation decreases the overall solute concentration in the matrix, therefore hindering the subsequent aging response as a lower density of fine-scale precipitates is formed [46,123].

For example, Zhang et al. [123] conducted SAXS experiments on samples cooled over a wide range of cooling rates and calculated that both solute concentration and volume fraction of hardening precipitates decrease when lowering the cooling rate; concurrently, the average size of the hardening precipitates increases. Other studies instead support that quench-induced precipitates at GBs and on dispersoids reduce the solute concentration only in the immediate matrix surroundings, leaving the aluminium matrix far from the precipitates unchanged in terms of the alloying element concentration [39,44,45].

Dumont et al. [45] and Deschamps et al. [44] reached the same conclusion through using TEM micrographs to carefully examine the aluminium matrix. In addition, Deschamps et al. [44] established that these precipitation features occur even when using cooling rates as low as roughly 0.1 °C/s. This finding is surprising because, at these very low cooling rates, the homogeneous growth of large η precipitates is sometimes detected [46]. In other words, a consistent quantity of solute atoms in the matrix is participating in the precipitation process.

These different findings about the inner matrix precipitation features during cooling suggest that more contributions are needed to clarify how this portion of the alloy microstructure is influenced by cooling rate variations.

2.13: Constraints of the HFQ® aging step

During the precipitation hardening treatment of 7000 aluminium alloys, the selection of the aging parameters (steps, durations and temperatures used) greatly influences the final mechanical and corrosion performances of the component. The choice of appropriate aging parameters in the HFQ® process needs to consider that the auto panels produced are subjected to additional thermal steps linked with the downstream car manufacturing process.

In fact, the high-strength aluminium auto panels are joined to the other car components to form the body-in-white (BiW), and after a cleaning step, this assembly is subjected to a coating process where various layers are applied.

Those coating layers have both a protective and aesthetical function and must be implemented through multiple

stages of oven curing, also called the paint-baking cycle (Fig.2.36).

Depending on the specific car manufacturer, the paint-baking cycle can include different thermal steps over a time span of indicatively 20–60 minutes

and a temperature range of 125 °C–180 °C [125,126]. The heat

treatments linked with these operations constitute an additional aging step for the 7000 aluminium alloy components included in the BiW and alter the microstructure imparted during the previous aging step. Unfortunately, skipping the aging step and relying just on the paint-baking cycle to promote the final hardening response is not a feasible strategy; the paint-baking thermal steps alone cannot sufficiently develop the optimal distribution of fine hardening precipitates required [127,128,129].

For example, Li et al. [129] simulated a paint-baking process through the aging of 7000 aluminium alloy samples at 180 °C for various progressive durations. The researchers reported that the peak hardness of those specimens was reached



Figure 2.36: BMW MINI body-in-white being oven cured during one of the paint-baking steps [124].

after 10 hours of heat treatment (Fig.2.37). Therefore, the findings suggest that the usual paint-baking cycle duration is too short to develop a peak-aged microstructure in the auto panels.

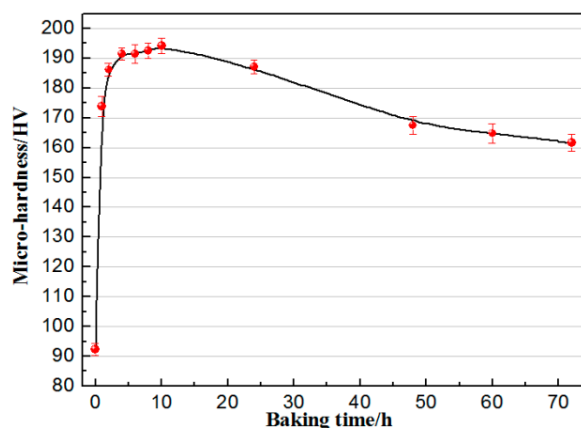


Figure 2.37: Micro-hardness as a function of paint-baking time during heat treatment of Al-Zn-Mg-Cu samples at 180 °C [129].

Conversely, reaching the peak aging state with the aging step and then subjecting the workpieces to the paint-baking process is also an unsuccessful approach when using 7000 aluminium alloys.

This strategy reportedly results in an excessive overaging of the aluminium auto panels and an unacceptable worsening of their final mechanical properties [128,130]. In fact, Min et al. [128] registered an 8% strength decrease and a 17% elongation to break decrease when processing peak-aged samples through the usual paint-baking cycle. To solve these thermal treatment difficulties, the most adopted strategy consists of applying a shorter aging step than the typical peak-aging treatment, referred to as the 'preaging step', and then sending the workpieces to the paint-baking cycle.

The literature has consistently shown that the use of the preaging step enhances the hardening response of the material during paint-baking to levels that are comparable to those of the peak-aging state [50,128,129,130]. A relevant number of studies also investigated which optimised preaging parameters should be applied to maximise the subsequent bake hardening response of 7000 aluminium alloys [128,131]. For example, Dehghani et al. [131] explored the effectiveness of various combinations of preaging and paint-baking parameters for AA7075 via a response surface methodology approach.

From a microstructural point of view, the enhanced bake hardening response associated with preaging has been linked to the formation of stable GP zones that survive when reaching paint-baking temperatures that aid in the nucleation of strengthening η' precipitates [128,130].

Although the mechanical properties and microstructural evolution during preaging/paint-baking have received more attention in the literature, how this aging schedule affects the SCC resistance specifically and the corrosion properties of the auto panels generally remain unexplored and needs further investigation. In a rare example, Li et al. [129] reported that the corrosion resistance of a member of the 7000 aluminium alloy family subjected to the preaging/paint-baking strategy improves when compared to the corrosion resistance linked with samples only paint-baked.

When designing the HFQ[®] aging step, a second constraint is linked to the management of the natural aging effect after the cooling step: during natural aging, the tensile strength of the workpieces slowly grows with increasing storage time, and this growth can complicate the possible following riveting operations (Fig.2.38) [50].

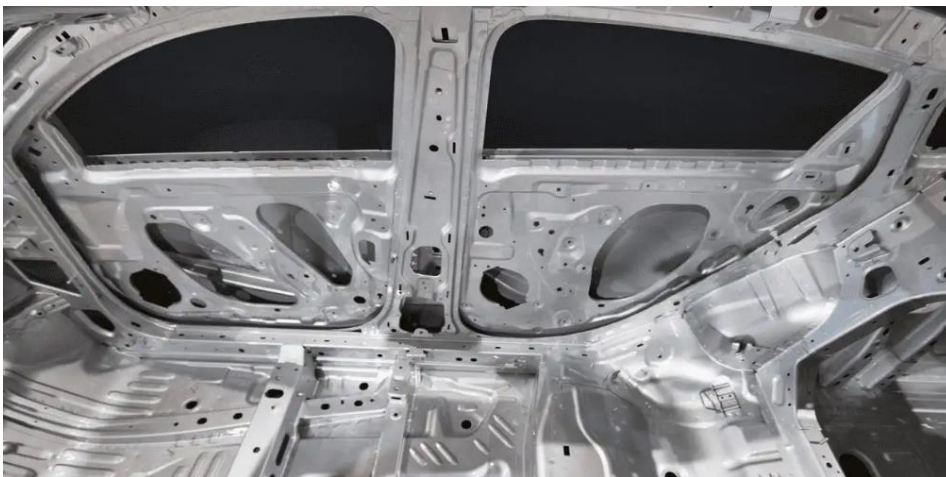


Figure 2.38: Interior view of an aluminium body-in white. A complex pattern of holes is needed to enable riveting with other components [132].

This strength increase is also detrimental because an aging step performed after a prolonged storage duration determines a reduced hardening response of the material and a sub-optimal final strength. Instead, if the aging step is imparted immediately after cooling, the workpieces will benefit from the maximum hardening response achievable, and the post-aging variations linked with natural

aging are drastically reduced [127]. In fact, aging treatments are commonly believed to have a 'stabilisation effect' on the samples' microstructure; therefore, aging strategies are also evaluated and designed regarding their ability to mitigate the negative effect of natural aging.

In the current state of the literature about this topic, preaging strategies have been found capable of imparting the desired stabilising effect for certain alloy systems [50,127]. Certain members of the 7000 aluminium alloy family instead are still being studied to determine if their aging process can reduce the natural aging strengthening effect. Ongoing research is still being conducted on these alloys [50].

For example, Osterreicher et al. [50] fully stabilised AA7021 via an optimised preaging step, but did not find preaging parameters that worked well for AA7075. From a microstructural point of view, although the topic remains unclear, GP zones formed at room temperature during natural aging (called GP(I) zones) are seemingly unstable during subsequent aging steps and cannot facilitate the η' formation. On the contrary, preaging at higher temperatures provides stable GP zones (called GP(II) zones) that can successfully help the η' nucleation [50,128].

In sum, from the literature emerges the need to evaluate the SCC resistance and corrosion properties linked to the use of the preaging/paint-baking schedule. Regarding the HFQ[®] aging step, the proposed aging parameters should be tailored to consider the integration with the paint-baking cycle and to consider the effect of the subsequent natural aging period.

2.14: Basic principles of age hardening

Among the different hardening mechanisms available, precipitation strengthening is the main strengthening mechanism for 7000 aluminium alloys. The presence of alloying solute atoms means the precipitation of secondary phases is realised artificially through the precipitation hardening heat treatment schedule: solution heat treatment, rapid cooling and aging treatment.

As the solution heat treatment raises the temperature of the system above the solvus (State 1 in Fig.2.39), the second phases generated from the previous thermo-mechanical history of the material are dissolved. The alloying elements also become evenly distributed in the material.

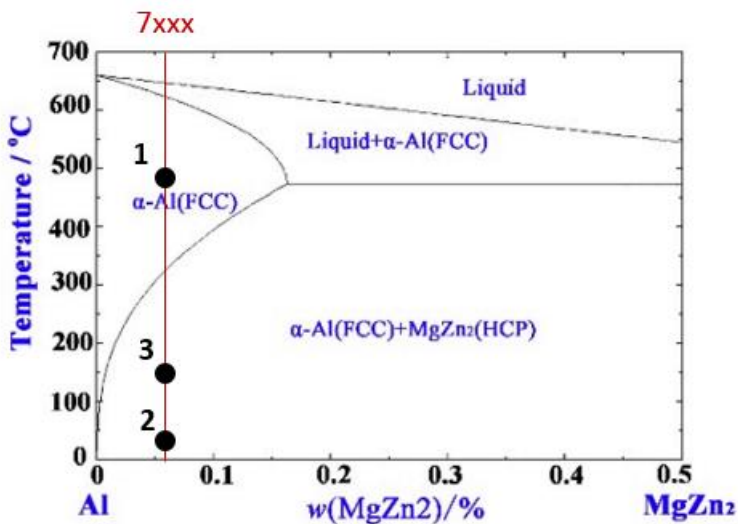


Figure 2.39: Pseudo equilibrium diagram of the Al-MgZn₂ system. The typical composition of a 7000 aluminium alloy (red line) and the sequence of thermodynamic states linked to the precipitation hardening sequence (States 1, 2 and 3) are highlighted [136].

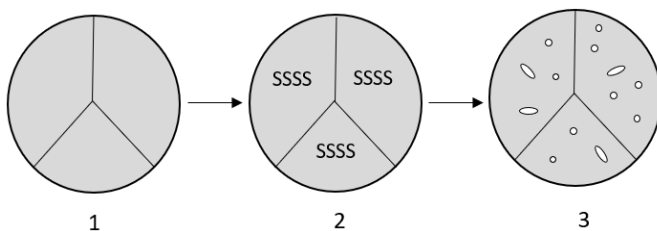
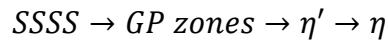


Figure 2.40: Schematic representation of the matrix microstructural changes linked to the different states of the precipitation hardening sequence.

When rapidly cooling to room temperature (State 2 in Fig.2.39), the system gains a high thermodynamic driving force for nucleation and the growth of precipitates. However, the phase transformation is kinetically hindered by the low temperature, and the material remains in a condition of supersaturated solid

solution (SSSS). The aging treatment (State 3) is then used to activate the transformation pathway of the matrix precipitates. From a thermodynamic point of view, the stable phase promoted should be directly $MgZn_2$, but the precipitates evolution follows the accepted sequence below:



In fact, the formation of the stable $MgZn_2$ directly from the SSSS would require more energy than reaching the same final η phase through the sequence of evolving metastable precipitates. This sequence provides that the η phase formation is realised via smaller energy steps rather than via a considerable energy variation.

The literature has consistently established that GP zones are coherent, η' precipitates are semi-coherent and $MgZn_2$ is incoherent with the aluminium matrix. The formation of coherent interfaces needs a smaller energy contribution compared to semi-coherent interfaces (η' phase) or incoherent interfaces (η phase). This difference explains why the precipitate evolution sequence is linked to smaller energy steps.

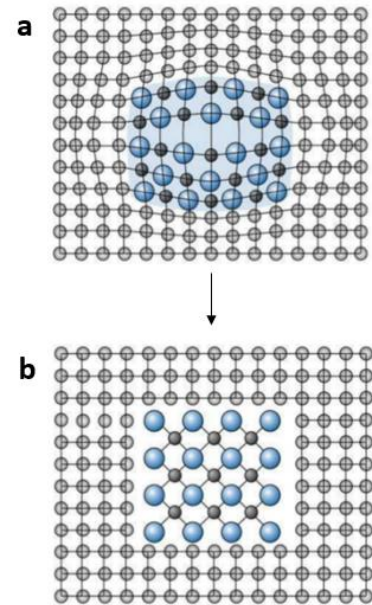


Figure 2.41: Schematic example of the transformation from (a) precipitate coherent with the matrix to (b) precipitate incoherent with the matrix [134].

$MgZn_2$ is the most abundant precipitate type in 7000 aluminium alloys, but the possible precipitation of θ (Al_2Cu), T ($Al_2Mg_3Zn_3$) and S (A_2CuMg) is commonly reported [59]. Among the different parameters that regulate the relative fraction of all these secondary phases, the content of alloying elements in the sample plays a fundamental role. For example, the quantity of T phase is believed to increase proportionally to the Mg content [135], while Cu has a stabilising effect on the S phase formation [133,135].

2.15: Aging strategies for 7000 aluminium alloys

After solution heat treatment and rapid cooling, the most common way to reach the peak-aged state in 7000 aluminium alloys is via aging at 120 °C for 24 hours (T6 temper). This heat treatment promotes a refined matrix precipitate distribution of mostly η' precipitates and fewer GP zones (Fig.2.42), which is responsible for the excellent tensile properties achieved [136].

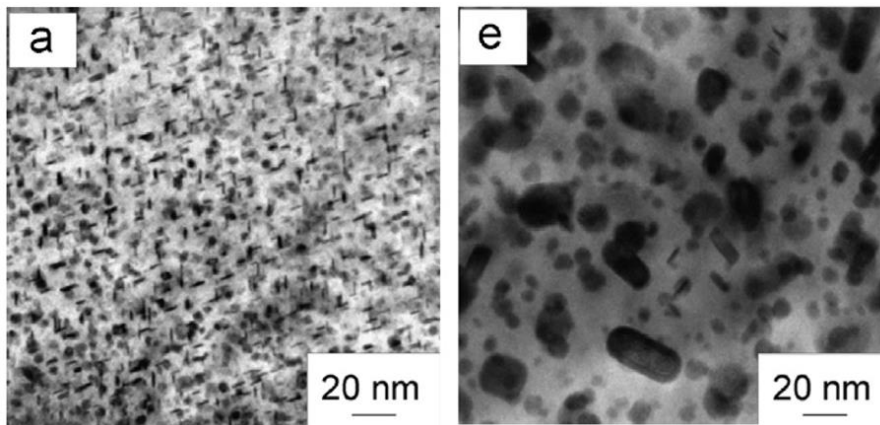


Figure 2.42: Examples of the matrix microstructure of AA7150 samples: (a) T6 temper and (e) T73 temper [137].

GBs also display an interconnected distribution of small GBPs (Fig.2.43) with lower copper content: this microstructural feature has been linked to the high susceptibility of the T6 temper to SCC [139]. If temperatures higher than 120 °C are applied, the peak-aged state can be achieved with shorter aging durations as precipitation kinetics result accelerated.

For example, Zou et al. [140] reached the peak-aged state in AA7085 samples via aging at 175 °C for 8 hours. However, the use of a higher temperature more easily activates the conversion of η' into η phase, and this conversion can reduce the maximum mechanical strength achievable [141].

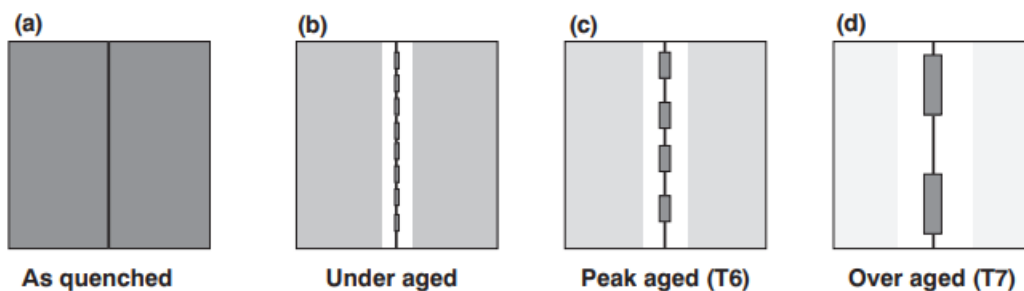


Figure 2.43: Schematic representation of grain boundary microstructures when varying the aging state of 7000 aluminium alloys [110].

Although reducing the aging time from 24 hours to 8 hours already constitutes a remarkable improvement, the reduction would still considerably hinder the overall HFQ® productivity target. The most consolidated way to accelerate aging kinetics is using two consecutive thermal steps, where the first one is performed at a lower temperature than the second one. This aging strategy, called two-step aging or double aging, can impart strength levels comparable to the T6 levels and drastically reduce the heat treatment duration [142,143].

For example, Emani et al. [142] achieved peak hardness in AA7075 samples with the first aging step at 121 °C for 55 minutes followed by a second step at 177 °C for the same duration (Fig.2.44). Besides a few studies, however, most of the

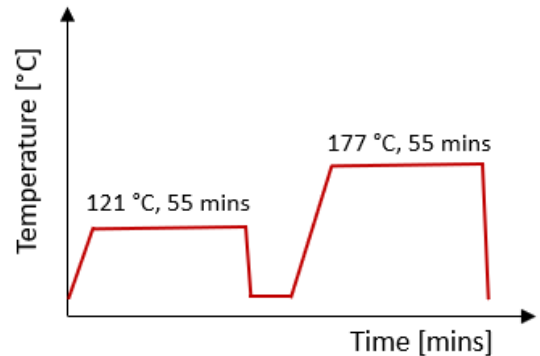


Figure 2.44: Time-temperature profile (two-step aging strategy) used by Emani et al. [142] to reach the peak hardness state in AA7075 samples.

examples of two-step aging strategies examined in the literature do not usually achieve a competitive time reduction. The evaluation of the SCC resistance of time-efficient two-step aging strategies is poorly documented, but some studies have been conducted for longer double aging schedules.

Jegdic et al. [144], for instance, assessed the SCC resistance of 7000 aluminium alloy samples in the T6 temper and aged via a first step at 100 °C (5 hours) plus a second step at 160 °C (5 hours). While T6 and double aged specimens showed similar mechanical properties, the SCC resistance of the two-step aging schedule was reasonably improved. As with preaging/paint-baking strategies, the acceleration of the hardening response in two-step aging schedules is based on the growth of stable GP zones (first thermal step) that aid in the nucleation and refinement of the η' strengthening phase (second thermal step) [142,143].

Interestingly, the time span and temperature between the first and the second step of the double aging strategy also appreciably influence the final mechanical properties achievable [145,146]. Precipitation occurring during this time gap at low temperatures has been termed 'secondary aging' in the literature [145,146]. For example, Buha et al. [146] studied the microstructural evolution and

hardening response of AA7050 with a first aging step at 130 °C is followed by an isothermal holding at 22 °C or 65 °C.

When the time efficiency of the process is not a concern, the typical solution to gain acceptable SCC resistance is prolonging the T6 treatment with an additional time-consuming step at higher temperature, for example, 30 hours at 160 °C. The overaged state produced, termed T7x, acquires protection from SCC but at the expense of a 10%–15% strength loss [147]. The prolonged thermal step at high temperature causes the coarsening of the matrix precipitates (Fig.2.42) and their partial conversion from η' to η (mechanical strength reduction), while the enlargement of GBPs and increased interspacing (Fig.2.40), also coupled with their increased copper content, has been linked to the substantial improvement of SCC resistance [43,147].

The use of the T7x temper is completely incompatible with the HFQ[®] heat treatment schedule because of the unacceptable loss of strength and prohibitive step duration. Although equally time-consuming, the so-called RRA strategies can

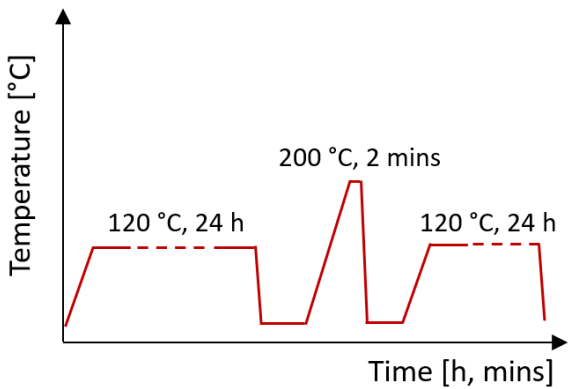


Figure 2.45: Time-temperature profile (retrogression and reaging strategy) used by Viana et al. [139].

substantially improve the SCC resistance of the and maintain strength levels equal to peak-aged samples [121,139,147]. RRA schedules consist of applying a high temperature isothermal step of limited duration called retrogression (in the range of 180 °C–240 °C and 5 seconds–2400

seconds [42]) to a T6 tempered specimen and then reaging the material with a second peak-aging treatment, such as 120 °C for 24 hours (Fig.2.45).

RRA cannot be selected as an aging strategy for the HFQ[®] process because the duration is more than double the length of a peak-aging treatment. The parameters used for the retrogression step can modulate the final mechanical strength and SCC resistance achieved by the 7000 aluminium sheets [121,139].

For example, Baydogan et al. [52] explored different combinations of retrogression temperatures and times to optimise the hardness and SCC

resistance of AA7075 sheets. During retrogression, the coarsening of GBPs and an increase of their interdistance occurs, while small η' precipitates and GP zones dissolve, thus enriching the matrix with solute elements [42,121,139]. At the same time, larger η' precipitates grow, and some conversion to the η phase takes place [42,121,139].

This succession of microstructural changes in the material dictates the appearance of the typical trend shown by Park et al. in Figure 2.46 when plotting hardness against retrogression time [121].

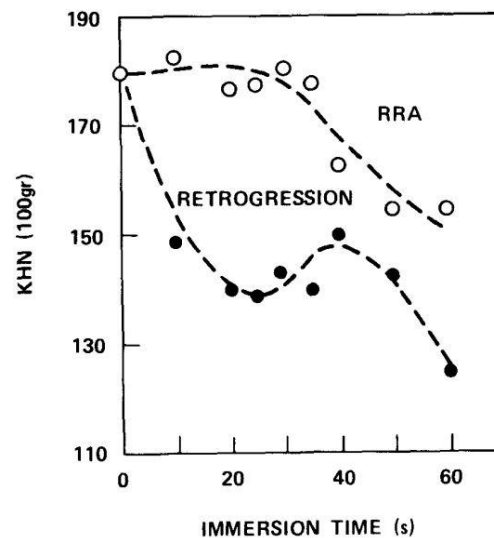


Figure 2.46: Plot of hardness versus retrogression time of retrogressed AA7075-T651 samples. [121].

During the reaging process instead, the solute enrichment causes the formation of fine η' precipitates [42,121,139], which in turn cause a step hardness increase in the treated samples (Fig.2.46).

In conclusion, the optimised mechanical and corrosion properties imparted by RRA strategies are linked to GB microstructures like the T73 tempered materials and matrix precipitates comparable to T6 tempered samples [42,121,139].

Besides these microstructural features, other studies also mention the role of the dislocation density reduction during reaging when describing the properties of RRA specimens [148,149].

The increasing complexity of time-temperature profiles during aging is the current trend followed to achieve the required mechanical and corrosion properties in the final components and preserve an acceptable duration of the heat treatment. Strategies involving the use of temperature ramps across a wide range of temperatures (Fig.2.47) have recently received attention from the literature and they have been called non-isothermal aging strategies (NIA) [53,150].

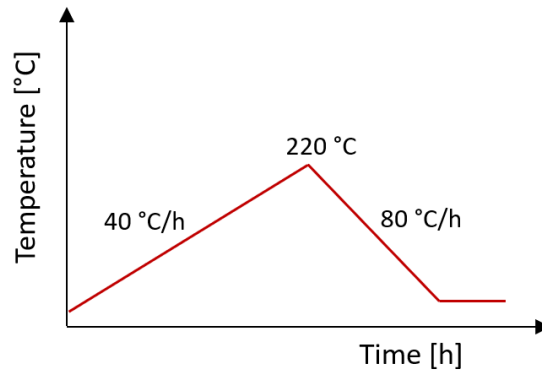


Figure 2.47: Time-temperature profile of the non-isothermal aging strategy used by Jiang et al. [150].

For example, Jiang et al. [150] obtained satisfactory mechanical and corrosion properties in AA7050 samples when using a heating ramp of 40 °C/h with heating rate between 100 °C and 220 °C followed by a cooling ramp at 80 °C/h, with the total duration of the aging step at roughly 5 hours.

In addition to the efficient use of time and the attainment of optimized final properties, NIA strategies temperature profiles follow patterns that might unlock the accelerating kinetic principles of two-step aging strategies and the beneficial retrogression effects of RRA strategies. The final microstructures imparted in the workpieces treated are also comparable to the microstructures delivered via RRA heat treatments [53,121].

In the literature, attempts to design a complex aging strategy for the HFQ[®] process that meets the property requirements whilst minimizing process time is currently missing. The design of such aging strategy is therefore a key goal of this thesis. Further, although some examples in the literature show how complex aging strategies can affect the sample microstructure [53,150], more contributions are needed to rationalise the link between the temperature profiles realised during aging and the microstructural evolution of 7000 aluminium alloys.

Chapter 3:

Research Methodology

The previous chapter provided an overview of relevant studies on the metallurgical optimisation of the HFQ® process and identified areas where further research is needed. In the Research Methodology chapter, an experimental plan is presented to address these gaps in the literature. The plan involves optimising each step of the HFQ® process separately, without considering the effects of deformation during cooling.

This chapter contains a description of the starting materials and experimental layout, as well as a detailed description of methods that are not commonly used in 7000 aluminium alloy metallurgy, such as small-angle x-ray scattering or anodic polarization experiments. Standardized tests, on the other hand, are not covered in this chapter, but can be found in specialized literature sources.

3.1: The experimental plan

3.1.1: Solution heat treatment

To better understand the dissolution process during the solution heat treatment step, it would be beneficial to investigate how temperatures above the conventional industrial limit and extremely short step durations (especially when low heating rates are used) can influence the process.

To contribute towards this direction, the starting material for this study was solution heat treated using different relevant combinations of temperatures and durations, while maintaining a constant cooling rate and fixed aging step. The Vickers hardness of the metallurgical conditions generated was then recorded. In fact, a higher degree of precipitate dissolution during solution heat treatment causes a greater concentration of solute elements in the matrix. This larger concentration, in turn, leads to a finer distribution of precipitates during aging, resulting in an improved hardness in the workpiece: the Vickers hardness recorded is directly proportional to the extent of the precipitate dissolution that occurred during solution heat treatment.

The literature review also revealed that the extent to which incipient melting is required to deteriorate the mechanical properties of the alloy is still not clearly documented. Likewise, how solution heat treatment temperatures above the eutectic limit impact the degree of this occurrence also remains unclear.

Thus, scanning electron microscopy (SEM) micrographs of samples exposed to temperatures above the eutectic limit were collected and compared to a reference SEM micrograph of a specimen solution heat treated at conventional temperature. In this way, the microstructural differences linked with possible incipient melting could be identified.

Finally, as the evolution of recrystallisation and grain growth linked to thermal exposure above the eutectic limit also requires further investigation, grain size distributions were acquired for the same relevant metallurgical conditions mentioned above and then compared to a reference sample.

While previous studies documented that raising the heating rate can accelerate precipitate dissolution, they also revealed that the effect of this parameter on the precipitate dissolution process remains unclear. Similarly, challenges exist to separate the effect of the heating ramp and the effect of the total holding time of the solution heat treatment on the second phase dissolution.

To help answer these unsolved research questions, samples were subjected to solution heat treatments with varying heating rates and total holding times, while the remaining part of the precipitation hardening sequence was kept constant. In this experiment, the fine control required for the solution heat treatment parameters was realised via automatically controlled resistance heating.

Vickers hardness measurements and differential scanning calorimetry (DSC) were then used to characterise the heat treated specimens and understand how the heating rate and total holding time affected the precipitate dissolution process. DSC is widely adopted in the literature to study the matrix microstructural features of 7000 aluminium alloys [137,139].

More contributions would be needed in the literature to define the link between the heating rate magnitude and the grain structure refinement achieved. Thus, the grain size distribution of the specimen solution heat treated with high heating rate was obtained and compared with that of the slow heated samples.

3.1.2: Cooling step

Regarding the cooling step, different papers suggest [37,38] that moderately reducing the cooling rate from the maximum value achievable can greatly improve the stress corrosion cracking (SCC) resistance of the samples tested without compromising their hardening potential. To demonstrate the feasibility of this strategy for the HFQ[®] process, specimens cooled at different rates but with a fixed solution heat treatment and aging step were tested to evaluate how mechanical properties and SCC susceptibility varied with different cooling rates. Uniaxial tensile tests were used to assess the samples' mechanical properties, while U-bends exposed to a salt-spray fog environment were used to evaluate the samples' SCC resistance. The SCC susceptibility rankings of the metallurgical conditions derived from this type of test reportedly correlate well with the results of standardised constant load tests [101].

The literature review also indicated that the characteristics of the grain boundary (GB) microstructure with varying cooling rates remain a subject of debate. For this reason, for the same metallurgical conditions mentioned, distributions of grain boundary precipitate (GBP) lengths were generated from the analysis of transmission electron microscopy (TEM) micrographs.

The study of the GBP compositional evolution as a function of the cooling rate also requires further investigation from researchers. Due to the intrinsic experimental difficulties to obtain this data, a modelling approach was used to simulate the GBP microchemistry evolution with varying cooling rates. The CALPHAD-informed phase-field model (CIPHER) developed by Liu et al. [111] was used for the simulation work because excellent agreement between simulation and experimental results is documented when using this phase-field model [111]. Generally, as more contributions are needed to strengthen the link between heat treatment parameters and GBP composition, CIPHER was also used to predict the microchemistry evolution at GBs with varying aging temperatures and durations.

As previously mentioned, the effect of cooling rate reductions on matrix solute levels and on the aging response of the material remains a topic of discussion in

the literature. For this reason, the matrix precipitation state after aging with varying cooling rates is quantified via DSC traces and small-angle x-ray scattering (SAXS) experiments. SAXS is a useful technique adopted in the literature to assess matrix precipitate features, and the technique offers a good sampling ability [123].

The microstructural and microchemical characterisations proposed are also useful to connect the final properties reported with the variation of cooling rate.

3.1.3: Aging step

When focusing on the aging step, the literature still lacked enough attempts to create a valid aging strategy for the HFQ[®] process that satisfies property requirements and minimises process time. As a result, designing such a strategy is a critical objective of this thesis. The aging strategy proposed, the retrogression and reaging double aging (RRDA) strategy, is built through merging two-step aging with retrogression and reaging (RRA) strategies and includes a sequence of five thermal steps. The tuning of the RRDA steps is achieved through the development of Vickers hardness plots as a function of aging parameters. This choice is made based on the ease and rapidity of hardness tests compared to full-scale tensile tests, exploiting the close correlation between hardness and yield strength observed in aluminium alloys. This allows exploration of a wide range of metallurgical conditions in a short time span.

The characterisation of the RRDA strategy is carried out by comparing the microstructural features and final properties generated by this aging schedule with those of other industrially relevant tempers for 7000 aluminium alloys. For these experiments, while the aging step varied, the solution heat treatment and cooling step were kept constant. T6 tempered samples were used as being exemplars of the peak aged state, while T73 specimens were representative of overaged materials. In addition, two-step aged samples (referred to as FA samples) were also included in the comparison, as microstructurally close to preaged/paint-baked specimens.

The matrix precipitate characteristics of these metallurgical conditions were investigated via DSC and the SAXS experiments, while the GB microstructure was investigated through the creation of GB length distributions, which are based on the analysis of TEM micrographs.

The final properties generated were instead quantified via tensile tests and U-bend SCC tests. As previously discussed, the evaluation of the SCC resistance of two-step aged samples is intrinsically valuable since it is rarely reported in the literature. This fact also justifies the choice of including FA samples among the aged materials examined.

Further, the link of electrochemical parameters with the SCC performance of samples heat-treated differently is another direction worth exploring. Therefore, anodic polarisations of samples with varying cooling or aging steps were acquired, and the associated electrochemical parameters were compared with the SCC resistance for matching metallurgical conditions.

Generally, despite the existence of examples showing how complex aging strategies impact the microstructure of the samples, further research is necessary to clarify the connection between time-temperature aging profiles and the evolution of the microstructure and properties in 7000 aluminium alloys. For this reason, DSC and the SAXS experiments were performed on samples subjected to each of the RRDA steps, while tensile tests and U-bend SCC tests were used to characterise their property evolution.

In addition, because HFQ[®] auto panels are subjected to the paint-baking thermal cycle after aging, the developed RRDA strategy should ideally be integrated with this last thermal step. Although more experiments would be required to perform this integration process, the tensile tests characterising each RRDA step are also repeated again after 3 months of natural aging. In this way, the microstructural stabilisation effect of each step can be evaluated, as can the possibility of merging the RRDA aging strategy with the paint-baking cycle.

3.2: Starting materials

AA7075 is the reference material in this study because this traditional alloy is one of the benchmark materials in the aerospace sector; the metallurgy of the material has also been extensively studied in the literature.

F tempered AA7075 sheets with a 1.5 mm thickness were provided by Constellium with the typical composition listed in Tab.3.1. These sheets are the starting material used in this study.

Zn	Mg	Cu	Fe	Si	Mn	Cr	Ti	Al
5.1-6.1 wt%	2.1-2.9 wt%	1.2-2 wt%	0-0.5 wt%	0-0.4 wt%	0-0.3 wt%	0.18-0.28 wt%	0-0.2 wt%	87.1-91.4 wt%

Table 3.1: Typical composition of AA7075 [151].

High purity aluminium (99.99 wt%) with dimensions of 50 mm x 50 mm x 1 mm was provided by Thermo Fisher Scientific and used in DSC and the SAXS experiments.

3.3: Layout of the experiments

3.3.1: The optimisation of the solution heat treatments at low heating rates

Fig.3.1 shows the experimental flow diagram for the set of experiments related to the optimisation of solution heat treatments at low heating rates.

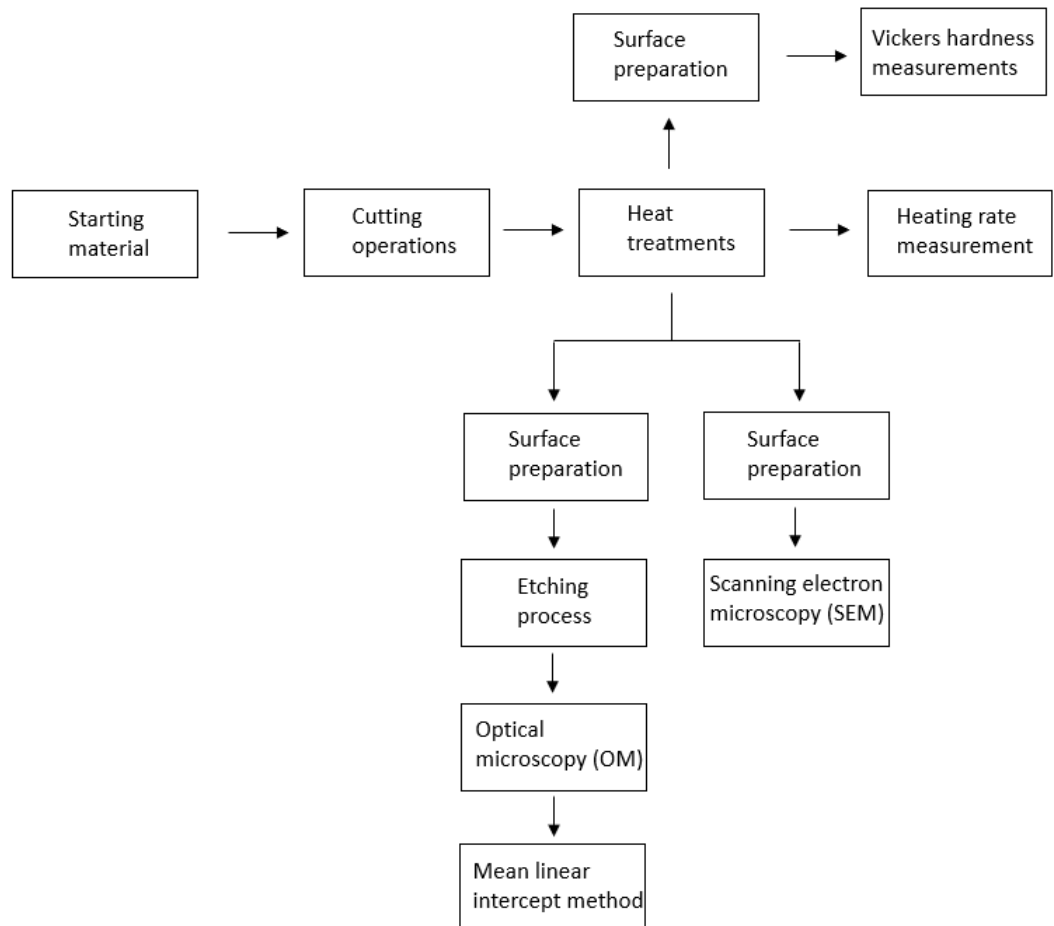


Figure 3.1: Experimental flow diagram of the experiments related to the optimisation of the solution heat treatment at low heating rates.

F-tempered AA7075 A4 size sheets were cut into 10 mm x 10 mm x 1.5 mm coupons and then heat treated. Each sample was subjected to different solution heat treatment steps, where the solution heat treatment temperature varied in a range between 470 °C and 530 °C, and the solution heat treatment duration varied between 1 minute and 10 minutes. In addition, a benchmark sample processed at 470 °C for 1 hour was also generated. The average heating rate to reach the solution heat treatment temperature was 2.5 °C/s (see Section 3.4.2).

All the samples solution heat treated were identically water quenched and then artificially aged using the two-step 'fast aging' aging strategy. Fast aging is a double aging strategy with an initial thermal step at a low temperature (between 80 °C and 120 °C) lasting multiple hours, followed by a second step performed at a higher temperature (150 °C–180 °C) and a shorter duration than the previous step. The time-temperature profile adopted for the current set of experiments is presented in Fig.3.2.

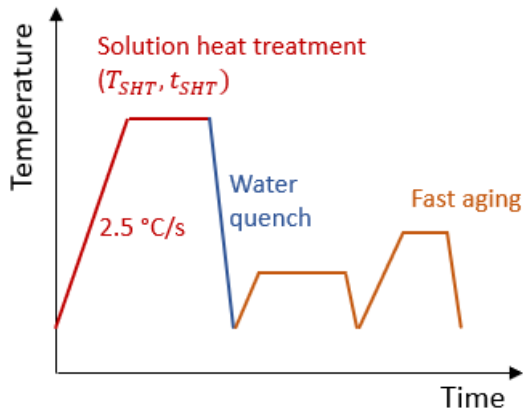


Figure 3.2: Sequence of thermal steps related to the optimisation of the solution heat treatment at low heating rates.

Because the eutectic temperature for AA7075 is reported as 475 °C, most of the temperatures selected for this experimental design surpass the safe eutectic limit. In addition, the holding times chosen are extremely reduced compared to the usual industrial practice [30,71]. For this reason, the proposed experimental conditions were considered adequate to study the optimisation of the HFQ® solution heat treatment at high temperature and competitive duration. The comparison between the microstructural features of the sample solution heat treated at high temperature and short holding time, and the microstructural features of the benchmark sample (470 °C for 1 hour) is useful to investigate the changes in grain structure and the possible onset of incipient melting.

After the heat treatment sequence, samples were subjected to different surface preparation steps (Section 3.4.4), depending on which characterisation method was used.

Specimens intended for hardness testing (see Section 3.4.5) were cold mounted in epoxy resin and polished to a surface finishing of 1 µm.

Samples analysed via SEM (see Section 3.4.8) were instead subjected to a surface finishing of 0.3 μm –0.05 μm with the use of oxide polishing suspension (OPS).

Samples intended for optical microscopy (OM) were polished to 1 μm finishing and then etched with Keller's reagent to highlight GBs (Sections 3.4.7 and 3.4.8).

The acquired OM micrographs were used to quantify the samples' grain structure via the mean linear intercept method (see Section 3.4.9).

3.3.2: The effect of the heating rate

Figure 3.3 displays the experimental flow diagram for the group of experiments that investigates how the heating rate affects the solution heat treatments.

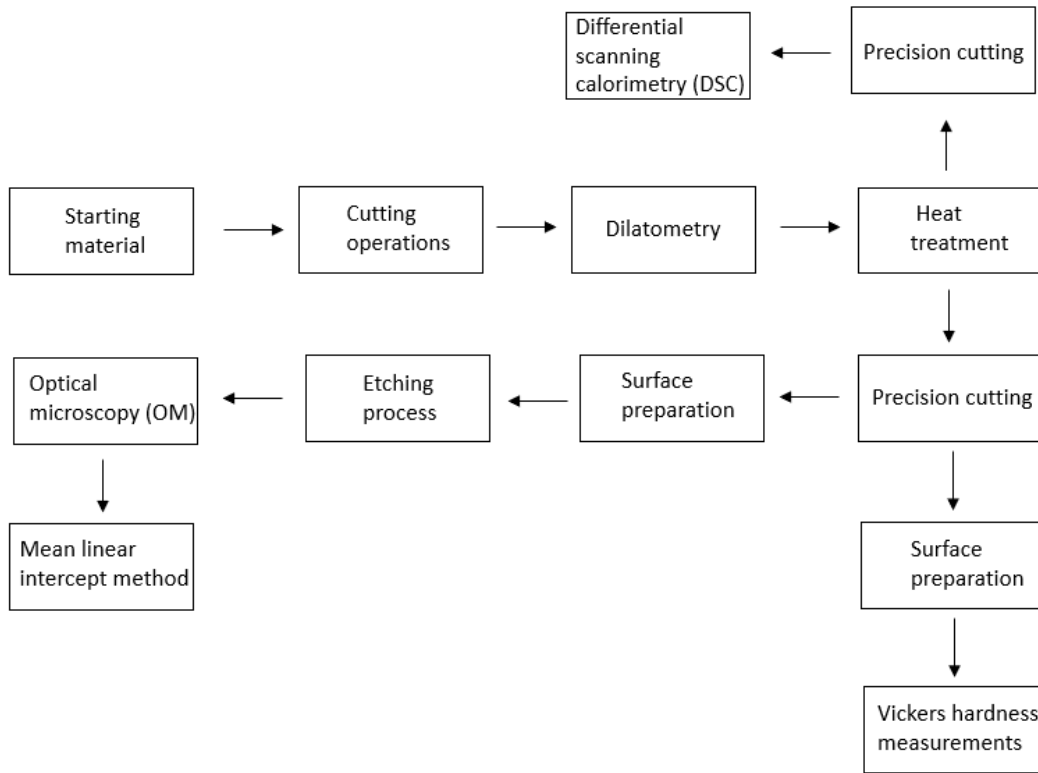


Figure 3.3: Experimental flow diagram of the experiments related to the effect of the heating rate.

AA7075-F sheets were cut into samples designed for the dilatometry experiments (see Section 3.4.3). Dilatometry was used as a technique to realise precisely controlled heating rates and durations for the solution heat treatments in this set of experiments, but no deformation was imparted to the samples processed. The heat treatments provided via dilatometry raised the temperature of the samples to 470 °C and included fast cooling with blown N₂ (average cooling rate 106.5 °C/s) that mimics water quenching (see Section 3.4.2). Because the critical cooling rate for AA7075 is commonly reported to be in the order of 100 °C/s [31], no relevant quench-induced precipitation was promoted during the fast-cooling step. After rapid cooling, all the specimens were fast aged in circulating air furnaces.

To isolate the effect of the heating rate on precipitate dissolution, an initial set of specimens was heated at 470 °C with a 3 °C/s heating rate, while a second set was heated at the same final temperature but with a heating rate of 200 °C/s (Fig.3.4).

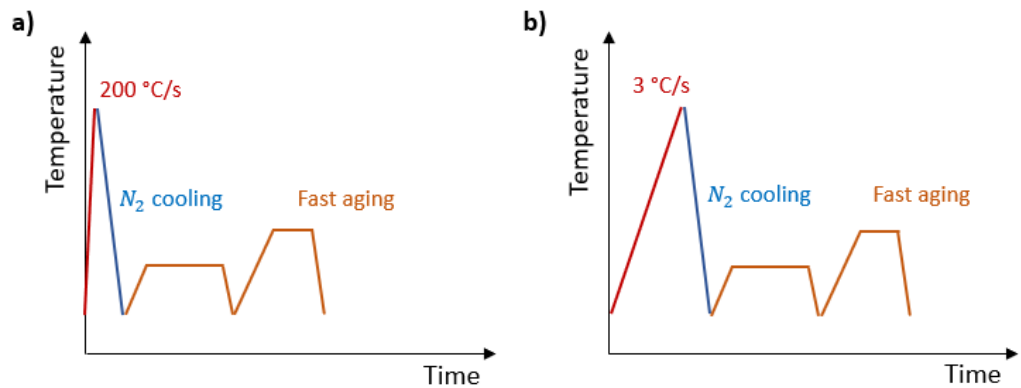


Figure 3.4: Time-temperature profile of (a) 200 °C/s sample and (b) 3 °C/s sample.

The 3 °C/s heating rate was selected because it is representative of the typical circulating furnace heating rate, while 200 °C/s was adopted for two reasons. First, the latter was adopted because it is a considerably high value. Second, comparing the 200 °C/s heating rate with the 3 °C/s rate allowed for more easily emphasising the precipitate dissolution differences among these two metallurgical conditions.

Notably, the total duration of the solution heat treatment with a 200 °C/s heating rate lasted only a few seconds as the specimens were rapidly heated to 470 °C and then immediately cooled. The solution heat treatment characterised by the 3 °C/s heating rate, however, instead lasted approximately 2.5 minutes.

To compare the precipitate dissolution effect of solution heat treatments with different heating rates but the same total duration, the 200 °C/s and hold temperature profile was defined (Fig.3.5). This solution heat treatment consisted of raising the sample temperature to 470 °C via the 200 °C/s heating ramp and then prolonging the solution heat treatment for 2.5 minutes. In this way, the 3 °C/s sample and 200 °C/s and hold sample had the same total duration for the solution heat treatment (see Fig.3.5).

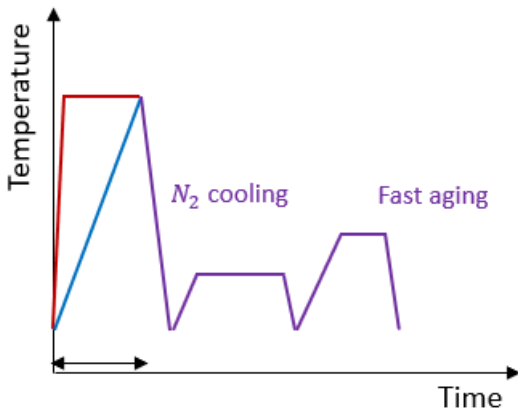


Figure 3.5: Comparison between the 3 °C/s time-temperature profile and the 200 °C/s and hold time-temperature profile.

Finally, although the 3 °C/s time-temperature profile and the 200 °C/s and hold time-temperature profile had the same solution heat treatment total duration, the holding time at 470 °C for the heat treatment with fast heating was observed to be considerably greater.

Therefore, the 3 °C/s and hold time-temperature profile was created so that its holding time at 470 °C matched that of the 200 °C/s and hold sample (Fig.3.6).

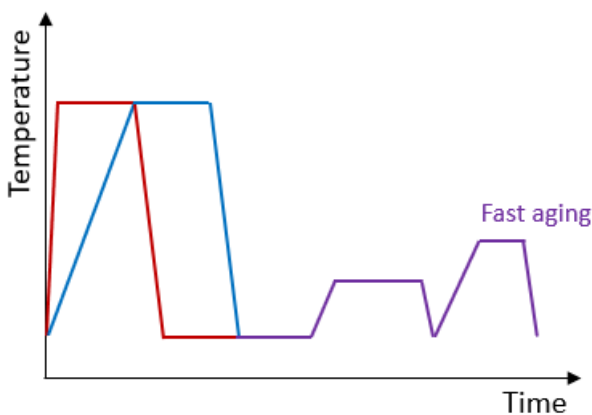


Figure 3.6: Comparison between the 3 °C/s and hold time-temperature profile and the 200 °C/s and hold time-temperature profile.

The comparison among the DSC traces and the hardness values of the different metallurgical conditions generated is expected to help clarify the effect of the heating rate ramp and subsequent holding time at the solution heat treatment temperature during the precipitate dissolution process.

After heat treatments, the dilatometry samples intended for Vickers hardness measurements or OM analysis were subjected to a stage of precision cutting (see Section 3.4.1) where coupons with the dimensions of 10 mm x 5 mm x 1.5 mm

dimensions were obtained. The coupons were then processed towards the pathways to acquire hardness measurements or OM micrographs in the same way explained in Section 3.3.1.

The OM micrographs acquired were then processed with the mean linear intercept method to quantify the grain size of samples subjected to the 200 °C/s heating rate and compare the grain size with that of slow heated samples. In this way, the order of magnitude for the grain size reduction linked to a wide heating rate variation could be identified.

Before testing, the specimens allocated for DSC (Section 3.4.6) were subjected to a combination of manual grinding and precision cutting to obtain 3 mm x 3 mm x 1 mm samples.

3.3.3: The optimisation of the cooling step

Figure 3.7 shows the experimental flow diagram for the set of experiments associated with the study of the cooling step.

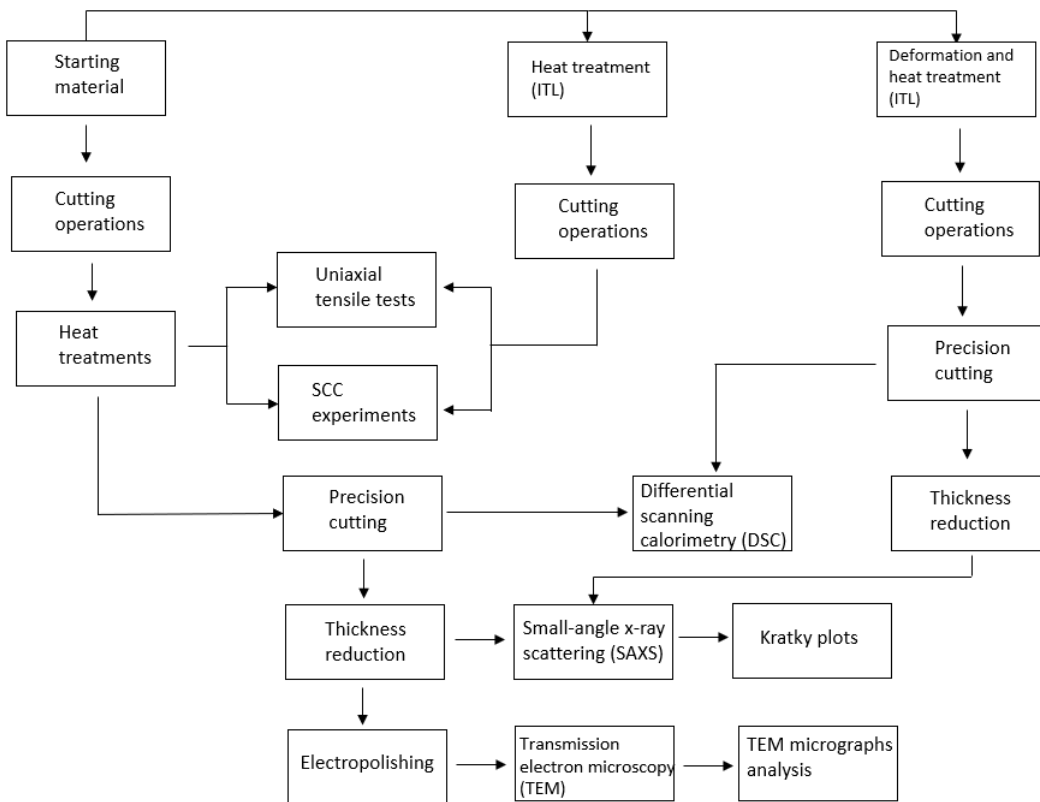


Figure 3.7: Experimental flow diagram of the experiments related to the optimisation of the cooling step.

F tempered A4 AA7075 sheets (starting material) were cut into samples with the dimensions required for uniaxial tensile tests (Section 3.4.15), SCC experiments (Section 3.4.16), and coupons of 10 mm x 10 mm x 1 mm. The latter of which were used for DSC and the SAXS experiments (Section 3.4.11) and TEM (3.4.13).

These specimens were subjected to a fixed solution heat treatment at 470 °C for 1 hour and then cooled with two different methods: water quenching and die-cooling. The calculated average cooling rate of samples die-cooled was 30.7 °C/s. After the cooling step, workpieces were identically fast aged.

As water quenching determines a cooling rate of hundreds of degrees Celsius per second, the two cooling rates selected resulted in a wide-spaced cooling rate range and therefore could validly describe the effect of this parameter on the microstructure and properties.

To improve the experimental design, Impression Technologies Ltd (ITL) heat treated the starting material and performed the cooling step using additional cooling rates while adopting the same solution heat treatment and aging step of the current work.

Table 3.2 summarises the total average cooling rates used in this set of experiments (cooling rate definition and calculations are outlined in Section 3.4.2).

Average cooling rate in the 450 °C-250 °C range [°C/s]	Average cooling rate in the 470 °C-50 °C range [°C/s]	ITL
Water quench	Water quench	
817.8	73.2	
362.5	48.0	
269.6	30.7	
182.5	13.6	

Table 3.2: Summary of the average cooling rates used in the cooling step experiments.

Average cooling rates calculated in the 470 °C–50 °C temperature range were used to define the cooling rates in this work.

The material heat treated by Impression Technologies Ltd was equally cut to produce tensile samples and SCC experiment samples, while coupons for DSC, the SAXS experiments and TEM were not created. The analysis with these latter techniques was performed only on water quenched and die-cooled (30.7 °C/s) samples because of the project time constraints.

In addition to the water quenched and die-cooled samples, an additional metallurgical condition was created for DSC and the SAXS experiments: F tempered sheets were solution heat treated (470 °C, 1 hour), simultaneously cooled (average cooling rate 73.2 °C/s) and deformed, and finally fast aged by Impression Technologies Ltd. This metallurgical condition was investigated as a preliminary result to investigate the effect of deformation during cooling, typical of the HFQ® process.

Water quenched samples, die-cooled samples and the cooled/deformed samples were cut into 3 mm x 3 mm x 1 mm specimens (via precision cutting) and used for DSC tests. For the same metallurgical conditions, coupons of 8 mm x 8 mm x

1.5 mm were obtained and then manually ground to achieve a thickness of 80 μm . These foils were used for the SAXS experiments and to generate Kratky plots.

For the water quenched and die-cooled samples, the produced foil were also subjected to electropolishing (Section 3.4.12) and TEM. The TEM micrographs obtained were used to create GBP length distributions (3.4.14).

3.3.4: The design of the RRDA strategy

F tempered AA7075 A4 sheets were cut into 10 mm x 10 mm x 1.5 mm samples and subjected to heat treatment. The heat treatment is constituted of a solution heat treatment at 470 °C for 1 hour, followed by water quenching and variable aging steps that were used to optimise the developed multi-step aging strategy.

While a complete discussion about the design principles of the RRDA strategy is presented in Section 6.1.1, the principles are only briefly summarised in this section.

The RRDA strategy consists of the use of a two-step aging schedule to reach the peak aged state in the material, followed by a retrogression step at high temperature. In the last portion of the strategy, the material is reaged after retrogression with a second two-step aging sequence (Fig.3.8).

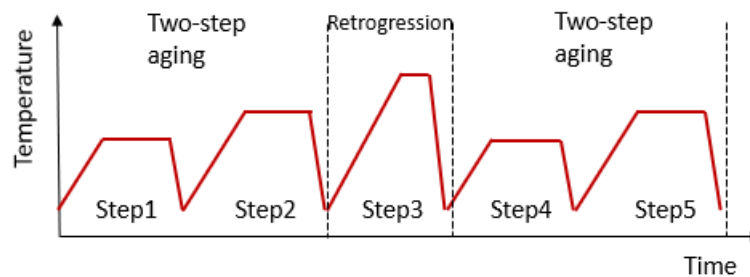


Figure 3.8: Time-temperature profile of the retrogression and reaging double aging strategy, showing the subdivision in 5 steps and the role of the steps in the strategy.

To optimise this complex sequence of thermal steps, first, the aging parameters of Step1 and Step2 were selected with the aim to reach the peak aging state in the shortest time span possible. To reduce the complexity of this optimisation problem, Step1 and Step2 were set at an equal duration. In addition, with reference to the work of Emani et al. [142], the first step was performed at 120 °C, while the second one was performed at 175 °C. Once these parameters were fixed, heat treatments were carried out with a varying total duration of Step1 + Step2 in a range between 30 minutes and 180 minutes. For example, the total duration of 30 minutes corresponds to 15 minutes for Step1 and 15 minutes for Step2. After the samples generated were cold mounted and polished to a 1 µm finishing, the Vickers hardness of each sample was calculated and an optimum value for the total duration of the thermal step was found. Once the

characteristics of Step1 and Step2 were defined, a second round of heat treatments was performed. This time, after the abovementioned solution heat treatment and water quenching, samples were subjected to the optimised Step1 + Step2 and then retrogressed at 220 °C for variable durations, ranging from 30 seconds to 1000 seconds. The selection of 220 °C as the retrogression temperature is discussed in Section 6.1.1 and based on the work of Park et al. [121].

The specimens generated were cold mounted and polished to a surface finishing of 1 µm. After this step, the Vickers hardness levels of the samples were measured, and the optimal retrogression time was evaluated. Step4 and Step5 simply consisted of reusing the optimised time-temperature profile found for Step1 + Step2. In this way, the overall RRDA strategy was defined, and its characteristics were examined in other sets of experiments.

3.3.5: Microstructure and property evolution during RRDA steps

Fig.3.9 presents the experimental flow diagram of the set of experiments used to characterise the microstructural evolution and final properties of the samples during the RRDA steps.

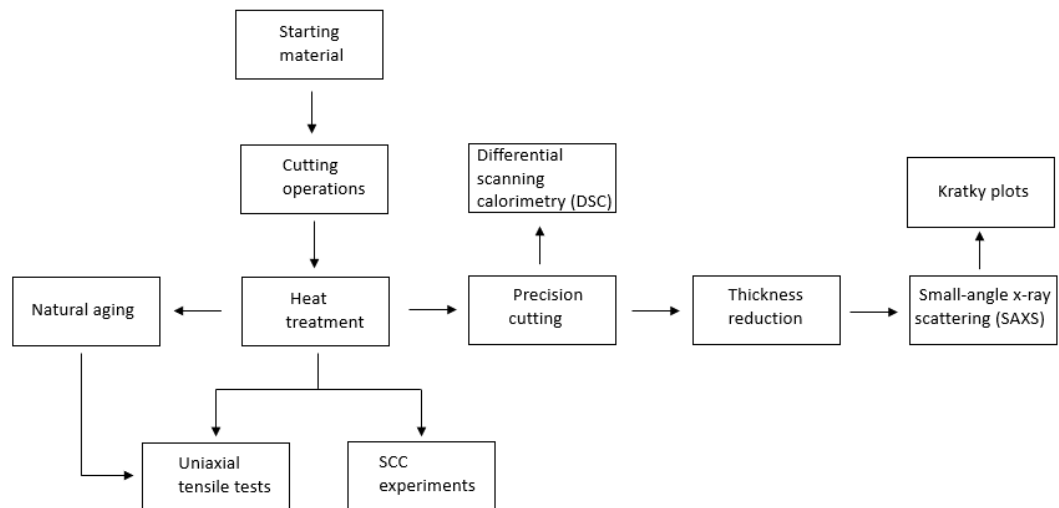


Figure 3.9: Experimental flow diagram of the experiments linked to the study of microstructure and property evolution during the retrogression and reaging double aging steps.

F tempered AA7075 sheets were cut into samples fit for tensile testing and SCC experiments. In addition, coupons of 10 mm x 10 mm x 1.5 mm dimensions were made for DSC and the SAXS experiments. Subsequently, all the specimens were processed with the heat treatment.

The heat treatment consisted of a solution heat treatment at 470 °C for 1 hour, followed by water quenching and a variable aging strategy where each sample was subjected to the sequence of RRDA steps and interrupted at a selected step. For example, Step4 samples were heat treated with the sequence of Step1, Step2, Step3 and Step4 (Fig.3.10).

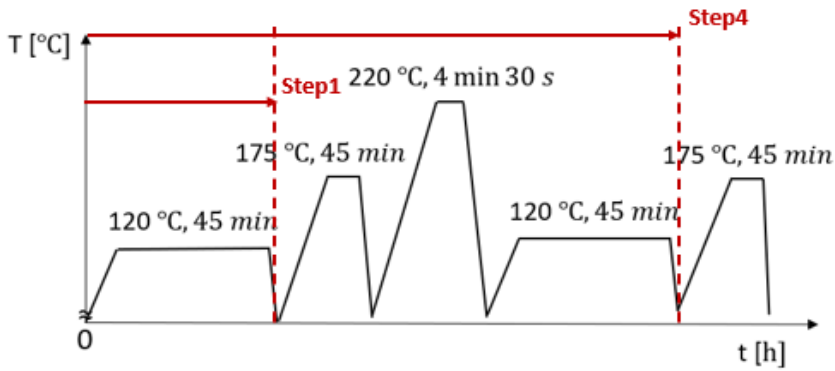


Figure 3.10: Example of the sequence of the retrogression and reaging double aging steps carried out for Step1 and Step4 samples.

Samples for each RRDA step were made: a group of these was tensile tested directly after heat treatment, while a second group was tensile tested after storage at room temperature for 3 months. A set of samples for each RRDA step was also intended for SCC experiments. The first group of the heat treated coupons was thinned to a final thickness of 80 μm and used for the SAXS experiments. However, the last group of coupons was instead subjected to a stage of precision cutting to obtain specimens of 3 mm x 3 mm x 1 mm dimensions. These samples were used for DSC.

3.3.6: The RRDA properties compared to industrially relevant tempers

Figure 3.11 displays the experimental flow diagram for the set of experiments aimed at comparing the microstructure and properties of the RRDA strategy with industrially relevant tempers for 7000 aluminium alloys.

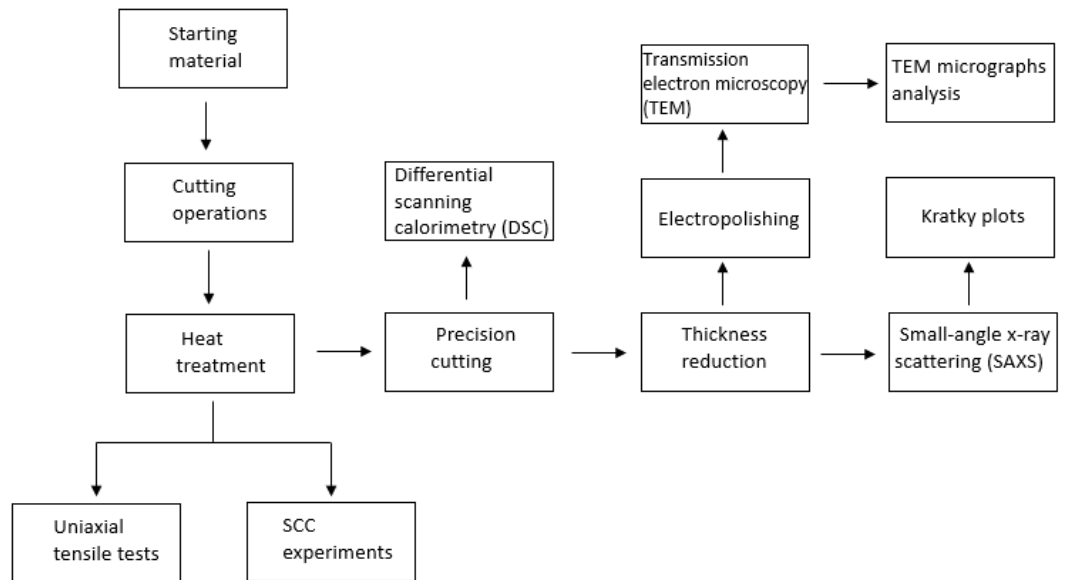


Figure 3.11: Experimental flow diagram for the set of experiments related to the comparison of the retrogression and reaging double aging characteristics with those of other industrially relevant tempers.

The starting material was cut into samples with the specified dimensions for tensile tests and SCC experiments. Coupons of dimensions 10 mm x 10 mm x 1.5 mm were also made for DSC, the SAXS experiments and TEM.

Aging strategy	Time-temperature profile
T6	120 °C, 24 h
T73	(120 °C, 24 h)+(160 °C, 30 h)
FA	Typical two-step aging strategy [13,15]
RRDA	(120 °C, 45 min)+(175 °C, 45 min)+ (220 °C, 4.5 min)+(120 °C, 45 min)+ (120 °C, 45 min)

Table 3.3: Summary of the aging schedules used in the current set of heat treatments.

The heat treatment process involved subjecting the material to a solution heat treatment of 470 °C for 1 hour, followed by water quenching and a variable aging schedule. The different aging schedules used are summarised in Table 3.3.

The RRDA microstructure and properties were compared with those of T6 and T73 tempered samples as they are widely used in the literature as representative of peak aged and overage samples, respectively. In addition, two-step aged samples (fast aging strategy) are included in the comparison as their microstructure and properties are typical of double aging strategies and preaging/paint-baking strategies [131].

After undergoing heat treatment, a batch of specimens was tested for tensile strength. Additionally, another set of samples was allocated for SCC experiments. A portion of the heat-treated coupons were thinned down to a final thickness of 80 µm, and this group was used for the SAXS experiments. Samples with reduced thickness were also subjected first to electropolishing and then to TEM analysis. Meanwhile, the last batch of coupons underwent a stage of precise cutting, resulting in specimens with dimensions of 3 mm x 3 mm x 1 mm. These samples were used for DSC.

3.3.7: The link of anodic polarisation parameters with SCC susceptibility and the OM observation of the corroded surfaces

Anodic polarisations of heat treated samples were analysed and compared with the SCC experiment results. For this scope, the starting material was cut into 30 mm x 30 mm x 1.5 mm specimens and subsequently heat treated. All samples were solution heat treated for 1 hour at 470 °C.

To explore how the cooling rate affects the anodic polarisation curves, a first group of samples was water quenched and then fast aged, while a second group was die-cooled (average cooling rate 30.7 °C/s) and fast aged.

To explore the effect of the aging step, a third group of samples was water quenched and aged to the T6 temper (120 °C for 24 hours), while a fourth group was identically water quenched and the T73 temper (120 °C for 24 hours followed by 160 °C for 30 hours) was imparted.

Due to the complementary nature of this set of experiments and the time constraints of the project, the investigation was limited to just these metallurgical conditions.

The heat treated samples were ground and polished to reach a 1 µm surface finishing and finally subjected to the electrochemical tests. A complete description of the anodic polarisation experiments is provided in Section 3.4.17.

After the anodic polarisation experiments, the samples were washed in ethanol; the corroded surface characteristics were then observed via OM.

3.4: Experimental techniques and experimental procedures

3.4.1: Cutting operations and precision cutting

The cutting operations were performed by the University of Manchester mechanical workshop. The F temper coupons used for most of the experimental work were produced from the original AA7075 A4 sheets through metal cutting guillotine. Samples intended for uniaxial tensile tests, SCC experiments and dilatometry heating require a more complex geometry than that of the coupons. In this case, electrical discharge machining (EDM) was used in the mechanical workshop to achieve the required geometrical specifications.

Precision cutting was used to make specimens suitable for DSC, the SAXS experiments and TEM. Precision cutting was carried out manually with the use of Struers Accutom-50.

3.4.2: Heat treatments

Heat treatments are the subject of study in this work and the core steps of each set of experiments.

Besides the thermal operations carried out via dilatometry resistance heating (Section 3.4.3), the totality of heat treatments was performed with circulating air furnaces (Carbolite furnace type 3216). In circulating air furnaces, samples are heated up through air convection via being preheated with a resistive heating element.

When working with metallic sheets, temperature measurements during heat treatment are greatly simplified as temperature uniformity in the material can be assumed. This simplification is used due to the reduced thickness of the samples (1.5 mm) and the high thermal conductivity of the aluminium alloy.

For this study, the record of the relevant time-temperature profiles was completed with Lascar temperature data logger type k thermocouples. This equipment was coupled with a dedicated software used to store the data in digital form.

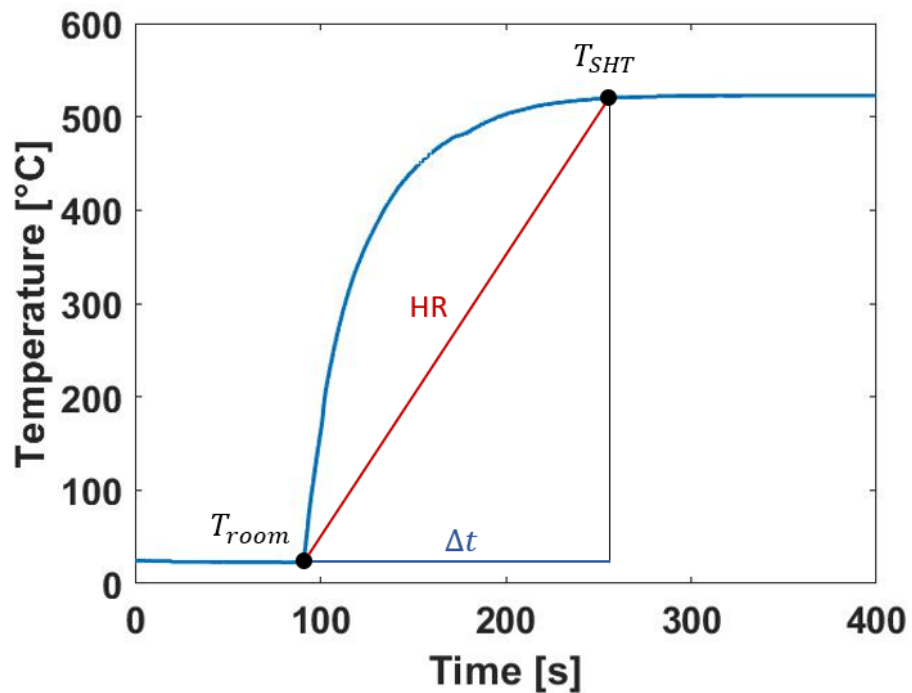


Figure 3.12: Recorded time-temperature profile showing the heating phase during solution heat treatment with Carbolite furnaces type 3216. A schematic representation of the average heating rate calculation is also displayed.

The probe is connected to the alloy through a small hole (1 mm diameter) practiced on the RDxST planes of the tested samples.

The time-temperature profile of samples heated to solution heat treatment temperature with Carbolite furnaces type 3216 is shown in Fig.3.12. The average heating rate (HR) was calculated by dividing the temperature difference between solution heat treatment temperature (T_{SHT}) and room temperature (T_{room}) by the duration of the heating phase (Δt). For all the operations involving Carbolite furnaces type 3216, regardless the final temperature reached during the heat treatment, the calculated average heating rate was 2.5 °C/s.

The water quenching from the solution heat treatment was carried out by transferring the hot samples from the furnace to a water bucket, with particular attention paid to performing this step as rapidly as possible to avoid unexpected quench-induced precipitation. In addition, the volume of water used during the cooling procedure was large to the extent that water temperature variations after the cooling step are negligible. As the commonly reported cooling rate imparted by water quenching was at least one order of magnitude higher than the critical cooling rate for AA7075 [31], the evaluation of this parameter in the case of water cooling was not attempted.

Die-cooling was carried out with the use of two iron plates with the dimensions of 30 cm x 30 cm x 3 cm. Hot samples from the solution heat treatment were rapidly transferred and held between the cast two iron plates.

The holding pressure of the two dies on the transferred specimen arose from the weight of the upper plate. Using 7.8 g/cm³ for iron density, the calculated holding pressure was roughly 0.03 MPa.

The relevant average cooling rates (CR) calculated in this work were defined as the temperature difference between solution heat treatment temperature (T_{SHT}) and 50 °C divided by the time span to reach 50 °C from T_{SHT} during the cooling

phase (Fig.3.13). The average cooling rate of the die-cooling operation was roughly 30 °C/s.

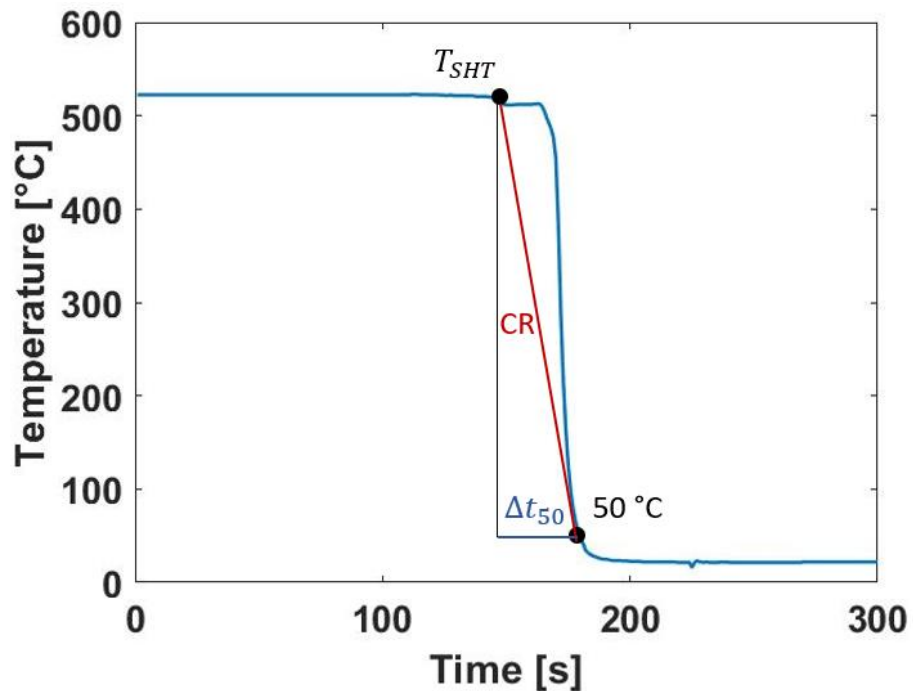


Figure 3.13: Time-temperature profile recorded during die-cooling from the solution heat treatment temperature. A schematic representation of the cooling rate calculation is also presented.

For 7000 aluminium alloys, cooling rates are usually reported by calculating their average value in the temperature range sensitive to quench-induced precipitation [31]. Therefore, to allow the comparison of the results of this work with other related studies in the literature, the average cooling rates between 450 °C and 250 °C were also calculated. For example, the average cooling rate in the 450 °C–250 °C temperature range linked to die-cooling was approximately 270 °C/s.

After the cooling step, all samples were stored in the freezer at -20 °C to avoid the onset of natural aging. Aging schedules were carried out in Carbolite furnaces type 3216, and the heating phase of each of these thermal steps was characterised by a heating rate of 2.5 °C/s. The cooling phase for each aging step was then carried out with water quenching, and for those aging schedules that consist of a sequence of multiple thermal steps, freezer storage (-20 °C) was used when steps were not carried out consecutively.

3.4.3: Dilatometry heat treatments

In this study, dilatometry heating was used to finely control the solution heat treatment parameters when studying the effect of the heating rate. The dilatometer used was the TA instruments DIL 805 A/D/T, which can impart precisely controlled heating rates during testing through induction heating.

For the heating rate experiments, the heating phase was realised via a linear increase of temperature with the holding time due to being the easiest option to implement.

The cooling step after the solution heat treatment was realised via nitrogen forced convection, and the average cooling rate imparted was 106.5 °C/s.

Because the critical cooling rate for AA7075 was estimated at around 100 °C/s [31], the quench-induced precipitation is supposedly negligible during this operation.

Samples intended for dilatometry heating require a specific geometry, which is displayed in Fig.3.14.

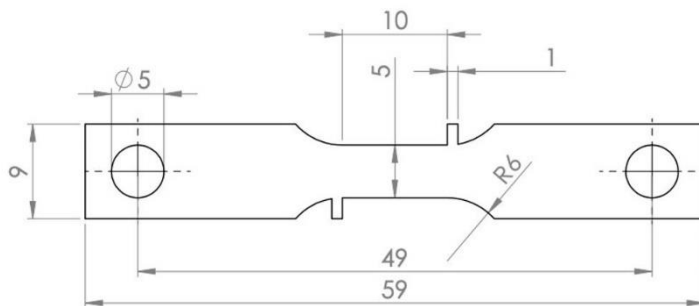


Figure 3.14: Samples' geometry used for dilatometry heating.

Because the portion of the sample connected to the cables had the most accurate temperature control, only this portion of the material was used for microstructural and property characterisation.

3.4.4: Surface preparation and thickness reduction

To perform Vickers hardness measurements, OM, and SEM on samples, preliminary surface preparation steps are required. These steps aim to bring the surface roughness of the treated sample to a standard level, which might vary depending on the technique for which the samples are intended. Consequently, the number and type of steps for the surface preparation sequence might vary as well.

Before starting the surface preparation procedure, samples assigned to OM or Vickers hardness measurements were mounted in epoxy resin. Grinding and polishing steps were performed with Tegrapol-31. The sequence of grinding steps included 320, 600, 800, 1200, and 4000 grit numbers. Once treated with the 4000-grit grinding step, samples underwent polishing steps. The first polishing step used a polishing cloth embedded with a 3 μm abrasive diamond oil-based solution, while the second step used a 1 μm abrasive diamond oil-based solution. After the second step, the sample had a 1 μm surface finishing. Finally, the last polishing step was carried out with 0.3 μm –0.05 μm oxide polishing suspension (OPS). Samples that underwent the complete surface preparation sequence achieved a 0.3 μm –0.05 μm surface finishing. Between each of the polishing steps, the samples were rinsed and dried in ethanol.

Samples assigned to TEM or SAXS experiments needed to reach a final thickness of 80 μm . In this case, the 600-grit step was used to grind the sample from the initial thickness of 1.5 mm to the final 80 μm thickness. This dimension was monitored with a manual calliper to ensure the correct final width.

3.4.5: Vickers hardness measurements

In this work, Instron micro-hardness indenter was used to practice indents of 1 kgf for 10 seconds. For each metallurgical condition tested, 10 Vickers hardness measurements were taken; the average value of these measurements and 2 standard deviations were then reported.

The selection of the specific surface of the alloy to be indented is a fundamental choice for the consistency of the measurements. As the production of the alloy sheets involves stages of hot and cold rolling (Section 2.1), the grain size of the workpieces varied along the thickness of the material (RDxST plane). Specifically, the average grain size was smaller for those portions of the material closer to the rollers, and the grain size was larger in the core of the sheet (Fig.3.15).

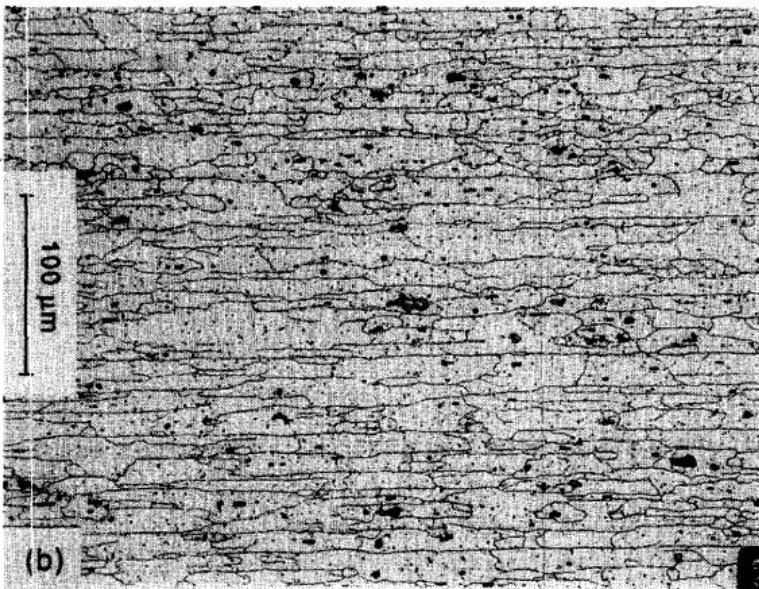


Figure 3.15: Typical grain structure of AA7075 sheets (RDxST) plane [61].

For this reason, if Vickers hardness measurements are carried out onto the RDxLT plane, special care must be applied. In fact, for each sample, the duration of the previous grinding process can influence which grain size is encountered on the tested surface; the thickness of the sheet decreases with a prolonged grinding step. To avoid this complexity, all samples in this work were indented on the RDxST plane in the portion of the material characterised by a smaller average grain size.

3.4.6: Differential scanning calorimetry

In this study, DSC was conducted using a TA Q1000 instrument. The samples were heated from room temperature to 400 °C at a linear heating rate of 20 °C/min. To prepare the samples for DSC, each alloy sample was sealed in an aluminium pan and lid (TA instruments) and weighed on a precision scale (Ohaus precision scale). The prepared samples were then loaded into the TA Q1000 instrument for testing. An empty pan-lid assembly served as the reference sample, while a pure aluminium sample (99.99 wt% by Thermo Fisher Scientific) was used as the background sample.

The heat flow data for each tested sample was then adjusted by subtracting the heat flow of the pure aluminium, thereby eliminating the background noise. In this work, precipitation reactions (exothermic) were characterised by a positive heat flux, while dissolution reactions (endothermic) were characterised by a negative heat flux (Fig.3.16).

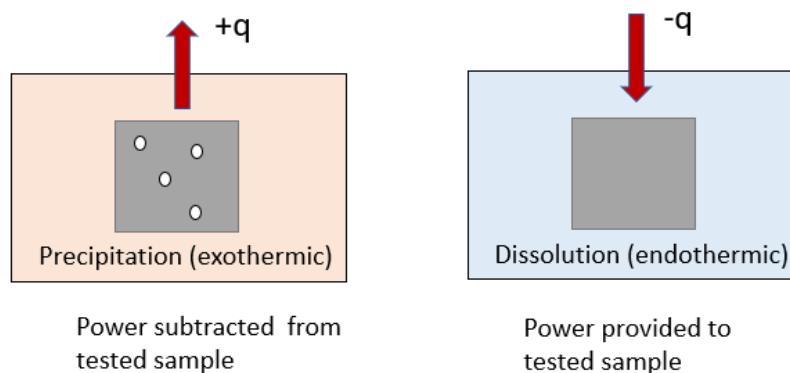


Figure 3.16: Schematic representation of the heat flux conventions selected for DSC.

As discrepancies still exist among researchers regarding the interpretation of DSC results for this class of alloys, this study builds upon the highly relevant work of Richard et al. [152], who linked DSC traces and precipitation features of AA7075 using hot-stage TEM.

3.4.7: Etching

In this work, etching was used to reveal GBs on the specimen surfaces, which are then observed via OM. Keller's reagent (95.0 %vol distilled water, 2.5 %vol nitric acid, 1.5 %vol hydrochloric acid and 1.0 %vol hydrofluoric acid) was used as the etching solution. Samples were immersed in Keller's reagent for 10 seconds and then rinsed in ethanol.

The selection of the optimal etching time is fundamental as reduced immersion durations would determine inadequate GB corrosion. Conversely, a prolonged immersion time would cause general pitting of the matrix, which could potentially cover the microstructural features of interest (Fig.3.17).

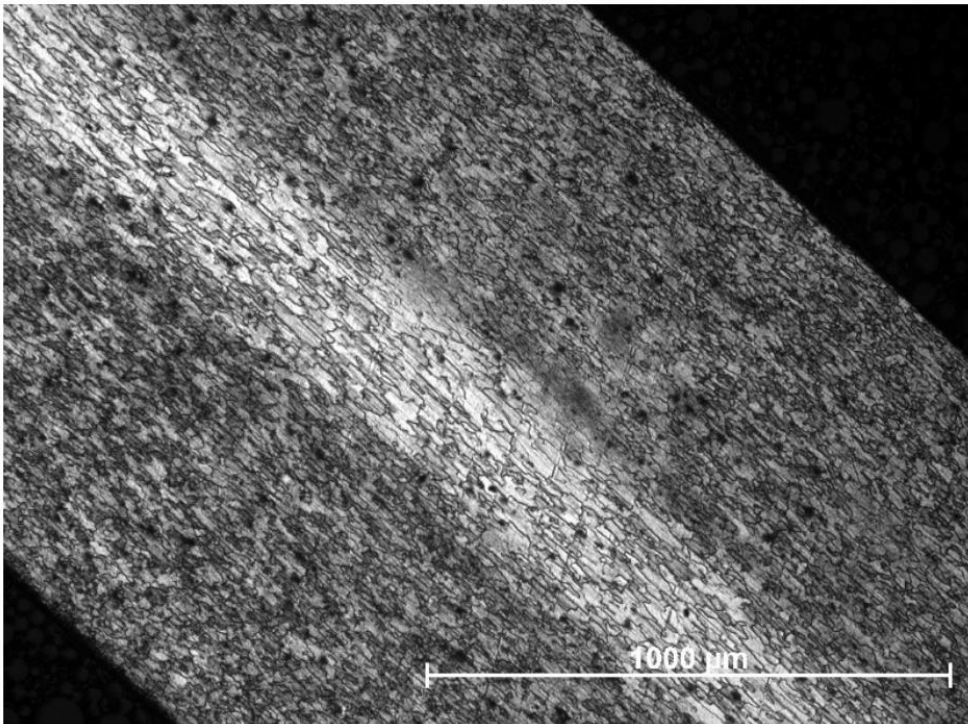


Figure 3.17: RDxST plane after prolonged etching process (optical microscopy micrograph). Interestingly, the rate of the corrosion process varies along the thickness of the sample due to the different average grain sizes. Pitting corrosion is visible on the surface portions close to the edges, but not in the core of the sheet.

3.4.8: Optical microscopy

OM micrographs have been acquired from etched samples as part of the average grain size evaluation procedure. The surface displayed in OM micrographs is the RDxLT: this choice facilitates the subsequent analysis via the mean linear intercept method. In fact, as the sectioned grains look equiaxed on this plane, only one characteristic dimension was needed to quantify the average grain size.

Because of the previously discussed variability of average grain size along the thickness of the sheet, the grinding process was applied to the RDxLT surface while assigning a constant duration (45 seconds) for each grinding step. This process ensures that the microstructure observed for each sample via OM is roughly located at the same sheet thickness. OM micrographs of corroded surfaces after anodic polarisation experiments were also obtained.

An Olympus light microscope in bright field mode was used to generate and collect the OM micrographs.

3.4.9: Mean linear intercept method

The distribution generated from the collected set of mean linear intercept lengths is assumed to be representative of the spatial grain size distribution. Notably, the variability of mean linear intercept lengths is also caused by a sectioning effect on the 3D set of grains.

In this work, 10 OM micrographs (RDxLT plane) were collected for each metallurgical condition, and 10 horizontal test lines were manually drawn for each micrograph, counting the intersections with GBs and calculating the mean linear intercept length (Fig.3.18). Consequently, 100 mean linear intercept lengths were obtained for each sample.

Particular attention was applied to ensure each grain was crossed by just one test line, which ensures statistical consistency. Finally, the distributions of the mean linear intercept lengths were characterised by their modes and standard deviations.

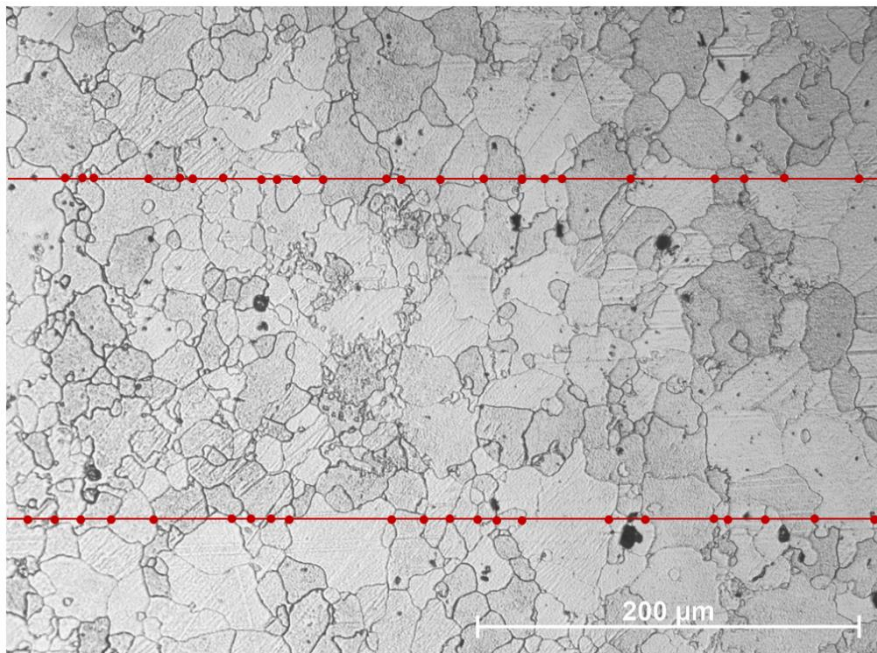


Figure 3.18: Test lines and counts of the grain boundary intersections for an etched AA7075 optical microscopy micrograph (RDxLT plane).

3.4.10: Scanning electron microscopy

In this work, Zeiss Ultra 55 was used to acquire SEM micrographs. This instrument uses a field electron gun as electron source, and the accelerating voltage was set at 5 kV. Secondary electrons are the signal used for the SEM micrographs; the working distance selected was 5.6 mm, and the selected spot size was 3.

To operate the SEM, the sample is first inserted in the microscope, and the vacuum levels in the column are restored. Once the appropriate accelerating voltage and the signal type of interest are selected, the image is first focused at low magnification, and the working distance is brought to the decided value.

When increasing the magnification, the focus and brightness/contrast must be tuned again. Because the levels of magnification of the SEM images obtained in this work were modest, astigmatism correction was not needed. Finally, the SEM images obtained were saved digitally.

3.4.11: Small-angle x-ray scattering

SAXS is an experimental technique used to characterise the structure of materials in the nanometric and micrometric range. In the literature, SAXS has been successfully used to study matrix precipitate features of 7000 aluminium alloys. The experiment consists of targeting the sample under study with x-rays and then measuring the characteristics of the deflected beam (Fig.3.19).

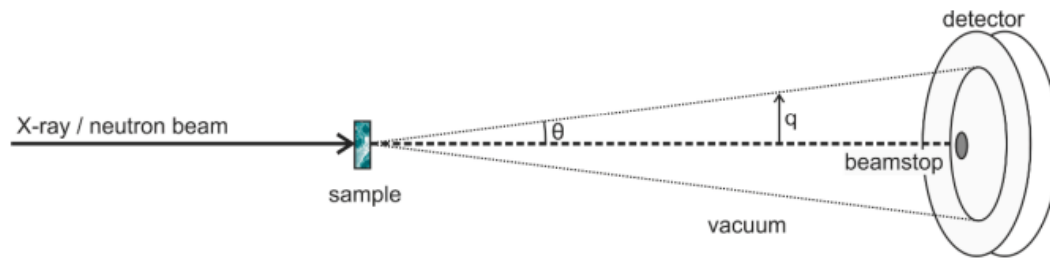


Figure 3.19: Schematic working principle of small-angle x-ray scattering experiments [153].

The elastic scattering of the x-ray photons with the material electrons is a function of the distribution of electron densities in the sample. Each microstructural feature in the alloy produces a characteristic deflected intensity of the beam and a scattering angle, which are collected by a dedicated detector and recorded.

The SAXS experimental output is a set of scattered intensities collected as a function of the scattering vector q . The module of the scattering vector q is defined as it follows:

$$|q| = \left| \frac{4\pi \sin \theta}{\lambda} \right|$$

The module of q is directly proportional to the scattering angle θ .

The length scale of the microstructural features investigated is associated with specific ranges of q : the smaller the microstructural structure scattered, the greater the q value. This principle is a direct consequence of Bragg's law and explains why the detection of the scattered intensity is confined to small angles (0.1° – 5.0°). In this range of scattering angles, the information of the matrix microstructural features relevant for 7000 aluminium alloys is contained.

The findings obtained through SAXS require careful consideration as the data analysis process is quite challenging and relies on several simplified assumptions. While a thorough explanation of how the output of a SAXS experiment relates to the properties of precipitates is outside the scope of this study, understanding that, under simplified assumptions, the scattered intensity can be correlated with a parameter known as the radius of gyration (R_g) is crucial. This parameter serves as an effective way to measure the average size of matrix precipitates in the aluminium alloy. The radius of gyration R_g is defined as follows:

$$R_g = \left[\frac{1}{V\rho} \int r^2 dV \right]^{1/2}$$

Is the radius that the hypothetical sphere of the same material as the scattered object should have if its electron distribution would be all concentrated in the centre and this point would give the same scattering effect of the real object.

To establish a connection between the experimentally obtained scattered intensity and R_g , two assumptions are made. The first assumption is that the system is dilute, meaning that the interaction effect of multiple precipitates on the signal is neglected, and each precipitate is considered an isolated entity. The second assumption is that the population of precipitates consists of identical precipitates with fixed dimensions. This study assumes that the spherical precipitates in the matrix follow a log-normal distribution.

The second assumption is bold as the matrix precipitates in the aluminium system exhibit a high degree of polydispersity and vary in shape. Nevertheless, according to the Guinier law under these assumptions, the scattered intensity can be correlated with the gyration radius using the following equation:

$$I = I_0 \cdot e^{-\frac{q^2 R_g^2}{3}}$$

Deschamps et al. [154] observed that the valid q range for these assumptions is unclear when dealing with a polydisperse distribution of nanometric precipitates. As a result, this study introduces an additional assumption—that the q range employed in the analysis is consistent with the underlying approximation. In this study, the q range investigated falls between $0.02 \text{ }^\circ\text{A}^{-1}$ and $0.64 \text{ }^\circ\text{A}^{-1}$.

In the scientific literature, the gyration radius is often determined using Kratky plots, which involve plotting Iq^2 as a function of q . These plots exhibit a maximum, and the corresponding q_{max} value can be used to determine the gyration radius using the following equation:

$$R_g = \frac{q_{max}}{\sqrt{3}}$$

Beginning with Guiner's law is a straightforward way to demonstrate the relationship. By multiplying both sides by q^2 and differentiating with respect to q , the relationship can be easily derived via the equation below:

$$Iq^2 = I_0q^2 \cdot e^{-\frac{q^2R_g^2}{3}}$$

$$\frac{dIq^2}{dq} = -2I_0q\left(\frac{R_g^2q^2}{3} - 1\right) \cdot e^{-\frac{q^2R_g^2}{3}}$$

The maximum of the Iq^2 function can be determined by solving the equation

$\frac{dIq^2}{dq} = 0$, which corresponds to the following equation:

$$R_g = \frac{q_{max}}{\sqrt{3}}$$

After obtaining a Kratky plot, finding the maximum allows for the determination of the gyration radius, which is commonly referred to as the pseudo-Guinier radius [154]. However, the Kratky plot can provide additional information beyond just the gyration radius. Within the range of q investigated, the scattered intensity reflects interactions with precipitates in the nanometre scale. Thus, integrating Iq^2 over the q range is proportional to the volume fraction of the precipitates. While an absolute volume fraction measurement would require a calibration process not attempted in this work, a relative measure of the volume fraction is possible when using a reference volume fraction, as shown in the below equation:

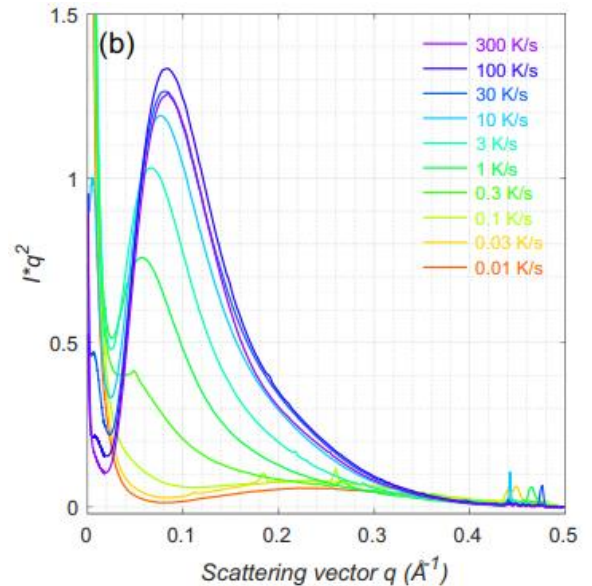


Figure 3.20: Example of Kratky plots calculated in the work of Zhang et al. [123].

$$Vf_{relative} = \frac{\int Iq^2 dq}{(\int Iq^2 dq)_{reference}}$$

In this work, the reference precipitate volume fraction used is the one calculated for samples solution heat treated for 1 hour at 470 °C, water quenched and then aged 24 hours at 120 °C (T6 temper). The instrument used was Hecus S3-Micro, and the x-ray source was Cu K α .

The experiment began by creating a vacuum environment in the equipment. Then, the q vector was calibrated using x-rays and a standard silver behenate sample. After calibration, the aluminium alloy samples were processed. A fixed exposure time of 1000 seconds was used for all experiments to collect sufficient signal while minimising any heating effects on the samples. The experiment yielded a 2D scattering pattern of intensities (in arbitrary units) as a function of the q vector, which was manipulated using specialised software to obtain the intensity values as a function of q. Pure aluminium was also tested, and its intensity pattern was automatically subtracted to remove its contribution from the result. Additionally, contributions from the stage and air were automatically removed as part of the background noise. For each metallurgical condition studied, the repeatability of the I vs q plots was verified, and then the Kratky plots were generated to derive the pseudo Guinier radii. Finally, the volume fractions relative to the T6 temper were calculated.

3.4.12: Electropolishing

Electropolishing is a widely used step to prepare samples suitable for TEM analysis. In this study, the chosen technique was twinjet electropolishing, using Struers Tenupol-5 for this purpose. The initial material for this procedure was 80 μm thin specimen foils.

For the experiment, an electrolyte solution composed of 25% vol of nitric acid and 75% vol of methanol was used. The first step of the procedure involved punching the aluminium alloy foils using a Gatan disk puncher to create 3 mm disks.

To prepare the electrolyte solution, the cooling unit was set to -40°C and used to mix methanol and nitric acid in the system. During twinjet electropolishing, a voltage of 11 V–13 V was applied, and the flow rate of the electrolyte jet was carefully controlled. The jet had to be stable on both sides to ensure electrical connection, but not too powerful to deform the foil.

Once the parameters were set, it took roughly 3 minutes of twinjet operation to create holes in each aluminium foil. The extracted samples were then rinsed in pure methanol and dried before being stored

3.4.13: Transmission electron microscopy

To conduct the imaging in this study, the FEI Tecnai T20 (FEG) was used in bright field imaging mode, with an electron voltage of 200 kV and a spot size of 1.

To use the equipment, the first step involved filling the dedicated compartment with liquid nitrogen, followed by inserting the sample (single tilt holder) into the column and achieving vacuum conditions. After turning on the beam and selecting the appropriate accelerating voltage and spot size, the desired area of the sample was chosen, and the beam's intensity was adjusted.

Once the alignment procedures were completed, the CCD camera was inserted, and the image acquisition process started. The sample was magnified to the desired level, and the focus was tuned by adjusting the specimen height. Finally, the micrographs were obtained and saved digitally.

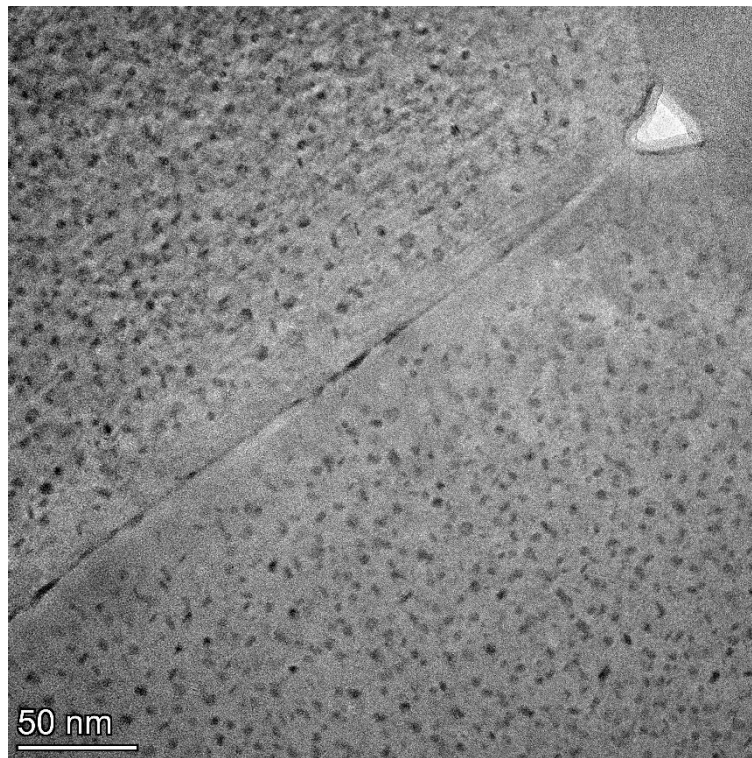


Figure 3.21: Example of a bright field image of AA7075-T6. Due to the high magnification of transmission electron microscope micrographs, identifying grain boundaries can be a challenging task. In the top-right corner, a triple junction is clearly visible, which is even rarer

3.4.14: Distribution of grain boundary precipitate lengths and average precipitate-free zone width

Distributions of GB lengths and average precipitate-free zone (PFZ) width were obtained from the TEM micrographs and used to quantify the GB microstructure for the metallurgical conditions of interest. Each GBP's size, defined as L , was determined as the maximum distance between the borders of the precipitate section (Fig.3.22).

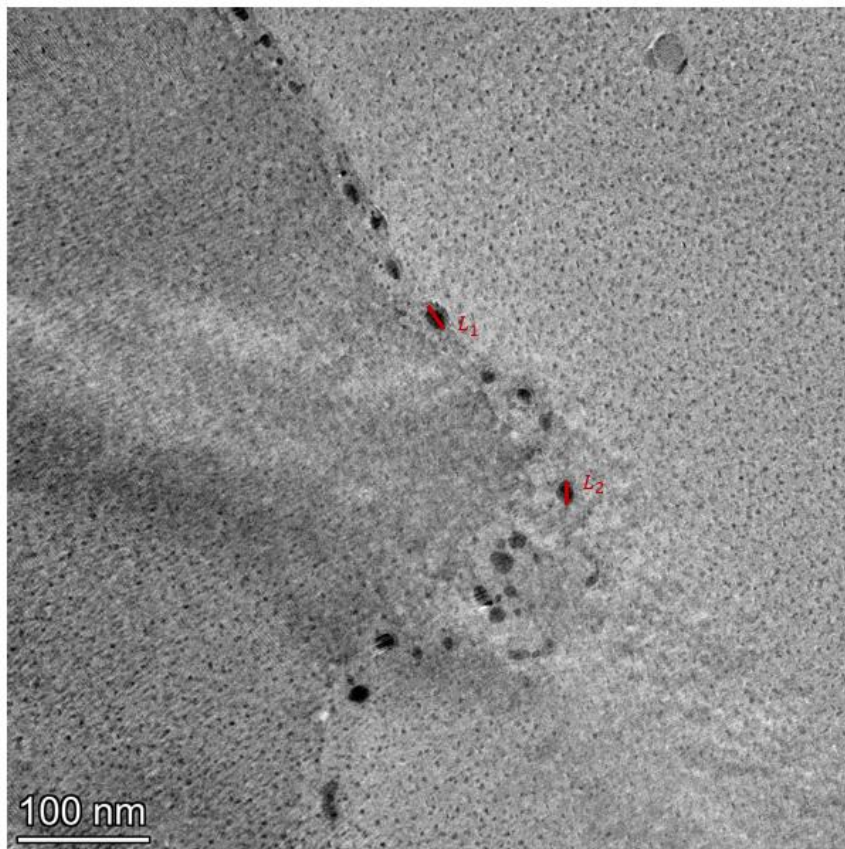


Figure 3.22: Example of grain boundary precipitate length evaluation for a transmission electron microscope micrograph of AA7075-T6.

For each metallurgical condition, 100 length measurements were manually extracted from the TEM images using ImageJ® software, and the resulting histograms provided an estimation of the distribution of GBP dimensions. For each metallurgical condition, the PFZ average width was also obtained. To determine the average size of PFZs, the width of such zones was measured in 20 different locations for each metallurgical condition, and the resulting values were averaged.

Notably, while the GBP sizes as calculated from 2D micrographs is correlated with the true GBP sizes, the two values are not identical. Additionally, the electropolishing process could chemically affect the GB microstructure, resulting in smaller GBPs compared to their original size. However, since the aim of the study is to compare the effects of different heat treatments and all samples were electropolished in the same manner, this potential alteration of size was not considered significant for the purpose of this study.

3.4.15: Uniaxial tensile tests and Kocks-Mecking plots

Following heat treatment, the specimens in this work underwent cutting to produce samples suitable for uniaxial tensile tests (Fig.3.23).

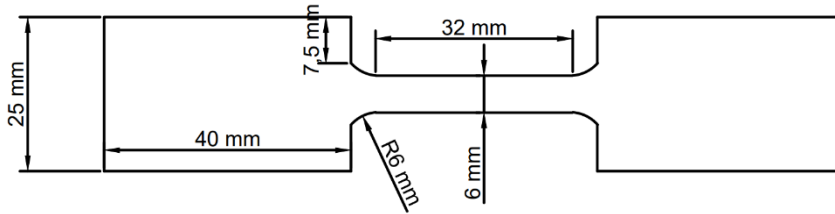


Figure 3.23: Geometry and dimensions of the tensile specimens used.

The tensile specimens were manufactured to ensure the material's rolling direction was perpendicular to the applied tensile load. The reasoning behind this design decision is covered in Section 3.4.16.

In this study, Instron 5967 and Instron 5569 were employed as the tensile tester, using a 50 kN load cell and an MTS 25 extensometer. The load was applied using a constant strain rate of 0.25 mm/min.

In this work, after ensuring the repeatability of the engineering stress-strain curves obtained for the samples of interest, the tensile curves were analysed to determine their yield strength (σ_y), ultimate tensile strength (UTS) and elongation to break. The yield strength was calculated as 0.2% proof stress.

The conversion of engineering stress (σ_{eng}) and strain (ε_{eng}) into true stress (σ_{true}) and true strain (ε_{true}) was carried out using the following equations:

$$\sigma_{true} = \sigma_{eng}(1 + \varepsilon_{eng})$$

$$\varepsilon_{true} = \ln(1 + \varepsilon_{eng})$$

Kocks-Mecking plots were then obtained plotting $\frac{d\sigma_{true}}{d\varepsilon_{true}}$ against $\sigma_{true} - \sigma_{y,true}$ for selected values of the stress-strain curves in the plastic range of each alloy.

3.4.16: Stress corrosion cracking experiments

Exposure of U-bends in the salt-spray environment was used as the SCC experiment in this work. Notably, the susceptibility ranking obtained from this test is highly correlated with those obtained from constant load tests performed in alternating immersion environments (ASTM G47-99), which is a widely recognised test in the aerospace industry [101]. In addition, the selection of U-bends for exposure to a corrosive environment is also based on the bending procedure being less complicated compared to 4-point bends. In fact, the stress distribution in U-bends is easier to replicate, making consistent and repeatable results more easily achievable.

According to ASTM G30-97, U-bend samples were machined as shown in Fig.3.24. The RDxLT surface under tensile stress during testing and the two RDxST surfaces were polished to a 1 μm finish. These steps were taken to minimise the impact of surface conditions on the SCC susceptibility.

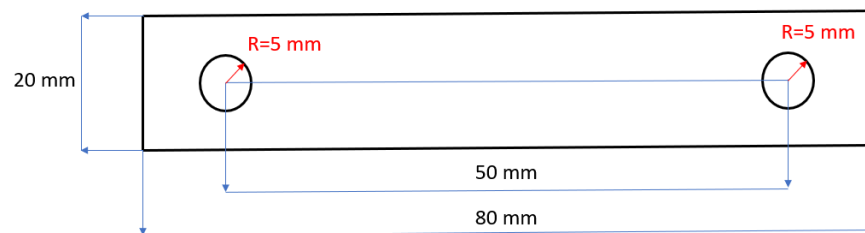


Figure 3.24: Geometry of the U-bend samples machined from AA7075-F sheets.

The U-bends were manufactured so that the material's rolling direction was perpendicular to the applied tensile load during the bending procedure. In fact, the RDxST plane exhibits a higher velocity of stress corrosion crack propagation compared to other planes. This higher velocity occurs because the grains' primary dimension aligns with the rolling direction, resulting in a less convoluted path for the crack to spread within the RDxST plane [97].

Due to the sheet's geometry, stressing the sheet to the most vulnerable plane mentioned is challenging. Therefore, SCC resistance must be tested allowing crack propagation on the RDxLT plane.

The RDxLT plane was subjected to tensile stress perpendicular to the rolling direction as this choice has been evaluated less often in the literature.

While 4-point bend tests were part of the original experimental plan for the overall SCC resistance evaluation, these experiments could not be carried out due to time constraints.

Therefore, the uniaxial tensile test also followed the same stressing convention abovementioned, as tensile properties are required to prepare 4-point bend tests.

The U-bends (Fig.3.25) were obtained using the experimental setup displayed in Fig.3.26 and followed the ASTM G30-97 standard during the bending operations.

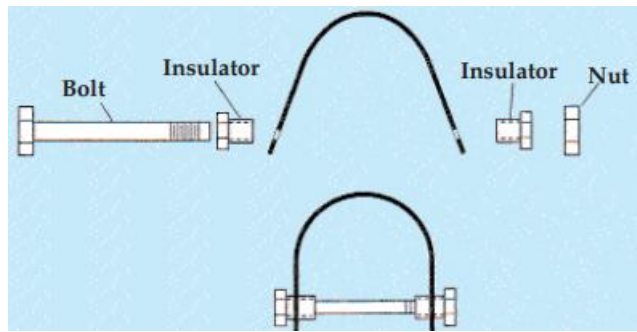


Figure 3.25: Procedure to make a U-bend starting from the partially curved samples, nut, bolt and insulators.

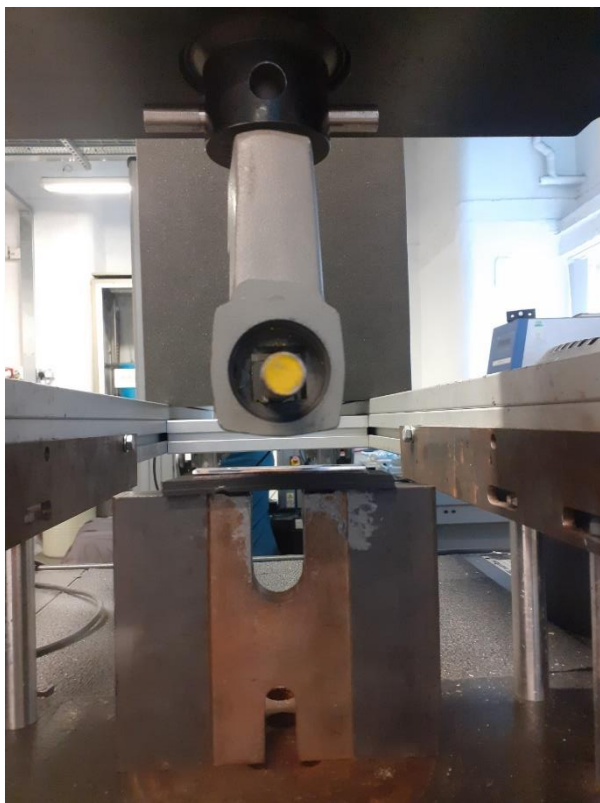


Figure 3.26: Experimental setup to impress the pre-shape to the specimens.

The bending process generally involves first creating a curved pre-shape in the sample, followed by using a bolt-nut system to bring the sample into its final U position. A metallic bar attached to a mechanical tester in compression mode is used to push the specimen into the shaping mould and impress the pre-shape.

The mechanical tester used for the pre-shape step in this work was Instron 5967, and a 13 mm

diameter carbon steel bar was used. The shaping mould had a 40

mm deep cavity before reaching the final curvature, with a curvature radius of 15 mm. During the operation, an EPDM rubber stage was employed to support the sample. The bolt and nuts used were zinc-plated steel M8 x 65 mm. To ensure a

consistent bending process, the bar was adjusted to travel 27 mm towards the cavity from the point of contact with the sample by using a velocity of 1 mm/min. To avoid galvanic corrosion, the contact points between the nut, bolt, sample and surrounding surfaces were coated with beeswax, thus eliminating the need for insulators.

The salt-spray chamber experiment was conducted in accordance with the B117-11 standard. For each metallurgical condition, 3 U-bends were prepared, but some of the samples could not be tested due to COVID-19 disruptions. Following the bending process, the specimens were placed in a salt-spray chamber (Liebisch Constamaticwin SK 400 M-TR) and subjected to the

corrosive environment for 60 days. The samples inside the chamber were positioned in a way that the fog flow was aligned parallel to the RDxLT surface experiencing tensile stress. The cracking and release of tensile stress from the RDxLT surface was considered sample failure, and the time until failure (in days) was recorded.

Salt-spray chambers are devices that deliver a controlled supply of corrosive mist, which is pumped as liquid solution from an external reservoir. The temperature inside the chamber can be regulated to achieve the desired testing conditions. By accelerating all types of corrosion phenomena, salt-spray chambers are frequently employed by researchers to investigate different forms of metal corrosion. This study employed a testing solution consisting of 5 %wt sodium chloride in deionised water, and the spraying mode was set to continuous. Prior to testing, the salt-spray chamber was calibrated to dispense 2.5 mL of mist per 80 mm² of internal chamber surface area. The testing temperature was maintained at 35 °C.



Figure 3.27: Liebisch Constamaticwin SK 400 M-TR salt-spray chamber.

3.4.17: Anodic polarisations

Anodic polarisation plots were used as a preliminary experiment to establish a correlation between the derived electrochemical parameters and the SCC performance of the alloy. To prepare the samples for anodic polarisation, they were polished to a 1 μm surface finishing on the RDxLT surface. During anodic polarisation, only an area of approximately 1 cm^2 was exposed to the electrolyte, while the remaining surface was coated with beeswax to prevent electrochemical reaction.

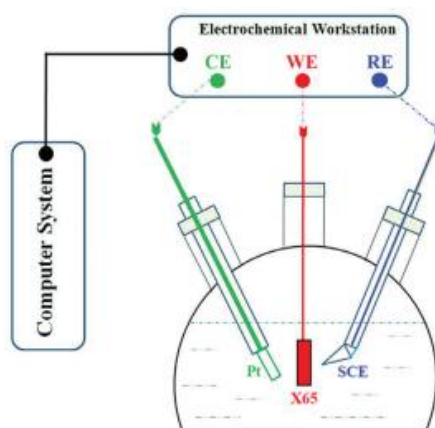


Figure 3.28: Schematic representation of the electrochemical cell used for polarisation experiments of aluminium alloys.

Fig.3.28 displays the electrochemical cell used to carry out anodic polarisations on aluminium alloys.

The electrochemical cell consists of several components, including the working electrode, reference electrode, counter electrode, electrolyte and control system. The control system used in this study was the potentiostat ACM GillAC, which was responsible for applying a positive potential between the aluminium sample (working electrode) and the reference electrode, as well as measuring the current flowing from the specimen to the reference electrode with varying potential and providing the data in digital form.

The aluminium alloy served as the anode in this system, while the reference electrode acted as the cathode, with a Sentek Ltd Ag/AgCl electrode serving as the reference electrode. As the potential variation was applied between the aluminium alloy and the Ag/AgCl electrode, the reference electrode cannot conduct the current without altering the electrode's potential. To allow the flow of electrical current, a third electrode, referred to as the counter electrode, is used. In this experiment, a Pt wire counter electrode (Sentek Ltd) was employed for that purpose.

The electrolyte completed the electrical circuit created by the potentiostat and served as a medium for the ions that conduct the electrical current, with a 5 wt% NaCl solution in deionised water serving as the electrolyte in this experiment. After evaluating the open-circuit potential (OCP), the experiment applied an electrostatic potential ranging from 0 mV to 300 mV relative to the OCP, with a scan rate of 10 mV/min increasing towards higher potentials.

Anodic polarisations were carried out until reaching repeatability of the results, and the output data from the experiment was reported as the base-10 logarithm of the current density versus the range of electric potential. The polarisations were analysed and compared with the results of the SCC experiments. Further, the corroded surfaces after polarisation were examined with an Olympus optic microscope in bright field mode.

3.5: CIPHER simulations

In this study, the CALPHAD-informed phase-field model (CIPHER) developed by Liu et al. [111] was used to predict the atomic fraction and average size of the η phase at GBs while changing the heat treatment parameters.

The phase field of each elemental volume is characterised by its phase ϕ , elemental concentrations (C_{Al} , C_{Zn} , C_{Cu} and C_{Mg}), and temperature (T). The evolution of these variables is governed by thermodynamic and kinetic functions that consider the minimisation of the Gibbs free energy, the mobility of interfaces and the mobility of chemical elements. The accurate thermodynamic and kinetic parameters necessary for this operation are obtained from a CALPHAD database. Although this work provides only a brief description of the CIPHER model, readers are encouraged to refer to Liu et al.'s study [111] for a more detailed discussion of the model and its numerical implementation.

To limit the computational cost of the simulations, the phase field was constructed as a 512 nm x 512 nm square in the 2D space, including a GB where nucleation and growth of the η phase can occur. These specifications were included in the first input file.

The second input file contained all the necessary thermodynamic and kinetic parameters essential for the functioning of the CIPHER model. Although most of these variables have already been established as they apply to the entire 7000 family of aluminium alloys, additional data must be included for AA7075, specifically the equilibrium compositions and free Gibbs energy of the matrix and η phase within the temperature range under investigation. This data was obtained via JMatPro[®] software calculations by specifying the initial composition of AA7075 and the specific temperature range needed.

The final input file required was a discrete table of values representing the time-temperature profile for the chosen heat treatment. In the first set of simulations the time-temperature profiles used were ramps of decreasing temperature, from solution heat treatment temperature to room temperature, where the cooling rate varied between 15 °C/s and 110 °C/s. The selection of this cooling rate range

was based on maintaining numerical simulation stability and ensuring the cooling rates were relevant to the industrial practices.

The second series of experiments employed isothermal holdings within the temperature range of 120 °C to 220 °C, which is the relevant aging temperature range for 7000 aluminum alloys, with holding times ranging from 5 to 30 minutes. Notably, these time-temperature profiles differ from the thermal steps typically used in the aging processes. However, this range of parameters was the only feasible option to achieve results without compromising the stability of the numerical simulation.

After the input files were defined as described, they were executed through the CF3 computer cluster at the University of Manchester, which runs CIPHER and launched the simulation. With each thermal profile employed, the simulation generated the temporal development of the phase field and the associated elemental compositions of Zn, Mg, Cu and Al. Throughout the execution of the time-temperature profile, η phase typically nucleated and grew on multiple sites of the GB, altering its elemental composition and affecting the elemental content of the matrix (Fig.3.29).

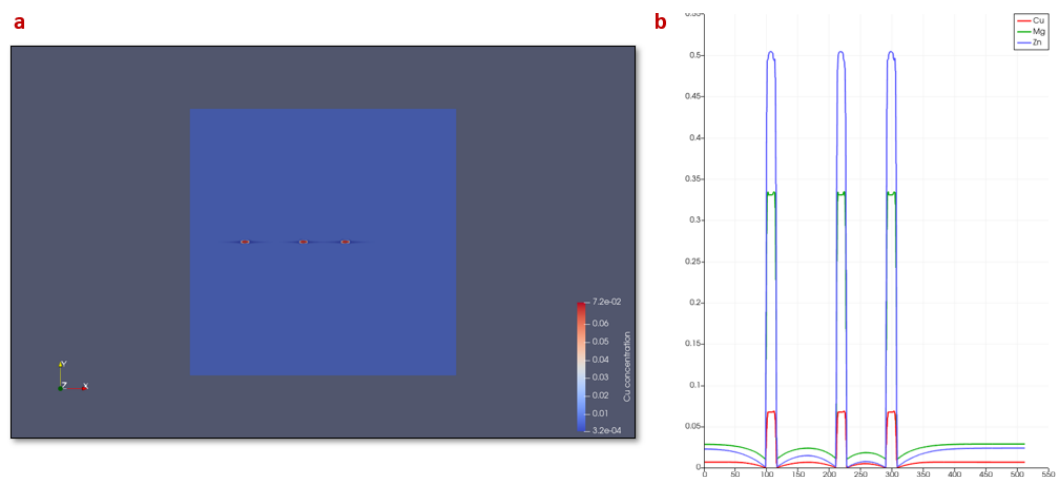


Figure 3.29: (a) The 2D simulation box that displays the growth of grain boundary precipitates during the CIPHER simulation, and (b) the elemental concentration profiles along the cutting line that coincides with the grain boundary.

The Paraview® software was used to analyse the obtained phase field and elemental composition evolution under different heat treatment parameters. The average composition, length, and area of the η phase were then evaluated.

Chapter 4:

Solution heat treatment step

This chapter introduces the research findings and discusses the optimization of the solution heat treatment step. The results are presented in two sections: first for low heating rates and then for high heating rates.

The discussion primarily examines the impact of reduced holding times and high temperatures on the process of precipitate dissolution and incipient melting, and how this applies to HFQ[®]. Additionally, the effect of heating rate on the dissolution process during solution heat treatment and on the grain structure is investigated.

4.1: Results

4.1.1: Experiments at low heating rate

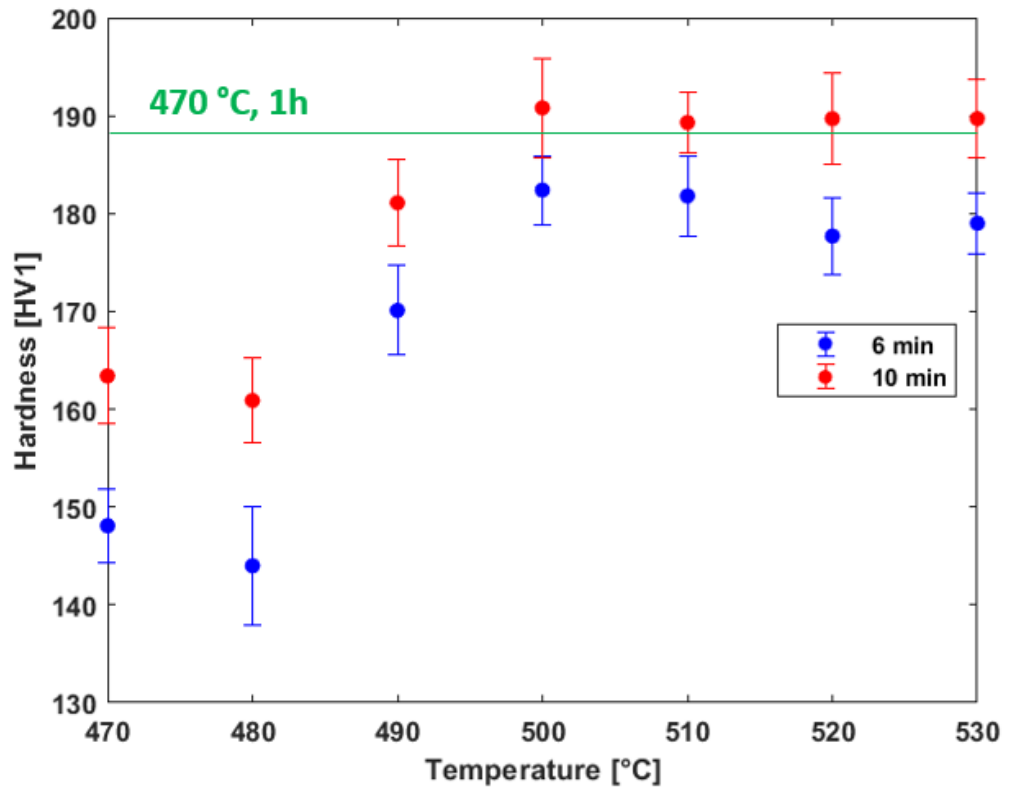


Figure 4.1: Vickers hardness of samples with different solution heat treatment temperatures and holding times.

Fig.4.1 shows the average Vickers hardness of samples solution heat treated with varying temperatures, which were then water quenched and fast-aged. The data was collected for two holding times: 6 minutes and 10 minutes. The green line specifies the Vickers hardness of a sample subjected to the standard solution heat treatment of 1 hour at 470 °C. All the samples experienced a low heating rate ramp (2.5 °C/s) to reach the solution heat treatment temperature.

Therefore, the total holding time always included 200 seconds (3.5 minutes) of heating time. The temperature range explored was 470 °C - 530 °C, and a data point was collected at each 10 °C temperature interval. The Vickers hardness of the samples increased when raising the temperature in the 470 °C - 500 °C range, while the hardness levels stayed constant in the 500 °C - 530 °C temperature range. In the 6-minute dataset, the hardness values rose from approximately 145 HV1 to approximately 180 HV1. In the 10-minute dataset, the hardness levels increased from approximately 165 HV1 to approximately 190 HV1. Consequently,

increasing the holding time from 6 to 10 minutes boosted the hardness values in the explored temperature range. The hardness levels of the reference solution heat treatment (green line) could only be reached by the 10-minute data set in the 500 °C - 530 °C interval.

Fig.4.2 represents the Vickers hardness of samples solution heat-treated at 500 °C, then water quenched and fast-aged. Holding times were every 1 minute from 1 - 10 minutes, and the low heating rate ramp heating time lasted 3.5 minutes.

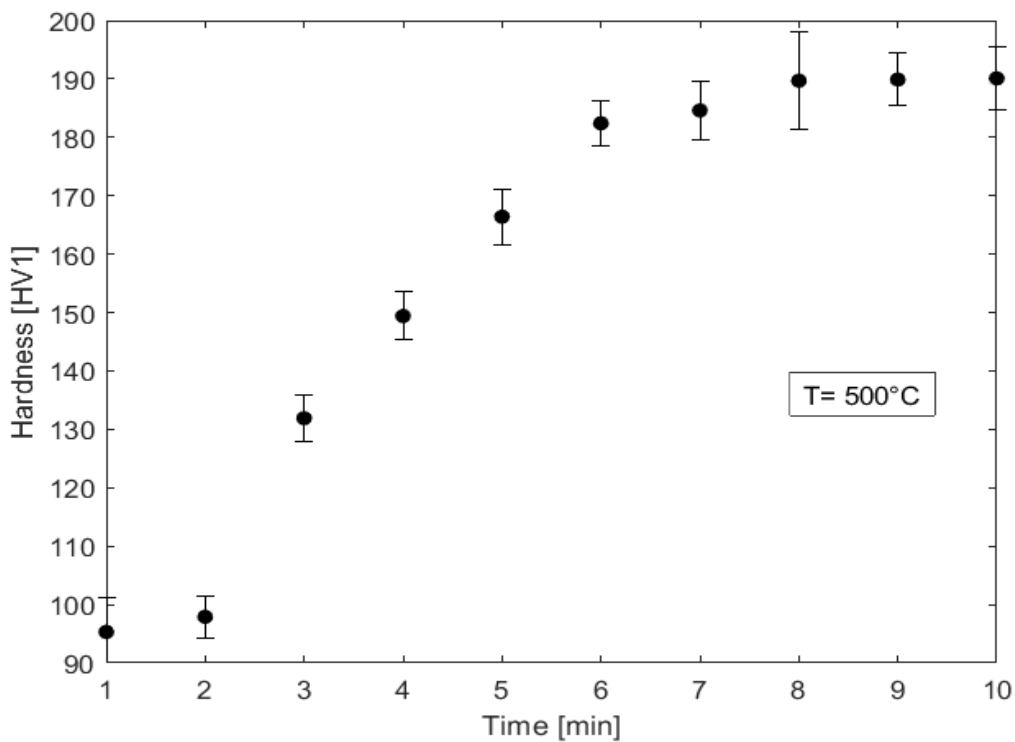


Figure 4.2: Vickers hardness of samples solution heat-treated at 500 °C for different holding times.

Consequently, samples held for less than 3.5 minutes were water quenched during the heating ramp. The two lowest holding times (1 and 2 minutes) shared a similar Vickers hardness, around 95 HV1. The holding time increments from 2 - 6 minutes improved the hardness values monotonically, reaching roughly 190 HV1 while increasing the holding time to 6 - 10 minutes did not improve the hardness level.

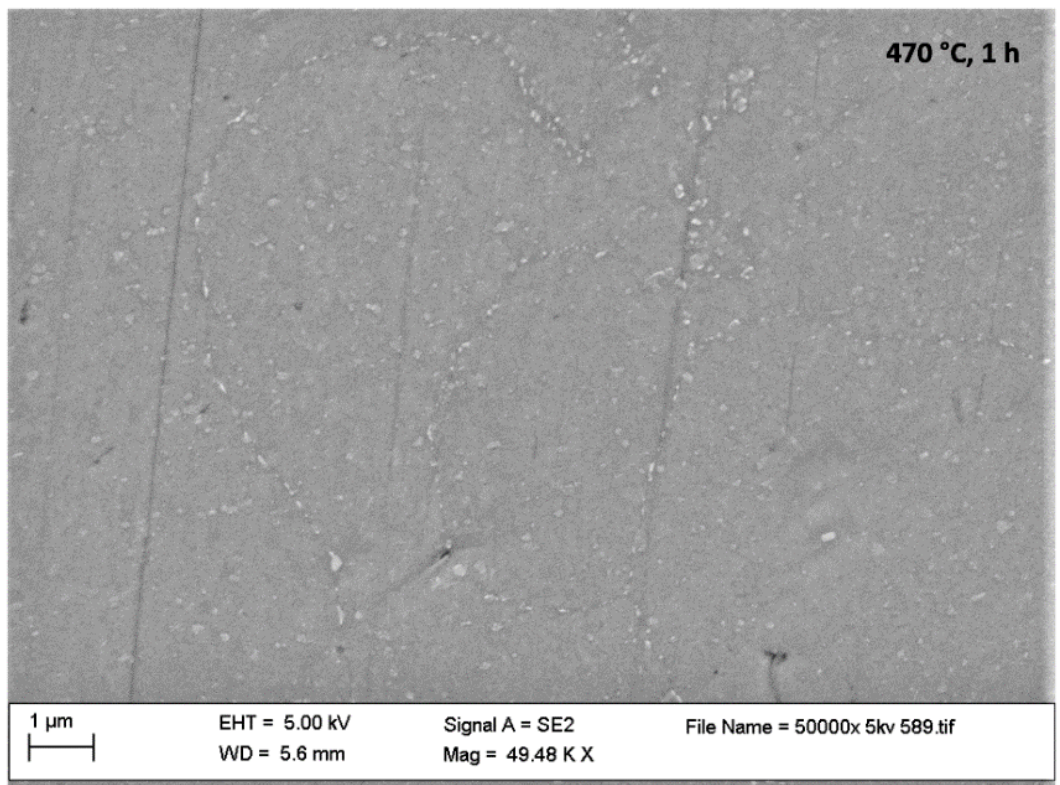


Figure 4.3: Scanning electron microscope micrograph of the sample solution heat-treated for 1 hour at 470 °C.

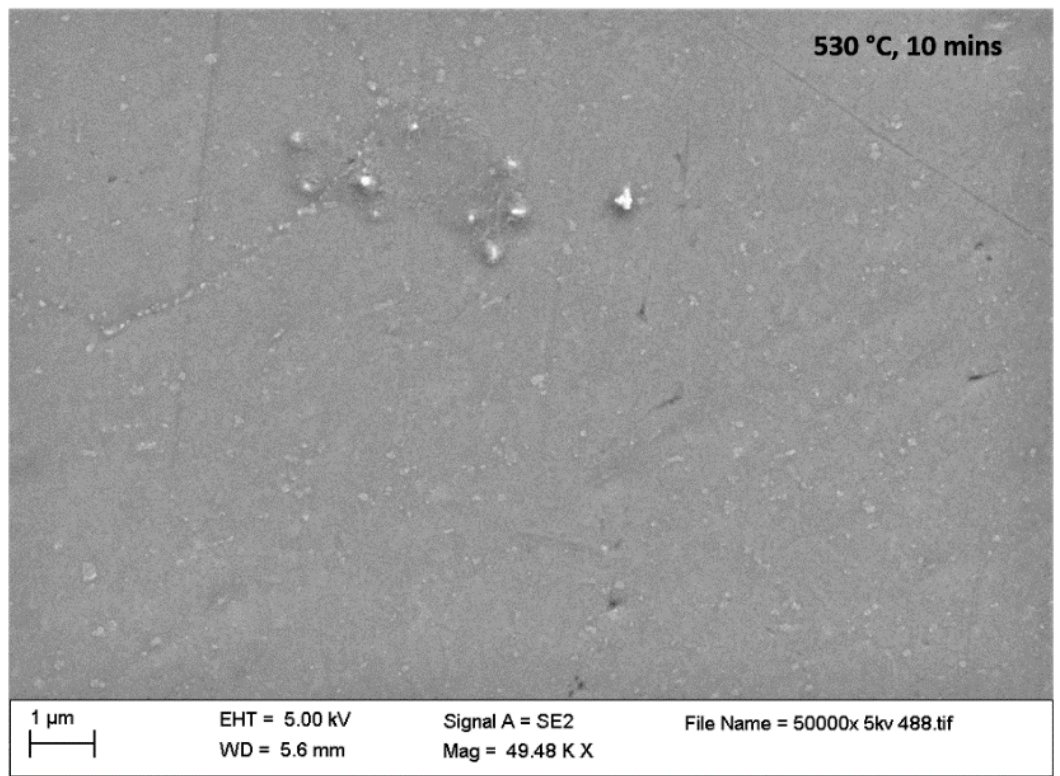


Figure 4.4: Scanning electron microscope micrograph of the sample solution heat-treated for 10 minutes at 530 °C.

Fig.4.3, Fig.4.4, and Fig.4.5 show scanning electron microscope (SEM) micrographs of samples solution heat-treated with a low heating rate ramp for 1

hour at 470 °C, 10 minutes at 530 °C, and 10 minutes at 500 °C, respectively. In all three micrographs, besides the grey aluminium matrix, it is possible to recognize brighter second phases. Grain boundaries (GBs) and grain boundary precipitates (GBPs) are also easily identified.

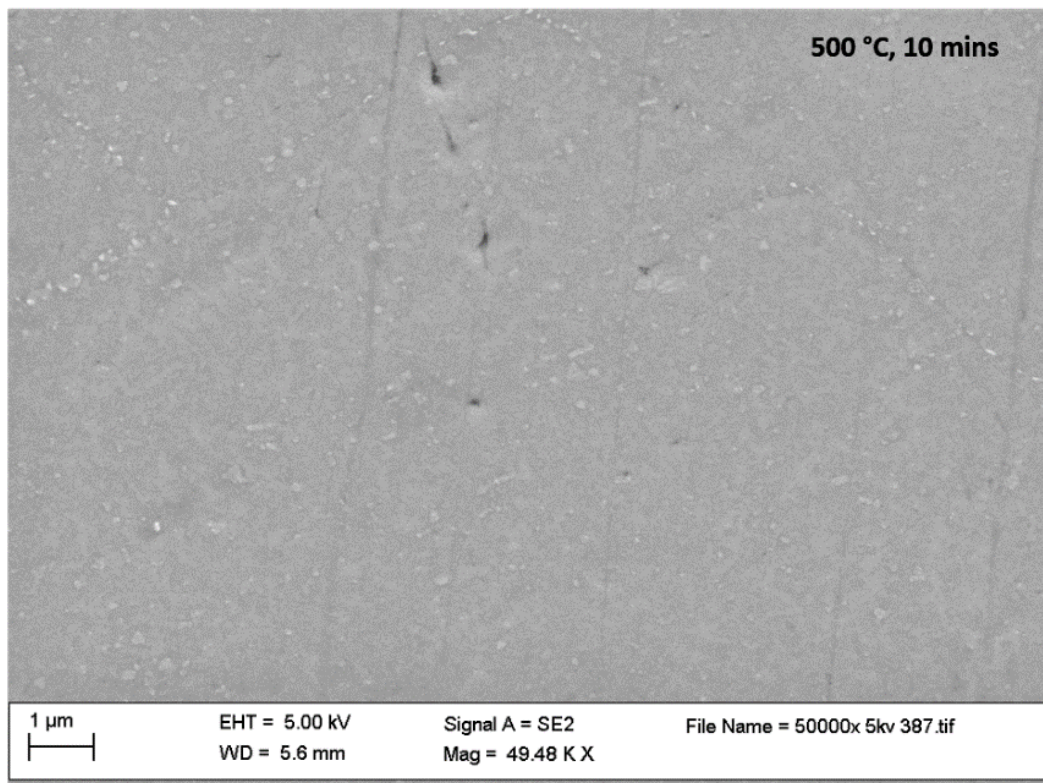


Figure 4.5: Scanning electron microscope micrograph of the sample solution heat-treated for 10 minutes at 500 °C.

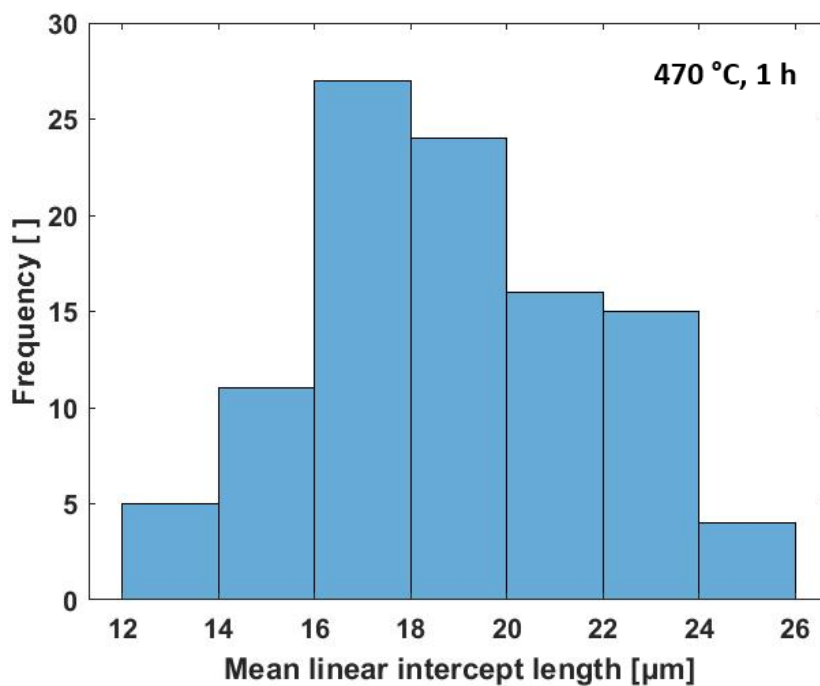


Figure 4.6: Distribution of mean linear intercept lengths for the sample solution heat treated at 470 °C for 1 hour.

Fig.4.6, Fig.4.7 and Fig.4.8 display the distributions of mean linear intercept lengths of samples subjected to solution heat treatment at 470°C for 1 hour, 500°C for 10 minutes, and 530°C for 10 minutes, respectively. The heating phase used the low heating rate ramp (2.5 °C/s).

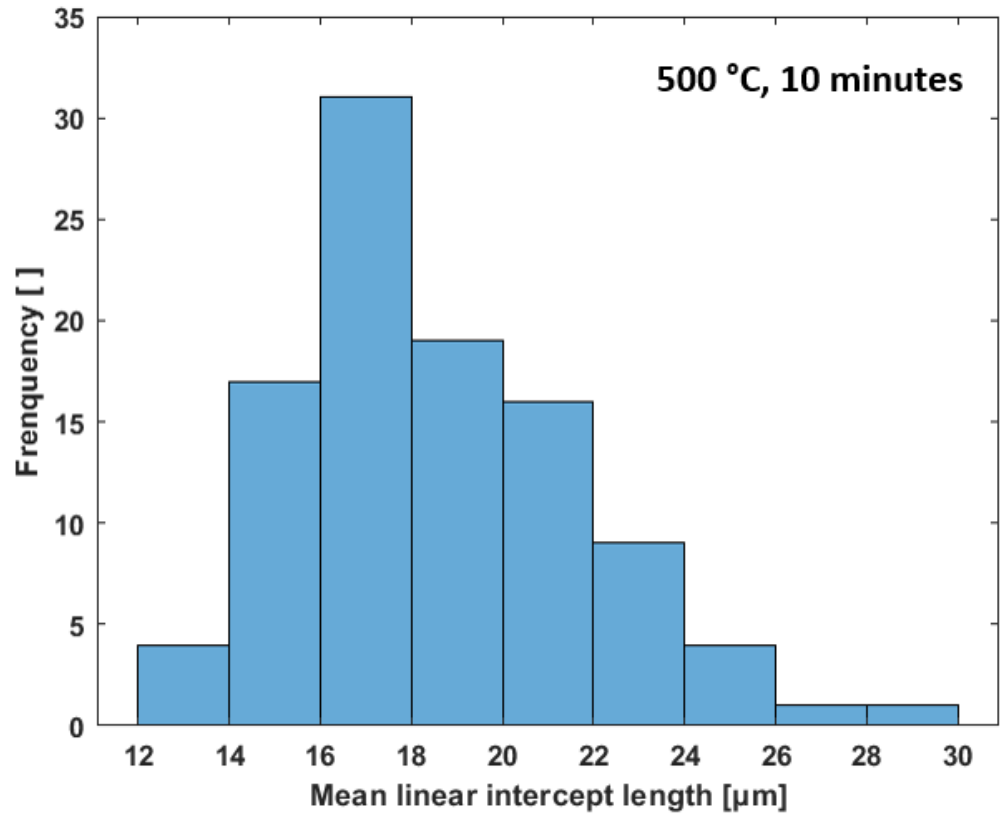


Figure 4.7: Distribution of mean linear intercept lengths for the sample solution heat treated at 500 °C for 10 minutes.

All the distributions show a nearly symmetrical and single-peaked shape, with the mode of the distributions falling inside the 16 μm – 18 μm bin in every case. The 470 °C for 1 hour and the 530 °C for 10-minute distributions have a range between 12 μm and 26 μm, while the range of the 500 °C for 10 minutes distribution was between 12 μm and 30 μm

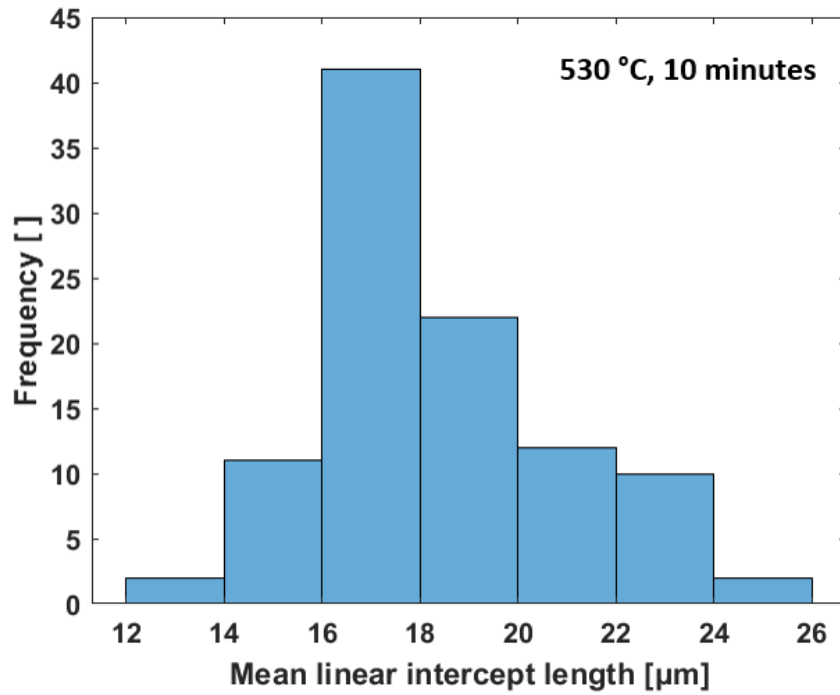


Figure 4.8: Distribution of mean linear intercept lengths for the sample solution heat treated at 530 °C for 10 minutes.

Fig.4.9 presents the optical microscope (OM) micrograph of a sample solution heat-treated for 1 hour at 470 °C. Besides the grain structure, the distribution of black second phases are also recognizable.

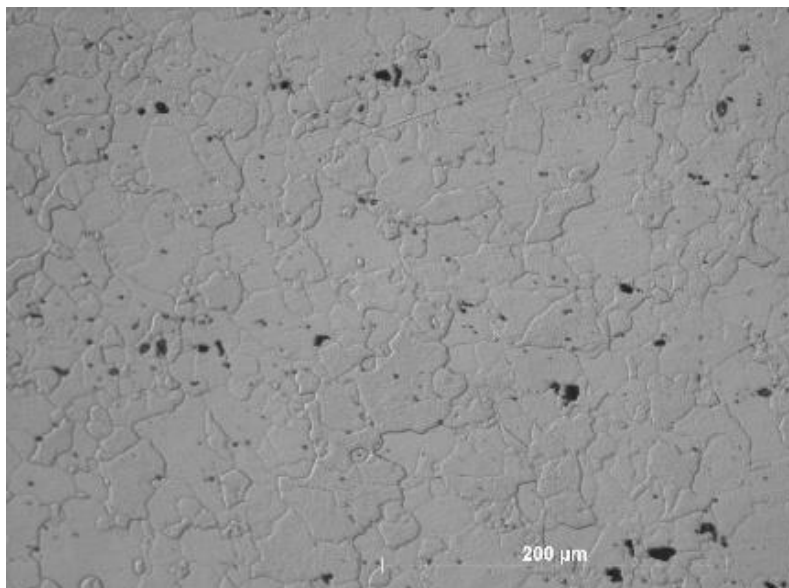


Figure 4.9: Optical microscope micrograph showing the grain structure of a sample solution heat-treated at 470 °C for 1 hour with the slow heating ramp (RDxLT plane).

4.1.2: Experiments at high heating rate

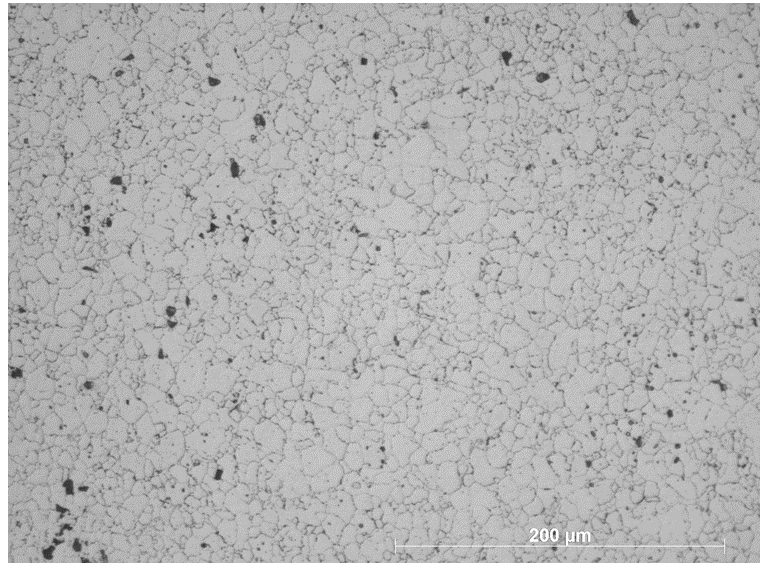


Figure 4.10: Optical microscope micrograph showing the grain structure of the sample solution heat treated at 470 °C for 1 hour with a slow heating ramp (RDxLT plane).

In Fig.4.10 the OM micrograph of the 200 °C/s and hold sample is displayed. The grain structure of the RDxLT plane, which was treated with Keller's reagent, includes a distribution of grains with different projected lengths on the surface,

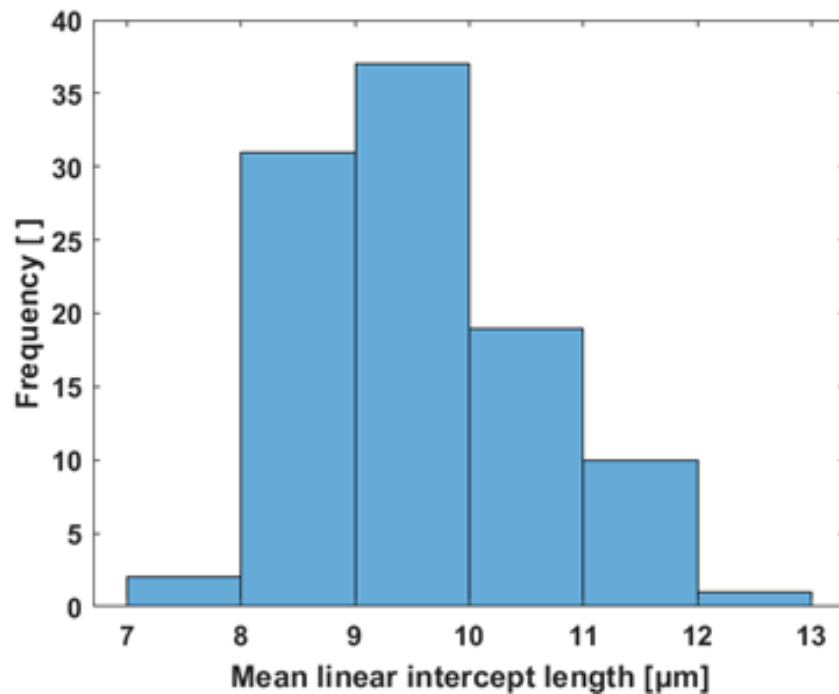


Figure 4.11: Distribution of mean linear intercept lengths for the 200 °C/s and hold sample.

from few micrometres to 20-30 micrometres. A group of black second phases is also easily noticeable.

Fig.4.11 shows distributions of mean linear intercept lengths for the grain structure of the 200 °C/s and hold sample. The distribution has a symmetrical

Metallurgical condition	Hardness [HV1]	2σ []
F temper	95.2	5.9
200 °C/s	108.8	2.9
3 °C/s	165.2	4.5
3 °C/s and hold	170.0	3.2
200 °C/s and hold	191.2	4.6

Table 4.1: Set of the hardness measurements carried out for the metallurgical conditions generated varying the solution heat treatment parameters.

and single peaked shape and the mode of the distribution is the 9 μm – 10 μm bin. The variability of the distribution ranges between 7 μm and 13 μm.

In Tab.4.1 is presented the set of the Vickers hardness measurements carried out for the samples heated up at the two different rates studied and the ones that include the isothermal holding at 470 °C. In particular, the “3 °C/s and hold” sample is achieved adding a 2.5 minutes isothermal hold to the “3 °C/s” sample. In this way, the “3 °C/s and hold” and the “200 °C/s and hold” sample share the same isothermal hold time at 470 °C, but they differ in the total duration of the solution heat treatment. In fact, the “3 °C/s and hold” solution heat treatment lasts overall 5 minutes, double the time of the “200 °C/s and hold” treatment.

Finally, the starting material “F temper” is added to the list of metallurgical conditions studied. The F temper is characterised by a Vickers hardness of 95.2 on average, a value which is close to the one reported for the 200 °C/s heating rate (108.8 HV1). An intermediate level of Vickers hardness is reached by both the 3 °C/s and the 3°C/s and hold samples, with average values of 165.2 HV1 and

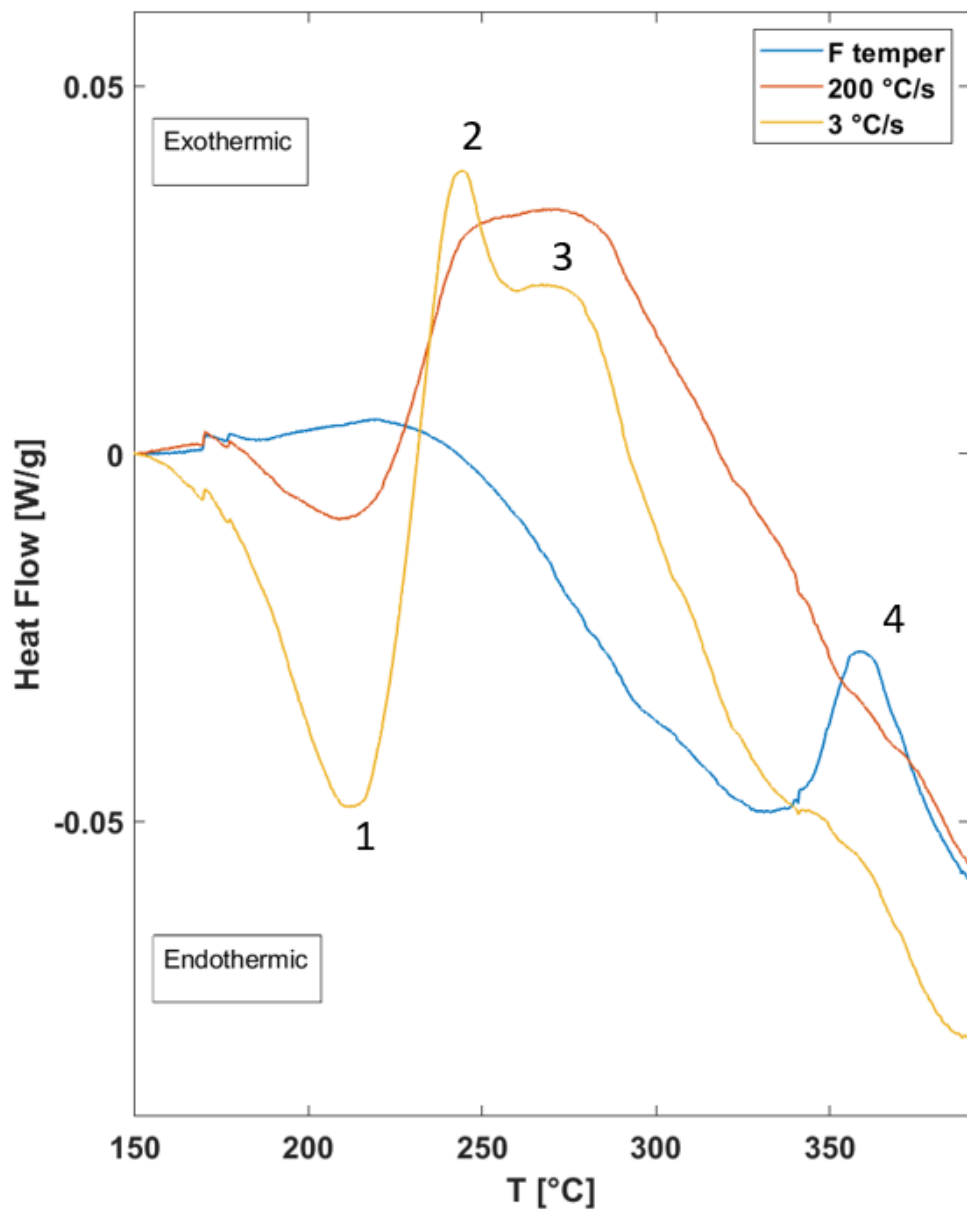


Figure 4.12: Differential scanning calorimetry traces of the F temper, 200 °C/s and 3 °C/s samples.

170 HV1, respectively. The highest level of Vickers hardness is achieved by the 200°C/s and hold sample, with an average value of 191.2 HV1.

Fig.4.12 shows a comparison among the differential scanning calorimetry (DSC) traces of the F temper, 200 °C/s and 3 °C/s heating rate samples. In the 150 °C – 220 °C temperature range, while the 200 °C/s sample and the 3 °C/s sample exhibit the endothermic peak '1' (dissolution), the F temper sample is characterised by a moderate exothermic plateau.

The temperature at which the two dissolution peaks are observed is almost identical (roughly 210 °C), but the endothermic event is far more pronounced in

the case of the 200°C/s heating ramp. After the dissolution peak, both the fast and the slow heating rate ramp samples undergo an exothermic event (peak '2' and peak '3'): while in the 200 °C/s sample this event is characterised by a consistent exothermic plateau ranging from approximately 255 °C to 280 °C, in the 3°C/s sample two exothermic peaks take place and the magnitude of the first

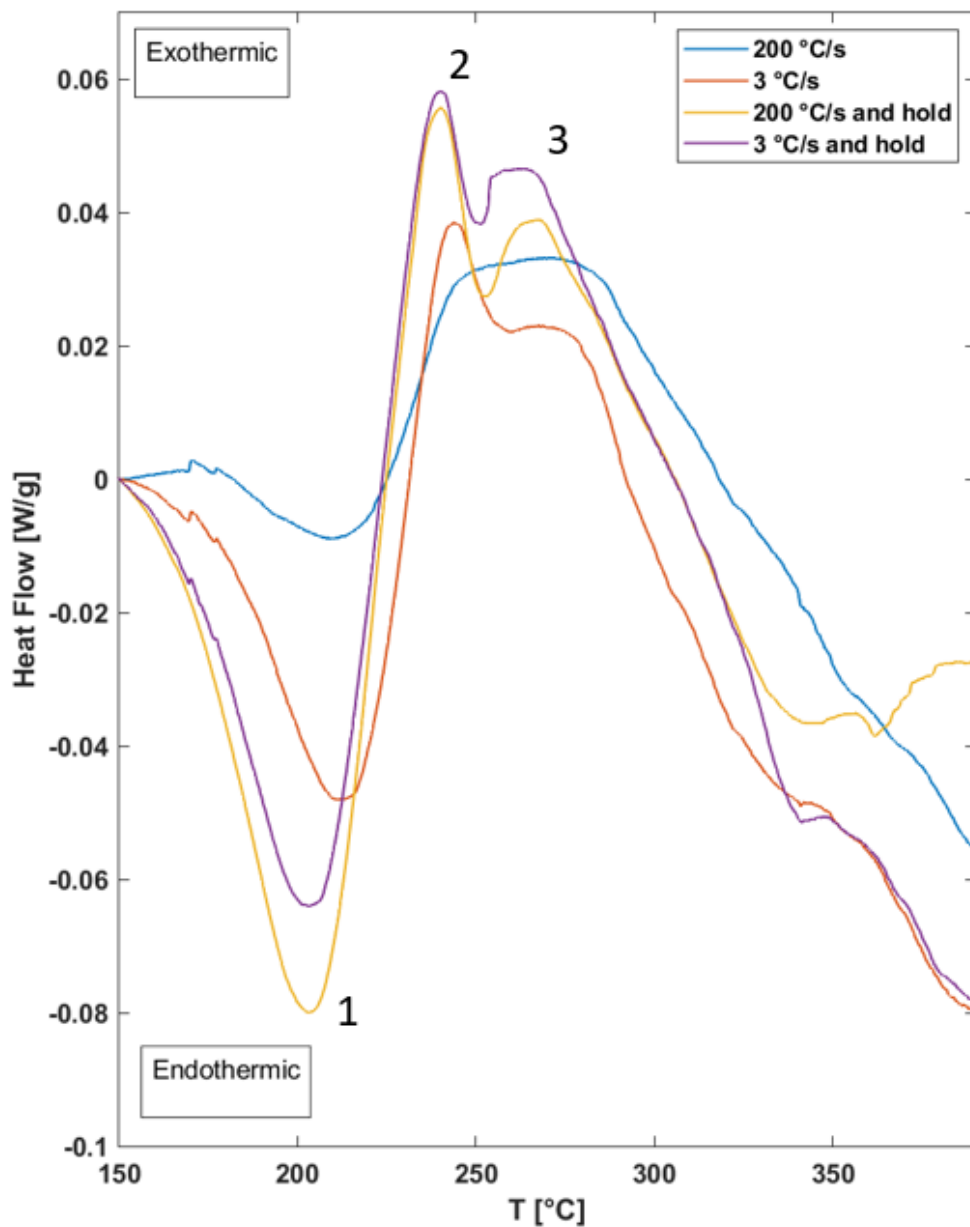


Figure 4.13: Differential scanning calorimetry traces of the 200 °C/s, 3 °C/s, 200 °C/s and hold, 3 °C/s and hold samples.

one is much higher than the magnitude of the second one. The characteristic temperature of the two exothermic peaks is 245 °C and 275 °C, respectively.

Compared to the two differently heated samples, the F temper material follows a totally different trend, displaying a broad endothermic event instead of the

exothermic peak '2' and peak '3' abovementioned. This endothermic event is characterised by a minimum at roughly 335 °C. After that, while still being globally an endothermic event, the F temper shows a relative maximum at approximately 360 °C. Instead, the 200 °C/s sample and the 3°C/s sample experience a marked endothermic event that extends from the previous exothermic parts of the trace to the final temperature of the scan (400 °C).

In Fig.4.13 is presented a comparison of the DSC traces of 4 different metallurgical conditions: 200 °C/s, 3 °C/s, 200 °C/s and hold, 3 °C/s and hold samples. In the 150 °C – 220 °C range all the DSC traces show firstly the endothermic peak '1', but while for the samples subjected just to the heating ramp (200 °C/s, 3 °C/s) the temperature of the peak is about 210 °C, the samples that include the isothermal hold after the ramp (200 C/s and hold, 3 °C/s and hold) show a temperature associated to the peak of approximately 205 °C/s. Also, the samples where the isothermal hold is imparted after the ramp display a much deeper endothermic peak '1' than the samples just heated up at different heating velocities. The 200 °C/s and hold sample shows the most prominent endothermic peak '1', followed by the 3°C/s and hold sample and then the 3°C/s sample. Finally, the least marked endothermic peak is attributed to the 200 °C/s sample.

In the temperature range between 220 °C and 300 °C, all the traces display an exothermic event: the 200°C/s sample is the only metallurgical condition characterised by an exothermic plateau, while all the other samples show in their trace two distinct exothermic peaks (peak '2' and peak '3'). The two exothermic peaks are located roughly at the same temperatures for all metallurgical conditions investigated: around 210 °C for peak '2' and around 265 °C for peak '3'.

In addition, the exothermic events of the samples hold isothermally are much more prominent than the ones of the samples just heated up by the slow or fast heating ramps. In particular, exothermic peak '2' has the same magnitude for the 200 °C/s and hold and the 3 °C/s and hold samples., while exothermic peak '3' is greater in the 3°C/s and hold sample. In the high temperature range of the scan

between 300 °C and 400 °C all the traces display a broad and consistent endothermic event.

4.2: Discussion

4.2.1: The precipitate dissolution process at high temperatures and low holding times

Fig.4.1 investigates how a short holding time and a high temperature affects the dissolution rate of precipitates during the solution heat treatment. In fact, the average Vickers hardness values recorded for each metallurgical condition are directly proportional to the level of precipitate dissolution achieved in the material. A higher precipitate dissolution during the solution heat treatment translates into a larger alloying element concentration in the matrix, which then causes a refined precipitate distribution after aging and therefore an enhanced hardness response in the workpiece.

	470 °C	500 °C	530 °C
D_{Mg}	$1.26 \cdot 10^{-13} m^2/s$	$2.75 \cdot 10^{-13} m^2/s$	$5.66 \cdot 10^{-13} m^2/s$
D_{Zn}	$8.46 \cdot 10^{-14} m^2/s$	$1.81 \cdot 10^{-13} m^2/s$	$3.64 \cdot 10^{-13} m^2/s$

Table 4.2: Mg and Zn diffusion coefficient in Al when varying the solution heat treatment temperature. Data obtained from [156].

In the temperature range between 470 °C and 500 °C, the Vickers hardness values increase with a rising temperature for both the 6- and 10-minute dataset. To understand the temperature effect on the dissolution process it is useful to break it down in a sequence of steps. In fact, the literature has established that the precipitate dissolution occurs as the sequence of precipitate decomposition, migration of the alloying elements across the precipitate/matrix interface and finally diffusion of the alloying elements towards the surrounding aluminium matrix [155].

The diffusion of alloying elements towards the matrix is the rate-limiting step, so the velocity of the dissolution matches the velocity of the elemental diffusion [155]. As diffusion coefficients increase when the temperature is raised (Tab.4.2), the dissolution process and, consequently, the final hardness of the material are improved. The temperature increase also lowers the thermodynamic stability of the second phases [84].

However, because the dissolution of the more stable constituents, such as Al_2CuMg (S phase), reportedly requires far longer holding times than 10 minutes, the dissolution of such constituents are unlikely to contribute to the increase of alloying elements in the matrix. In fact, only the dissolution of MgZn_2 is dominant with these treatment durations [84].

In the 500 °C–530 °C range, both the 10- and 6-minute dataset exhibit a plateau with increasing temperatures. For the 10-minute dataset, this plateau can be explained by the dissolution being fast enough at the 500 °C–530 °C interval that the vast majority of precipitates turn into a solid solution regardless of the temperature selected. This hypothesis is also supported by the close match between the hardness levels of this plateau and those of the samples subjected to the benchmark solution heat treatment.

The Vickers hardness values of the 6-minute solution treatment dataset are also constant in the 500 °C–530 °C range. This finding is surprising because the faster elemental diffusion enabled by higher temperatures should boost the dissolution process and make the hardness values reach the same levels as the 10-minute dataset when going from 500 °C to 530 °C. One possible explanation is that, when the temperature surpasses a certain threshold, the diffusion of the alloying elements no longer constitutes the rate-limiting step of the dissolution process.

The results in Fig.4.1 can be compared with the other studies examining the precipitate dissolution during the solution heat treatment. For example, Liu et al. [32] solution heat treated AA7075 sheets for 30 minutes while adopting a wide range of temperatures between 430 °C and 550 °C. As similarly shown in Fig.4.1, the researchers reported a hardness plateau in the temperature interval between 490 °C and 530 °C, and the Vickers hardness values determined after aging were similar at approximately 190 HV1. In addition, when selecting 510 °C as the solution heat treatment temperature, Liu et al. showed an almost constant hardness level for the holding times of 10 minutes and 30 minutes. This finding means the dissolution process can be completed with a total holding time of 10 minutes: this result completely matches the one obtained in Fig.4.1.

The ability to complete the dissolution process in the 10-minute time span also aligns with the study of Milkereit et al. [31]. In fact, from calorimetric studies, the

researchers concluded that the dissolution process is mostly complete when solution heat treating AA7075 sheets for 15 minutes at 480 °C. Thus, it can be deduced that the use of 500 °C might reduce the required time from 15 minutes to 10 minutes. Finally, the hardness levels that Milkereit et al. reported after aging also fell in the same range of those in Fig.4.1.

Overall, Fig.4.1 informs that, when adopting 3 °C/s as the heating rate, the dissolution of hardening precipitates can be completed in the 10-minute time range if using 500 °C. However, the selection of a temperature higher than 500 °C does not further accelerate the dissolution process. The hardness plateau reached in the 6-minute dataset between 500 °C and 530 °C was not expected, nor is that plateau documented in the current literature.

For this reason, more work is necessary to confirm whether, at high temperatures and short holding times, the precipitate dissolution kinetics are no longer diffusion controlled. Confirmation of this notion would constitute a beneficial milestone and help improve the existing models that predict the duration of the dissolution process during solution heat treatment since they are built considering the rate-limiting step in the diffusion of alloying elements for the temperature range used [155,157].

4.2.2: Incipient melting at high solution heat treatment temperatures

The comparison of Fig.4.3, Fig.4.4 and Fig.4.5 allows for investigating the extent of incipient melting when using the combination of high temperatures, low heating rates and low holding times in solution heat treatments. Fig.4.3 displays the Scanning electron microscopy (SEM) micrograph of the sample solution heat treated at 470 °C for 1 hour, water quenched and fast-aged.

Because the solution heat treatment temperature of the sample is below the eutectic temperature for AA7075 (475 °C), the sample is unaffected by the incipient melting phenomenon. Therefore, Fig.4.3 is used as the reference SEM micrograph for comparing those obtained for the other two metallurgical conditions. As the microstructural features observed in the SEM micrographs of the sample held 10 minutes at 500 °C and 10 minutes at 530 °C mirror the reference case, incipient melting can be concluded not to be predominant in the selected range of temperatures and holding times.

In fact, all three microstructures analysed exhibited similar patterns of matrix precipitates and a similar grain boundary (GB) structure with well-developed grain boundary precipitates (GBPs). Xu et al. [84] characterised the microstructures of as rolled AA7150 thick plates when subjected to solution heat treatment at high temperatures, long holding times and fast heating rates.

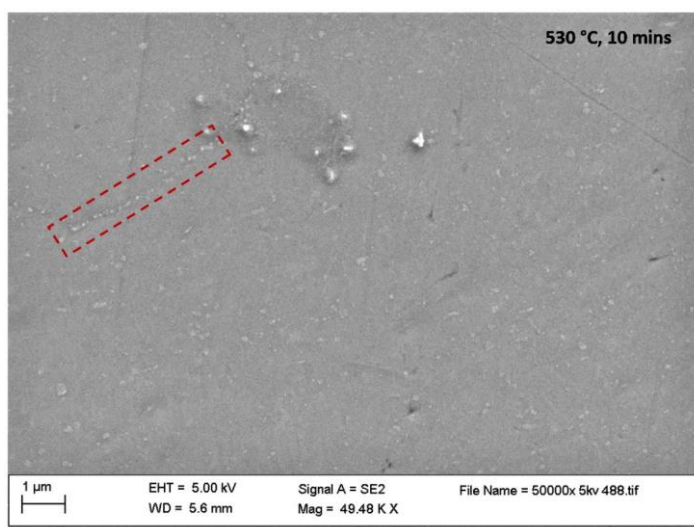


Figure 4.14: AA7075 scanning electron microscopy micrograph of the sample solution heat treated at 530 °C for 10 minutes at low heating rate where the developed GB structure is highlighted.

The first microstructural feature associated with incipient melting when moving towards higher temperatures was reported as the appearance of porosity that increases in size with increasing temperature. At temperatures close to the eutectic temperature, the holes sizes are mostly in the submicrometric range, but they can reach even tens of micrometres when the temperature is considerably higher than the eutectic one [84].

While large porosity in the 10 μm range was not detected even in the sample held at 530 $^{\circ}\text{C}$, some features of the two micrographs at high temperatures might be associated with submicrometric or micrometric porosity. However, further investigation would be needed to clarify the nature of those features.

Interestingly, large porosity is reported in the work of Xu et al. even at 490 $^{\circ}\text{C}$ but is clearly not present in Fig.4.4, where 530 $^{\circ}\text{C}$ is used as the solution heat treatment temperature. The absence of large porosity in the 530 $^{\circ}\text{C}$ sample might be associated with the low heating rate adopted. In fact, the precipitate alloying elements have enough time to diffuse away during the low heating rate ramp, and the dissolution process results favoured over melting [84].

Xu et al. also showed that incipient melting becomes far more relevant at temperatures significantly higher than the safe eutectic limit, for example, 515 $^{\circ}\text{C}$ for AA7150. In this case, incipient melting develops significantly at GBs, where a network of eutectic second phase is formed. This feature is also commonly reported when incipient melting is detected in non-homogenised microstructures heated above the safe temperature limit [60].

As highlighted in Fig.4.14 (dashed rectangle), eutectic networks are not detected in the SEM microstructures for the sample solution heat treated at 530 $^{\circ}\text{C}$. This lack of detection therefore provides further evidence that incipient melting is not a predominant phenomenon in the range of solution heat treatment parameters used in this study. Consistent with the observation of large pores, the eutectic network at GBs is present only in the experimental condition of Xu et al. (Fig.2.8 of Section 2.3) and not in the sample solution heat treated at 530 $^{\circ}\text{C}$ for 10 minutes.

Once again, the slow heating rate used in this work is believed to enable the dissolution needed to prevail over melting since the precipitates are already

mostly dissolved at temperatures where melting becomes thermodynamically favourable. Conversely, the high heating rate used by Xu et al. makes the precipitates survive and experience the high temperature and, consequently, melting occurs instead of dissolution as melting is kinetically faster.

The absence of incipient melting in Fig.4.4 aligns with the work of Liu et al. [32], in which this detrimental phenomenon is only detected for AA7075 at 550 °C. Instead, matching the reference sample microstructure in Fig.4.3 with the Fig.4.4 microstructure does not align with the work of Milkereit et al. [31], who stated that AA7075 sheets can only be kept in the solid state at a temperature below 490 °C.

The discrepancies among these studies might be linked to the various heating rates used in the different works, and these parameters greatly influence the presence of incipient melting in the workpieces. In addition, no agreement is generally reached about the frequency of the features described, which is needed to define incipient melting.

In summary, Fig.4.3, Fig.4.4 and Fig.4.5 demonstrate that there is a broader temperature range in which a solution heat treatment temperature can be chosen compared to the typical homogenization treatment temperature range, as the microstructural modifications linked with incipient melting are barely noticeable. In fact, the alloying elements average concentration in homogenised workpieces is much more uniform than the one in as cast samples. The sample regions where the alloying concentrations resemble the eutectic one are thus highly rare, as is the occurrence of incipient melting.

4.2.3: Optimisation of the HFQ® solution heat treatment parameters

Based on Fig.4.1, 500 °C can be deduced to be the optimised temperature for the HFQ® solution heat treatment when using 3 °C/s as the heating rate. In fact, 500 °C promotes the dissolution of precipitates just like the benchmark solution heat treatment (470 °C for 1 hour) and does not induce significant changes in the sample microstructure related to incipient melting. In addition, based on the comparison of Fig.4.6 with Fig.4.7, the use of 500 °C for a short holding time can thus determine a very similar grain structure to one of the benchmark solution heat treatments.

Once 500 °C is selected as the solution heat treatment temperature, the total holding time can be optimised using Fig.4.2. This plot shows that, when incrementing the holding time, the hardness levels first increase linearly up to the 6-minute duration and then stabilise in the 6- to 10-minute range. For this reason, 6 minutes is selected as the optimised holding time for the HFQ® solution heat treatment when using the 2.5 °C/s heating ramp.

The result shown in Fig.4.2 generally agrees with the related literature. For example, Tanaka et al. [83] used 480 °C for 5 minutes to successfully solution heat treat 1 mm AA7475 sheets, while Xu et al. [84] stated that a solution heat treatment at 475 °C for 5 minutes can completely dissolve the η phase in the matrix. The result presented in Fig.4.2 also aligns well with the work of Liu et al. (Fig.2.9 in Section 2.4) [85].

These authors also recorded the average Vickers hardness values after aging when solutionising at 480 °C and varying the total holding time in the 1- to 10-minute range. Based on the hardness plot (bare sheets), the Vickers hardness levels can reach a plateau for durations of at least 8 minutes, appearing to a hardness trend like the one shown in Fig.4.2. Generally, the small mismatches of the optimised solution heat treatment parameters from the different studies cited might be related to differences in the alloy chemistry, starting microstructure, sample thickness and heating rate.

As reported in various studies [33,85,87], the increase of the heating rate for the solution heat treatment temperature can further decrease the required holding

time to complete the precipitate dissolution process. In fact, the average Vickers hardness value of the sample fast heated (200 °C/s) to 470 °C and held at this temperature for 2.5 minutes is roughly identical (around 190 HV1) to one of the samples subjected to the benchmark solution heat treatment (470 °C for 1 hour) and one of the samples heated with low heating rate to 500 °C for 10 minutes.

Similarly, Zhang et al. [33] achieved peak strength for AA7075 sheets when using a high heating rate (15.8 °C/s) and solutionising the samples at 475 °C for 40 seconds. Choi et al. [87] instead applied a 100 °C/s heating ramp to 475 °C to AA7055 and achieved peak hardness in the material when holding for 40 seconds. In another study, using a radiative furnace and appropriate emissive coatings, Liu et al. [85] obtained optimised tensile properties and hardness in AA7075 sheets when the fast heating ramp reached 480 °C, and the solution heat treatment lasted around 3 minutes.

Besides the differences in alloy chemistry, starting microstructure and sample thickness, the results of the optimisation processes of the above studies might differ because of the varying magnitudes and characteristics of the heating ramps used. For example, the linear heating ramp used in this study via resisting heating (Fig.4.15) is qualitatively different than the ramp obtained through contact solid solution in the work of Zhang et al. [33] (compare Fig.4.15 with Fig.2.11 in Section 2.4).

Because the final temperature of the 200 °C/s and hold sample is lower than the eutectic temperature for AA7075 (475 °C), microstructural changes linked to incipient melting are not expected. As the heating rate greatly influences the magnitude of incipient melting [84], further work would be needed in case a high heating rate is used in conjunction with a solution heat treatment temperature higher than the eutectic one.

Besides the reduction of the total holding time, which is shortened from 6 minutes to 2.5 minutes, the use of a high heating rate greatly modifies the grain structure of the sample. In fact, when comparing Fig.4.6, Fig.4.7 and Fig.4.11, the use of a high heating rate ramp appears to almost halve the average mean linear intercept obtained, going from 16 μm –18 μm for the low heating rate samples to 9 μm –10 μm in case of fast heating. The grain refinement achieved is aligned with the results of the other studies focused on the effect of the heating rate [33,79].

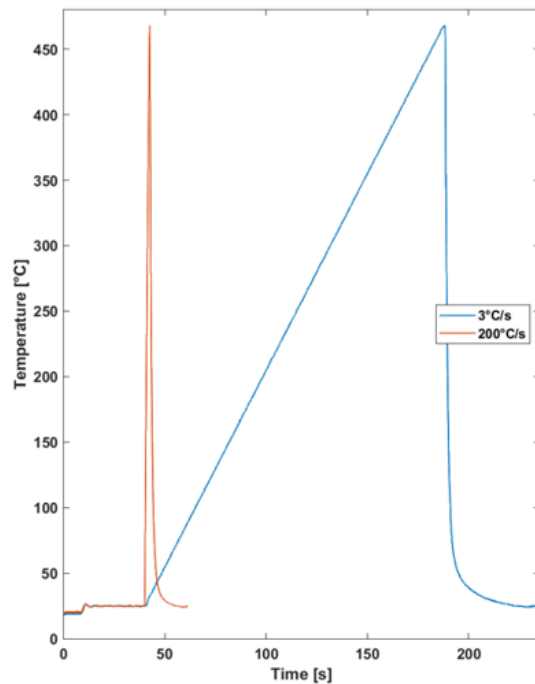


Figure 4.15: Linear time-temperature heating profile generated via dilatometer.

In conclusion, the parameters selected to carry out an accelerated solution heat treatment for the HFQ[®] process depend on the heating rate used. If the circulating air furnaces typical heating rate is adopted (2.5 °C/s–3.5°C/s), then a temperature of 500 °C held for at least 6 minutes is suggested. Instead, if a high heating rate can be applied (above 10 °C/s), the selection of 470 °C for 2.5 minutes is recommended.

4.2.4: The heating rate effect on the precipitate dissolution process

4.2.4.1: *The effect of the heating ramp*

The analysis of Fig.4.12, Fig.4.13 and Tab.4.1 helps to clarify the effect of the heating rate on the precipitate dissolution process during the solution heat treatment. In fact, Differential scanning calorimetry traces characteristics can be linked to the microstructural features of the sample investigated [152,158] and therefore to the effectiveness of the dissolution process. However, as dissolution and precipitation reactions overlap in the temperature range at which the traces are recorded [152,158], the interpretation of these results vary slightly among different researchers.

In F tempered samples, the η phase is the most abundant precipitate type [34,60], and solute atoms are released mainly due to the dissolution of this phase. The extent of dissolution depends on the parameters selected for the solution heat treatment. After quenching and aging, new precipitates form and grow in the matrix, and their characteristics depend on the concentration of the alloying atoms previously released. These differences in the precipitation behaviour among the different metallurgical conditions are then highlighted during the differential scanning calorimetry (DSC) experiment as such differences influence the characteristics of the trace recorded.

According to the work of Richard et al. [152], the endothermic peak registering in the 150 °C–220 °C range is due to the dissolution of GP zones and the small size of the η' phase. Partially overlapping with this reaction is the exothermic coarsening of large η' precipitates. The dissolution/coarsening behaviour of η' depending on its size might be caused by the capillarity effect [137].

Fig.4.12 shows that the depth of the endothermic peak '1' is larger for the sample subjected to the 3 °C/s heating rate ramp than for the 200 °C/s one. Instead, the F tempered sample displays a weak exothermic peak in this same temperature range. A higher concentration of GP zones and small η' can thus be assumed to be present in the slow heated sample compared to the fast heated one. Consequently, more solute atoms were released, and a higher degree of

precipitate dissolution occurred when the sample was heated up with the 3 °C/s ramp.

This result is also supported by the average Vickers hardness of the 3 °C/s sample being greater than the one for the 200 °C/s sample (Tab.4.1): the slow heating ramp determines a higher-volume fraction of the strengthened second phases precipitated after aging. The enhanced dissolution promoted during the slow heating ramp is a consequence of the longer heating time compared to the high heating rate case. This gap in the heating time duration regulates the dissolution during the heating step rather than the temperature rise (Fig.4.16).

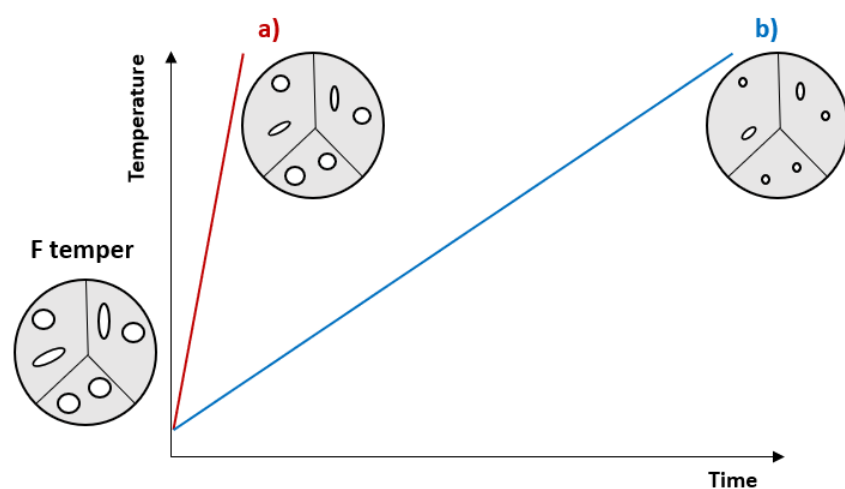


Figure 4.16: Schematic proposed precipitate dissolution during (a) high heating rate ramp and (b) low heating rate ramp.

This result agrees with the study of Wang et al. [34], who similarly concluded that a higher degree of dissolution occurs when using a low heating rate ramp instead of a high heating rate one. Conversely, this result disagrees with the works of Zhang et al. [33] and Chang et al. [159]. In fact, both research groups suggested a higher degree of dissolution occurs during a high heating rate step than in a low heating rate one. This discrepancy could stem from the intrinsic experimental difficulties in trying to rapidly cool the material immediately after the heating ramp, without accidentally including any isothermal holding time. As explained in the next paragraph, the inclusion of an isothermal holding time can greatly affect the dissolution process.

In the current work, automatically controlling both the heating and cooling phases allowed for high precision when the temperature profiles are imparted to

the material. In Fig.4.12, instead of the endothermic peak '1', a weak exothermic peak is reported for the F tempered sample. This peak is believed to be linked with the growth of already large η' precipitates, and this exothermic reaction overpowers the dissolution reactions typical of this temperature range as GP zones and small η' precipitates have a low concentration in F tempered samples [34,60].

In the 220 °C–300 °C range, while the fast heated sample shows a broad exothermic peak, the slow heated sample displays the succession of the exothermic peak '2' followed by the exothermic peak '3'. In this same temperature interval, the F temper material is characterised by a broad endothermic event. Richard et al. [152] reported that different reactions overlap in this temperature range. The exothermic peak '2' is linked to the nucleation and growth of η phase onto the existing η' precipitates, while a minor second contribution to the exothermic event also comes from the nucleation and growth of η phase directly from the matrix. The local minimum between the exothermic peaks '2' and '3' is associated with the endothermic dissolution of η' . Finally, the exothermic peak '3' is linked with the enlargement of η precipitates at the expense of the dissolving η' phase.

As previously mentioned, the endothermic peak '1' is the deepest in the slow heated sample, so this metallurgical condition has the highest availability of alloying atoms in the matrix and therefore a greater enlargement of the pre-existing η' precipitates. Consequently, the slow heated sample is characterised by a more pronounced exothermic peak '2' since a greater amount of the η phase can nucleate onto the existing η' precipitates.

Conversely, the lower concentration of alloying elements developed in the fast heated sample during the endothermic peak '1' causes a reduced coarsening of η' , less formation of η phase onto the existing η' and thus a very weak exothermic peak '2'. The bigger size of η' precipitates can also explain why the 3 °C/s sample displays a slightly more developed exothermic peak '3' than the 200 °C/s sample. After the exothermic peak '2', the dissolution of larger η' precipitates results in an increased concentration of solute atoms in the matrix.

This, in turn, facilitates the growth of the η phase associated with the exothermic peak '3'.

In the F tempered sample, the absence of the endothermic peak '1' results in a lack of alloying elements in the matrix. Therefore, as the growth of η phase onto the existing η' is considerably reduced, a broad endothermic event linked with the dissolution of η' characterises the 220 °C–300 °C temperature range.

As agreed by many calorimetric studies related to precipitation kinetics in 7000 aluminium alloys [137,152,158], the dissolution of η precipitates is the main reaction occurring above 300 °C. In fact, both the slow and fast heated samples show a broad endothermic event after the exothermic peak '3'. The F tempered sample, while following the same trend of a broad dissolution event above 300 °C, also displays the endothermic minimum '4'. This minimum might be explained by considering the building up of alloying elements during the wide dissolution event between 220 °C and 320 °C. The increase of solute atoms in the matrix might trigger the coarsening of the η phase (exothermic reaction) linked to the endothermic minimum '4', which momentarily mitigates the thermal effect of the η dissolution.

Generally, the DSC trace of the 200 °C/s sample can be observed as qualitatively closer to the one of the 3 °C/s samples rather than the one of the F tempered samples. This closeness might suggest that some degree of precipitate dissolution occurs during the fast heating rate ramp, even if the duration of this thermal step is very limited (a few seconds). The presence of the dissolution event is also compatible with the slightly higher hardness level obtained after aging for the 200 °C/s sample, as compared to the F tempered sample.

4.2.4.2: The effect of the isothermal holding time after the heating ramp

When analysing Fig.4.13, the endothermic peak '1' appears far more marked in the 200 °C/s and hold sample than in the 3 °C/s and hold sample. Thus, the 200 °C/s and hold sample has a higher concentration of GP zones and small η' precipitates developed after aging [152]. The stronger precipitation comes from a higher concentration of alloying elements released in the matrix and a greater extent of precipitate dissolution achieved when using these solution heat treatment parameters. This deduction is also supported by the higher Vickers hardness obtained for the 200 °C/s and hold sample compared to the 3 °C/s and hold sample (Tab.4.1).

Notably, the 200 °C/s and hold sample and the 3 °C/s and hold sample share the same isothermal holding time at 470 °C (2.5 minutes), but the total time of the solution heat treatment is almost doubled in the 3 °C/s and hold sample. The fast heating rate ramp of the 200 °C/s and hold sample can therefore be assumed to improve the ability to dissolve precipitates during the following isothermal holding time (Fig.4.17).

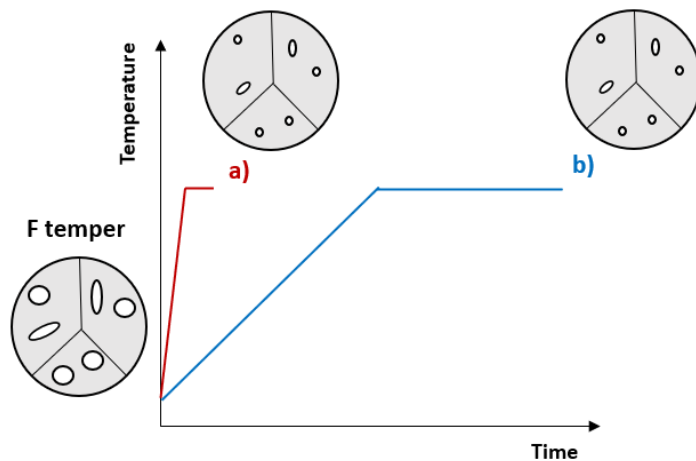


Figure 4.17: Schematic effect of the holding time on precipitate dissolution after: (a) high heating rate ramp, (b) low heating rate ramp.

This result can be explained by considering different factors: during the high heating rate ramp, a reduced fraction of GP zones and small η' precipitates dissolves, leaving the microstructure almost unchanged when approaching the isothermal holding time at high temperature. Conversely, during the slow

heating ramp, a greater number of GP zones and small η' pass into the solid solution; the heating time is also sufficient to promote some coarsening of both large η' and η precipitates. The coarsening of the second phases makes the microstructure of the slow heated sample harder to solutionise when the isothermal hold at high temperature is applied [85].

A second factor to consider is the effect of the heating rate on the grain structure and density of dislocations. In fact, the finer grain size (greater concentration of GBs per unit volume) and the higher density of dislocations preserved when using a high heating rate might enhance the diffusion of the alloying elements towards the matrix and consequently accelerate the dissolution process during the isothermal holding time [87].

The concept of the improved quality of the isothermal holding time after a fast rate ramp is not present in the study of Wang et al. [34]. Rather, Wang et al. reported that, after the completion of solution heat treatments with both slow or fast heating ramps and the same isothermal holding time, the levels of precipitate dissolution measured in the material afterwards were basically the same.

The mismatch of the above results with the findings of this study could be linked with the differences in the magnitude of the isothermal holding time used: while the duration in this study is in the order of minutes, the duration in the study of Wang et al. [34] is 1 hour. Consequently, the isothermal holding time of 1 hour might offset the dissolution differences related to the fast or slow heating ramps and promote complete dissolution in both cases investigated.

The improved quality of the isothermal holding time after the high heating rate ramp is a concept that agrees with the findings in the study of Choi et al. [87]. Like this study, they used solution heat treatments with a 100 °C/s or 3 °C/s heating rate and the same isothermal holding for roughly one minute at 475 °C: the fast heated sample showed higher hardness levels than the slow heated one.

Regarding the analysis of the endothermic peak '1' in Fig.4.13, the second feature observed is that the temperature of the endothermic maximum is the same for both the '200 °C/s and hold' and the '3 °C/s and hold' samples.

Moreover, this temperature is lower than that of the endothermic maxima of the

200 °C/s and 3 °C/s samples, where no subsequent isothermal hold is applied. As deduced from other calorimetric studies related to 7000 aluminium alloys [160], the reduction of the endothermic peak '1' maximum temperature can be explained by assuming that the two samples subjected to the additional isothermal holding are characterised by a more refined distribution of precipitates than the sample subjected only to the heating ramps.

The finer distribution of matrix precipitates developed in these samples after the aging determined by their higher concentration of solute elements. A greater enrichment of solute atoms is linked to the time spent at high temperature during the isothermal holding. As the endothermic maximum '1' occurs at the same temperature for the 200 °C/s and hold and the 3 °C/s and hold samples, the two metallurgical conditions have similarly sized matrix precipitates.

This conclusion is similarly reported in the works of Choi et al. [87] and Huo et al. [79], who both conducted microstructural observations of the matrix precipitates in the case of slow or fast heating. Overall, the DSC traces of the 200 °C/s and hold and the 3 °C/s and hold samples are qualitatively like that of the 3 °C/s sample. As explained in the previous paragraph, the magnitude of the exothermic peaks '2' and '3' corresponds to the degree of dissolution realised during the solution heat treatment. Therefore, these two peaks are less pronounced when considering the 3 °C/s sample.

4.2.5: The effect of accelerated solution heat treatments on the grain structure

The comparison of Fig.4.6, Fig.4.7 and Fig.4.8 shows that the mode of the distributions falls inside the 16 μm –18 μm bin for each metallurgical condition and that each distribution displays almost the same mean linear intercept length range. For this reason, the samples solution heat treated at 500 °C for 10 minutes and 530 °C for 10 minutes can be assumed to have a very similar grain size to that of the solution heat treated at 470 °C for 1 hour.

The similarity of the grain size between the benchmark sample (470 °C for 1 hour) and the sample solution heat treated at the highest temperature (530 °C for 10 minutes) also suggests that the use of a very high temperature for the solution heat treatment does not accelerate recrystallization and grain growth from the baseline level of the benchmark sample. In this case, the reduced holding time and the low heating rate are probably the main factors controlling the stability of the grain structure.

Generally, during a heating ramp at a low rate, recovery consistently decreases the stored energy in the form of dislocations and reduces the drive for recrystallization and grain growth [34,79]. However, the use of high temperatures enhances the thermal energy available and speeds up the recrystallization and grain growth process [84]. Finally, the short total holding time can also help lower the extent of the microstructural changes.

The conclusions drawn from this result can be also explained in relation to the work of Xu et al. [84]. While adopting a low heating rate, they studied how the amount of the recrystallized fraction changes when using different temperatures and total holding times for AA7150 thick plates. The researchers reported that the recrystallised fraction is small when solution heat treating the material at 475 °C for 24 hours, but the fraction becomes appreciable for solution heat treatments at 495 °C for 8 hours. Therefore, the increase of the solution heat treatment temperature greatly accelerated the recrystallization process under the experimental conditions. However, because the holding times Xu et al. adopted are orders of magnitude longer than the solution heat treatment durations used in the current work, the short holding time can reasonably be

assumed to contribute to the stability of the microstructure in the sample treated at 530 °C for 10 minutes, even if the temperature used is considerably high.

Nevertheless, the stored energy available in the starting materials for the work of Xu et al. [84] and the current work are completely different given that a plate of 80 mm thickness and sheets of 2 mm thickness are used, respectively. This difference justifies the investigation carried out in the current work for these solution heat treatment parameters since a higher level of stored energy is expected in the starting material.

The comparison between Fig.4.6 and Fig.4.11 shows that the mode of the distribution for the sample fast heated is reasonably smaller (9 μm –10 μm) than the that of the distribution for the slow heated sample. In addition, the total range of the mean linear intercept length distribution is smaller when using the 200 °C/s heating ramp compared to the slow heating rate ramp. This result aligns with most of the works related to the heating rate effect during solution heat treatments of 7000 aluminium alloys [33,86,87].

For example, Zhang et al. [33] reduced the average grain size of AA7075 2 mm sheets from 57 μm to 44 μm when raising the heating rate from 0.4 °C/s to 15.8 °C/s. For the same starting material, Xu et al. [86] lowered the average grain size from 53 μm to just 15 μm when substituting the circulating air furnace heating with alternate current resistance heating.

Through analysing these varied examples and other related studies, the following can be deduced: the higher the heating rate, the greater the reduction of grain size imparted. In addition, a critical heating rate below which the stored energy cannot sufficiently sustain the recrystallization process must exist. The thermomechanical steps that lead to the production of the starting material to be solutionised also play a vital role in the grain size reduction process.

For example, opposite of the results of this work and the examples cited, Choi et al. [87] found that increasing the heating rate from 3 °C/s to 100 °C/s did not reduce the grain size, which was an average of 17 μm in both cases. This result occurred because the 30 mm billet used as the starting material needed less hot

and cold working to be produced compared to the 2 mm sheets of the other works, therefore leading to a lower density of dislocations in the material.

In conclusion, the adoption of a high heating rate can be used to refine the sample grain structure. Despite not appreciably influencing the strength of the material (GB strengthening does not play a decisive role for 7000 aluminium alloys [79]), the average grain size reduction could help to improve the toughness of the workpieces.

Chapter 5:

Cooling step

This chapter highlights the research findings and the corresponding discussion regarding the optimization of the cooling step. Firstly, it quantifies the microstructural changes in the matrix and grain boundaries (GB) associated with different cooling rates.

Subsequently, it determines the tensile behaviour and corrosion properties under varying cooling rates.

The discussion primarily revolves around identifying the optimal cooling rate that strikes a balance between mechanical and corrosion properties in the workpiece. Furthermore, it aims to establish a connection between the magnitude of the cooling rate and the resulting changes in the microstructure of the samples.

5.1: Results

5.1.1: Microstructural evolution with varying cooling rate

Fig.5.1 displays transmission electron microscopy (TEM) micrographs of samples cooled between iron dies after solution heat treatment (30.7 °C/s of cooling rate) and finally fast-aged.

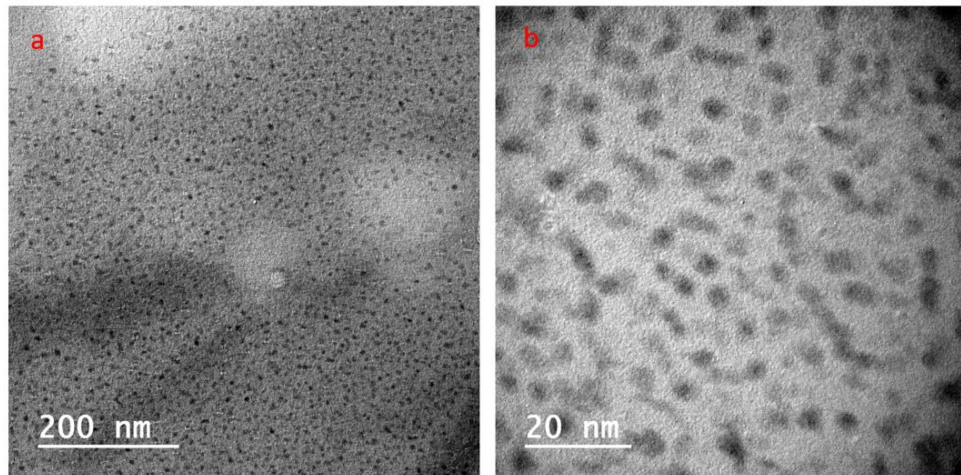


Figure 5.1: Transmission electron microscopy micrographs of samples cooled at 30.7 °C/s after solution heat treatment and fast-aged showing inner matrix precipitates. (a) low magnification, (b) high magnification.

The aluminium matrix looks brighter while the nanometric precipitates appear darker.

Fig.5.2 presents Kratky plots of samples subjected to different average cooling rates after solution heat treatment and then fast aged, while Tab.5.1 summarises the main features calculated from the Kratky plots.

Cooling rate	Pseudo-Guiner radius [°A]	Volume fraction relative to T6 % []
Water quench	24.5	89.2
73.2 °C/s + deformation	28.2	93.4
30.7 °C/s	23.7	84.6

Table 5.1: Summary of the Pseudo-Guiner radii and relative volume fractions calculated from the Kratky plots.

As the sample cooled at 73.2 °C/s was also deformed, its Kratky plot characteristics are influenced by the combined effect of deformation and cooling rate. All the Kratky plots presented display the typical trend with a maximum.

While the sample water quenched and the one cooled between iron dies (30.7°C/s) have almost matching Kratky plots, the HFQ® B-Pillar Kratky plot is slightly shifted toward lower values of q and is characterised by a more pronounced maximum.

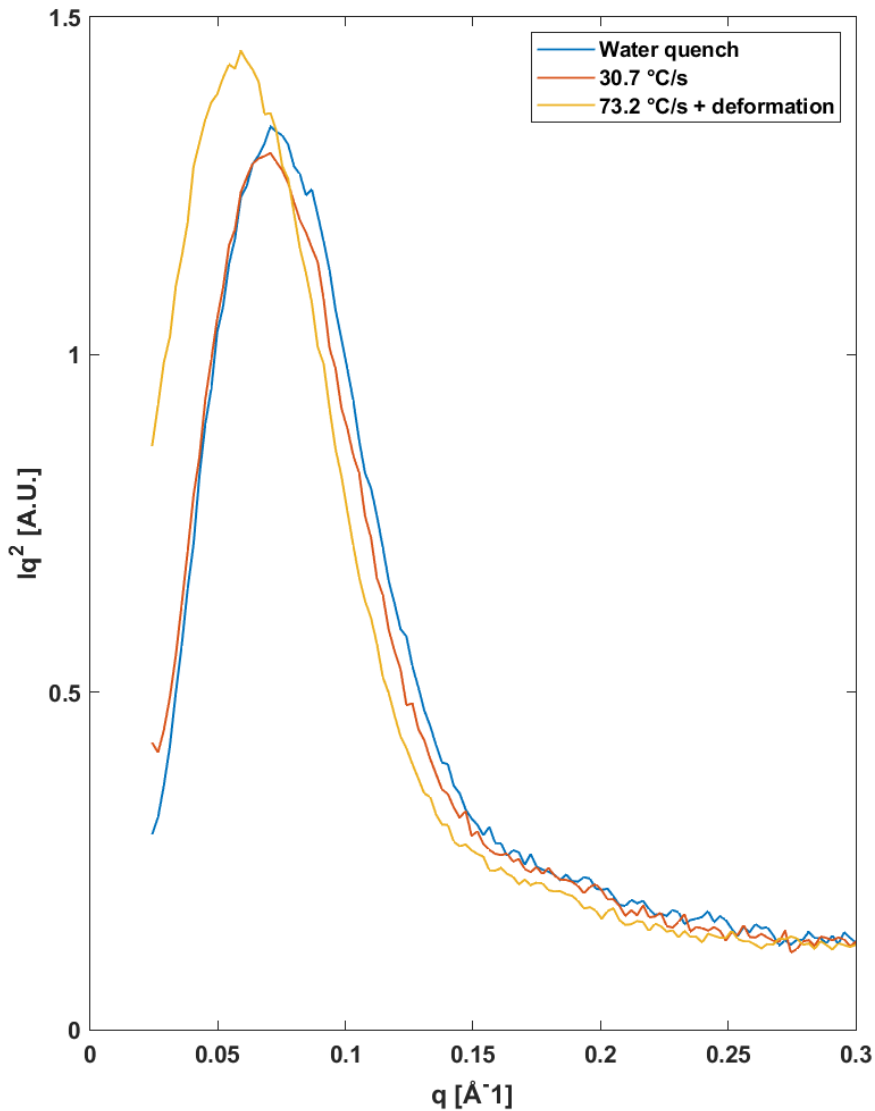


Figure 5.2: Kratky plots of samples subjected to different cooling rates after solution heat treatment and then fast aged. The 73.2 °C/s sample was also deformed during the cooling step.

Consequently, as highlighted in Tab.5.2, the two samples just cooled have very similar Pseudo-Guinier radii, while the sample subjected additionally to deformation has a slightly higher Pseudo-Guinier radius. Similarly, Tab.5.1 shows that the volume fraction of precipitates relative to T6 increases in the following order: 30.7 °C/s, water quench, 73.2 °C/s + deformation.

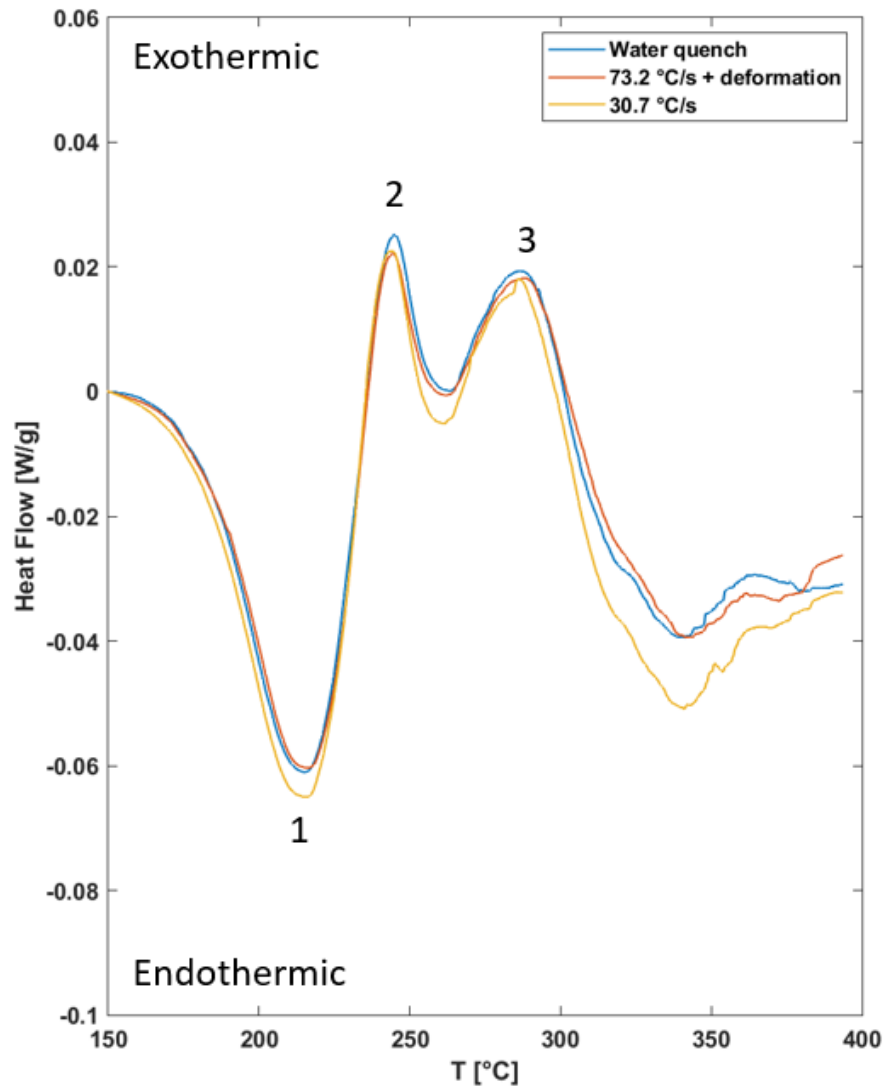


Figure 5.3: Differential scanning calorimetry traces of samples subjected to different cooling rates after solution heat treatment and then fast aged. The 73.2 °C/s sample was also deformed during the cooling step.

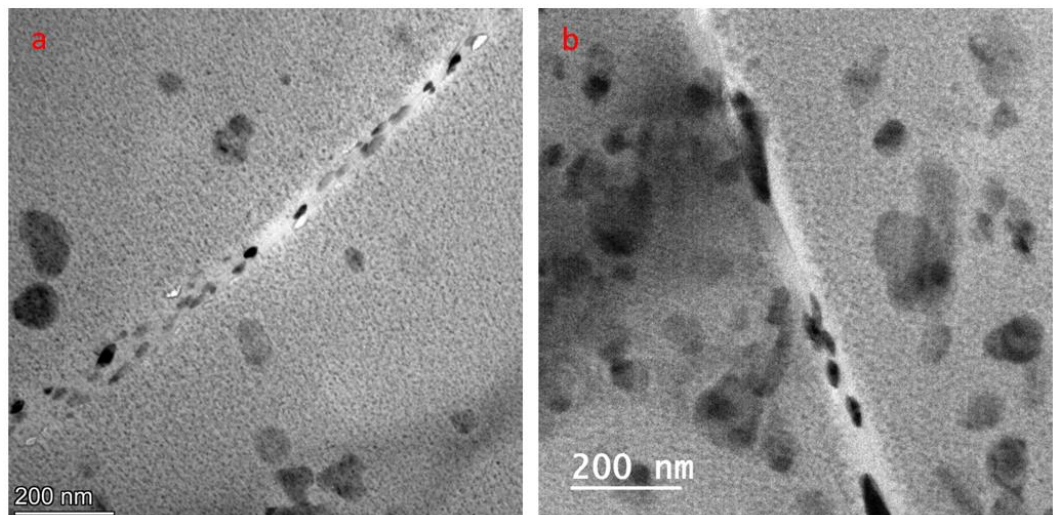


Figure 5.4: Transmission electron microscopy micrographs showing grain boundary microstructures: sample water quenched (a) and sample cooled with iron dies (b).

In Fig.5.3 the DSC traces of samples cooled at different velocities after solution heat treatment and fast aged are presented. As previously mentioned, the

sample cooled with the average rate of 73.2 °C/s was also deformed during the cooling step. All the DSC traces recorded display the endothermic peak '1', which is followed by the exothermic peak '2' and the exothermic peak '3'. It is noticeable that for all the metallurgical conditions tested the DSC traces are almost matching.

Fig.5.4 shows a comparison between the grain boundary microstructure of the sample water quenched (a) and the one cooled between iron dies (b) after solution heat treatment. The grain boundary area is characterised by grain

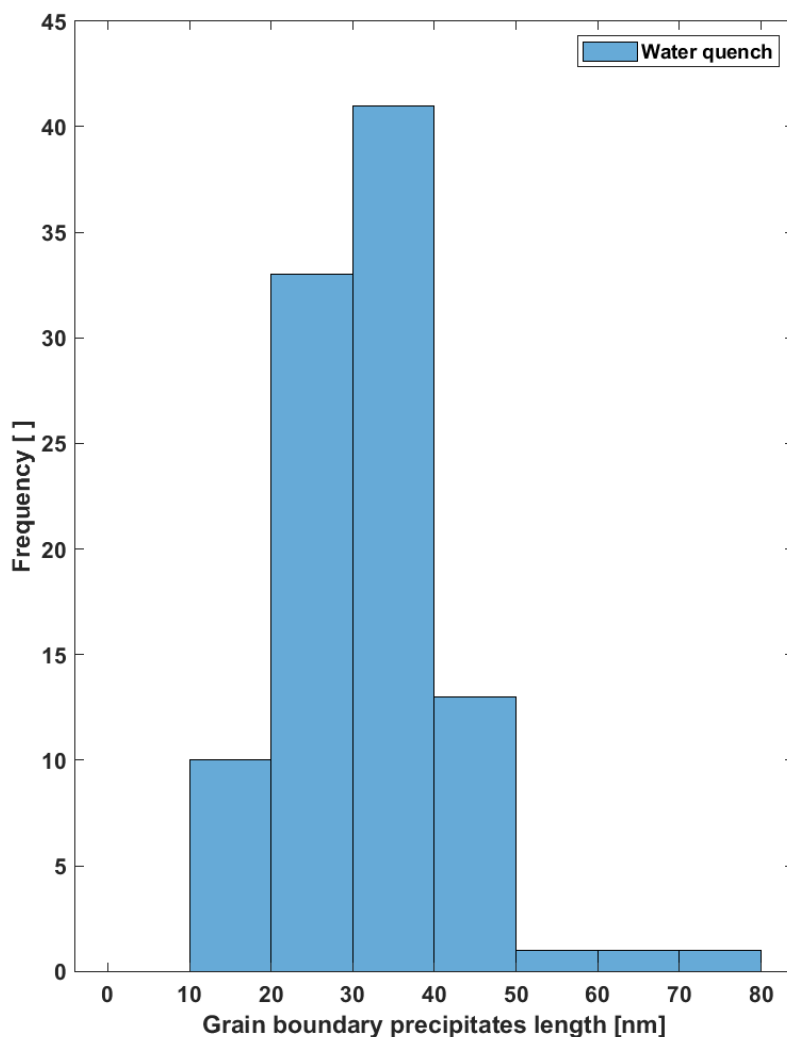


Figure 5.5: Grain boundary precipitate length distribution of the sample water quenched after solution heat treatment and fast aged.

boundary precipitates (GBPs) and precipitates-free zones (PFZs) in both samples, but the GBPs of the sample cooled between iron dies (30.7 °C/s) appear larger and more spaced apart. Large and dark dispersoids are clearly visible in both micrographs and so are the finer matrix precipitates.

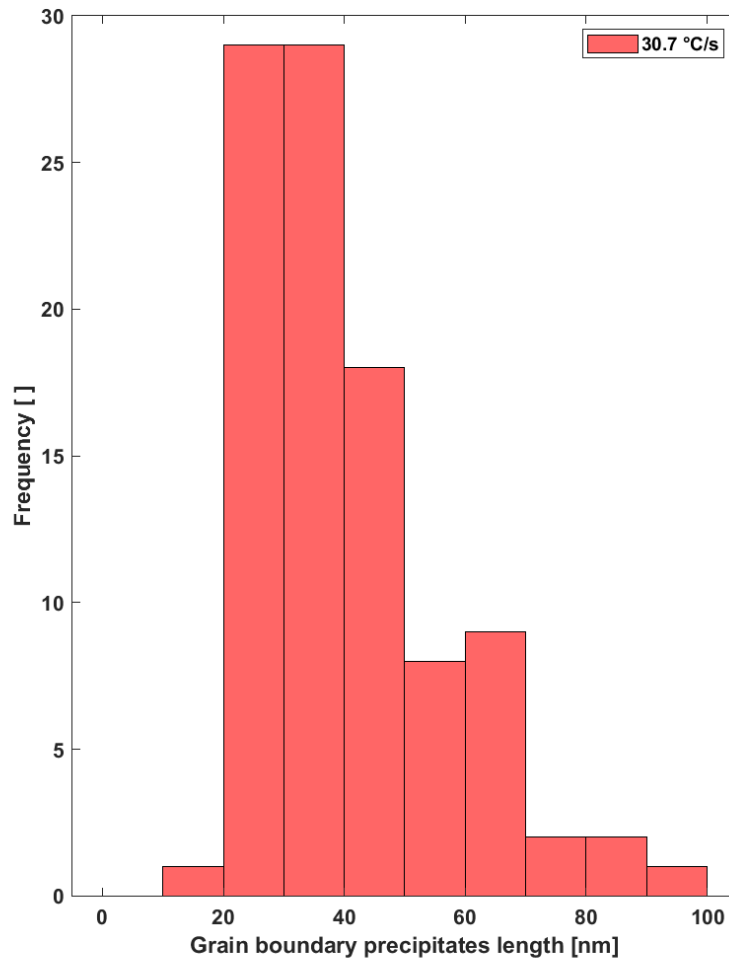


Figure 5.6: Grain boundary precipitate length distribution of the sample cooled with iron dies (30.7 °C/s) after solution heat treatment and fast aged.

In Fig.5.5 the GBP distribution of lengths along the GB of the sample water quenched and fast aged is presented. The distribution is characterised by a nearly symmetrical and single-peaked shape, with the mode of the distribution falling inside the 30 μm – 40 μm bin and with a range comprised between 10 μm and 80 μm .

Cooling rate [°C/s]	Average length	2 σ	Average PFZ length	2 σ
Water quench	32 nm	19.3 nm	36.6 nm	10.6 nm
30.7 °C/s	41.1 nm	34.4 nm	61.4 nm	14.9 nm

Table 5.2: Summary of the average grain boundary precipitate length and average precipitate-free zone length of the sample water quenched and the one cooled at 30.7 °C/s.

Fig.5.6 displays the GBP length distribution of the sample cooled with iron dies (average cooling rate of 30.7 °C/s) and then fast aged. The distribution shows a nearly symmetrical and single peaked shape, where the mode of the distribution falls into the 30 μm – 40 μm bin.

Compared to the water quenched sample, the range of the 30.7 °C/s cooling rate sample distribution is larger (between 10 μm and 100 μm). In addition, the bins in the 50 μm – 80 μm range are more populated than the ones in the water quenched sample distribution.

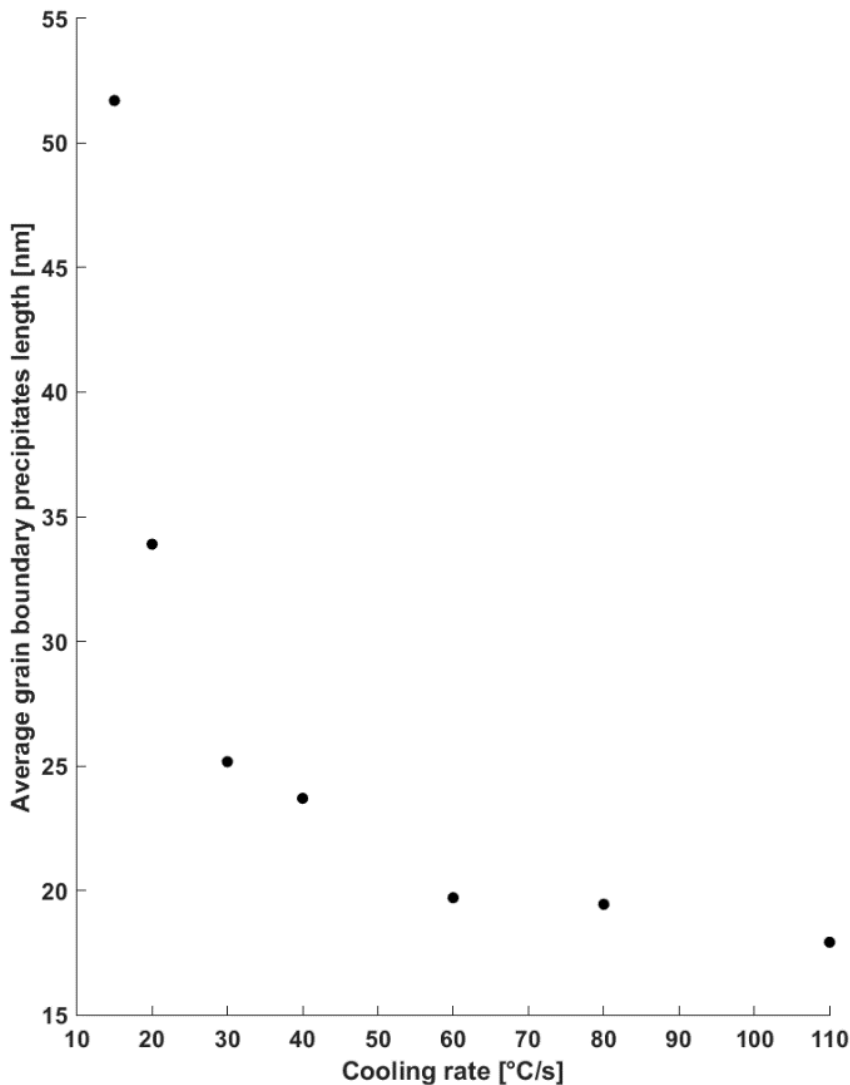


Figure 5.7: Average grain boundary precipitate length calculated via CIPHER model as function of cooling rate.

Tab.5.2 reports the average length of GBPs and the average length of the PFZ for the water quenched and the iron cooled samples. For both the lengths measured, two standard deviations are also recorded. The sample cooled after solution heat treatment at 30.7 °C/s is characterised by a larger average GBPs length and a larger standard deviation. Similarly, this sample displays a higher average PFZ length and standard deviation.

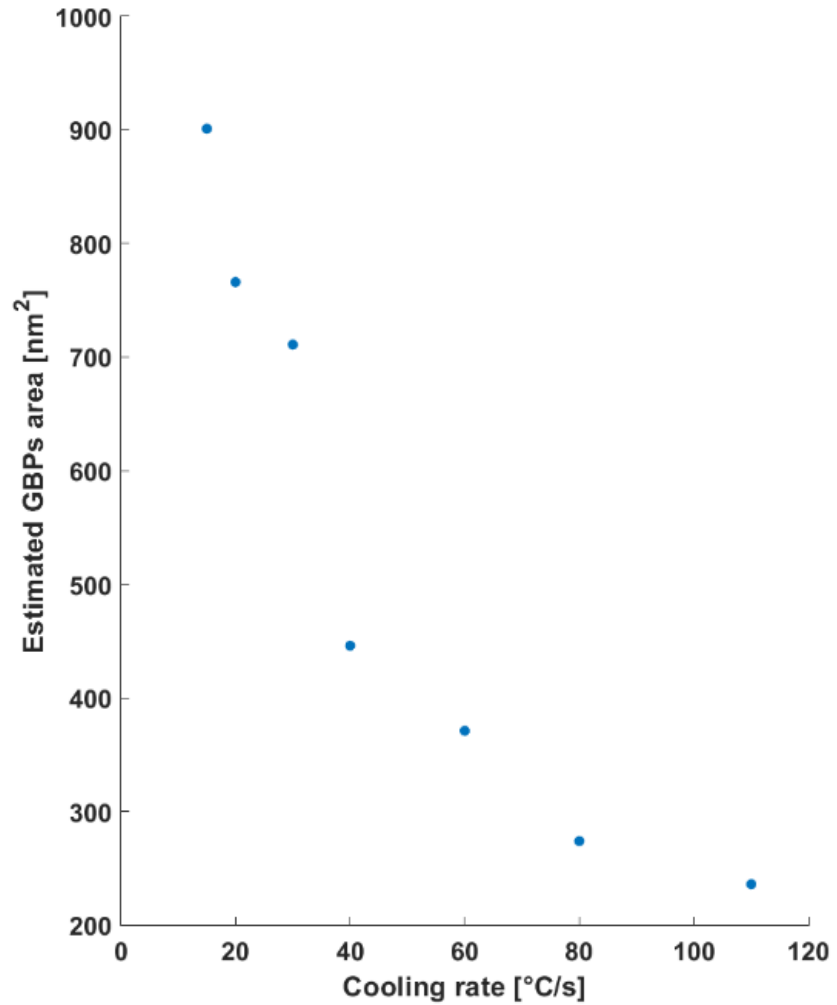


Figure 5.8: GBPs area estimated via CIPHER model as function of cooling rate.

Fig.5.7 shows the average GBP length along the boundary predicted by the CIPHER model (Section 3.5) when monotonically varying the cooling rate from 15 °C/s to 110 °C/s. The trend observed generally suggests that the increase of cooling rate reduces the average length of GBPs, but the magnitude of this reduction is strictly related to the range of cooling rates adopted (i.e. it is non-linear with cooling rate).

In the cooling rate range between 15 °C/s and 30 °C/s, small increases of cooling rate produce large average GBP size reduction. The use of 15 °C/s leads to a predicted average size of around 50 nm, while 30 °C/s to an average predicted GBPs size of 25 nm. In the cooling rate range between 30 °C/s and 60 °C/s, the increase of cooling rate is translated in a less marked reduction of predicted GBP average size, going from 25 nm associated with 30 °C/s to 20 nm linked with 60

°C/s. Finally, in the range of cooling rates between 60 °C/s and 110 °C/s, a raise of cooling rate has little effect on the predicted GBP average size. In this case, the increase of cooling rate from 60 °C/s to 110 °C/s results in the predicted average GBPs size going from 20 nm to roughly 18 nm.

The GBPs area predicted via CIPHER model as function of cooling rate is presented in Fig.5.8.

When increasing the cooling rate from 15 °C/s to 40 °C/s, the GBPs area is greatly reduced (from 900 nm² to roughly 445 nm²). Instead, in the cooling rate range between 40 °C/s and 110 °C/s, the area reduction linked with the cooling rate increase is predicted to be less marked, going from around 445 nm² (40 °C/s) to roughly 235 nm² (110 °C/s).

Tab.5.3 shows the average elemental composition of GBPs as a function of cooling rate predicted via CIPHER model. While the magnesium concentration is stable at about 32 at% for all the cooling rates explored, both the aluminium and copper concentration rise with increasing cooling rate.

Cooling rate [°C/s]	Al [at %]	Zn [at %]	Mg [at %]	Cu [at %]
15	15.5	44.1	32.6	7.8
20	16.4	43.1	32.6	7.9
30	17.6	42.4	32.1	7.9
40	17.7	41.8	32.3	8.2
60	18.0	41.6	32.2	8.2
80	18.1	40.8	32.4	8.7
110	20.0	39.3	32.0	8.7

Table 5.3: Average elemental composition of grain boundary precipitates as function of cooling rate predicted via CIPHER model.

Interestingly, the increase of the aluminium atomic percentage is much more marked than the copper one, about a 5 at% increase across the whole cooling rate range compared roughly to a 1 at% increase. Consequently, the GBPs zinc concentration decreases from about 44 at% to roughly 39 at% when changing the cooling rate from 15 °C/s to 110 °C/s.

5.1.2: Tensile properties with varying cooling rate

Fig.5.9 shows the stress-strain curves of samples cooled at different rates after solution heat treatment and fast-aged.

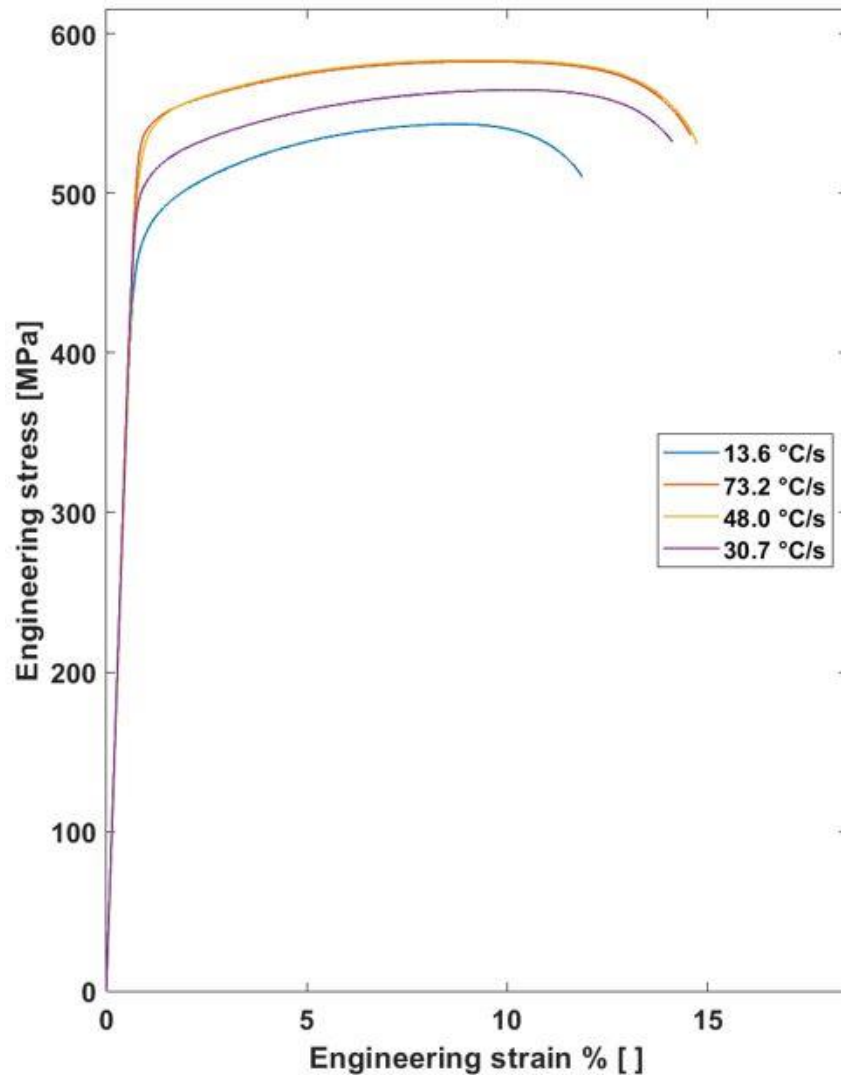


Figure 5.9: Stress-strain curves of samples cooled at different rates after solution heat treatment and then fast-aged.

While both yield strength and ultimate tensile strength show a maximum for both the two highest cooling rates adopted (73.2 °C/s and 48.0 °C/s), both these tensile properties steadily decrease when a lower cooling rate is used, reaching their lowest point in case of 13.6°C/s. When decreasing the cooling rate in the range investigated, the elongation to break decreases as well: from a value of roughly 14% (common to the three highest cooling rates) to nearly 11% for the 13.6 °C/s cooling rate. The average work hardening rate increases when reducing the cooling rate.

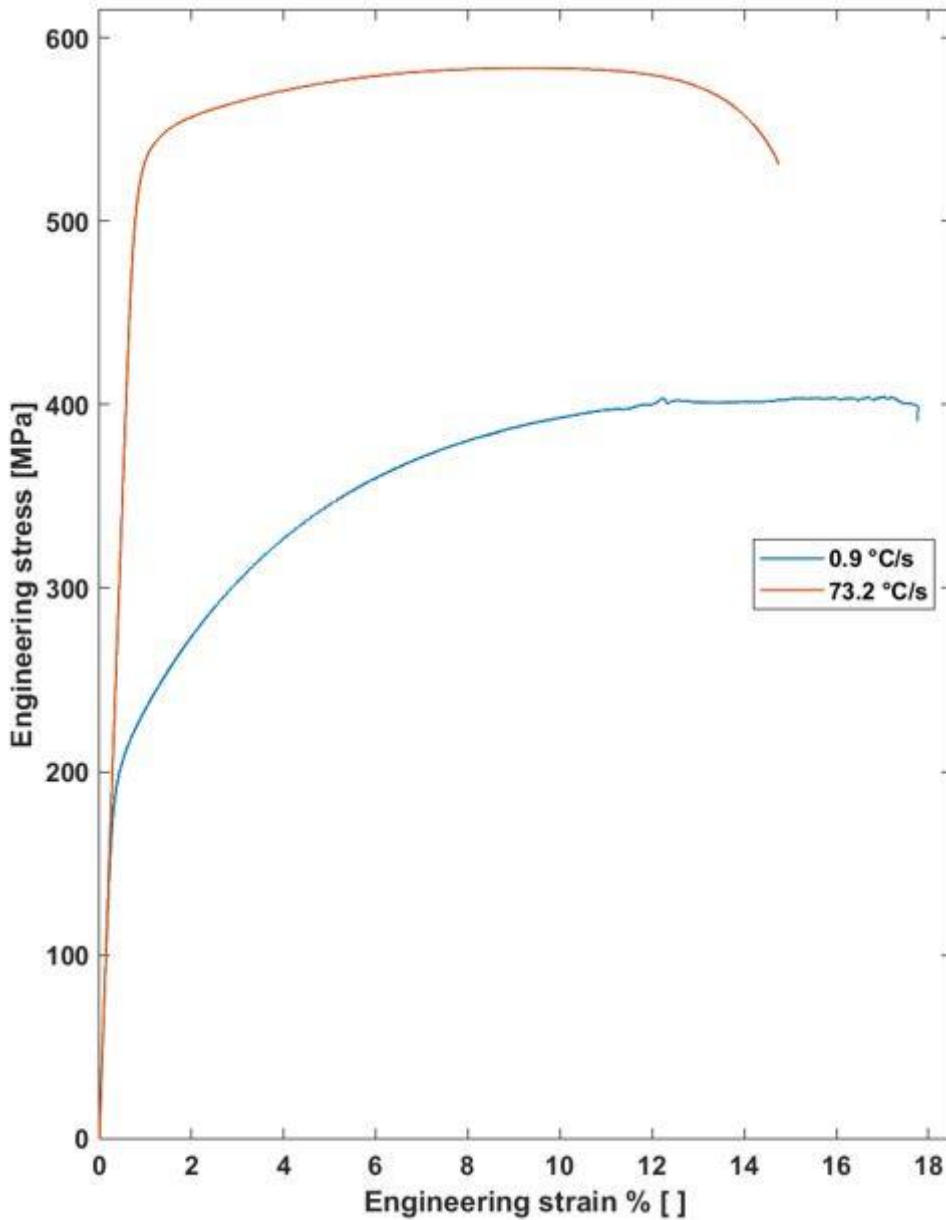


Figure 5.10: Stress-strain curves of the sample cooled at 73.2 °C/s and of the sample air cooled (0.9 °C/s). Both samples were fast aged after the cooling phase.

Cooling rate [°C/s]	Yield strength [MPa]	Ultimate tensile strength [MPa]	Elongation to break % []
73.2	537	582	14.6
48.0	531	582	14.7
30.7	502	564	14.1
13.6	467	543	11.8
0.9	207	404	17.8

Table 5.4: Summary of the main tensile properties of samples subjected to different cooling rates after solution heat treatment and then fast aged.

Fig.5.10 displays the stress-strain curve of the sample cooled at the average rate of 73.2 °C/s compared to the one of a sample air cooled (0.9 °C/s on average). While both yield strength and ultimate tensile strength are drastically reduced

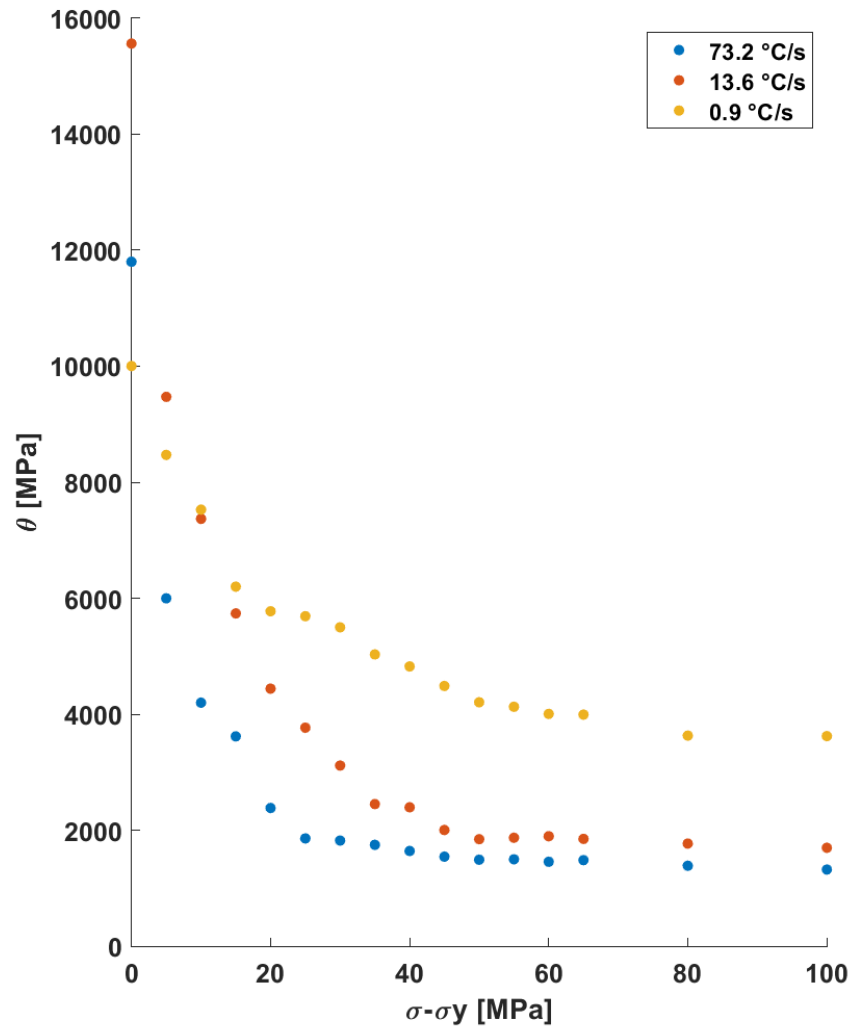


Figure 5.11: Kocks-Mecking plots of samples differently cooled and then fast aged.

when applying the air cooling, the elongation to break improves from 14.6% to 17.8%. The tensile properties of all the samples tested are also summarised in Tab.5.4. Fig.5.11 shows Kocks-Mecking plots of the samples cooled at 73.2 °C/s, 13.6 °C/s and 0.9 °C/s. The strain hardening rate θ varies with true stress following the same functionality among all the cooling rates studied: θ decreases more consistently in the first range of true stresses close to yielding and then less appreciably in the subsequent range of higher true stresses. When comparing the strain hardening rate among the different cooling rates, it can be deduced that the lowest the cooling rate, the highest the strain hardening rate in the whole range of true stresses explored.

5.1.3: Corrosion properties with varying cooling rate

Tab.5.5 presents the time to failure of U-bend samples exposed to a salt-spray fog environment as function of cooling rate. Samples water quenched failed after 15, 17 and 20 days, while samples cooled at 73.2 °C/s resisted 28, 32 and 33 days in the salt spray chamber before breaking. While not showing a clear failure, samples cooled at 48 °C/s displayed deep cracks on the main stressed surface. No failure or cracks were associated with the samples cooled at 30.7 °C/s or 13.6 °C/s. Similarly, the sample held at 400 C° for 10 seconds and then quenched did not fail after the 60 days of exposure to the aggressive environment.



Figure 5.12: Water quenched and fast aged U-bend sample after 20 days of exposure to the salt spray fog environment.

Cooling rate [°C/s]	Time to failure [days]
Water quench	15, 17, 20
73.2	28, 32, 33
48.0	Visible cracks
30.7	No
13.6	No

Table 5.5: Time to failure of U-bend samples exposed to salt spray environment as function of cooling rate after solution heat treatment. Samples were fast aged after the cooling phase.

Fig.5.12 shows a water quenched U-bend sample after 20 days of exposure to the salt spray fog environment. The deep crack that caused the sample failure is clearly noticeable on the main stressed surface and is orthogonal to the main stress direction.

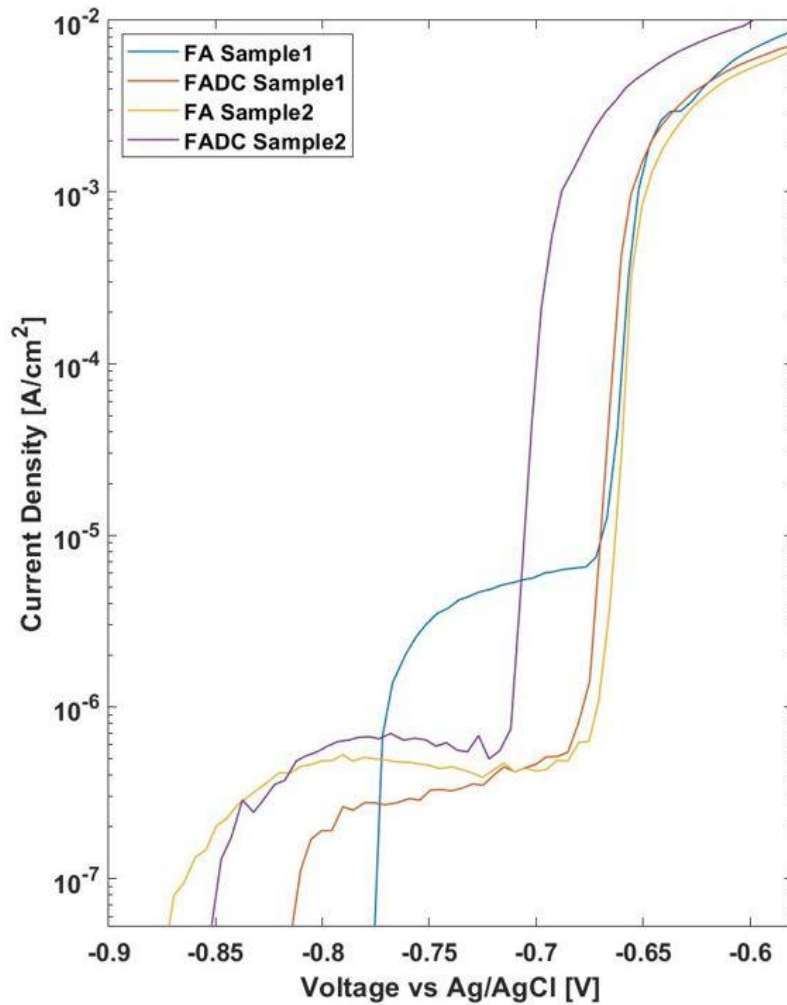


Figure 5.13: Comparison between the anodic polarisation of samples water quenched and fast-aged and samples die-cooled and fast-aged.

Fig.5.13 shows the relation between electrostatic potential and current density during anodic polarisation of samples solution heat treated, water-quenched and

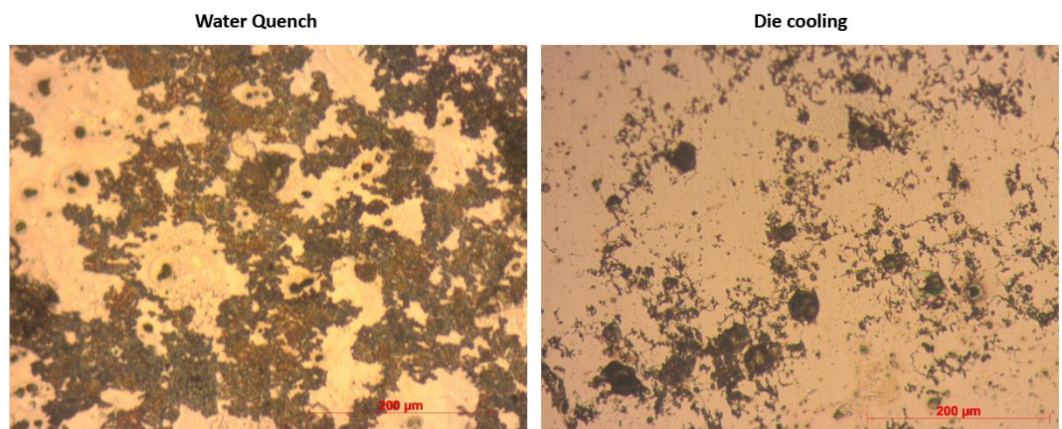


Figure 5.14: Optical microscopy micrographs showing micro-surfaces of samples corroded after anodic polarisation. Fast aged sample (left) is compared with the fast aged die-cooled sample (right).

fast-aged (FA) compared to samples solution heat treated, die-cooled and fast-aged (FADC).

The two samples exhibit a comparable behaviour concerning the current density evolution within the investigated potential range. However, due to the variability observed in the recorded traces for the FA and FADC samples, it is not possible to establish a direct link between anodic polarization parameters and SCC performance.

Fig.5.14 presents a comparison between OM micrographs showing corroded micro-surfaces after anodic polarisation of the FA and FADC samples. While the micro-surface of the sample water quenched (FA) is characterised by a corrosion damage more uniformly distributed, the sample die-cooled displays corrosion attack mostly located near GBs.

5.2: Discussion

5.2.1: The effect of cooling rate on matrix precipitation

While the previous chapter discussed the results related to the solution heat treatment step, this one focuses on the cooling step. This section specifically addresses how the cooling rate affects the matrix precipitate characteristics.

The use of water quenching or die-cooling resulted in a very similar Pseudo-Guinier radius and relative precipitate volume fraction for the samples subjected to small-angle x-ray scattering (Tab.5.1). Therefore, the different cooling rates imparted appeared to not appreciably modify the nanometric matrix precipitation after aging.

Zhang et al. [123] obtained Kratky plots for aged AA7055 samples as a function of a wide range of linear cooling rates (between 0.01 K/s and 300 K/s). When considering cooling rates comparable to those in Fig.5.2, the correspondent Kratky plots in Zhang et al.'s study were almost identical and likewise for the calculated values of Pseudo-Guinier radius and volume fractions. For this reason, the conclusions suggested from Fig.5.2 align with Zhang et al.'s work.

The features of the Kratky plots in Fig.5.2 also align with the study of Graf et al. [161], who reported that, for cooling rates higher than 30 K/s, the precipitate volume fractions calculated via SAXS experiments using aged AA7075 samples are almost the same.

In addition, the analysis of Fig.5.3 supports the conclusion that the cooling rates used did not appreciably modify the nanometric matrix precipitate characteristics. In fact, the DSC traces in Fig.5.3 are almost superimposed on each other regardless of the different cooling rates adopted.

When studying quench-induced precipitation of 7000 aluminium alloys, most of the DSC traces are recorded as a function of the cooling rate during the cooling step [44,95]. This choice makes it challenging to compare Fig.5.3 with the literature since the DSC traces in this study are obtained for aged samples. Despite this challenge, this result matches what has already been suggested

based on the SAXS experiments and the conclusions of various studies in the literature.

The idea that a cooling rate reduction below the critical value reduces the available solute concentration and hinders the refinement of the nanometric matrix precipitates is deeply rooted in the literature [31,35]. However, the results presented in this study and the analysis of the related works in the literature suggest that a cooling rate range exists where GB microstructures can vary appreciably but that the nanometric matrix precipitate distribution is only marginally affected.

This concept has important implications because it opens the possibility of more effectively optimizing the core properties of 7000 aluminium alloys. In fact, the development of GBPs without a linked coarsening of the matrix precipitates results in an overall desirable final microstructure [121].

Instead, for values of the cooling rate below the range proposed, both GBPs and nanometric matrix precipitates grow substantially, and the homogeneous growth of the large η phase in the matrix is also possible [60,155]. This subdivision in different cooling rate ranges could rationalise some of the experimental results available in the literature (Fig.5.15), although a few discrepancies remain.

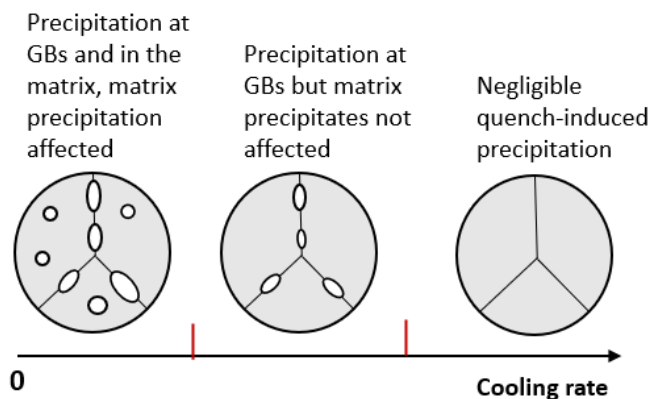


Figure 5.15: Proposed cooling rate ranges and their schematic effect on samples' microstructure.

For example, through the examination of SAXS data and Transmission electron microscopy (TEM) micrographs, Deschamps et al. [44] concluded that no changes in the nanometric precipitation characteristics occur even when using an extremely low cooling rate (about 0.1 °C/s). In this example, it is possible that the presence of dispersoids containing Zr may significantly reduce the quench

sensitivity of the alloy when compared to the AA7075 of this study, which only contains Cr-bearing dispersoids

Fig.5.2 and Tab.5.1 also provide information about the effect of deformation on the matrix precipitation kinetics. Because both the Pseudo-Guinier radius and the relative volume fraction of precipitates are higher in the sample subjected to the forming step than in those obtained for the sample just cooled, the deformation process can be assumed to have accelerated the matrix precipitation kinetics since all the samples were also artificially aged the same way.

Exploring the effect of deformation on the matrix precipitation kinetics is the focus of numerous contributions in the literature but falls beyond the scope of this study. A simple explanation of this result can be given when considering that the dislocation density increase promoted by deformation can also improve the diffusion rate of solute elements and speed up the precipitation events [162].

5.2.2: The effect of cooling rate on the GB microstructure

When comparing the length distributions of GBPs between the two cooling rates employed (Fig.5.5 and Fig.5.6), although the average length slightly increases with lower cooling rates, the range of the lengths recorded increases the most. This experimental observation can be explained by considering that the temperature range in which quench-induced precipitation occurs is enlarged when the lowest cooling rate is applied. For this reason, the extended superimposition of nucleation and growth of GBPs determines the higher heterogeneity of the final dimensions.

This result confirms the findings of Liu et al. [46], who recognized the increase of GBP size variability as one of the main features caused by the cooling rate decrease. This concept is rarely reported in the literature; most of the studies that focus on the effect of the cooling rate on microstructural features use TEM micrograph observations without a statistical approach for the evaluations [37,44,119].

Based on direct observation, most of the studies cited reported that the average length of GBPs increases with a decreasing cooling rate [44,119,122]. However, the length distributions linked in this study show that the average GBP main length changes little when moving from water quenching to die-cooling.

Overall, establishing a general functionality between the GBP average length and cooling rate is challenging since most of the relevant studies can hardly be related to each other due to the different quench sensitivities of the alloys and the dissimilar cooling rates investigated.

Even with these intrinsic difficulties, proposing that the average GBP length increases exponentially with decreasing cooling rate is reasonable. For example, Liu et al. [46] showed that the GBP lengths are similar when using room temperature water (1510 °C/s) and boiling water (72 °C/s) as quenching media, but the average GBP length is consistently higher in cases of air cooling (3 °C/s). Similarly, an exponential trend of the average GBP length with a decreasing cooling rate could be inferred from the work of Xiao et al. [39], in which the GBP

average lengths were similar when using water (90 °C/s) or polyalkylene glycol (30 °C/s) but reasonably higher with the use of quenching oil (5 °C/s).

The little change in the average GBP length reported in this study could also fit the exponential trend proposed, but how cooling rates lower than the die-cooling rate affect the average GBP length must be explored. While the main goal of the CIPHER model was to predict the microchemistry variations occurring at GBs depending on the cooling rate used, the model was also used to calculate the average GBP length and area developed as a function of cooling rate (Fig.5.7 and Fig.5.8). For both these parameters, an exponential trend with a decreasing cooling rate seems plausible.

The increase of the GBP area with a decreasing cooling rate is also experimentally well-known and commonly observed in numerous studies [44,46]. Similarly, the literature consolidates around the idea that the width of the precipitate-free zones (PFZs) increases with a decreasing cooling rate [44,46,95]: the measurements obtained in Tab.5.2 align with this notion. The PFZ width increase is usually explained by considering that the greater quench-induced precipitation linked to a lower cooling rate depletes the GB adjacent regions from solute atoms [44]. The absence of precipitates in the PFZs could also be explained by assuming a depletion of vacancies as they annihilate at GBs, but because PFZs are commonly found around dispersoids as well, the explanation supporting the depletion of solute atoms seems more plausible [44].

In general, the use of a statistical approach to evaluate GB microstructures with varying cooling rates ultimately revealed features that are hard to detect when performing only a direct observation of TEM micrographs. The use of length distributions might therefore benefit the 7000 aluminium alloys metallurgy and contribute to a better prediction of the final properties of these alloys.

5.2.3: The effect of cooling rate on tensile properties

Based on the information presented in Fig.5.9 and Tab.5.4, it can be observed that the tensile strength of samples cooled at a rate faster than 48°C/s is maintained. However, using a cooling rate below this threshold appears to result in a reduction of both the yield strength and the ultimate tensile strength of the tested specimens.

Generally, the decrease of yield strength when lowering the cooling rate is a well-established trend found in the literature [35,119]. This trend is usually explained considering that quench-induced precipitation lowers the quantity of solute atoms in the matrix and promotes a less refined distribution of matrix precipitates. The characteristics of the matrix precipitate distribution are not optimised to hinder the dislocation movements, and thus, the yield strength is not maximised.

An additional explanation is that the concentration of quenched-in vacancies from the solution heat treatment temperature is reduced when applying a low cooling rate, and this fact slows down the diffusion process of alloying elements and inhibits the initial clustering process that causes precipitates to nucleate [35,122].

Interestingly, the sample cooled at 30.7°C/s displays worse tensile properties than the other samples cooled at faster rates. Based on the microstructural investigation carried out in this work, however, the matrix microstructure of the die-cooled (30.7°C/s) sample matches that of the sample water-quenched.

This observation could be explained in different ways. It might be that the techniques used to characterise the matrix microstructure (SAXS, TEM, DSC) did not detect the small microstructural changes responsible for the different tensile behaviours of the die-cooled specimen. For example, some large η phase precipitates might not have been identified in the matrix during the microstructural examination. Even if the overall solute atom concentration was not appreciably influenced by these precipitates, the deformation behaviour of the material slightly changed.

If the matrix microstructures of the 30.7 °C/s and the water-quenched samples substantially match, then the different tensile behaviour must be linked to the microstructural differences at GBs: the different width of the PFZs and the different size distribution of GBPs.

However, in the literature, the microstructure at GBs is commonly reported to mostly influence the fracture toughness of the specimens and not their strength levels [163,164].

From the tensile tests performed, a second interesting finding emerges: the elongation to break of the samples first decreases when reducing the cooling rate and then increases again (0.9 °C/s sample). In the literature, the effect of the cooling rate on the elongation to break or fracture toughness in 7000 aluminium alloys is still under discussion. Some studies report an increase in ductility when lowering the cooling rate [35], while other studies suggest a decrease in ductility concomitant with a cooling rate decrease [119,163].

Because similar microstructural changes are expected in the material when applying a low cooling rate or in the case of overaging, the study of the effect of the elongation to break can be also supported by studies that focus on the aging step.

The findings in this work and the related existing literature can be rationalised when considering the study of Kirman et al. [164]. In that study, the fracture toughness of AA7075 samples originated from the superimposed effect of the specimen strength and the average GBP size. Following explanation of this research group, macroscopical fracture during tensile tests is the result of microcracks and microvoids coalescence. Therefore, the harder microvoids nucleation and growth, the higher the ductility of the samples under tensile loading.

When solely considering the effect of the alloy strength, the elongation to break would increase with a decreasing yield strength. In fact, when the yield strength diminishes, the extent of the stress concentration ahead of a microcrack that can be relaxed by plastic deformation increases: microcracks propagate less easily, which results in a higher fracture toughness.

Instead, when solely considering the effect of the GBP length, the higher the average size, the lower the resultant elongation to break.

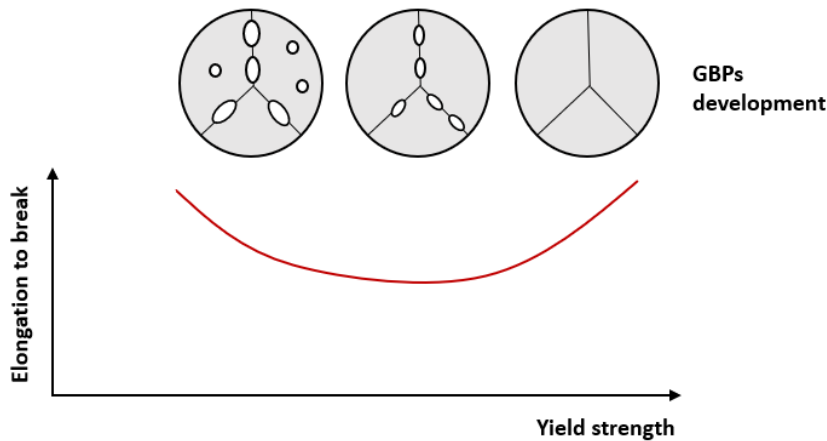


Figure 5.16: Elongation to break variation as a function of yield strength and GBP development, as explained by Kirman et al. [164]. While yield strength decreases with decreasing cooling rate, GBP development is higher with a decreasing cooling rate.

According to Kirman et al., since microvoids nucleate at the GBPs/matrix interface, coarser GBPs would provide a wider interface and a higher probability of microvoid nucleation [164].

Applying this theory (Fig.5.16) to explain the findings of this work suggests that, in the wide cooling rate range between the water-quenched sample and the 13.6 °C/s workpiece, the effect of the GBP size controls the elongation to break rather than the yield strength. In fact, the average GBP size increases with a decreasing cooling rate, and consequently, the elongation to break diminishes as well.

Instead, when considering the 0.9 °C/s sample, the reduction of yield strength is so consistent that it overpowers the influence of GBP average length on fracture toughness. This event results in an improved elongation to break compared with the other slow-cooled samples.

The studies related to the effect of cooling rate on the elongation to break found in the literature are sometimes contradictory, meaning that this phenomenon is not still well-understood. When following the explanation provided by Kirman et al. [164], the existing literature about this topic might be rationalised considering that the different thermo-mechanical history, alloy chemistry and cooling path realised in these studies could highlight only the effect of strength or the effect

of the GBPs on the elongation to break, missing the overall picture. Fig.5.11 shows that the regime work hardening rate is constant with increasing true stress for all the cooling rates considered. Following the classification of Cheng et al. [117], the Kocks-Mecking plots derived show a non-linear functionality between θ and true stress in the stage 3 range. In addition, the Stage 3 work hardening rate increases when lowering the cooling rate, and this event is explained in the literature as an effect of the matrix precipitate distribution variation [35,117].

In fact, the quench-induced precipitation associated with a lower cooling rate reduces the quantity of solute atoms in the matrix and changes the precipitate formation process during subsequent aging. The lower availability of solute atoms then results in a less refined and coarser distribution of precipitates, which interacts with dislocations more predominantly through the bowing mechanism rather than the shearing mechanism. The looping of dislocations around precipitates generates an additional contribution to the dislocation accumulation during plastic deformation, which overall results in a higher work hardening rate [35,117]. The final elongation to break recorded is strongly correlated with the work hardening rate values. Specifically, samples with high values of work hardening rate exhibit reduced strain at necking, which enhances their resistance to necking and ultimately improves their final elongation to break.

The findings presented in Fig.5.11 align with the work of Scharifi et al. [35]. In their study, the use of a higher tool temperature during the cooling step of AA7075 samples reduced the cooling rate applied and caused a higher work hardening rate during plastic deformation. Instead, in the work of Dumont et al. [163], the work hardening rate differences highlighted with varying cooling rate are marginal, even when exploring a wide range of this parameter (between 850 K/s and 7 K/s). This finding could be attributed to the differences in quench sensitivity between AA7075 used in this work and AA7050 used in Dumont et al.'s study. AA7050 is expected to be much less quench sensitive than AA7075 due to difference in its composition and dispersoid phase.

5.2.4: The cooling rate optimisation for the HFQ® process

Based on Fig.5.9 and Tab.5.4, the tensile strength of the samples cooled above 48 °C/s is preserved, while cooling with a rate of 30.7 °C/s causes roughly a 5% yield strength loss. Overall, a cooling rate reduction from the maximum achievable to 30.7 °C/s has only a mild influence on tensile properties.

In addition, Tab.5.5 informs that only samples cooled at a rate equal to or below 30.7 °C/s had sufficient SCC resistance to not fail during exposure in the salt-spray chamber. For this reason, when fast aging (FA) is set as the aging strategy, a cooling rate of 30.7 °C/s would constitute a good compromise to optimise both yield strength and SCC of the workpieces (Tab.5.6).

Cooling rate	Yield strength	Average time to failure in salt-stray chamber
73.2 °C/s	537 MPa	32
30.7 °C/s	502 MPa	no
13.6 °C/s	467 MPa	no

Table 5.6: Summary of the core properties as function of cooling rate reported in the Results section and selection of the optimised cooling rate.

Because the final properties of the aluminium panel are a function of both the cooling rate and the aging strategy selected, the optimal cooling rate window might vary when adopting a different aging schedule. Therefore, the relevance of this finding is to propose the ability to reach acceptable mechanical and corrosion properties in the HFQ® process via a controlled reduction of the cooling rate from the maximum achievable.

Focusing on the cooling rate optimisation is an attractive option that could greatly benefit the overall productivity of the HFQ® process. The overaging strategies usually implemented to ensure an acceptable level of stress corrosion cracking (SCC) resistance are highly time-consuming and could be avoided by using a controlled reduction of the cooling rate during the cooling step. This approach would also be beneficial because the aging step of the HFQ® process is heavily constrained due to the necessity of the final paint-baking step.

The optimal cooling rate found in this study is in good agreement with the work of Chen et al. [37], in which a similar optimisation process for the cooling step

was carried out. For AA7085, the researchers similarly concluded that an intermediate cooling rate of 50 °C/s slightly worsens the tensile properties of the specimens but greatly improves their SCC resistance. Yuan et al. [38] also documented a similar optimised compromise between the strength and SCC resistance. They studied the combined effect of pre-strain and cooling rate on the tensile properties and SCC resistance of low-Cu containing 7000 aluminium alloys.

Even if the reduction of the cooling rate seems like an attractive solution for the HFQ® process, the fine control of the heat transfer during the forming step is technologically challenging. For this reason, using a precooling step followed by an isothermal holding in HFQ® before the deformation and final cooling stage is an attractive option that might be easier to realise and is worth exploring.

In this study, while the samples held at 400 °C for 10 seconds and then cooled were not tensile tested, the samples resisted during the full scheduled period in the salt-spray chamber, therefore displaying satisfying SCC resistance.

Huang et al. [165] also reported a positive outcome when assessing the corrosion properties of 7000 aluminium alloy samples subjected to precooling and the isothermal holding step. Meanwhile, Ou et al. [166] concluded that a feasible optimisation of tensile properties and SCC resistance for AA7050 with this alternative cooling path is possible.

Regardless the studies cited, the optimisation of the precooling and isothermal holding strategy for the heat treatment of 7000 aluminium alloys remains a topic under discussion in the literature and requires more contributions.

5.2.5: Simulated GBP composition with varying cooling rate

Tab.5.3 shows that GBPs are enriched with Al and Cu atoms at the expense of Zn when increasing the cooling rate. More specifically, the substitution of Zn with Al is approximately five-fold larger than the one with Cu atoms (roughly 5 at% increase of Al in MgZn₂ precipitates compared to 1 at% increase of Cu when considering the whole cooling rate range explored).

While the effect of GBP copper enrichment on corrosion properties has already received attention in the literature [43,106], the influence of the increase of Al concentration in MgZn₂ has been overlooked. The incorporation of Al atoms in GBPs makes the η phase resemble the matrix more, and this event could reduce the electrochemical activity at GBs.

The rise of Cu concentration in GBPs with increasing cooling rate is similarly reported in the studies of Chen et al. [37] and Li et al. [167], but disagrees with the results of Song et al. [108], who reported a decrease of Cu concentration with increasing cooling rate. The discrepancies found in the literature might be related to the experimental difficulties to obtain compositional information of GBPs [110]. Overall, a consolidated explanation of this trend has not yet been provided.

Temperature	200 °C	250 °C	300 °C	350 °C
D_{Al}	2.77E-19 m ² /s	5.64E-18 m ² /s	6.79E-17 m ² /s	5.49E-16 m ² /s
D_{Cu}	7.97E-20 m ² /s	2.12E-18 m ² /s	3.19E-17 m ² /s	3.10E-16 m ² /s
D_{Zn}	1.21E-18 m ² /s	2.28E-17 m ² /s	2.56E-16 m ² /s	1.96E-15 m ² /s
$D_{Zn}-D_{Al}$	9.35E-19 m ² /s	1.71E-17 m ² /s	1.88E-16 m ² /s	1.41E-15 m ² /s
$D_{Zn}-D_{Cu}$	1.13E-18 m ² /s	2.06E-17 m ² /s	2.25E-16 m ² /s	1.65E-15 m ² /s

Table 5.7: Diffusion coefficients of Al, Cu and Zn in aluminium as a function of temperature [168].

The higher degree of Al and Cu substitution when increasing the cooling rate might be explained by the differences in the diffusion rates of the solute elements involved (Tab.5.7).

Tab.5.7 shows that the diffusion coefficient differences between Zn and Al or Zn and Cu increases at low temperature compared to high temperature. When a high cooling rate is used, the formation and growth of GBPs occur at just the most kinetically relevant temperatures for quench-induced precipitation (temperatures close to the nose temperature of the associated time-temperature-property (TTP) diagram [93]).

The range of temperatures where GBPs can develop is expanded in case a low cooling rate is adopted. Specifically, precipitation during cooling is believed to be preferentially unlocked in a low temperatures range (temperatures lower than the nose temperature) when a low cooling rate is applied. Following this hypothesis, because in this low temperature range mentioned the diffusion coefficient differences between Zn and Cu or Zn and Al atoms are exacerbated (the Zn atoms diffusing much faster than Cu or Al atoms), the formed η phase is characterised by a higher concentration of Zn and a lower concentration of Cu and Al.

Instead, when a high cooling rate is applied, precipitation in the low temperature range mentioned is locked, so most of the nucleation and growth events can occur only in the high temperature range close to the nose temperature.

As displayed in Tab.5.7, diffusion coefficient differences among the elements considered are less marked at high temperature. Therefore, the precipitates incorporate more Al and Cu in their structure compared to the low cooling rate case.

The understanding of the functionality between the cooling rate and the elemental modifications of GBPs might be a crucial element to understand the SCC specifically and the corrosion property evolution of 7000 aluminium alloys during heat treatments generally.

5.2.6: The effect of cooling rate on corrosion properties

Tab.5.5 suggests that reducing the cooling rate increases the SCC resistance of the specimens exposed to the salt-spray environment. From the GB microstructural analysis carried out (Fig.5.5, Fig.5.6), the cooling rate reduction slightly increases the average GBP length, but more consistently increases the variability of the GBP dimensions observed (the presence of larger GBPs becomes more statistically relevant).

The cooling rate reduction also widens the precipitate-free zones (Tab.5.2). In addition, based on the TEM micrograph qualitative observation, the interspacing among GBPs appears to also increase. Decreasing the cooling rate slightly reduces the atomic fraction of Cu and Al in the η phase at GBs, while the Zn fraction is slightly raised compared to the high cooling rate case (Tab.5.3).

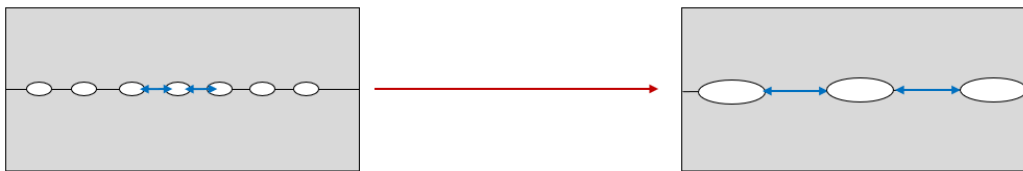


Figure 5.17: Schematic representation of the correlation between GBP area increase and increased disconnection among GBPs.

The increase of GBP sizes has been correlated with the increase of interspacing among GBPs (Fig.5.17) [37,54]. Thus, when considering the range of cooling rates studied, the developed disconnection of GBPs matured at low cooling rates would break the electrochemical active path at GBs and slow down the rate of anodic dissolution [37,54].

The reduction of the anodic dissolution rate would also decrease the velocity of the cathodic reactions and therefore the release of atomic hydrogen at the crack tip [170]. The release and interaction of the atomic hydrogen with the alloy microstructure causes hydrogen embrittlement [97]. In addition, larger GBPs (Fig.5.8) would constitute better traps for hydrogen: these atoms would recombine more easily into molecular hydrogen and lose their potential to promote SCC [37,54].

The breakdown of the electrochemical path caused by the increased disconnection of GBPs should also be based on the hypothesis that the segregation of solute atoms at GBs is considerably reduced, helping the electrochemical isolation of the active phases at GBs. This hypothesis would be plausible if the evolution of GBPs drags solute atoms not just from PFZs but also from the adjacent GBs. Some evidence of this concept already exists in the literature, pointing out that the GB segregation of solute atoms is reduced when GBPs develop during prolonged aging [43]. In fact, the segregation of Mg and Zn at GBs has already been described as a possible source of SCC susceptibility for 7000 aluminium alloys [171,172].

The increase of the Cu concentration of η precipitates at GBs has been linked to the improvement of SCC susceptibility in numerous studies [37,43,106]. The higher Cu fraction in η precipitates decreases the potential difference of this phase with the surrounding matrix, reducing the driving force of anodic dissolution [37,43,106]. Even if this observation has been mostly overlooked, the incorporation of Al atoms in GBPs would also likely decrease the anodic dissolution rate as the η phase becomes more like the aluminium matrix.

Because the simulation data obtained (Tab.5.3) show that the atomic fraction of Cu and Al present in $MgZn_2$ decreases when reducing the cooling rate, this microchemistry variation should worsen the SCC resistance of the samples tested. However, the results acquired from the U bend SCC tests confirm a reduction of the SCC susceptibility linked to a lower cooling rate. The same trend is similarly reported in the studies of Chen et al. [37] and Knight et al. [173].

In the current study, the estimated depletion of Cu (Tab.5.3) when lowering the cooling rate is small (around 1 at% across the whole cooling rate range). Therefore, for AA7075 sheets, the disconnection and enlargement of GBPs presumably played a more important role in influencing the SCC resistance of the specimens tested rather than the Cu concentration at GBs [37].

When trying to correlate cooling rate and SCC resistance, that different phases can nucleate and grow at GBs as a function of the cooling path used should also be considered [95,120] as the process could modify final corrosion properties achieved by the workpieces. For example, Zhang et al. [95] reported a more

consistent presence of S phase (Al_2CuMg) in conjunction with η phase when reducing the cooling rate during the heat treatment of AA7150 samples.

Chapter 6:

Aging step

This chapter presents the research findings and the accompanying discussion on the optimisation of the aging step. Firstly, it showcases the results pertaining to the development of a compact aging strategy for HFQ[®]. Subsequently, it quantifies the microstructural changes and variations in tensile and corrosion properties during each thermal step of the strategy. Additionally, the final properties achieved through the developed strategy are compared to industrially relevant tempers for 7000 aluminium alloys.

The discussion section explores the connection between the thermal steps devised, the evolution of the microstructure, and the resulting tensile and corrosion properties. Furthermore, the feasibility of implementing the strategy in the HFQ[®] process is also addressed.

6.1: Results

6.1.1: The design of the RRDA strategy

Fig.6.1 shows the average Vickers Hardness as function of total aging time of samples solution heat treated, water-quenched and then aged with a two-step aging strategy.

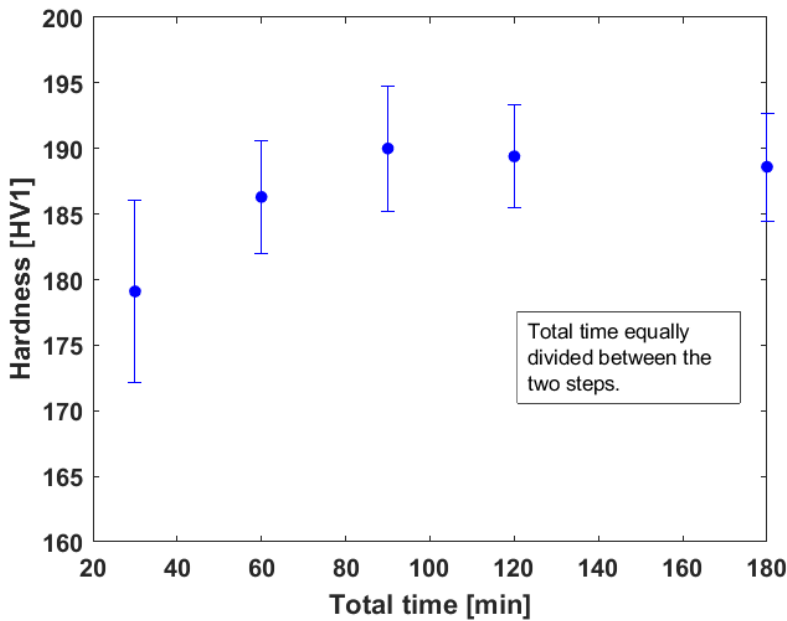


Figure 6.1: Vickers hardness as function of the total duration of the two-step aging strategy performed after solution heat treatment and water-quenching.

The total duration of the aging strategy is equally divided between the first step at 120 °C and the second step at 175 °C. The hardness increases monotonically with increasing holding time in the duration range between 15 minutes and 90 minutes and then it stays roughly constant when a longer total time is applied up to 180 minutes.

Fig.6.2 displays the Vickers Hardness of samples held at 220 °C for variable retrogression times after being subjected to the optimised two-step sequence (120 °C for 45 minutes followed by 175 °C for 45 minutes).

The plot of hardness as function of retrogression time presents a relative minimum correspondent to the holding time of 120 seconds, followed by a maximum of nearly 190 HV1 at 240 seconds (4 minutes). When retrogression

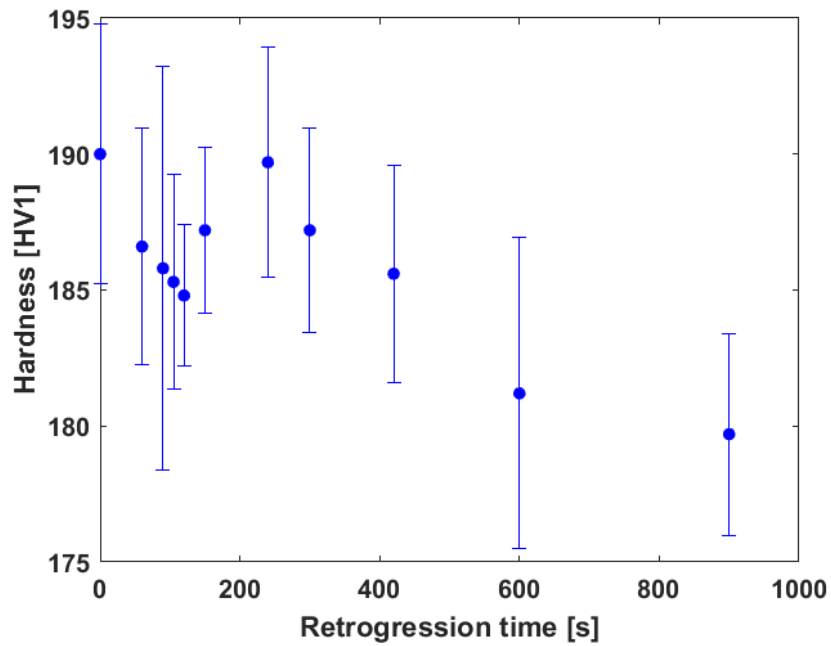


Figure 6.2: Vickers Hardness as function of retrogression time during Step3.

times longer than 4 minutes are applied, the hardness levels decrease steadily throughout the whole remaining duration range. It is important to acknowledge that the significant magnitude of the standard deviation in the measurements shown in Figure 6.2 necessitates caution when interpreting the reported trend.

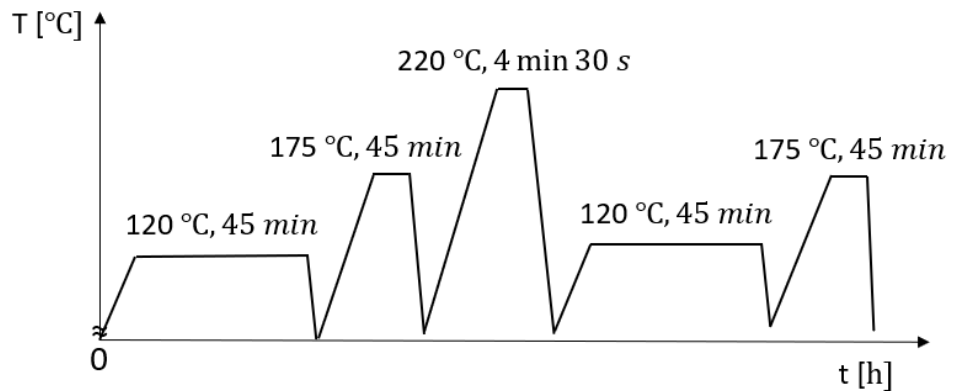


Figure 6.3: Time-temperature profile of the retrogression and reaged double-aging strategy.

Fig.6.3 presents the time-temperature profile of the retrogression and reaged double-aging (RRDA) strategy. The RRDA aging schedule consists of applying an optimised two-step aging sequence (120 °C for 45 minutes followed by 175 °C for 45 minutes) to reach peak hardness and subsequently use a retrogression step (220 °C for 4 minutes and 30 seconds). After the retrogression step, reaging is imparted through the same two-step aging procedure.

6.1.2: Microstructural evolution during the RRDA steps

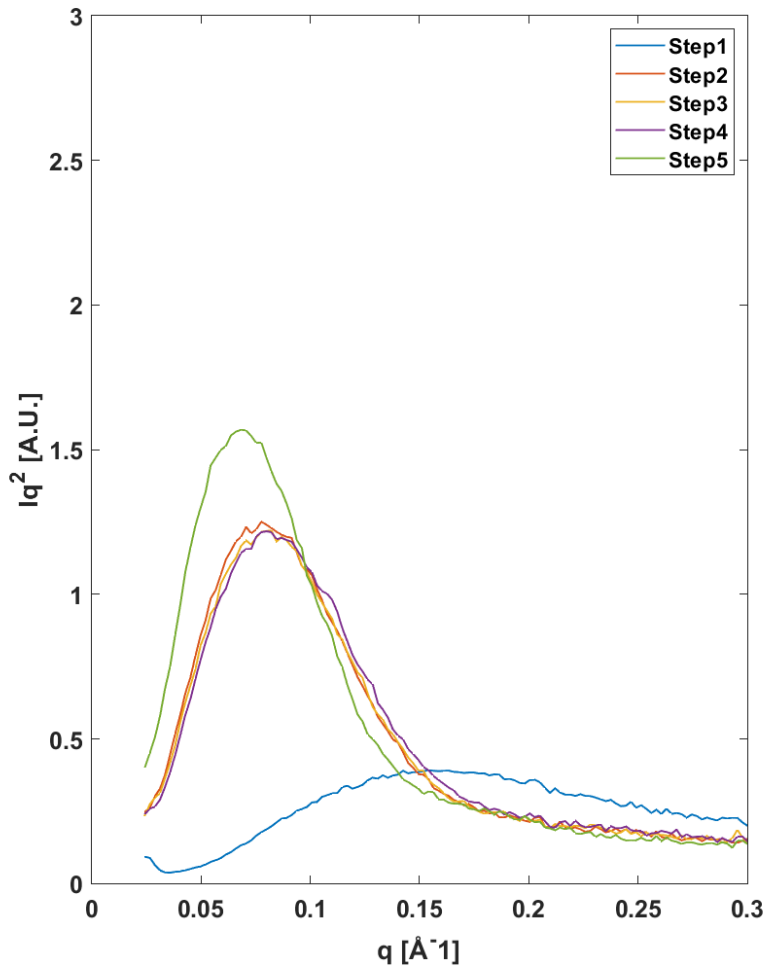


Figure 6.4: Kratky plots of samples subjected to the retrogression and reaged double aging strategy.

Fig.6.4 displays Kratky plots derived from small angle x-ray scattering measurements (Section 3.4.11) of specimens subjected to the RRDA strategy where the sequence is carried out and interrupted at different steps.

In addition, Tab.6.1 summarises the main features calculated from the Kratky plots.

Step	Pseudo-Guiner radius [°A]	Volume fraction relative to T6% []
1	10.9	72.7
2	22.3	95.4
3	21.7	93.7
4	21.7	95.9
5	25.3	102.9

Table 6.1: Summary of the Pseudo-Guiner radii and relative volume fractions calculated from the Kratky plots.

All the samples are characterised by a trend including a maximum, but while after Step1 the maximum is shifted towards higher values of q and appears broader, for all the other steps the maximum is better defined, less broad and located in a lower q range.

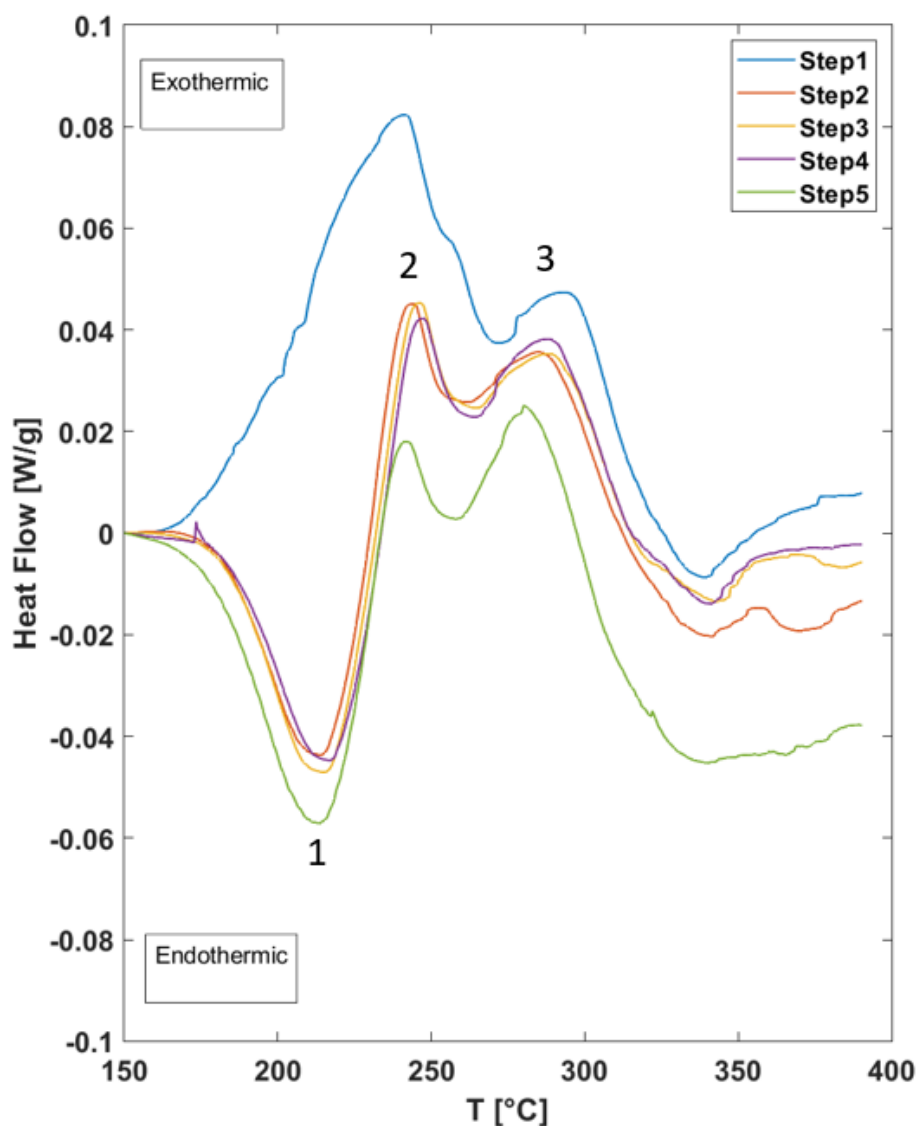


Figure 6.5: Differential scanning calorimetry traces of samples subjected to the sequence of steps of the retrogression and reaged double aging strategy.

The Kratky plots of Step2, Step3 and Step4 are almost matching, while the Step5 one shows a more prominent maximum for a slightly lower q value. From the calculations linked to the Kratky plots (Tab.6.1), it is possible to deduce that both the Pseudo-Guinier radius and relative volume fraction of precipitates increases when progressing from Step1 to Step5. In fact, Step1 is characterised by a Pseudo-Guinier radius of 10.9 \AA and a volume fraction of precipitates relative to T6 equal to 72.7%. The same parameters are equal to 25.3 \AA and 102.9% for

Step5. Owing to the almost matching Kratky plots of Step2, Step3 and Step4, also their Pseudo-Guinier radius and relative volume fractions are substantially matching, being both intermediate between the ones of Step1 and Step5.

Fig.6.5 shows the DSC traces of samples aged via the RRDA strategy where the sequence is interrupted at different steps.

Besides Step1, all the remaining specimens display in their traces the endothermic peak '1' followed by the exothermic peak '2' and the exothermic peak '3'. All the samples show a broad endothermic event in the final high temperatures range (between 300 °C and 400 °C). Instead, the Step1 trace is characterised by a consistent exothermic event in the temperature range of peak '1', which displays a maximum at roughly 230 °C, which is similar to the peak '2' maximum temperature of the other specimens. Besides this difference, the remaining Step1 DSC trace is qualitatively similar to those of the others metallurgical conditions tested.

Step2, Step3 and Step4 are characterised by almost matching DSC traces, while Step5 differs from those samples only in the endothermic peak '1' being deeper and the exothermic peak '2' and peak '3' being less prominent. Finally, the temperature of the endothermic peak '1' is slightly higher in Step2, Step3 and Step4, roughly 215 °C, while it is closer to 210 °C for Sample5.

6.1.3: Tensile properties of the RRDA Steps

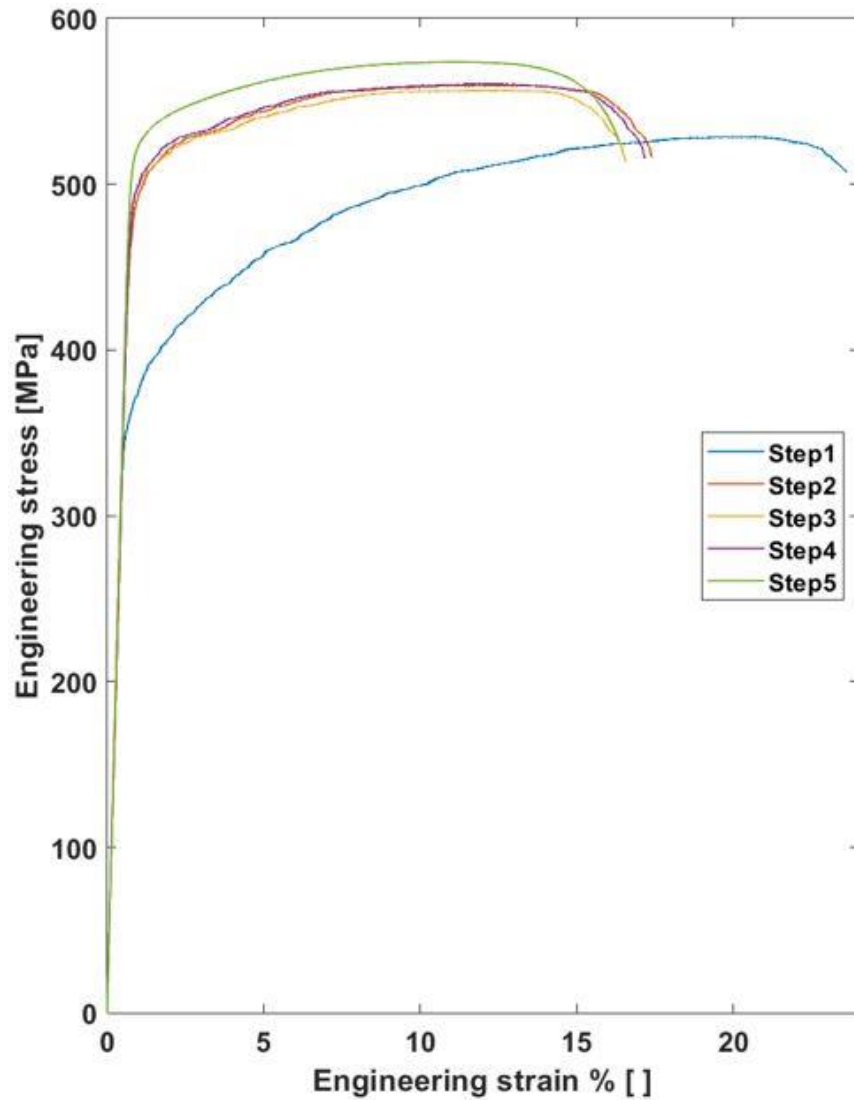


Figure 6.6: Relationship between engineering stress and strain of samples subjected to the retrogression and reaged double aging strategy.

Step	Yield strength [MPa]	Ultimate tensile strength [MPa]	Elongation to break % []
1	405	528	23.6
2	487	559	17.3
3	495	556	16.5
4	495	560	17.2
5	519	573	16.3

Table 6.2: Summary of the main tensile properties of samples subjected to different steps of the retrogression and reaged double aging strategy.

In Fig.6.6 the stress-strain curves of samples subjected to each of the RRDA sequence steps are presented; the tensile properties linked to Fig.6.6 are also summarised in Tab.6.2. Both the yield strength and the ultimate tensile strength increase when progressing from Step1 to Step5: from 405 MPa of yield strength

and 528 of ultimate tensile strength for Step1 to 519 MPa and 573 MPa for Step5.

It is also observed that the tensile properties of Step2, Step3 and Step4 are very similar to each other. The elongation to break of Step1 (23.6%) is considerably higher than the one of the other steps (around 16%-17%). When analysing qualitatively the stress-strain curves in Fig.6.6, it is also possible to deduce that, while the work hardening rate of Step2, Step3 and Step4 is qualitatively similar, it greatly differs for Step1, being substantially higher.

Tab.6.3 shows a summary of the tensile properties of samples subjected to the sequence of RRDA steps and then naturally aged (NA) for 3 months.

While the increase of yield strength and ultimate tensile strength with natural aging is below 5% for each one of the RRDA step, the elongation to break remains approximately constant.

Step	Yield strength [MPa]	Ultimate tensile strength [MPa]	Elongation to break % []
1 + NA	416	562	22.8
2 + NA	509	573	16.4
3 + NA	511	575	16.7
4 + NA	513	575	15.9

Table 6.3: Summary of the tensile properties of samples heat treated via retrogression and reaged double aging steps and naturally aged for 3 months.

6.1.4: Stress corrosion cracking resistance of the RRDA steps

Tab.6.4 displays the time to failure of U-bend samples exposed to salt-spray environment after Step1, Step2 and Step5 of the RRDA strategy.

Step	Time to failure [days]
1	1, 1, 1
2	6, 9, 9
5	35, 36, 38

Table 6.4: Average time to failure of U-bend samples exposed to salt-spray environment after Step1, Step2 or Step5 of the retrogression and reaged double aging strategy.

Samples subjected just to Step1 failed on average after just 1 day, while samples where the aging strategy was interrupted with Step2 resisted to the aggressive environment without breaking for 9 days on average. After the samples underwent all the 5 steps, their resistance to SCC improved further, as their time to failure reached on average 36 days.

6.1.5: Microstructure of RRDA samples compared to relevant industrial tempers

Fig.6.7 shows TEM micrographs of samples solution heat treated, water-quenched and then aged with the RRDA strategy.

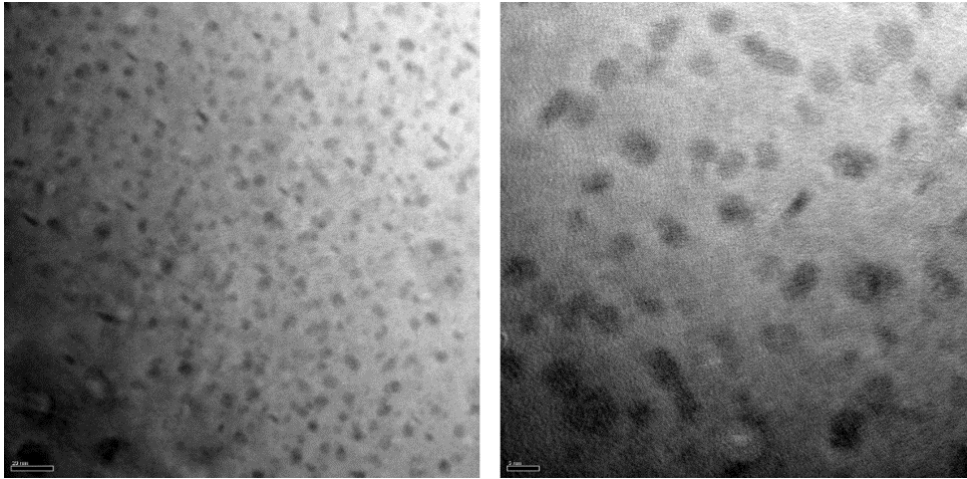


Figure 6.7: Transmission electron microscopy micrographs showing the matrix microstructure of samples aged via the retrogression and reaged double aging strategy. The right-hand portion of the figure (scale 5 nm) is the magnification of the left-hand portion (scale 20 nm).

The nanometric precipitates are characterised by higher contrast than the aluminium matrix.

Kratky Plots of the samples subjected to the different aging strategies are presented in Fig.6.8, while Pseudo-Guinier radii and precipitate volume fractions (Section 3.4.11) relative to T6 are summarised in Tab.6.5.

Temper	Pseudo-Guinier radius [nm]	Volume fraction relative to T6 % []
T6	1.7	100
FA	2.4	89.2
RRDA	2.5	102.9
T73	4.2	107.8

Table 6.5: Summary of the Pseudo-Guinier radii and relative precipitate volume fractions calculated from the Kratky plots for the different aging strategies studied.

The T73 temper has the highest volume fraction of precipitates relative to T6 (107.8%), but this value could be due to a marked compositional change of the precipitates in the T73 temper with respect of the other tempers. T73 shows also the largest Pseudo- Guinier radius (4.2 nm). Both FA and RRDA have a smaller and similar Pseudo- Guinier radius between 2 and 3 nanometres, but RRDA has a substantially higher precipitate volume fraction when compared to FA, 102.9%

against 89.2%. Lastly, the T6 temper is characterised by the smallest Pseudo-Guinier radius, 1.7 nm.

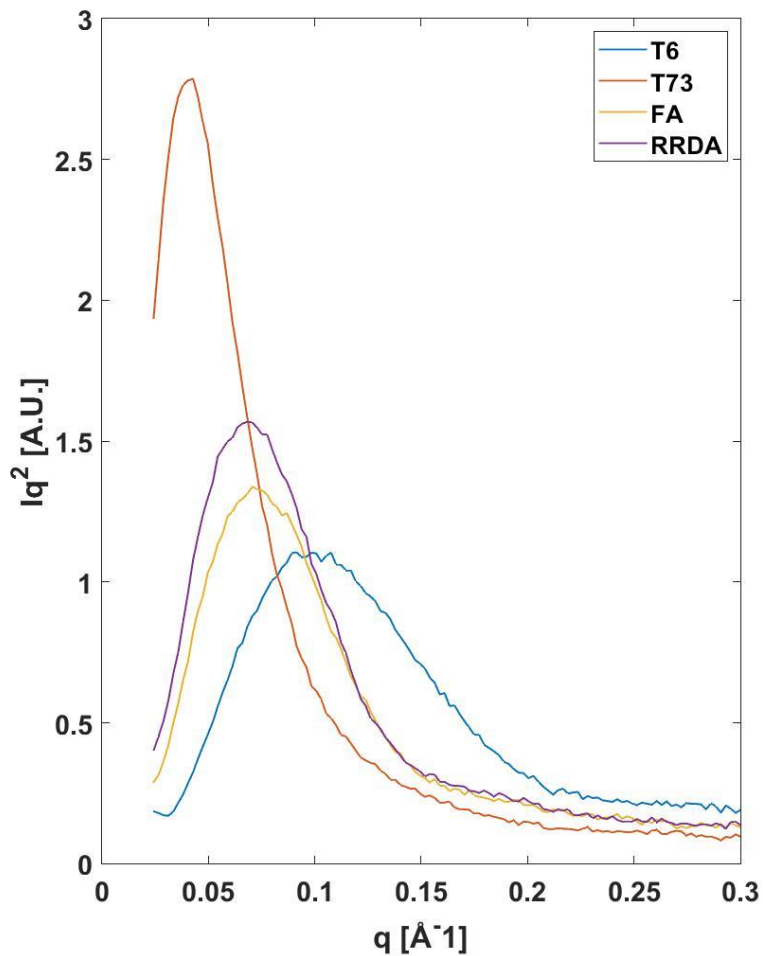


Figure 6.8: Kratky Plots of the samples subjected to the different aging strategies investigated.

DSC traces for the different aging strategies used are displayed in Fig.6.9.

All the tempers are characterised by the low temperature endothermic peak '1', where the temperature associated with these peak increases when going from the T6 temper to the FA, RRDA and finally the T73 temper. In addition, the magnitude of this endothermic event is much more pronounced in the T6 than in the other tempers studied. After peak "1", all the samples experience a superimposition of endothermic and exothermic reactions. With exception of the T73 temper, which shows only a single exothermic peak, this superimposition of thermal events creates the exothermic peaks '2' and '3' for the other metallurgical conditions investigated. The heat flow associated with the exothermic peaks '2' and '3' is higher for the T6 temper than in the FA and RRDA tempers, for which these maxima have similar magnitudes. In this range of

temperatures, the T73 temper is characterised by a single exothermic peak of lower magnitude than the FA and RRDA tempers. All samples are also

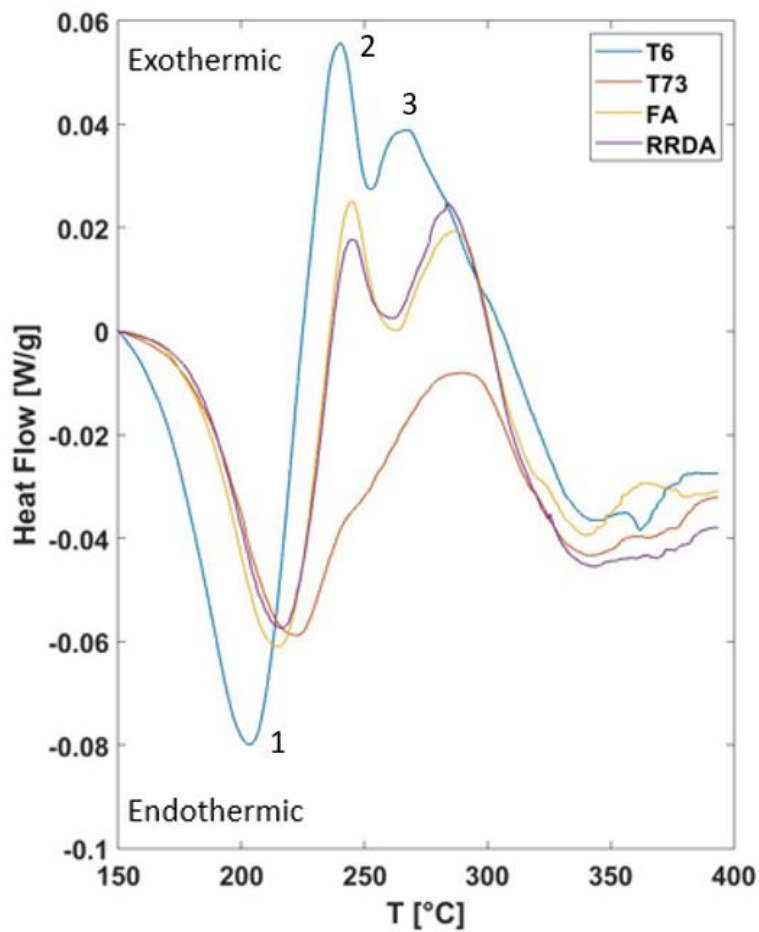


Figure 6.9: Differential scanning calorimetry traces of the T6, T73, retrogression and reaged double aging and fast aged samples.

characterised by a broad endothermic event in the temperature range between 300 °C and 400 °C. Fig.6.10 shows a comparison among the GBs microstructures of the T6, RRDA and T73 samples.

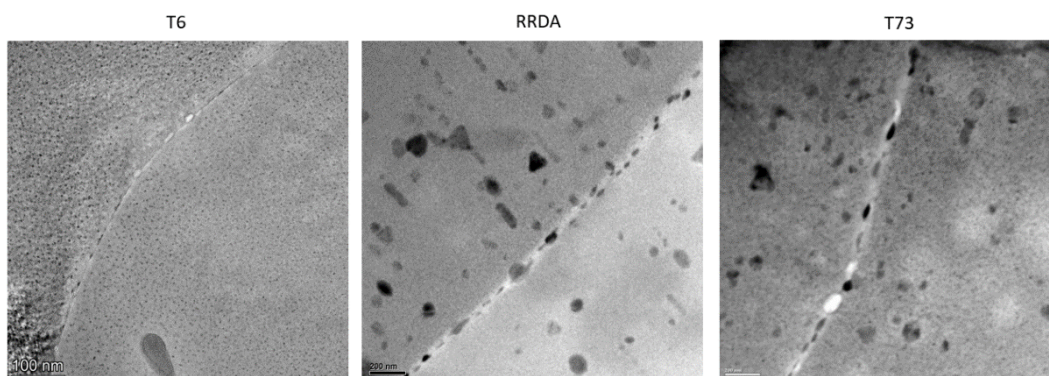


Figure 6.10: Comparison among the transmission electron microscopy micrographs of the T6, retrogression and reaged double aging and T73 grain boundary microstructures.

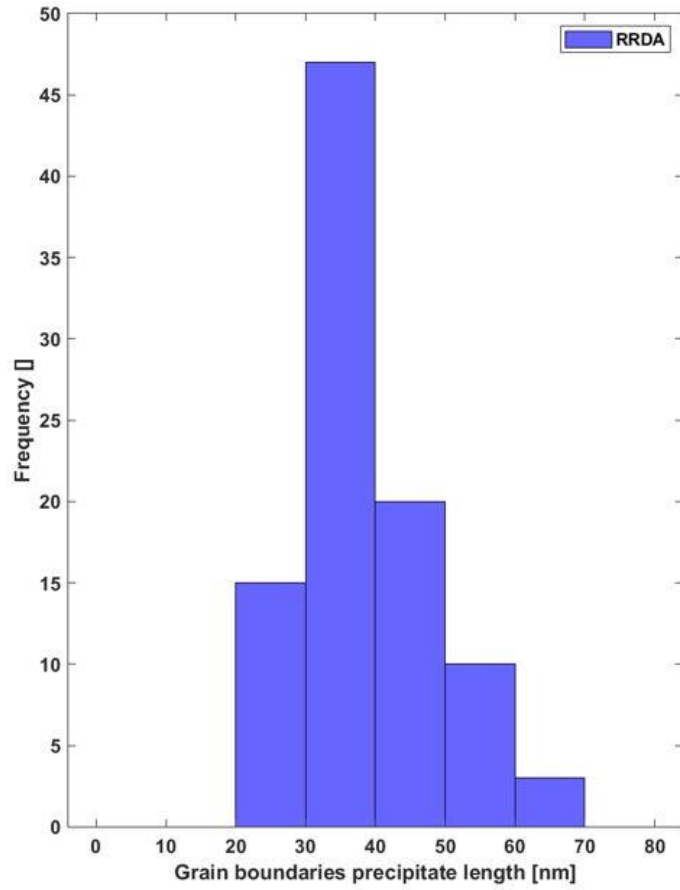


Figure 6.11: Grain boundary precipitate length distribution of the retrogression and reaged double aging sample.

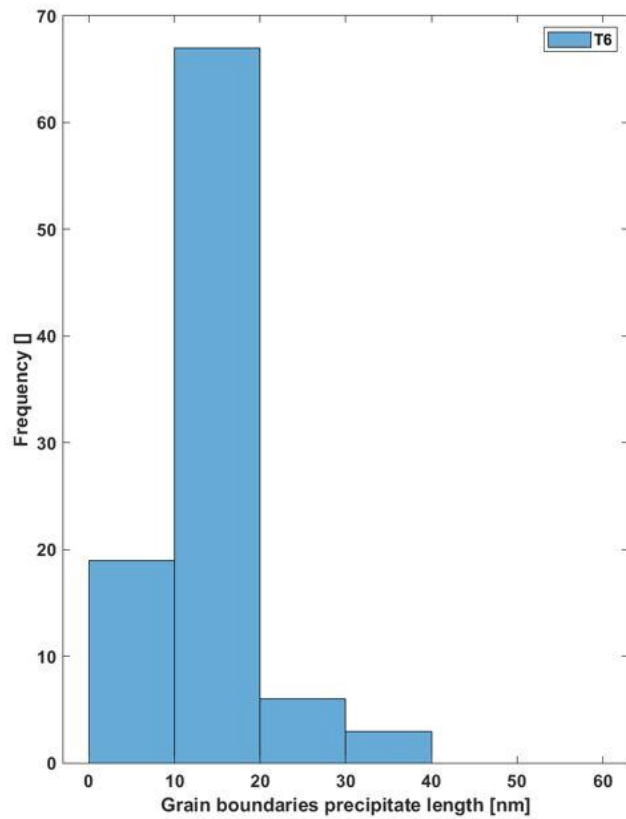


Figure 6.12: Grain boundary precipitate length distribution of the T6 sample.

The GB area is characterised by GBPs and PFZs, and while the RRDA and T73

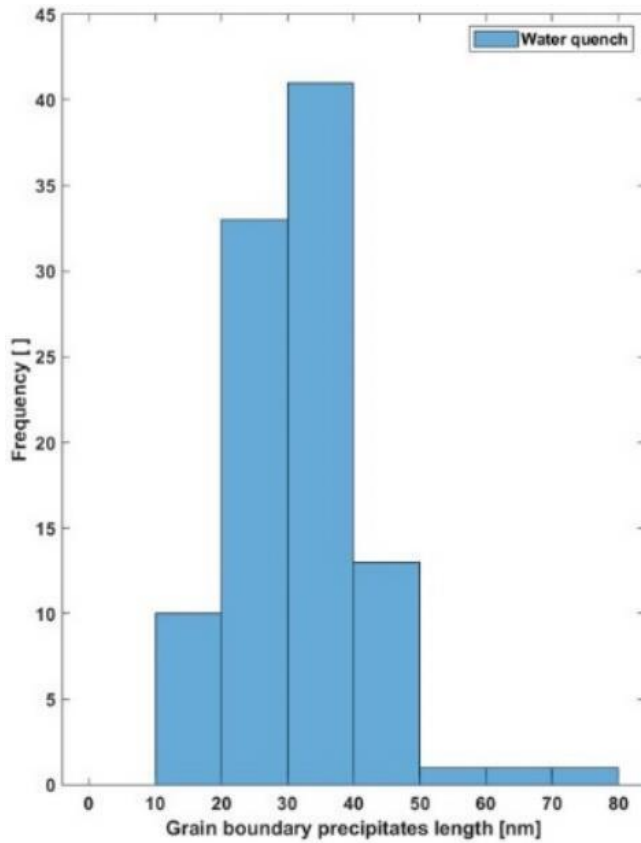


Figure 6.13: Grain boundary precipitate length distribution of the fast aged sample.

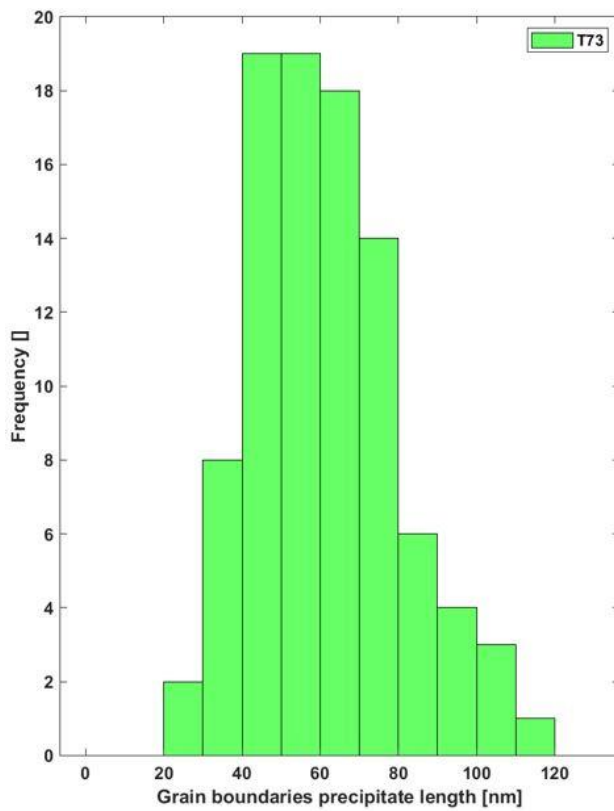


Figure 6.14: Grain boundary precipitate length distribution of the T73 sample.

microstructures look qualitatively similar, the T6 microstructure differs considerably, as GBPs appear less developed and the PFZs width is smaller.

Dispersoids and nanometric precipitates are also clearly visible in the surrounding matrix for all the metallurgical conditions considered.

GBP length distributions (Section 3.4.14) are shown in Fig.6.11, Fig.6.12, Fig.6.13 and Fig.6.14 of the RRDA, T6, FA and T73 tempers, respectively. In addition, the average GBP length and PFZ width for the tempers under investigation are summarised in Tab.6.6

Temper	Average length	2 σ	Average PFZ length	2 σ
T6	14.3 nm	11.0 nm	29.4 nm	7.9 nm
FA	32.0 nm	19.3 nm	36.6 nm	10.6 nm
RRDA	39.1 nm	19.1 nm	45.3 nm	10.2 nm
T73	63.6 nm	42.7 nm	64.9 nm	20.4 nm

Table 6.6: Summary of the average length and average precipitate-free zone length calculated from the distributions of the T6, fast aging, retrogression and reaged double aging and T73 samples.

All the distributions presented are characterised by a nearly symmetrical and single-peaked shape. The mode of the T6 temper GBP length distribution falls into the 10 μm – 20 μm bin, while the total range of the distribution is comprised between 10 μm and 40 μm . For the FA and RRDA samples, the mode of their distributions falls into the 30 μm – 40 μm bin for both the metallurgical conditions, while the total range is 10 μm – 80 μm for the FA sample and 20 μm – 70 μm for the RRDA sample. Finally, the mode of the T73 temper GBPs main length distribution falls into the 60 μm – 70 μm bin, and the total range is 20 μm – 120 μm .

From Tab.6.6 it is possible to deduce that the average main length and the standard deviation of the distribution increases following the ascending order: T6, FA, RRDA and T73. In addition, FA and RRDA tempers display similar values of both the parameters. The PFZs width also increases with the same order: the T6 temper has the smallest width, then FA, RRDA and finally T73 tempers.

Tab.6.7, Tab.6.8, Tab.6.9 and Tab.6.10 display the average elemental content (Al, Zn, Mg, Cu) of GBPs calculated via the CIPHER model when varying the aging parameters.

	Al concentration at% []			
	120 °C	160 °C	200 °C	220 °C
5 mins	12.3	15.0	15.8	16.1
10 mins	16.9	15.7	15.6	15.8
15 mins	15.3	14.8	15.3	15.9
20 mins	13.6	14.2	15.1	15.7
25 mins	14.8	15.1	15.1	15.8
30 mins	14.3	14.3	15.5	15.7

Table 6.7: Aluminium average composition of grain boundary precipitates calculated from the CIPHER model varying aging parameters.

Zn concentration at% []				
	120 °C	160 °C	200 °C	220 °C
5 mins	49.6	46.3	44.6	43.6
10 mins	46.1	46.2	44.7	43.9
15 mins	47.1	46.9	44.9	43.8
20 mins	48.1	47.2	44.9	43.9
25 mins	47.5	46.6	44.9	43.9
30 mins	47.9	47.1	44.7	44.0

Tab.6.8: Zinc average composition of grain boundary precipitates calculated from the CIPHER model varying the aging parameters.

In the range of durations and temperatures explored, the average composition of GBPs does not change appreciably, as all the element contents fluctuate in a small percentages range when varying the aging parameters.

Mg concentration at% []				
	120 °C	160 °C	200 °C	220 °C
5 mins	31.2	32.0	32.4	32.3
10 mins	31.0	31.8	32.5	32.9
15 mins	31.2	32.1	32.7	32.8
20 mins	31.9	32.3	32.8	32.9
25 mins	31.5	32.1	32.9	32.9
30 mins	31.7	32.4	32.6	32.9

Tab.6.9: Magnesium average composition of grain boundary precipitates calculated from the CIPHER model varying the aging parameters.

Cu concentration at% []				
	120 °C	160 °C	200 °C	220 °C
5 mins	6.7	6.7	7.2	7.5
10 mins	6.3	6.3	7.1	7.5
15 mins	6.3	6.2	7.1	7.4
20 mins	6.3	6.1	7.1	7.5
25 mins	6.1	6.2	7.1	7.4
30 mins	6.1	6.1	7.1	7.5

Tab.6.10: Copper average composition of grain boundary precipitates calculated from the CIPHER model varying the aging parameters.

Fig.6.15 and Fig.6.16 show the average GBPs length evolution and the GBP area evolution when varying the aging parameters as result of the CIPHER calculations. The variables in Fig.6.15 and Fig.6.16 are function of aging duration and aging temperature.

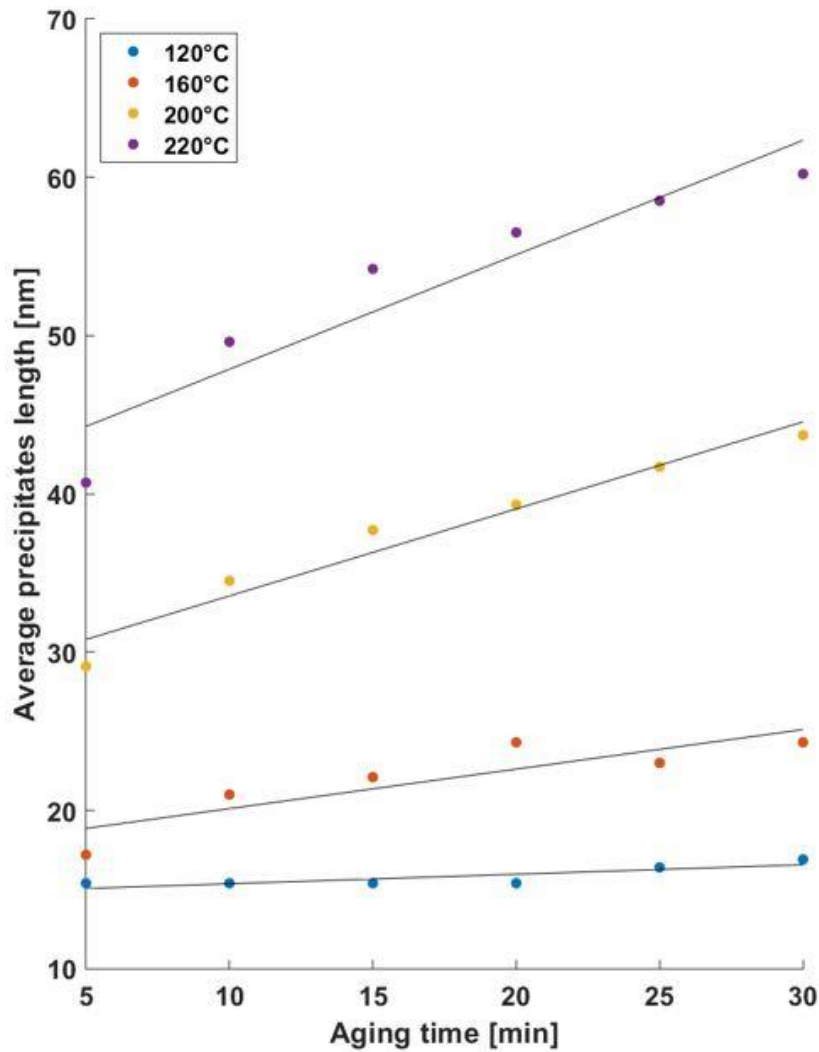


Figure 6.15: Average grain boundary precipitate length evolution calculated from the CIPHER model as function of aging time and aging temperature.

From these two plots is possible to deduce that, depending on the temperature selected for the aging step, the impact on the length and area development is different.

When selecting 120 °C as aging temperature, the duration improvement from 5 minutes to 30 minutes did not modify appreciably the average GBPs length or area.

Instead, if a temperature higher than 120 °C is chosen, the average length or area of GBP increases more rapidly with longer holding times. The degree of increase in length or area increases accordingly to the temperature used.

Moreover, when the aging temperature is set at 220 °C, the increase in linked area is more significant with aging time than the increase in length.

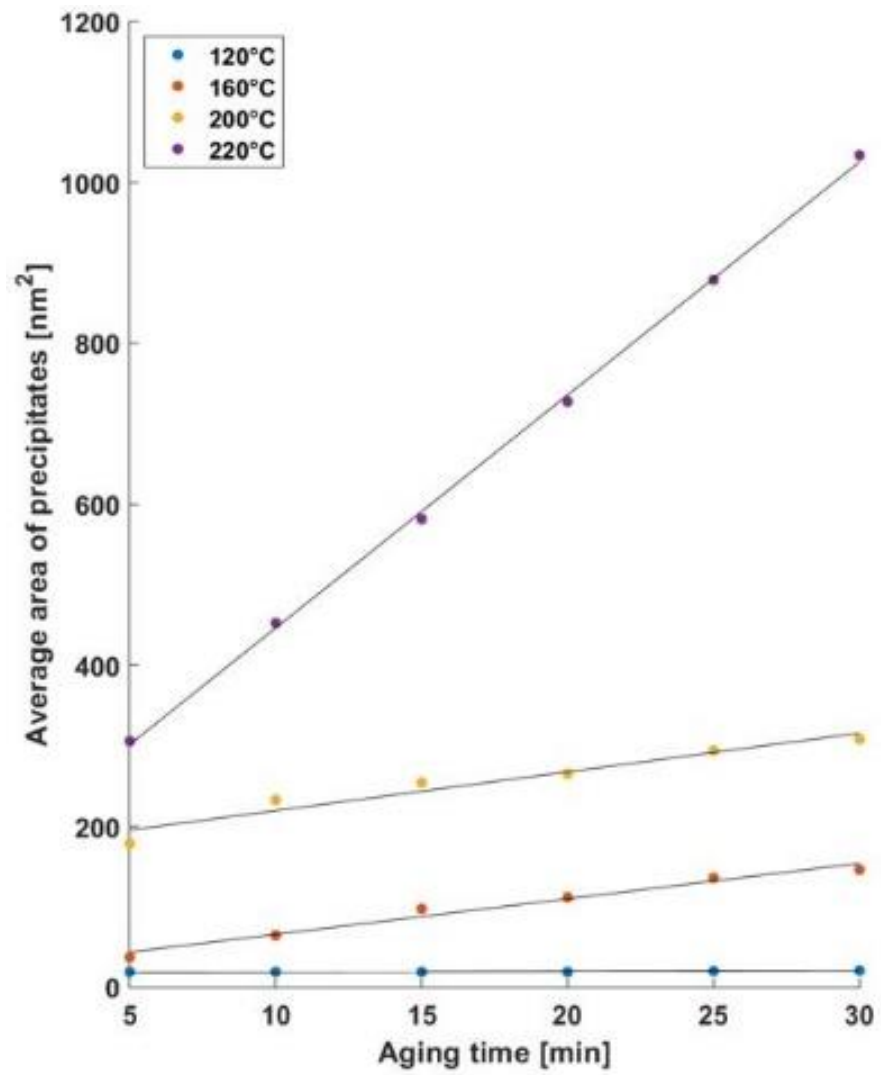


Figure 6.16: Average area of precipitates estimated via CIPHER model as function of aging duration and aging temperature.

6.1.6: Tensile properties of the RRDA strategy compared to relevant industrial tempers

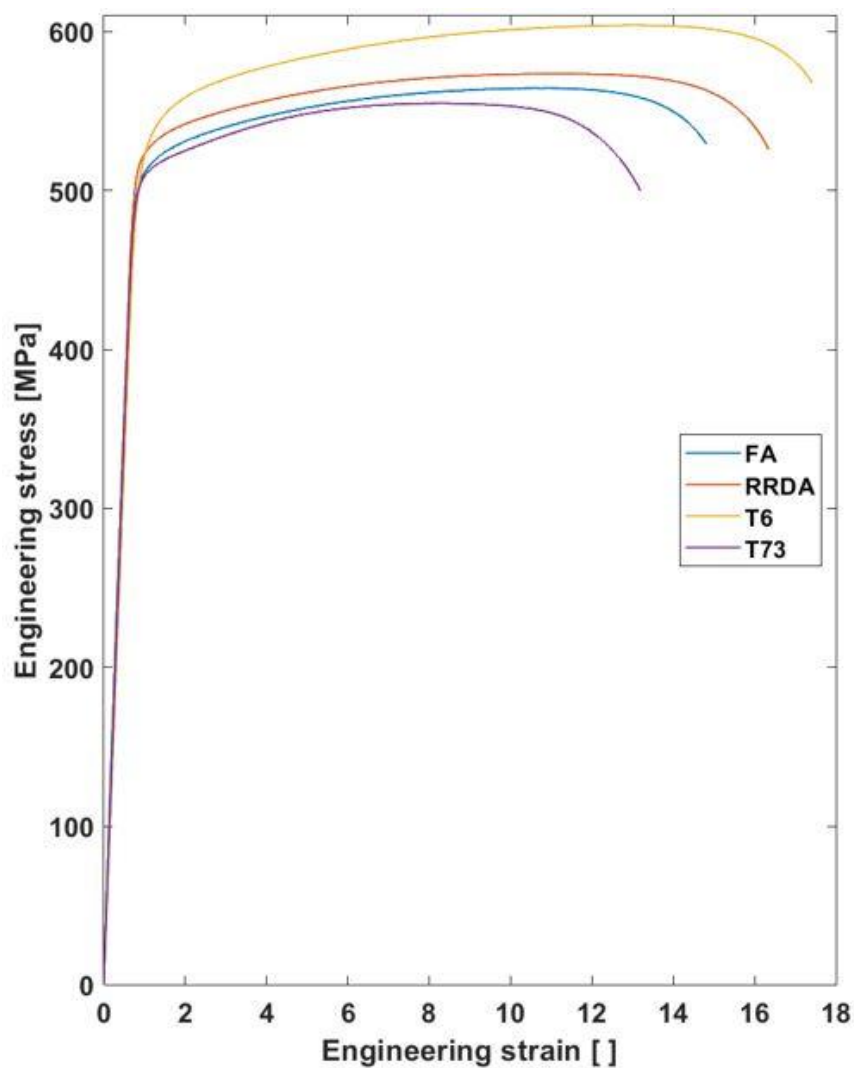


Figure 6.17: Stress-strain curves during tensile loading of the T6, retrogression and reaged double aging, fast aging and T73 samples.

Fig.6.17 shows the relationship between engineering stress and engineering strain during tensile loading for the different aging treatments investigated.

Temper	Yield strength [MPa]	Ultimate tensile strength [MPa]	Elongation to break % []
T6	522	604	17.4
RRDA	519	573	16.3
FA	507	564	14.8
T73	501	554	13.2

Table 6.11: Summary of the main tensile properties of the T6, T73, fast aging and retrogression and reaged double aging samples.

The tensile properties of the different metallurgical conditions tested are also summarised in Tab.6.11.

Considering yield strength and ultimate tensile strength, the T6 temper exhibits the highest values of both, followed by RRDA, FA and finally T73. The T6 temper

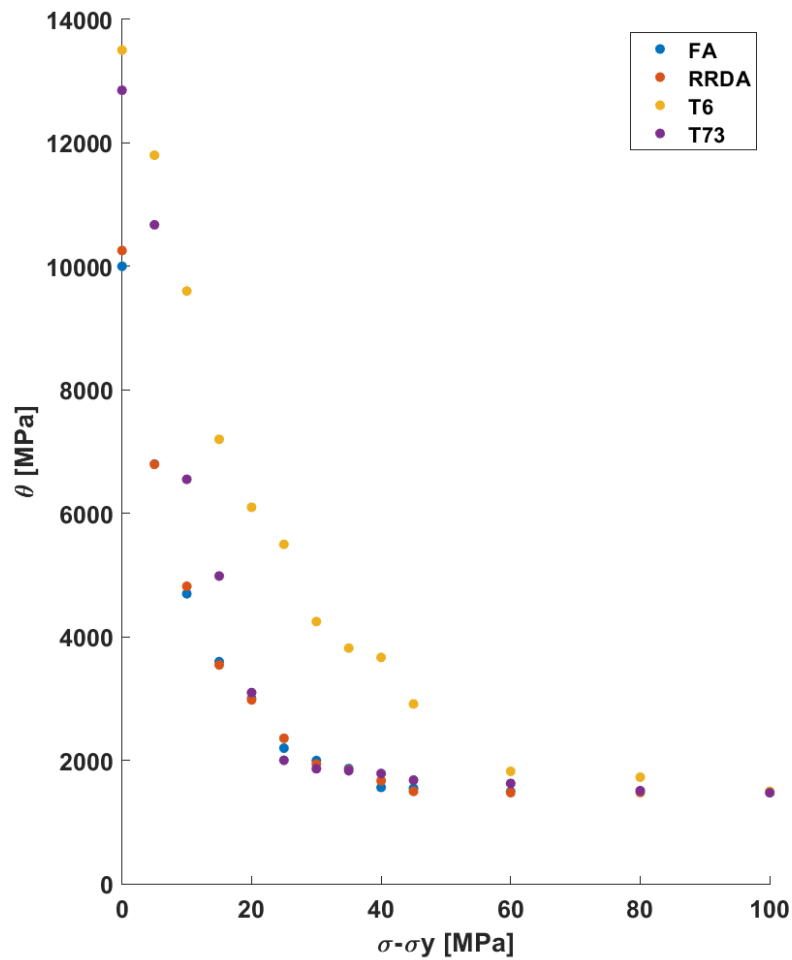


Figure 6.18: Kocks-Mecking plots of the T6, fast aging, retrogression and reaging double aged and T73 samples.

is also the aging strategy that provides the highest elongation to break, while the RRDA shows the second highest value. FA displays a slightly lower elongation to break compared to the RRDA sample, followed by the least ductile T73. In Fig.6.18 the Kocks-Mecking plots of the samples subjected to the different aging strategies are presented. All the specimens reach the same Stage 3 regime value, which is constant with increasing true stress. However, while the strain hardening rate regime value is reached in a lower true stress range for the FA, RRDA and T73 tempers, this θ value is attained just at higher true stresses for the T6 temper, as its work hardening rate decreases with a slower pace from the elastoplastic transition (Stage 1) than the other tempers.

6.1.7: The RRDA strategy corrosion properties compared to relevant industrial tempers

Temper	Time to failure [days]
T6	2, 2, 3
FA	18, 19, 23
RRDA	35, 36, 38
T73	No

Table 6.12: Average time to failure of U-bend samples aged with different aging strategies after exposure to the salt-spray fog environment.

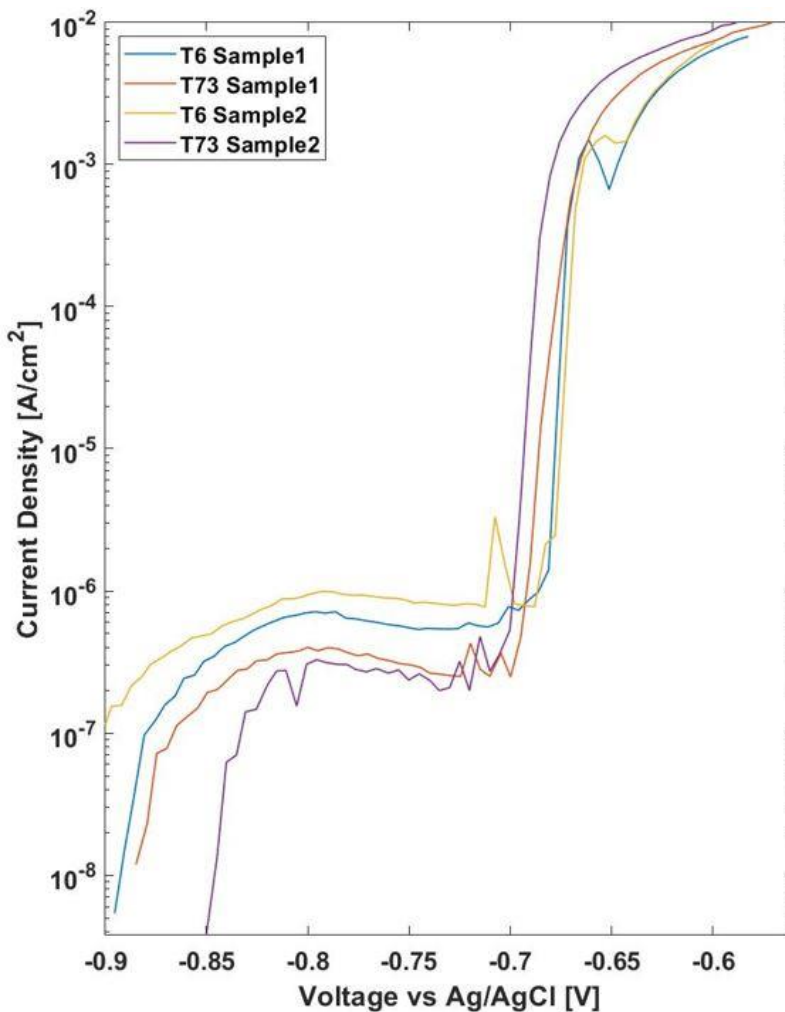


Figure 6.19: Comparison between the anodic polarisation of samples in the T6 and T73 tempers.

Tab.6.12 shows the time to failure of U-bend samples in the T6, T73, FA and RRDA tempers exposed to the salt-spray fog environment. While the T6 temper samples failed after just 2 days or 3 days of exposure, the T73 specimens resisted without breaking the whole 60 days test period. In between these 2 extremes, the FA samples failed after 18, 19 and 23 days of exposure, and the RRDA samples instead after 35, 36 and 38 days of exposure.

Fig.6.19 shows the relation between electrostatic potential and current density during anodic polarisation of the T6 and T73 samples. The development of current density with voltage is similar for the two tempers, and similar are the values of open-circuit potential and breakdown potential.

The current density evolution within the investigated potential range is similar for both the T6 and T73 samples. However, the presence of variability in the recorded traces for these samples prevents establishing a direct connection between anodic polarization parameters and SCC performance.

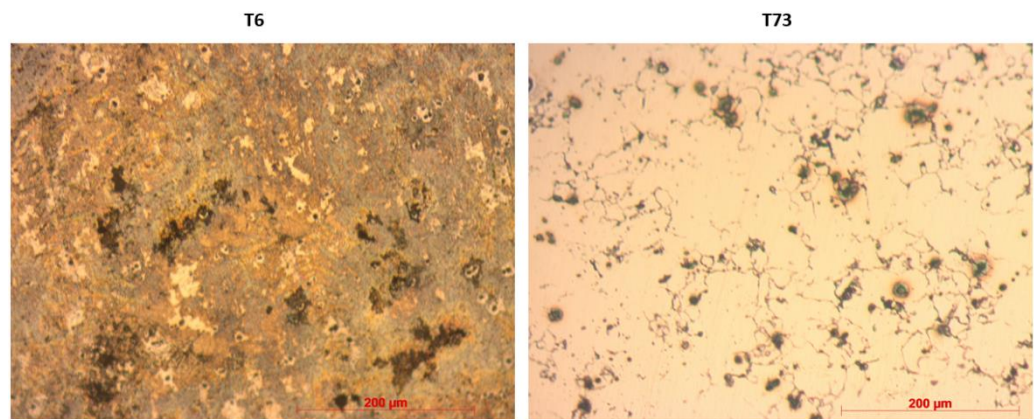


Figure 6.20: Optical microscopy micrographs showing micro-surfaces of samples corroded after anodic polarisation. T6 sample (left) is compared with the T73 sample (right).

In Fig.6.20 the OM micrographs of corroded T6 and T73 samples after anodic polarisation are presented. While the T6 micro-surface shows a generalised corrosion damage, in the T73 temper the attack is mostly localised at GBs.

6.2: Discussion

6.2.1: The design of the RRDA strategy

When designing a valid aging strategy for the HFQ[®] process, final acceptable mechanical properties and SCC resistance must be achieved, but the step duration must also remain highly time efficient. To accomplish this goal, different principles that characterise other successful aging strategies reported in the literature must be combined. In particular, the RRDA strategy is based on both RRA and two-step aging features.

As previously discussed, the RRA strategy consists of applying a short retrogression step at high temperature to a peak-aged sample and subsequently reapplying an additional peak aging treatment. For 7000 aluminium alloy sheets, this procedure has been proven successful to impart mechanical properties comparable to T6 tempered specimens and considerably reduce the SCC susceptibility of the components [175,176].

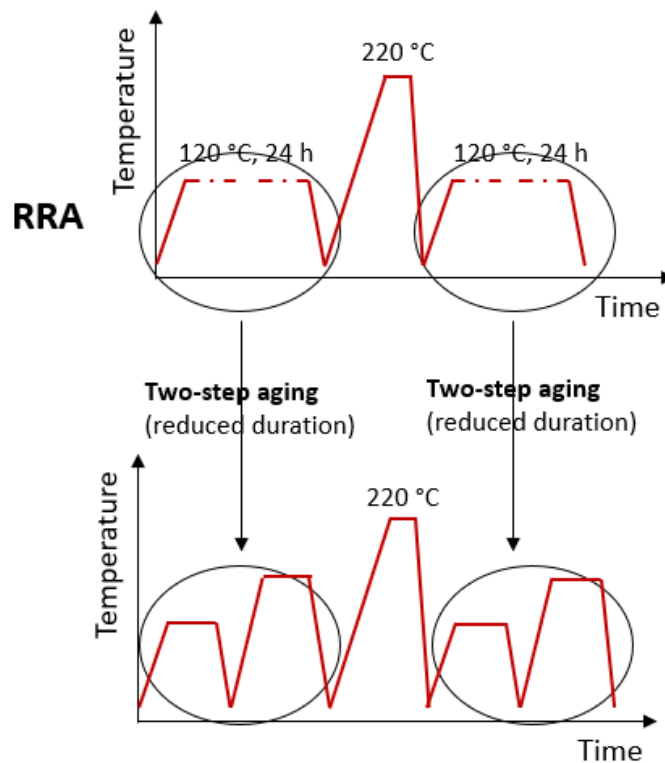


Figure 6.21: Representation of the core principle of the RRDA strategy. The two peak aging treatments typical of the RRA strategy are substituted with the more time-efficient two-step aging sequences.

Although the final properties achieved via RRA strategies are nearly optimal, the need to use a sequence of two peak aging treatments (120 °C for 24 hours) is highly inefficient. Therefore, the idea behind the design of the RRDA strategy is to use the same RRA approach but accelerate the two necessary peak aging treatments.

The literature has consolidated around the notion that two-step aging strategies can deliver mechanical properties like those of T6 tempered specimens and achieve a considerable shortening of the aging treatment [142]. Therefore, the RRDA strategy seeks to first obtain a peak aged state in the material via a two-step aging schedule. Then, the strategy uses the typical retrogression step of RRA strategies and finally imparts again the peak aged state through a second two-step aging sequence (Fig.6.21).

The final RRDA aging treatment schedule spans five different steps based on the assumption that microstructures generated via two-step aging can be equally retrogressed like those achieved via the step at 120 °C for 24 hours.

The two-step aging portions included in the RRDA strategy must bring the material to a peak aged state in the shortest time span possible. As the optimisation of double aging schedules requires the selection of multiple parameters (combination of temperatures and durations), a simplified approach is needed. The design of the two-step aging portions of the final strategy is based on the work of Emani et al. [142], who previously studied the optimisation of two-step aging strategies for AA7075 extrusions.

Based on this study, 120 °C is the selected temperature for the first step of the RRDA strategy, while 175 °C is chosen for the second step. In addition, while the same duration is set for both thermal steps (Fig.6.22), the total duration of the two-step aging schedule is optimised in Fig.6.1.

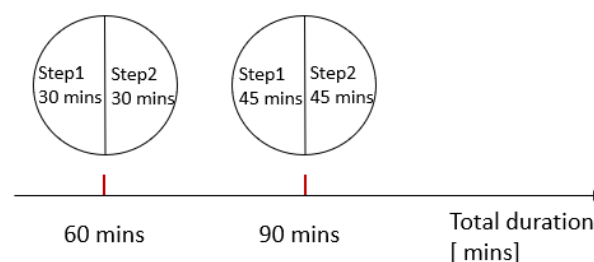


Figure 6.22: Partition of the Fig.4.26 total heat treatment duration in two equal steps.

Because 90 minutes is the shortest total holding time that determines the maximum hardness increase of the specimens, the time spans of the first and second steps are both 45 minutes. The total duration decided qualitatively

resembles the one selected by Emani et al. [142] since their optimised aging strategy consists of a first step at 121 °C for 55 minutes followed by a second step at 177 °C for 55 minutes.

Although further contributions are needed to clarify the kinetic principles behind double aging schedules, the distribution of GP zones is presumably realised during the first step of the strategy that promotes the nucleation of strengthening η' phase during the second step [142,143].

Fig.6.1 also shows that the hardness of samples subjected to the two-step strategy as a function of the total holding time presents a maximum: surpassing the total 90-minute duration causes a decrease of the hardness levels. If the duration of the first step is extended past 45 minutes, a fraction of the GP zones formed could start to convert to η' phase. Thus, the converted GP zones fraction can no longer accelerate the nucleation of strengthening η' precipitates occurring during the second step, therefore limiting the final hardness increase achievable [142].

Once the peak-aged state with the optimised double aging section of the strategy is reached, samples are subjected to the retrogression step. The selection of the retrogression parameters (temperature, duration) greatly influences the final properties of RRA samples, and these parameters are expected to also be crucial in the RRDA aging schedule.

The literature shows that the optimal duration of the retrogression step decreases with increasing retrogression temperature [175,176]. In this work, the retrogression temperature has been set at 220 °C, as per the study conducted by Park et al. [175]. Based on this selection, it has been found that the optimal retrogression time would be a few minutes.

The time span selected for the optimal retrogression duration is highly convenient as the selected span preserves the time efficiency of the aging step. In addition, the optimal time span is easier to control from an industrial point of view when compared to a retrogression step of few seconds.

Once the retrogression temperature is set, the optimisation of the retrogression duration is typically carried out by analysing the plot of hardness as a function of

the retrogression time [121,175,176]. For samples double aged and then held at 220 °C, Fig.6.2 shows the hardness of the retrogressed specimens against the retrogression duration.

The trend displayed in this plot is commonly reported in the literature and qualitatively resembles the one shown in the works of Park et al. [121,175] and Kanno et al. [176].

The similarity of Fig.6.2 with the results from previous studies (Fig.2.46 in Section 2.15) suggests that the microstructures obtained via two-step aging can be retrogressed in a similar manner as the typical microstructures resulting from low temperature aging (for example, 120 °C for 24 hours).

When examining the trend in Fig.6.2, the hardness level decreases with an increasing retrogression time, reaching a minimum. The hardness minimum is attained because a fraction of GP zones and small η' precipitates dissolved during the regression step, releasing solute atoms in the aluminium matrix and no longer participating in the strengthening mechanism [139,177].

The literature has established the need to select the retrogression time correspondent to the minimum results in the highest hardness possible during reaging. In fact, when approaching the hardness minimum, the concentration of solute atoms released in the matrix is the highest possible, and this concentration translates into the greatest hardness response of the material, even slightly higher than the level reached by T6 tempered samples [177,178].

Past the hardness minimum, longer retrogression durations promote the precipitation of η' and η phases; this event causes the hardness level to reach a local maximum [175,177,179]. When the retrogression holding time is set to correspond to this local hardness maximum, the hardness achieved after reaging is comparable to one of the peak-aged samples or just slightly inferior [177,178].

Once the local maximum is reached, further prolonging the retrogression time causes the hardness values to drop monotonically; this trend is related to the coarsening of η' and its transformation to η phase [177,178].

Because the retrogression treatment continuously increases the GBP dimensions and spacing proportionally to the holding time used, the SCC resistance of

retrogressed samples is enhanced with increasing retrogression duration [139,175,179]. After considering the previous studies related to the retrogression step optimisation, 4 minutes and 30 seconds is set as the retrogression duration for the RRDA strategy. The holding time selected roughly corresponds to the local hardness maximum displayed in Fig.6.2.

In fact, the selection made for the retrogression duration gives rise to the perfect compromise between hardness and SCC resistance after reaging. Strength levels after reaging are expected to resemble those of T6 tempered specimens, while the GBP development is supposed to sufficiently protect against SCC. Once the retrogression step is defined, a second cycle of double aging is used as a reaging strategy. The final aging schedule realised (RRDA) is then presented in Fig.6.3.

Undoubtedly, the aging time-temperature profile developed is complex to apply at the industrial level, due to the multiple steps and different temperatures used. The total duration of the heat treatment, however, is extremely competitive with the total holding time of the RRDA strategy of roughly 3 hours. Besides the validity of the RRDA strategy, the design of this aging schedule constitutes a valid tool to understand all the kinetic mechanisms that regulate 7000 aluminium alloy aging strategies. The understanding of these kinetic principles can help the future design of performant aging steps for various manufacturing processes involving these alloys.

6.2.2: The evolution of microstructure and final properties during the RRDA steps SAXS experiments (Fig.6.4), DSC traces (Fig.6.5), uniaxial tensile tests (Fig.6.6) and SCC experiments (Tab.6.4) were analysed in conjunction to understand the microstructural features developed during each RRDA step (Fig.6.23).

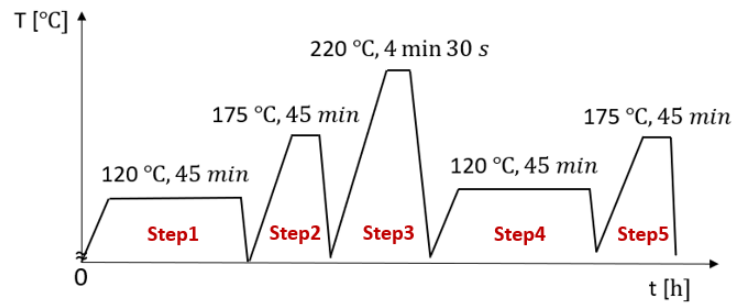


Figure 6.23: RRDA time-temperature profile divided into a sequence of 5 steps.

6.2.2.1: Step1

The reduced precipitate volume fraction and Pseudo-Guinier radius calculated from the Kratky plot for the Step1 sample (120 °C, 45 minutes) suggest that the material is in a typical underaged condition. In fact, the Kratky plot shifts to higher values of the scattering vector and presents a reduced Iq^2 maximum compared to a peak aged sample. Similar features between the Kratky plots of underaged and peak aged specimens are reported by Deschamps et al. [180] during their characterisation of AA7075 specimens with coarse grain structure. Dumont et al. [45] also obtained Kratky plots for underaged AA7050 specimens, confirming the features described. In addition, the researchers' Guinier radius calculated for underaged specimens resembles the one calculated in this work (both radii are roughly 10 °Å).

The Step1 DSC trace suggests that a high solute concentration is still present in the aluminium matrix. Following the work of Richard et al. [152], the presence of an endothermic peak in the 150 °C–220 °C temperature range is linked with the dissolution of GP zones and small η' precipitates. Consequently, because the Step1 DSC trace instead shows a marked exothermic peak in this temperature range, indicating that the precipitation of GP zones and small η' precipitates occurred during the DSC heating ramp. Step1 specimens should thus be characterised by a high quantity of solute atoms in the matrix.

A similar display of an exothermic peak in the 150 °C–220 °C range has also been reported by Lumley et al. [181] and Papazian et al. [160] when testing as quenched or moderately aged at room temperature AA7075 samples.

The stress-strain curve linked to Step1 is also aligns with the microstructural features deduced from SAXS experiments and DSC traces. In fact, the low volume fraction of small precipitates justifies the reduced yield strength of the material since dislocations can easily propagate in the matrix via the cutting mechanism [45,117]. In addition, the highly concentrated solute atoms likely cause the oscillations found in the Step1 stress-strain curve: these oscillations might be caused by dynamic interaction of solute atoms with moving dislocations (Portevin-Le Chatelier effect).

Although this phenomenon is still not well-understood in the literature [182], the interaction among free alloying atoms in the matrix and moving dislocations gives also rise to an exceptionally high work hardening rate in the material, greater than the one typical of peak aged or overaged tempers [117]. Similar tensile properties for underaged 7000 aluminium alloys have also been derived by Cheng et al. [117] during uniaxial tensile testing of AA7030 specimens and by Fribourg et al. [182] when testing AA7449.

Finally, the greater elongation to break of the Step1 stress-strain curve among the other metallurgical conditions of Fig.4.31 suggests a minimal development of the GB microstructure, which is proposed to be constituted by closely spaced small η precipitates and narrow PFZs. In fact, large GBPs aid nucleation and growth of microvoids at GBs that can lead to a premature fracture and limited elongation to break [164].

The minimal development of the suggested GB microstructure is also strengthened by the poor SCC resistance displayed by Step1 U-bends during exposure in the salt spray chamber (average time to failure of 1 day) since high susceptibility to SCC is typically linked with this type of GB microstructure [97].

Overall, the microstructural features linked to the effect of Step1 are consistent with the general description of those for the underaged 7000 aluminium alloys found in the literature.

6.2.2.2: Step2

The consistent increase of precipitate volume fraction and Pseudo-Guinier radius linked to Step2 suggest that aging kinetics have been greatly accelerated because of the sequence of the two steps. Dumont et al. [45] and Deschamps et al. [44] also reported a similar marked enhancement of volume fraction and Guinier radius when using two-step aging strategies for 7000 aluminium alloys.

The achievement of matrix precipitate characteristics comparable to T6 tempered alloys can also be deduced from Fig.6.5. In fact, the DSC trace associated with Step2 displays the typical endothermic peak in the 150 °C–220 °C range caused by the dissolution of GP zones and small strengthening η' precipitates [152]. The Step2 DSC trace also qualitatively resembles those commonly obtained for peak aged samples [139,152] and those shown in the work of Papazian et al. [160], who investigated how double aging parameters influence the DSC trace features for AA7075.

The tensile properties achieved with Step2 are also coherent with the acceleration of the aging kinetics proposed since both yield strength and ultimate tensile strength greatly increased from the Step1 levels. In addition, when comparing the stress-strain curves of Step1 and Step2, the overall work hardening rate can be deduced as diminished when progressing with the second step of the RRDA strategy. This observation can be explained given that the formation of precipitates during Step2 limited the dislocation-solute interaction and therefore lowered the work hardening rate obtainable. This deduction aligns with the work hardening principles explained in the works of Cheng et al. [117] and Dumont et al. [45].

As the elongation to break considerably decreases when going from Step1 to Step2 samples (Fig.6.6), Step2 supposedly produced an enlargement of GBPs, and therefore, a development of the GB microstructure occurred. This hypothesis is also strengthened by the SCC experiment results (Tab.6.4): the time to failure of U-bends exposed to salt-spray environment increases, on average, from 1 day to 9 days when progressing from Step1 to Step2.

Interestingly, the SCC resistance observed for Step2 is also higher than the one reported for T6 tempered samples (time to failure of 2 days, on average). This finding suggests that the GB microstructure of Step2 specimens is more developed than that of peak aged samples.

The aging process acceleration achieved by the sequence of Step1 and Step2 (enhanced volume fraction of strengthening η' precipitates) is believed to be linked to the different type of GP zones that can be formed from as quenched specimens [130,146]. GP1 zones are commonly reported to develop over a wide range of temperatures (from room temperature to 140 °C), while GP2 zones only develop at temperatures above 70 °C due to also being dependant on the quenched-in vacancy concentration achieved and being more thermally stable than GP1 zones. [146,183]. Therefore, GP2 zones formed at 120 °C during Step1 can likely survive when reaching Step2 at 175 °C, boosting the nucleation and growth of a refined distribution of η' precipitates.

6.2.2.3: Step3

Interestingly, the Kratky plot, DSC trace and stress-strain curve of Step3 roughly match those obtained for Step2. More specifically, the Step3 Kratky plot produces only a moderate reduction of the volume fraction and Pseudo-Guinier radius, compared to Step2.

Meng et al. [183] and Liu et al. [184] reported a similar decrease of these two parameters with the retrogression step, although the magnitude of this reduction strictly depends on the retrogression temperature and duration. The greater the precipitate dissolution achieved, the higher the reduction of volume fraction and Guinier radius associated with the resultant Kratky plot.

The dissolution process occurring during the retrogression step can also be identified with DSC experiments since, the stronger the reversion achieved during this step, the shallower the endothermic dissolution peak observed in the 150 °C–220 °C temperature range. In fact, since a lower quantity of GP zones and small η' precipitates are present in the material after retrogression, a decreased

heat flow is needed for their dissolution during the DSC scan. The variation of the endothermic peak '1' as a function of retrogression parameters is commonly reported in the literature, for example, in the studies of Papazian et al. [158] and Viana et al. [139].

The degree of precipitate dissolution during retrogression influences the tensile properties of the samples. While a high degree of dissolution decreases yield strength and ultimate tensile strength of the retrogressed samples, a low degree of dissolution (long retrogression holding time) makes tensile properties highly resemble the pre-retrogression ones [179,185].

The unexpected similarity of the experimental outputs of Step2 and Step3 can be rationalised with the following considerations. First, even when dealing with conventionally retrogressed samples (those aged beforehand at 120 °C on a 24-hour schedule), the quantity of precipitates dissolved is just a fraction of the total distribution. The fraction of precipitates could be dissolved when retrogression is imparted to a double aged material even smaller than one of conventionally retrogressed alloys.

In fact, two-step aged specimens own a slightly coarser distribution of matrix precipitates compared to a low temperature peak aged material (compare Tab.6.1 and Tab.6.5 in the Results section), which might be harder to dissolve with usual retrogression parameters. Therefore, the sensitivity of the techniques used might be insufficient to detect the matrix microstructural changes occurring with Step3.

Secondly, the retrogression duration for the RRDA strategy is optimised while considering both mechanical properties and SCC resistance. This fact implies that the retrogression step does not aim to achieve the maximum degree of matrix precipitate dissolution achievable.

In conclusion, even if just a small fraction of the precipitate distribution underwent the reversion process, that dissolution presumably occurred during Step3. In fact, this event is indirectly identified by the level of final properties achieved after Step5, which is comparable to RRA materials (as later discussed in Section 6.2.3).

Regarding the GB microstructure, Step3 is believed to produce an increase of the GBP size and interparticle distance. This conclusion can be indirectly deduced from the SCC experimental results (Tab.6.4). In fact, compared to the average 9 days of Step2, the time to failure of U-bends exposed to salt-spray environment rose on average to 36 days after Step5. The literature has well-established that the increased GBP disconnection and enlargement correlate with the decrease of SCC susceptibility [37,104].

The simulation work carried out in this thesis (Fig.6.16) and the linked relevant literature [97,174] suggest that the enlargement of GBPs increases concurrently with aging temperature increases. Therefore, proposing that both Step3 (220 °C) and Step5 (175 °C) are responsible for the GB microstructural development occurring after Step2 is reasonable.

6.2.2.4: Step4

When the focus is on the microstructural evolution with Step4, the Kratky plot, DSC trace and stress-strain curve related to this step are also very similar to those of Step3. The experimental results linked with Step4 can be explained when considering the microstructural features proposed for Step3 as a starting point.

Because just a small fraction of matrix precipitates dissolved during the retrogression step (Step3), the solute concentration available for the reprecipitation process (Step4) is limited, and similarly limited the formation of precipitates during Step4. In conclusion, although precipitation might occur during this step, the techniques used are seemingly inadequate to discern between the microstructural differences between Step3 and Step4.

As previously mentioned, the occurrence of precipitation events during Step4 is coherent with the observation that the tensile strength after Step5 is enhanced when compared to the tensile strength after Step3 or Step4.

A second valid explanation to justify the experimental results linked to Step4 assumes that only Step5 caused reprecipitation after retrogression and that Step4 was ineffective. Generally, preaging steps at low temperature (100 °C–120

°C) have been proven successful for two-step strategies when heat treating as quenched samples since the considerable quantity of solute elements owned by this metallurgical condition is translated into a high driving force for precipitation.

When heat treating a retrogressed specimen, the use of Step4 (120 °C for 45 minutes) could no longer be kinetically effective to promote further precipitation events since longer durations or higher temperatures would be required. This 'inertia for precipitation' is a concept found in different papers in the literature.

For example, Emani et al. [142] acknowledged the lower final properties achieved from two-step aged samples if a low temperature step postpones the high temperature step. In another study, Lumley et al. [181] explained how secondary precipitation at low temperatures after a conventional high temperature aging step requires long holding times (in the magnitude of multiple hours) to be effective.

When focusing instead on the GB microstructure, Step4 likely cannot appreciably modify the features imparted by Step3 since GB microstructures develop more strongly with steps at high temperature.

In this section, the microstructural evolution linked to the advancement from Step1 to Step4 has been discussed. The final microstructure and properties associated with Step5 are analysed in Section 6.2.3 and are compared with other industrially relevant tempers for 7000 aluminium alloys.

6.2.3: Microstructure of RRDA samples compared to relevant industrial tempers

Kratky plots (Fig.6.8 and Tab.6.5), DSC traces (Fig.6.9) and TEM GBP length distributions (from Fig.6.11 to Fig.6.14) are used in conjunction to describe the microstructure and final properties of the RRDA strategy (Step5). These features are also compared with the ones of peak aged, overaged and two-step aged samples, T6, T73 and FA specimens, respectively.

Tab.6.5 shows that the RRDA Pseudo-Guinier radius is comprised between one of the T6 and T73 tempered materials, while the RRDA precipitate volume fraction is comparable to the one of T6 samples.

In the literature, Liu et al. [138] and Meng et al. [183] conducted SAXS experiments on differently tempered 7000 aluminium alloys, reporting similar relationships among the features of RRA specimens compared to those of peak aged or overaged samples. For this reason, the RRDA strategy would benefit from similar aging principles of typically RRA materials, while achieving similar final properties in a considerably shorter aging treatment duration.

Retrogression can be successfully applied not just to matrix microstructures typical of low temperature peak aged samples, but also to specimens that reached the peak aged state via a two-step aging schedule (Step2 samples of the RRDA strategy, for example). Double aged specimens are usually reported to be characterised by a more developed microstructure than T6 tempered materials: higher average size of η' precipitates and higher degree of conversion from η' to η phase [128]. Despite these differences, a portion of the Step2 precipitate distributions are small enough to be redissolved during retrogression, therefore unlocking the beneficial effect of the reaging step.

The observation that retrogression and reaging occurred during the use of the RRDA strategy can be also supposed by comparing FA (two-step strategy) and RRDA Kratky plots. While both strategies involve thermal exposures to similar temperature ranges, RRDA specimens show a higher precipitates volume fraction developed, implying that possible dissolution occurs during Step3 (220 °C for 4.5 minutes) and that reaging occurs during Step4 and Step5.

The similarity between RRA and RRDA strategies can be also suggested when studying the related DSC traces (Fig.6.9). Generally, as reported by Papazian et al. [158] and Park et al. [137], when compared to T6 samples, RRA specimens show a less marked endothermic peak '1', and this maximum is shifted to higher temperatures. In addition, DSC traces generated from RRA samples display less deep exothermic peaks '2' and '3' when compared to peak aged materials.

The existence of the sequence of peak '2' and peak '3' is also the main distinctive difference among RRA samples and T73 samples since the overaged samples instead show a broad exothermic plateau in the same temperature range considered.

Interestingly, the various trace differences described are also detected when comparing RRDA with T6 or T73 DSC traces. This observation strengthens the hypothesis of successful retrogression and reaging occurred during RRDA.

When comparing the stress-strain curves in Fig.6.17, results (Tab.6.11) show that the yield strength and ultimate tensile strength of RRDA samples are superior to those of FA samples and that the strength parameters obtained for RRDA samples are also comprised between those of the T6 and T73 specimens. Therefore, regarding matrix precipitates, a higher refinement seemingly occurs during the RRDA strategy compared to the T73 or FA aging schedules. Still, this observation makes plausible the idea that retrogression and reaging occurred during the RRDA strategy.

The trend that emerged from the tensile data is also aligned with the results of Dahn et al. [186] and Islam et al. [179]. In fact, when using retrogression durations aimed to balance both mechanical and corrosion properties, the strength of the reaged material is reportedly equal or slightly lower than that of the T6 tempered materials.

From the analysis of the experimental outputs discussed, although retrogression and reaging occurred during the RRDA strategy, the extent of precipitate dissolution and reprecipitation is presumably smaller when compared to materials retrogressed in the conventional way from the T6 temper state. In fact, although the SAXS experiments suggest that the volume precipitate fraction of RRDA samples is superior to that of FA samples and comparable to T6 samples,

RRDA and FA samples display an almost matching DSC trace. That similarity implies the matrix microstructural differences between these two metallurgical conditions might not be that marked.

As previously mentioned, the fraction of matrix precipitates that can experience retrogression during Step3 could be lower than the one of peak aged samples. After all, Step2 can enlarge η' precipitates and promote η formation, making the dissolution process harder to accomplish.

In addition, the lower levels of yield strength and ultimate tensile strength of the RRDA samples compared to T6 samples might also be caused by limited precipitate dissolution during the retrogression Step3, and not just linked to the prolonged retrogression duration used.

While the matrix precipitation features of RRDA specimens have been discussed in this section, the description of the RRDA GB microstructure and its comparison with the T6, FA and T73 microstructures is analysed in Sections 6.2.5 and 6.2.6.

6.2.4: The optimisation of the HFQ[®] aging step

The HFQ[®] cooling step is usually realised at the highest rate possible to avoid quench-induced precipitation and preserve the hardening potential of the material [31,35]. Therefore, the role of the HFQ[®] aging step is not just to develop the targeted strength levels but also to ensure acceptable final SCC resistance. In addition, the aging step should ideally be time-efficient and well-integrated with the overall automobile manufacturing process.

The most used design approach [128,129] consists of applying a preaging step at low temperatures (80 °C–130 °C) and adjusting the final properties of the workpiece with the final and mandatory paint-baking step (usually modelled in the literature as a thermal exposure at 180 °C for 30 minutes).

In this work, FA samples can be regarded as representative of preaged/paint-baked specimens since the two aging strategies share very similar time-temperature profiles. The results of this study suggested that, although FA samples displayed satisfactory tensile properties just slightly inferior to those of T6 tempered workpieces (Fig.6.17), the samples lack the necessary SCC resistance (Tab.6.12) to be considered a viable, definitive aging strategy for the HFQ[®] process. The RRDA strategy can impart strength levels in the material comparable to those of the T6 samples (Tab.6.11) and greatly surpass this temper regarding the final SCC resistance achieved (Tab.6.12). In addition, the RRDA strategy has a total duration of just 3 hours compared to the 24 hours required for the T6 treatment.

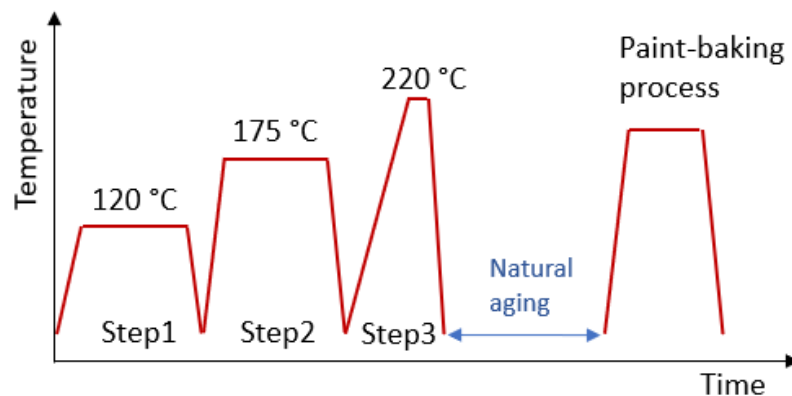


Figure 6.24: Suggested integration of the RRDA strategy with the paint-baking cycle.

The integration of the RRDA strategy with the paint-baking process could even further reduce the overall HFQ[®] process duration. To merge the RRDA strategy with the final paint-baking steps, Step1, Step2 and Step3 should be used to achieve retrogression of the samples' matrix precipitates and to promote reaging through the paint-baking process (Fig.6.24).

Although the suggested modification has not yet been tested and would require further investigation, some preliminary results that explore this direction are available in this work. First, the success of the integration process would require limited natural aging between Step3 and the paint-baking cycle.

Comparing Tab.6.2 and Tab.6.3 shows that the yield strength and ultimate tensile strength increase of Step3 samples after 3 months of natural aging is contained roughly below 3%. This finding confirms the possibility to merge the RRDA aging schedule and the paint-baking cycle.

Generally, the reason behind the low temperature microstructural stability or instability of aged 7000 aluminium alloys remains a topic of investigation among researchers, but the possible microstructural variations at room temperature are believed to be linked with the different quality of GP zones formed during the previous thermal history of the material [137,158].

Yet despite the progress made, the RRDA aging schedule cannot be considered the definitive solution for the HFQ[®] aging step. In fact, the complex time-temperature profile needed to realise the RRDA strategy can be challenging to obtain at an industrial level. Furthermore, the SCC resistance evaluated for the RRDA specimens is still unacceptable and inferior to that of the samples overaged with the T73 temper.

Despite these considerations, the development of the RRDA aging schedule showed the importance of including a retrogression step (200 °C–220 °C) during the aging of 7000 aluminium alloy sheets. These findings suggest that the use of this high temperature step is advantageous since it allows the refinement of the matrix precipitate distribution and provides the necessary coarsening of GBPs.

As reported by various authors [121,176], a second advantage of the retrogression step is the potential to modulate the final mechanical and

corrosion properties of the sample through the variation of the retrogression holding time.

NIA strategies are another possible option for the HFQ[®] aging step, although their effect on the microstructural evolution and final properties achieved remains a topic of discussion in the literature [53,150].

In conclusion, when a high cooling rate is used from solution heat treatment, the available options for the HFQ[®] aging step likely cannot satisfy the required criteria in terms of properties and overall step duration.

However, as discussed in Section 7.2, the combined variation of cooling rate and aging parameters could be a promising approach to further investigate.

6.2.5: Simulated GBP composition with varying aging parameters

Based on analysing Tab.6.7, Tab.6.8, Tab.6.9 and Tab.6.10, all the elemental concentrations appear to greatly fluctuate in the short time span simulated. This observation could suggest that, in the early stages of aging, the development of the η phase composition is kinetic in nature and far from equilibrium conditions.

The data presented also show the enrichment of Cu and Al, and the depletion of Zn in GBPs with the rise of the aging temperature selected. This trend, which has been consolidated in the literature by various authors [41,42], can be explained by the equilibrium concentration of Cu and Al in $MgZn_2$ rising with increasing temperature (Fig.2.25 in Section 2.10). This event is linked to the enhanced solubility of Al and Cu in $MgZn_2$ occurring at higher temperatures [41].

Both the retrogression and reaging (RRA) strategies and the newly developed non-isothermal aging (NIA) strategies use high temperature steps (200 °C–220 °C) in their thermal schedules. Importantly, these steps could be assumed to be the ones responsible for the increased concentration of Cu at GBs and, consequently, the enhanced SCC resistance matured in the samples [54,109,169]. For this reason, when considering the final GBP composition, including high temperature steps would be advantageous when designing aging strategies for 7000 aluminium alloys.

6.2.6 The effect of aging parameters on corrosion properties

When considering the effect of the aging parameters on the SCC susceptibility, Tab.6.4 and Tab.6.12 highlight how the resistance to SCC rises with increasing temperature and duration of the aging steps used. In fact, aging treatments involving higher temperatures and longer holding times more effectively raise the average GBP length and its standard deviation (Tab.6.6), in turn increasing the interspacing among GBPs. These microstructural features are linked with the decrease of the anodic dissolution and the production of atomic hydrogen at the crack tip [37,54,170]. Larger GBPs also provide effective traps for hydrogen atoms, lowering the hydrogen embrittlement at GBs [37,54].

Although the elemental content evolution of GBPs with aging was simulated just for reduced time spans (up to 30 minutes of isothermal holding), a higher concentration of Cu and Al can be assumed to be included in the η phase when raising the aging temperature. The Cu enrichment of GBPs decreases the SCC susceptibility through the reduction of the anodic dissolution rate since the potential difference between MgZn₂ and the aluminium matrix is lowered [37,43,106].

As commonly reported in the literature, the SCC resistance of retrogressed and reaged (RRA) samples is comprised between the one of the peak-aged (T6) and overaged (T73) samples [121,139]. In this work, the retrogression and reaged double aging (RRDA) samples time to failure (36 days) is also intermediate between the T6 samples (2 days) and T73 samples (no failure), meaning that the proposed aging strategy might achieve similar SCC properties of typically RRA materials.

The data presented in Tab.6.12 also suggest that double-aged specimens (FA) are characterised by a superior SCC resistance compared to T6 samples. This result agrees with the work of Li et al. [129], who concluded that preaging/paint-baking strategies develop better corrosion properties in the auto panels compared to peak aging treatments.

The lower SCC susceptibility of two-step aged samples can be explained considering that the high temperature exposure (usually in the 160 °C–180 °C range) realised during the second step of double aging schedules accelerates the development of all the GB microstructural characteristics that are beneficial to limiting the SCC susceptibility. The same acceleration cannot be realised during the conventional low temperature peak aging treatment (120 °C for 24 hours).

Overall, temperature raises appears more effective (and more advantageous) than applying a prolonged holding time to improve the SCC resistance. In fact, as highlighted in Fig.6.16, the enlargement and disconnection of GBPs increases exponentially with the aging temperature. As additional evidence, the RRDA time to failure is almost two-fold that of FA samples: this result might be caused by the retrogression step at high temperature, which is used only in the RRDA strategy (220 °C for 4.5 minutes) and not in the FA strategy.

After having examined the relationship between aging parameters and SCC susceptibility in the first part of this section, the last part studies the possible link between electrochemical parameters derived from anodic polarisations and the SCC resistance results.

Due to the similarity between the anodic polarisation curves of the fast cooled and slow cooled samples (Fig.5.13), identifying any correlation between the electrochemical parameters derived from this technique and SCC susceptibility was impossible. Specifically, the differences in the open circuit potential (OCP) or breakdown potential for the two metallurgical conditions examined are comparable to the intrinsic experimental variability of those curves. The same observation is valid when comparing the anodic polarisations of the T6 and T73 samples (Fig.6.19). The almost superimposition of polarisation curves related very different aging strategies is a feature found in various studies (compare, for example, the polarisation curves obtained in the studies of Jiang et al. [150] and Sun et al. [174]).

Interestingly, the corroded surfaces examined after anodic polarisation display totally different characteristics depending on the heat treatment parameters used (Fig.4.43, Fig.4.45). The type of corrosion attack during anodic polarisation presumably changes when reducing the cooling rate or when the time and temperature of the aging steps are raised. A high cooling rate or underaging generate a more uniform corrosion attack during anodic polarisation, while the corrosion reactions seemingly occur mostly at GBs when a low cooling rate or overaging is applied. The implications of these empirical observations with the associated SCC susceptibility of the metallurgical conditions require further investigation.

6.2.7: Impact of the research findings

The research findings presented in the discussion chapter carry practical implications, not only for the HFQ® technology but also for the heat treatments of 7000 aluminium alloy sheets in general. Additionally, this study contributes to the exploration of heat treatment parameter combinations that are unique to sheet materials, an aspect that has received comparatively less attention in the literature when compared to traditional heat treatments involving thicker components in the aeronautical field.

The experiments conducted for the solution heat treatment step investigated the combined impact of significantly shortened durations, temperatures surpassing the eutectic temperature limit, and a diverse range of heating rates.

The findings suggest that solution heat treatment durations for 7000 aluminium alloy sheets can be significantly reduced compared to thicker aerospace components. This reduction offers opportunities for industries, such as the automotive sector, that utilize sheet materials to enhance productivity and conserve energy. By employing higher heating rates instead of the typical circulating air furnace rates, the holding time during solution heat treatment can be further decreased. This shift in heating rate, particularly when starting from an F temper material, also leads to a notable refinement of the grain structure, potentially improving the mechanical properties of the workpieces. Consequently, automotive panel producers are encouraged to consider investing in technologies that facilitate rapid heating of the initial aluminium blanks.

The research findings on solution heat treatments also make valuable contributions to the field of metallurgy. For shorter holding times, the plateau of dissolution velocity observed at temperatures above 500 °C indicates the need for adjustments when modelling solution heat treatments at unconventional high temperatures. Additionally, the investigation of incipient melting signs at elevated temperatures helps identify parameter ranges where this phenomenon is negligible, which has been rarely reported in previous literature. Finally, the study of the dissolution process at high heating rates and its influence on subsequent holding times helps consolidate previously uncertain aspects within the literature.

The experiments carried out during the cooling step aimed to explore the identification of an optimal cooling rate that could enhance the final SCC resistance of the workpieces while maintaining the desired mechanical properties. Additionally, the study investigated the alterations in microstructural characteristics associated with different cooling rates.

The identification of an appropriate range of cooling rates, which can significantly enhance SCC resistance without compromising the final strength of the workpiece is a valuable suggestion not only to the HFQ® technology but also to all processes involving heat treatments of 7000 aluminium alloy sheets. Implementing the reduced cooling rate during the cooling step addresses the need for SCC-resistant final components and has the potential to boost process productivity by reducing reliance on overaging processes.

By lowering the cooling rate, the dimensions of grain boundary precipitates become more heterogeneous, whereas higher cooling rates lead to increased copper content within these precipitates. Moreover, the identification of a specific cooling rate range that selectively influences grain boundary precipitation without affecting matrix precipitation provides valuable insights that contribute to the advancement of metallurgical knowledge. These findings enhance the understanding of the relationship between final workpiece properties and cooling rate, as well as the possibility to refine existing modelling approaches.

Concerning the aging process, a compact strategy has been proposed when high cooling rates are adopted during the cooling step, leading to comparable mechanical properties as peak aged samples and enhanced resistance to stress corrosion cracking (SCC). Additionally, the kinetic principles underlying the influence of these thermal steps have been studied.

The combination of two-step aging and retrogression steps provides valuable insights for designers to develop optimized aging strategies. This is a crucial aspect in reducing the overall cost of 7000-series aluminium alloy body panels manufactured via HFQ® process and enhancing their presence in the market. Specifically, fine-tuning SCC resistance and strength in workpieces can be achieved through practical modulation of the retrogression step.

From a metallurgical standpoint, the correlation established between the proposed aging path and the resulting properties offers an opportunity to gain a better understanding of various contemporary aging strategies mentioned in the literature, such as non-isothermal aging (NIA) approaches. Moreover, this study contributes valuable insights by exploring the feasibility of applying retrogression on two-step aged samples and evaluating SCC resistance for paint-baked materials.

Chapter 7:

Conclusions

The current study aimed to provide a metallurgical optimisation of the HFQ® process to produce formed sheet components made of 7000 aluminium alloys. The research also aimed to explore unresolved research areas related to the heat treatment of this type of alloy. For the optimisation process, each step of the heat treatment schedule (solution heat treatment, cooling and aging step) was analysed separately, and the identified research gaps were categorised according to these steps. The main experimental techniques employed were small-angle x-ray scattering (SAXS), transmission electron microscopy (TEM) and differential scanning calorimetry (DSC) for microstructural characterisation, while uniaxial tensile tests and U-bends exposed to salt-spray environment were adopted for the mechanical and corrosion properties characterisation.

In this chapter, the key findings of the study are summarised and linked to the research questions and aims. Optimised sets of parameters for the HFQ® process are then subsequently suggested, and the interaction among the heat treatment steps is briefly discussed. Finally, recommendations for future research contributions are provided.

7.1: Key findings

The key findings of the study can be summarised as follows:

- The impact of a low heating rate, high temperature and short holding time on the precipitate dissolution process during the solution heat treatment of 7000 aluminium alloys was explored in detail. This study proposes that, when utilising the low heating rate typical of circulating air furnaces (approximately 3 °C/s), increasing the solution heat treatment temperature beyond 500 °C does not accelerate the dissolution process in the AA7075-F sheets. When using temperatures near this threshold, the dissolution process should be finished in durations below 10 minutes, and solution treatment longer than this is not beneficial.
- Typically, temperatures higher than the eutectic temperature of the chosen alloy are not employed for solution heat treatments in most previous studies due to the risk of incipient melting. However, the current study proposes that this phenomenon can be disregarded when processing AA7075-F sheets at low heating rates and holding times ranging from 1 to 10 minutes within the temperature range of 500 °C–530 °C.
- Implementing an accelerated solution heat treatment is crucial in the HFQ® process of 7000 aluminium alloys. The parameters chosen for the accelerated solution heat treatment vary depending on the heating rate utilised. When using the standard heating rate of circulating air furnaces (2.5 °C/s–3.5 °C/s), a temperature of 500 °C should be held for at least 6 minutes. On the other hand, if a higher heating rate is feasible (above 10 °C/s), a temperature of 470 °C should be selected and held for 2.5 minutes. This provides full solutionisation without risk of incipient melting.
- The impact of high heating rates on the precipitate dissolution process has previously been a topic of disagreement in the literature. This study suggests that a slower heating rate ramp (3 °C/s) leads to greater precipitate dissolution compared to a faster heating rate ramp (200 °C/s).

However, a high heating rate ramp enhances the effectiveness of the subsequent isothermal holding in dissolving precipitates compared to the adoption of a low heating rate ramp.

- The effect of solution treatment temperature and duration on the grain size evolution has been investigated. This study proposes that, when a low heating rate and short duration are employed, the grain structure of AA7075-F sheets remains unchanged even at 530 °C. Conversely, a high heating rate leads to a significant reduction in the average grain size of the tested samples.
- The effect of cooling rate on solute depletion in the interiors of grains is critical to understand since it may limit the application of the HFQ[®] process. This study proposes that, in the case of solutionised AA7075-F sheets, cooling rates exceeding 48 °C per second do not significantly alter the solute concentration within the grain, whereas cooling rates approximately below this threshold lead to a decrease in matrix solute concentration.
- The effect of cooling rate on the grain boundary precipitate (GBP) evolution has been comprehensively investigated. This study proposes that, within the investigated range of cooling rates from water quenching to die-cooling (30.7 °C/s), adopting the lowest cooling rate results in a slight increase in the average length of GBPs but a more significant effect is that the range of GBP sizes increases greatly as the cooling rate reduces.
- To enhance the final properties of aged HFQ[®] components, reducing the cooling rate from its maximum level is considered one possible approach. According to this research, AA7075 demonstrates acceptable tensile properties and improved stress corrosion cracking (SCC) resistance after aging when cooled at rates around 30 °C/s.
- The effect of cooling rate on precipitate composition along the grain boundaries has been explored using a phase field model, and the resulting predictions have been compared with the relevant literature. Based on the predictions obtained from the CIPHER model, the use of a higher cooling rate leads to a greater degree of substitution of Zn with Al

and Cu. Additionally, increasing the aging temperature and duration also promotes this substitution.

- The effect of ageing strategy when combined with the cooling conditions typical of HFQ® has been studied in detail, with its effect on microstructure, mechanical properties, and SCC resistance characterised. This study examined fast aged (FA) samples, which corresponds to a realistic paint-bake scenario. The findings suggest the FA samples exhibited better SCC resistance than T6 samples. However, despite the improvement, the FA samples remained highly vulnerable to SCC compared to a standard overaged (T73) temper.
- A new bespoke ageing strategy has been developed, optimized for a typical HFQ® high cooling rate with the aim of providing both good strength and SCC resistance in a highly efficient (shorter) ageing practice than a conventional T73 treatment. The proposed retrogression and reaged double aging (RRDA) strategy has been demonstrated to produce tensile properties comparable to T6 tempered samples, but with a much shorter treatment time (roughly 3 hours compared to 24 hours). Further integration with the car manufacturing process might be achieved by substituting the last 2 steps of the RRDA strategy with the paint-baking steps. While the SCC resistance of RRDA samples has been found to be significantly better than T6 and FA samples, it is still inferior to conventionally overaged (T73) specimens.
- Through studying the microstructural evolution imparted by the RRDA aging schedule, it is suggested that retrogression steps can be employed on two-step aged samples, although the amount of precipitates dissolved during retrogression using this approach is probably lower than that achieved via conventional retrogression and reaging (RRA) treatment.

7.2: Optimised heat treatment pathways for the HFQ® process

HFQ® of 7000 aluminium alloys is a complicated process, and achieving complete cost optimisation requires a multidisciplinary approach that involves many areas of engineering. One significant opportunity for cost reduction related to the metallurgy of 7000 aluminium alloys is to optimise the HFQ® heat treatment schedule.

However, due to the large number of variables involved in the heat treatment sequence and their possible interaction, simplification strategies are necessary to approach this complex problem, even when focusing solely on this aspect of HFQ® optimisation. This study separately examines each step of the heat treatment sequence (solution heat treatment, cooling and aging) and discusses the theoretical interaction among the steps.

The consensus is that, in general, the solution heat treatment must fully dissolve the nanometric precipitates and increase the solute levels in the matrix to their maximum level. If the solution heat treatment is incomplete, the volume and refinement of strengthening phases that contribute to the alloy's hardening response during aging would be hindered. Further, an incomplete solution heat treatment would require modifying the optimised parameters for the cooling and aging steps.

The solution heat treatment parameters necessary for achieving complete precipitate dissolution are dependent on the heating rate available with the specific heating system employed. If low heating rates typical of circulating air furnaces are used, samples should be held at 500 °C for at least 6 minutes.

If higher heating rates are available, the duration of the solution heat treatment can be decreased accordingly. In this study, complete precipitate dissolution was attained by using a heating rate of 200 °C/s to reach 470 °C and maintaining this temperature for 2.5 minutes.

Notably, the solution heat treatment temperature can cause slight modifications in the heat transfer process once the blank encounters the dies during the

pressing stage. Therefore, the solution heat treatment temperature choice can affect the optimal cooling rate that must be adopted.

The cooling and aging steps are strongly connected and have a combined impact on determining the final properties of the auto panel. Achieving acceptable SCC resistance in workpieces generally acknowledged to be linked to the development of the GB microstructure in 7000 aluminium alloys.

Research suggests that this development can be achieved by either reducing the cooling rate during the cooling step from the maximum attainable value or by prolonging the aging, which has been the traditionally used method.

On one end of the spectrum, employing the highest attainable cooling rate would need a lengthy and ineffective aging process to satisfy the minimum requirement for SCC. Conversely, on the other end, excessively reducing the cooling rate would greatly reduce the solute content in the matrix, impeding the workpieces' hardening response.

This study suggests that using a cooling rate between 30 °C/s and 35 °C/s after the solution heat treatment can enhance the development of GBPs without compromising the solute concentration in the matrix. Two possible optimised pathways can be proposed, but the integration with the paint-baking step must be considered.

The first potential approach is to implement a cooling rate of 30 °C/s and adopt the FA schedule, which is exemplificative of the preaging/paint-baking strategies commonly used in the literature. The current study suggests that this heat treatment process would result in SCC resistance in the specimens comparable to that of T73 specimens, while causing a 4% decrease in yield strength and a 7% decrease in ultimate tensile strength compared to T6 samples.

If the resulting strength reduction is considered unacceptable, the cooling rate should be slightly increased from the mentioned level and Step1, Step2 and Step3 of the RRDA strategy should be executed. The workpieces must be subjected to the paint-baking process afterwards.

In these heat treatment methods, the growth and separation of GBPs are attained through combining the cooling and aging steps. Moreover, if the paint-

baking process is assumed to be comparable to the Step4 and Step5 sequence of the RRDA strategy, the strength levels of the workpieces would be boosted due to the unlocked kinetics of retrogression and reaging. However, additional experimentation would be necessary to fully develop the latter heat treatment pathway.

Since the optimisation process conducted in this study did not consider the impact of deformation during the cooling phase, the optimised heat treatment parameters would likely undergo slight modifications when applied to the real HFQ® process. Typically, the deformation during the cooling stage is thought to accelerate the aging kinetics of the material, which could lead to an additional reduction in the total process time.

7.3: Future work

When identifying areas for future research, a first important point to consider is that the totality of the literature gaps identified would require not only a single study but a collection of studies to answer the research questions posed. The research questions addressed in this study can be classified into two distinct groups: those concerning debated topics in the 7000 aluminium alloy metallurgy and those specifically pertaining to the optimisation of the HFQ[®] process.

For the first category, which is not the focus of this section due to not being directly linked with the HFQ[®] process, multiple possible contributions exist. For example, additional research is necessary to clarify how the elemental composition of GBP varies with changes in cooling rate or to identify the boundaries of solution heat treatment parameters to prevent incipient melting. The research questions directly related to the HFQ[®] optimisation can be categorised based on the specific step of the heat treatment schedule each question addresses.

Further examining the precipitate dissolution process during accelerated solution heat treatments would require additional research to investigate the impact of heating rate when varying the alloy composition or temper of the starting material. In addition, to make the optimisation process more applicable to the real HFQ[®] process, repeating the experiments, including the deformation of the workpieces, would be necessary.

Regarding the cooling step optimisation, while reducing the cooling rate may seem like an appealing solution for the HFQ[®] process, precisely controlling the heat transfer during the forming step is a significant technological challenge. Consequently, implementing a pre-cooling step followed by an isothermal holding in HFQ[®] before the deformation and final cooling stage could be a more feasible and promising option worth investigating.

Due to the intricate shapes of auto panels produced using HFQ[®], locating and extracting the representative flat coupons from these specimens can be extremely difficult when assessing SCC resistance. Since the preliminary

experiments conducted in this study did not establish a correlation between the derived electrochemical parameters and the SCC resistance of the alloy, additional research is necessary to explore this direction.

Expanding the study to include variations in cooling rate and aging parameters would provide the opportunity to optimize the final properties attained by the aluminium body panels. Additionally, by examining different heat treatment parameters, such as formability under dies and post-process fracture toughness, other pertinent properties for the automotive sector could be analysed.

Furthermore, exploring a different 7000 alloy system for processing could aid in understanding the process's sensitivity to changes in the material's quench sensitivity.

The current study emphasizes the significance of combining two-step and RRA strategies to develop a competitive aging approach for [®]HFQ. However, additional investigation is required to achieve this objective since the final SCC attained by workpieces still falls short compared to the standard overaged samples. Furthermore, further research is necessary to fully integrate the HFQ[®] aging step with the paint-baking step by exploring optimized parameters for paint baking to be applied to samples after a multi-step aging strategy. Additionally, a more comprehensive understanding of the influence of multi-step and non-isothermal aging (NIA) strategies on the microstructural characteristics of 7000-series aluminium alloys is needed, as the underlying microstructural changes that occur have not been thoroughly consolidated in the available literature.

References

- [1] <https://www.davesbodyshop.com/blog/2018/11/highlighting-the-advantages-of-aluminum-car-frames/>, Accessed 21 August, 2022.
- [2] Schneider, R., Heine, B., Grant, R. J., & Zouaoui, Z. (2015). Mechanical behaviour of aircraft relevant aluminium wrought alloys at low temperatures. *Proceedings of the Institution of Mechanical Engineers, Part L: Journal of Materials: Design and Applications*, 229(2), 126-136.
- [3] ICCT. EU CO2 Emissions Standards for Passenger Cars and Light-Commercial Vehicles in International Council on Clean Transportation, 2019.
- [4] <https://www.iea.org/commentaries/growing-preference-for-suvs-challenges-emissions-reductions-in-passenger-car-market>, Accessed 25 August 2021.
- [5] Afseth, A. (2017). Ultra-High-Strength Aluminium Alloys — Vehicle Production's Next Big Thing. *Lightweight Design Worldwide*, 10(2), 12–15.
- [6] <https://www.engineering.com/story/the-battle-of-the-bodies-steel-vs-aluminum-in-automotive-production>, Accessed 25 August 2022.
- [7] <https://www.motortrend.com/features/15-automotive-aluminum-warriors/>, Accessed 25 August 2021.
- [8] <https://www.autoevolution.com/audi/a8/>, Accessed 19 August 2022.
- [9] <https://www.european-aluminium.eu/resource-hub/aluminium-automotive-manual/>, Accessed 27 August 2021
- [10] <http://www.matweb.com>, Accessed on 7 September, 2022.
- [11] Jayashree, P. K., Shankar, M. G., Kini, A., Sharma, S. S., & Shetty, R. (2013). Review on effect of silicon carbide (SiC) on stir cast aluminium metal matrix composites. *International Journal of Current Engineering and Technology*, 3(3), 1061-1071.
- [12] Sotirov, N., Simon, P., Chimani, C., Uffelmann, D., & Melzer, C. (2012). Warm deep drawability of peak-aged 7075 aluminium sheet alloy. In *Key Engineering Materials* (Vol. 504, pp. 955-960). Trans Tech Publications Ltd.

- [13] Choi, Y., Lee, J., Panicker, S. S., Jin, H. K., Panda, S. K., & Lee, M. G. (2020). Mechanical properties, springback, and formability of W-temper and peak aged 7075 aluminum alloy sheets: Experiments and modeling. *International Journal of Mechanical Sciences*, 170, 105344.
- [14] Jeshvaghani, R. A., Emami, M., Shahverdi, H. R., & Hadavi, S. M. M. (2011). Effects of time and temperature on the creep forming of 7075 aluminum alloy: Springback and mechanical properties. *Materials Science and Engineering: A*, 528(29-30), 8795-8799.
- [15] Tajally, M., & Emadoddin, E. (2011). Mechanical and anisotropic behaviors of 7075 aluminum alloy sheets. *Materials & Design*, 32(3), 1594-1599.
- [16] Huo, W., Hou, L., Zhang, Y., & Zhang, J. (2016). Warm formability and post-forming microstructure/property of high-strength AA 7075-T6 Al alloy. *Materials Science and Engineering: A*, 675, 44-54.
- [17] Sáenz de Argandoña, E., Galdos, L., Ortubay, R., Mendiguren, J., & Agirretxe, X. (2015). Room temperature forming of AA7075 aluminum alloys: W-temper process. In *Key Engineering Materials* (Vol. 651, pp. 199-204). Trans Tech Publications Ltd.
- [18] Leacock, A. G., Howe, C., Brown, D., Lademo, O. G., & Deering, A. (2013). Evolution of mechanical properties in a 7075 Al-alloy subject to natural ageing. *Materials & Design*, 49, 160-167.
- [19] Choi, Y., Ha, J., Lee, M. G., & Korkolis, Y. P. (2021). Observation of Portevin-le Chatelier effect in aluminum alloy 7075-w under a heterogeneous stress field. *Scripta Materialia*, 205, 114178.
- [20] N.R. Harrison, et al., "Optimization of High Volume Warm Forming of Lightweight Sheet," SAE technical paper No. 2013-01-1170, 2013.
- [21] Kumar, M., Sotirov, N., & Chimani, C. M. (2014). Investigations on warm forming of AW-7020-T6 alloy sheet. *Journal of Materials Processing Technology*, 214(8), 1769-1776.
- [22] Kumar, M., & Ross, N. (2015). Warm forming and paint bake response of AW-7xxx sheet in various tempers. In *Key Engineering Materials* (Vol. 651, pp. 47-52). Trans Tech Publications Ltd.

- [23] Österreicher, J. A., Tunes, M. A., Grabner, F., Arnoldt, A., Kremmer, T., Pogatscher, S., & Schlögl, C. M. (2020). Warm-forming of pre-aged Al-Zn-Mg-Cu alloy sheet. *Materials & Design*, 193, 108837.
- [24] Österreicher, J. A., Grabner, F., Tunes, M. A., Coradini, D. S., Pogatscher, S., & Schlögl, C. M. (2021). Two step–ageing of 7xxx series alloys with an intermediate warm-forming step. *Journal of Materials Research and Technology*, 12, 1508-1515.
- [25] Zheng, K., Politis, D. J., Wang, L., & Lin, J. (2018). A review on forming techniques for manufacturing lightweight complex—shaped aluminium panel components. *International Journal of Lightweight Materials and Manufacture*, 1(2), 55-80.
- [26] Hall, R.W., Foster, A. and Praturlon, A.H., 2017, September. Hot forming and quenching pilot process development for low cost and low environmental impact manufacturing. In *Journal of Physics: Conference Series* (Vol. 896, No. 1, p. 012088). IOP Publishing.
- [27] Raugei, M., El Fakir, O., Wang, L., Lin, J., & Morrey, D. (2014). Life cycle assessment of the potential environmental benefits of a novel hot forming process in automotive manufacturing. *Journal of Cleaner Production*, 83, 80-86.
- [28] Maeno, T., Mori, K.I. and Yachi, R., 2017. Hot stamping of high-strength aluminium alloy aircraft parts using quick heating. *CIRP Annals*, 66(1), pp.269-272.
- [29] Mendiguren, J., De Argandoña, E.S. and Galdos, L., 2016, November. Hot stamping of AA7075 aluminum sheets. In *IOP Conference Series: Materials Science and Engineering* (Vol. 159, No. 1, p. 012026). IOP Publishing
- [30] Robinson, J. S., Pirling, T., Truman, C. E., & Panzner, T. (2017). Residual stress relief in the aluminium alloy 7075. *Materials Science and Technology*, 33(15), 1765-1775.
- [31] Milkereit, B., Österreich, M., Schuster, P., Kirov, G., Mukeli, E., & Kessler, O. (2018). Dissolution and precipitation behavior for hot forming of 7021 and 7075 aluminum alloys. *Metals*, 8(7), 531.

- [32] Liu, Q., Chen, S., Gu, R., Wang, W., & Wei, X. (2018). Effect of heat treatment conditions on mechanical properties and precipitates in sheet metal hot stamping of 7075 aluminum alloy. *Journal of Materials Engineering and Performance*, 27(9), 4423-4436.
- [33] Zhang, Z., Yu, J., & He, D. (2019). Influence of contact solid-solution treatment on microstructures and mechanical properties of 7075 aluminum alloy. *Materials Science and Engineering: A*, 743, 500-503.
- [34] Wang, L., Yang, X., Robson, J. D., Sanders, R. E., & Liu, Q. (2020). Microstructural evolution of cold-rolled AA7075 sheet during solution treatment. *Materials*, 13(12), 2734.
- [35] Scharifi, E., Savaci, U., Kavaklioglu, Z. B., Weidig, U., Turan, S., & Steinhoff, K. (2021). Effect of thermo-mechanical processing on quench-induced precipitates morphology and mechanical properties in high strength AA7075 aluminum alloy. *Materials Characterization*, 174, 111026.
- [36] Zheng, K., Dong, Y., Zheng, J. H., Foster, A., Lin, J., Dong, H., & Dean, T. A. (2019). The effect of hot form quench (HFQ[®]) conditions on precipitation and mechanical properties of aluminium alloys. *Materials Science and Engineering: A*, 761, 138017.
- [37] Chen, S. Y., Chen, K. H., Peng, G. S., Liang, X., & Chen, X. H. (2012). Effect of quenching rate on microstructure and stress corrosion cracking of 7085 aluminum alloy. *Transactions of Nonferrous Metals Society of China*, 22(1), 47-52.
- [38] Yuan, D., Chen, K., Chen, S., Huang, L., Chen, G., & Chen, S. (2022). Effect of pre-strain and quench rate on stress corrosion cracking resistance of a low-Cu containing Al–Zn–Mg–Cu alloy. *Materials Science and Engineering: A*, 833, 142374.
- [39] Xiao, Q., Xu, Y., Huang, J., Li, B., Wang, B., Liu, S., & Fu, L. (2020). Effects of quenching agents, two-step aging and microalloying on tensile properties and stress corrosion cracking of Al-Zn-Mg-Cu alloys. *Journal of Materials Research and Technology*, 9(5), 10198-10208.

- [40] Sun, X. Y., Zhang, B., Lin, H. Q., Zhou, Y., Sun, L., Wang, J. Q., ... & Ke, W. (2013). Correlations between stress corrosion cracking susceptibility and grain boundary microstructures for an Al–Zn–Mg alloy. *Corrosion science*, 77, 103-112.
- [41] Garner, A., Euesden, R., Yao, Y., Aboura, Y., Zhao, H., Donoghue, J., ... & Prangnell, P. B. (2021). Multiscale analysis of grain boundary microstructure in high strength 7xxx Al alloys. *Acta Materialia*, 202, 190-210.
- [42] Marlaud, T., Deschamps, A., Bley, F., Lefebvre, W., & Baroux, B. (2010). Influence of alloy composition and heat treatment on precipitate composition in Al–Zn–Mg–Cu alloys. *Acta Materialia*, 58(1), 248-260.
- [43] Goswami, R., Lynch, S., Holroyd, N. J., Knight, S. P., & Holtz, R. L. (2013). Evolution of grain boundary precipitates in Al 7075 upon aging and correlation with stress corrosion cracking behavior. *Metallurgical and Materials Transactions A*, 44(3), 1268-1278.
- [44] Deschamps, A., Texier, G., Ringeval, S., & Delfaut-Durut, L. (2009). Influence of cooling rate on the precipitation microstructure in a medium strength Al–Zn–Mg alloy. *Materials Science and Engineering: A*, 501(1-2), 133-139.
- [45] Dumont, D., Deschamps, A., Bréchet, Y., Sigli, C., & Ehrström, J. C. (2004). Characterisation of precipitation microstructures in aluminium alloys 7040 and 7050 and their relationship to mechanical behaviour. *Materials Science and Technology*, 20(5), 567-576.
- [46] Liu, S. D., Zhang, X. M., Chen, M. A., & You, J. H. (2008). Influence of aging on quench sensitivity effect of 7055 aluminum alloy. *Materials Characterization*, 59(1), 53-60.
- [47] Liu, Y., Li, J., Wang, L., Wang, K., Zhu, B., & Zhang, Y. (2021). Hot stamping of a B-pillar reinforced panel with 7075 aluminum alloy and the feasibility study of short-time aging. *Frontiers in Materials*, 7, 617223.
- [48] Jiang, Y. F., Ding, H., Cai, M. H., Chen, Y., Liu, Y., & Zhang, Y. S. (2019). Investigation into the hot forming-quenching integrated process with cold dies for high strength aluminum alloy. *Materials Characterization*, 158, 109967.

- [49] Kumar, M., Sotirov, N., & Chimani, C. (2014). Characterization of high strength Al-Zn-Mg alloy sheet for hot stamping. In *Materials Science Forum* (Vol. 794, pp. 796-801). Trans Tech Publications Ltd.
- [50] Österreicher, J. A., Kirov, G., Gerstl, S. S., Mukeli, E., Grabner, F., & Kumar, M. (2018). Stabilization of 7xxx aluminium alloys. *Journal of alloys and compounds*, 740, 167-173.
- [51] Xiao, Y. P., Pan, Q. L., Li, W. B., Liu, X. Y., & He, Y. B. (2011). Influence of retrogression and re-aging treatment on corrosion behaviour of an Al-Zn-Mg-Cu alloy. *Materials & Design*, 32(4), 2149-2156.
- [52] Baydogan, M., Cimenoglu, H., Sabri Kayali, E., & Rasty, J. (2008). Improved resistance to stress-corrosion-cracking failures via optimized retrogression and reaging of 7075-T6 aluminum sheets. *Metallurgical and Materials Transactions A*, 39(10), 2470-2476.
- [53] Peng, X., Guo, Q., Liang, X., Deng, Y., Gu, Y., Xu, G., & Yin, Z. (2017). Mechanical properties, corrosion behavior and microstructures of a non-isothermal ageing treated Al-Zn-Mg-Cu alloy. *Materials Science and Engineering: A*, 688, 146-154.
- [54] Wang, D., Ni, D. R., & Ma, Z. Y. (2008). Effect of pre-strain and two-step aging on microstructure and stress corrosion cracking of 7050 alloy. *Materials Science and Engineering: A*, 494(1-2), 360-366.
- [55] Peppas, A., Kollias, K., Dragatogiannis, D. A., & Charitidis, C. A. (2021). Sustainability analysis of aluminium hot forming and quenching technology for lightweight vehicles manufacturing. *International Journal of Thermofluids*, 10, 100082.
- [56] Raugei, M., El Fakir, O., Wang, L., Lin, J., & Morrey, D. (2014). Life cycle assessment of the potential environmental benefits of a novel hot forming process in automotive manufacturing. *Journal of Cleaner Production*, 83, 80-86.
- [57] Qiao, W. G., & Shi, W. Y. (2014). Simulation and optimization of b-pillar crashworthiness based on virtual test. In *Applied Mechanics and Materials* (Vol. 505, pp. 380-383). Trans Tech Publications Ltd.

- [58] Lee, M. S., Lim, O. D., Kang, C. G., & Moon, Y. H. (2022). Optimization of multiple collision characteristics using an innovative crashworthiness diagram. *International Journal of Crashworthiness*, 1-11.
- [59] Ghosh, A., & Ghosh, M. (2018). Microstructure and texture development of 7075 alloy during homogenisation. *Philosophical Magazine*, 98(16), 1470-1490.
- [60] Zou, X. L., Hong, Y. A. N., & Chen, X. H. (2017). Evolution of second phases and mechanical properties of 7075 Al alloy processed by solution heat treatment. *Transactions of Nonferrous Metals Society of China*, 27(10), 2146-2155.
- [61] Starke Jr, E. A., & Staley, J. T. (1996). Application of modern aluminum alloys to aircraft. *Progress in aerospace sciences*, 32(2-3), 131-172.
- [62] Zhang, W. P., Li, H. H., Hu, Z. L., & Hua, L. (2020). Investigation on the deformation behavior and post-formed microstructure/properties of AA7075-T6 alloy under pre-hardened hot forming process. *Materials Science and Engineering: A*, 792, 139749.
- [63] Zheng, K., Dong, Y., Zheng, D., Lin, J., & Dean, T. A. (2019). An experimental investigation on the deformation and post-formed strength of heat-treatable aluminium alloys using different elevated temperature forming processes. *Journal of Materials Processing Technology*, 268, 87-96.
- [64] Li, Y., Yu, L., Zheng, J. H., Guan, B., & Zheng, K. (2021). A physical-based unified constitutive model of AA7075 for a novel hot forming condition with pre-cooling. *Journal of Alloys and Compounds*, 876, 160142.
- [65] Jiang, Y. F., Ding, H., Cai, M. H., Chen, Y., Liu, Y., & Zhang, Y. S. (2021). Effect of Forming-Die Temperature on Microstructure and Mechanical Properties of AA7075 Alloy During HFQ[®] Process. *Transactions of the Indian Institute of Metals*, 74(3), 725-734.
- [66] Ma, W. P., Wang, B. Y., Xiao, W. C., Yang, X. M., & Kang, Y. (2019). Springback analysis of 6016 aluminum alloy sheet in hot V-shape stamping. *Journal of Central South University*, 26(3), 524-535.

- [67] Decrozant-Triquenaux, J., Pelcastre, L., Prakash, B., & Hardell, J. (2021). Influence of lubrication, tool steel composition, and topography on the high temperature tribological behaviour of aluminium. *Friction*, 9(1), 155-168.
- [68] Chen, S., Gu, R., Liu, Q., Wang, W., & Wei, X. (2020). Experimental and Numerical Investigation on Strengthening Behavior of 7075 Aluminum Alloy Sheets in Hot Forming–Quenching Integrated Process. *Journal of Manufacturing Science and Engineering*, 142(6), 061005.
- [69] Rigas, N., Junker, F., Berendt, E., & Merklein, M. (2022). Tribological Behavior Of High-Strength Aluminum Alloys In Combination With Dry Lubricants At High Forming Temperatures. In *Defect and Diffusion Forum* (Vol. 414, pp. 125-130). Trans Tech Publications Ltd.
- [70] Wang, A., Zhong, K., El Fakir, O., Liu, J., Sun, C., Wang, L. L., ... & Dean, T. A. (2017). Springback analysis of AA5754 after hot stamping: experiments and FE modelling. *The International Journal of Advanced Manufacturing Technology*, 89(5), 1339-1352.
- [71] Attar, H. R., Zhou, H., & Li, N. (2021, June). Deformation and thinning field prediction for HFQ[®] formed panel components using convolutional neural networks. In *IOP Conference Series: Materials Science and Engineering* (Vol. 1157, No. 1, p. 012079). IOP Publishing.
- [72] Shao, Z., Jiang, J., & Lin, J. (2018). Feasibility study on direct flame impingement heating applied for the solution heat treatment, forming and cold die quenching technique. *Journal of Manufacturing Processes*, 36, 398-404.
- [73] Zheng, J. H., Dong, Y., Zheng, K., Dong, H., Lin, J., Jiang, J., & Dean, T. A. (2019). Experimental investigation of novel fast–ageing treatments for AA6082 in supersaturated solid solution state. *Journal of Alloys and Compounds*, 810, 151934.
- [74] Jiang, Y. F., & Ding, H. (2020). Investigations into Hot Form Quench Conditions on Microstructure Evolution and Bake-Hardening Response for High-Strength Aluminum Alloy. *Journal of Materials Engineering and Performance*, 29(12), 8331-8339.

- [75] Gáspár, M., Tervo, H., Kaijalainen, A., Dobosy, Á., & Török, I. (2018, May). The effect of solution annealing and ageing during the RSW of 6082 aluminium alloy. In *Vehicle and Automotive Engineering* (pp. 694-708). Springer, Cham.
- [76] Moon, C., Thuillier, S., Lee, J., & Lee, M. G. (2021). Mechanical properties of solution heat treated Al-Zn-Mg-Cu (7075) alloy under different cooling conditions: Analysis with full field measurement and finite element modeling. *Journal of Alloys and Compounds*, 856, 158180.
- [77] <https://www.active-robots.com/1-2-bore-32-pitch-aluminium-hub-gears.html>, Accessed 17 September 2022.
- [78] <https://www.heattek.com/aluminum-solution-heat-treat-furnaces.html>, Accessed 17 September 2022.
- [79] Huo, W., Sun, T., Hou, L., Zhang, W., Zhang, Y. and Zhang, J., 2020. Effect of heating rate during solution treatment on microstructure, mechanical property and corrosion resistance of high-strength AA 7075 alloy. *Materials Characterization*, 167, p.110535.
- [80] Mohamed, M., Foster, A.D. and Lin, J., 2008. Solution heat treatment in HFQ process. *Steel Research International*, 79(11), pp.160-167.
- [81] Xu, D. K., Rometsch, P. A., & Birbilis, N. (2012). Improved solution treatment for an as-rolled Al–Zn–Mg–Cu alloy. Part I. Characterisation of constituent particles and overheating. *Materials science and Engineering: A*, 534, 234-243.
- [82] Mahathaninwong, N., Plookphol, T., Wannasin, J. and Wisutmethangoon, S., 2012. T6 heat treatment of rheocasting 7075 Al alloy. *Materials Science and Engineering: A*, 532, pp.91-99.
- [83] Tanaka, H., Esaki, H., Yamada, K., Shibue, K., & Yoshida, H. (2004). Improvement of mechanical properties of 7475 based aluminum alloy sheets by controlled warm rolling. *Materials Transactions*, 45(1), 69-74.
- [84] Xu, D. K., Rometsch, P. A., & Birbilis, N. (2012). Improved solution treatment for an as-rolled Al–Zn–Mg–Cu alloy. Part II. Microstructure and mechanical properties. *Materials science and Engineering: A*, 534, 244-252.
- [85] Liu, Y., Zhu, B., Wang, Y., Li, S., & Zhang, Y. (2020). Fast solution heat treatment of high strength aluminum alloy sheets in radiant heating furnace

during hot stamping. *International Journal of Lightweight Materials and Manufacture*, 3(1), 20-25.

[86] Xu, X., Zhao, Y., Wang, X., Zhang, Y., & Ning, Y. (2016). Effect of rapid solid-solution induced by electropulsing on the microstructure and mechanical properties in 7075 Al alloy. *Materials Science and Engineering: A*, 654, 278-281.

[87] Choi, S., Jeon, J., Seo, N., Son, S. B., & Lee, S. J. (2021). Effect of Heating Rate on Microstructure and Mechanical Properties in Al 7055. *Metals and Materials International*, 27(3), 449-455.

[88] Ding, L., Zhao, L., Weng, Y., Schryvers, D., Liu, Q., & Idrissi, H. (2021). Atomic-scale investigation of the heterogeneous precipitation in the ϵ (Al₁₈Mg₃Cr₂) dispersoid of 7075 aluminum alloy. *Journal of Alloys and Compounds*, 851, 156890.

[89] Liu, S., Zhong, Q., Zhang, Y., Liu, W., Zhang, X., & Deng, Y. (2010). Investigation of quench sensitivity of high strength Al–Zn–Mg–Cu alloys by time–temperature-properties diagrams. *Materials & Design*, 31(6), 3116-3120.

[90] Deng, Y. L., Wan, L., Zhang, Y. Y., & Zhang, X. M. (2011). Influence of Mg content on quench sensitivity of Al–Zn–Mg–Cu aluminum alloys. *Journal of Alloys and Compounds*, 509(13), 4636-4642.

[91] Thompson, D. S., Subramanya, B. S., & Levy, S. A. (1971). Quench rate effects in al-zn-mg-cu alloys. *Metallurgical Transactions*, 2(4), 1149-1160.

[92] Staley, J. T., & Tiryakioglu, M. (2001, November). The use of TTP curves and quench factor analysis for property prediction in aluminum alloys. In *Materials Solutions Conference* (pp. 6-15).

[93] Staley, J. T. (1987). Quench factor analysis of aluminium alloys. *Materials Science and Technology*, 3(11), 923-935.

[94] Dolan, G. P., Flynn, R. J., Tanner, D. A., & Robinson, J. S. (2005). Quench factor analysis of aluminium alloys using the Jominy end quench technique. *Materials science and technology*, 21(6), 687-692.

[95] Zhang, Y., Milkereit, B., Kessler, O., Schick, C., & Rometsch, P. A. (2014). Development of continuous cooling precipitation diagrams for aluminium alloys AA7150 and AA7020. *Journal of alloys and compounds*, 584, 581-589.

- [96] B. F. Brown, "Stress Corrosion Cracking Control Measures", U. S. Government Printing Office, Washington, DC (1977).
- [97] Speidel, M. O. (1975). Stress corrosion cracking of aluminum alloys. *Metallurgical Transactions A*, 6(4), 631-651.
- [98] Burleigh, T. D. (1991). The postulated mechanisms for stress corrosion cracking of aluminum alloys: A review of the literature 1980-1989. *Corrosion*, 47(2), 89-98.
- [99] Lynch, S. (2012). Mechanistic and fractographic aspects of stress corrosion cracking. *Corrosion Reviews*, 30(3-4), 63-104.
- [100] Lynch, S. P. (2007). Progress towards understanding mechanisms of hydrogen embrittlement and stress corrosion cracking. *CORROSION* 2007.
- [101] Magaji, N., Mayrhofer, R., Kröger, B., Schnatterer, C., & Zander, D. (2019). Comparison of test methods used to analyze stress corrosion cracking of differently tempered 7xxx alloys. *Materials and Corrosion*, 70(7), 1192-1204.
- [102] Parkins, R. N. (1980). Predictive approaches to stress corrosion cracking failure. *Corrosion Science*, 20(2), 147-166.
- [103] Chemin, A., Marques, D., Bisanha, L., de Jesus Motheo, A., Bose Filho, W. W., & Ruchert, C. O. F. (2014). Influence of Al₇Cu₂Fe intermetallic particles on the localized corrosion of high strength aluminum alloys. *Materials & Design*, 53, 118-123.
- [104] Wang, D., & Ma, Z. Y. (2009). Effect of pre-strain on microstructure and stress corrosion cracking of over-aged 7050 aluminum alloy. *Journal of Alloys and Compounds*, 469(1-2), 445-450.
- [105] Fang, X., Song, M., Li, K., Du, Y., Zhao, D., Jiang, C., & Zhang, H. (2012). Effects of Cu and Al on the crystal structure and composition of η (MgZn₂) phase in over-aged Al–Zn–Mg–Cu alloys. *Journal of Materials Science*, 47(14), 5419-5427.
- [106] Knight, S. P., Birbilis, N., Muddle, B. C., Trueman, A. R., & Lynch, S. P. (2010). Correlations between intergranular stress corrosion cracking, grain-boundary microchemistry, and grain-boundary electrochemistry for Al–Zn–Mg–Cu alloys. *Corrosion Science*, 52(12), 4073-4080.

- [107] Song, Y., Zhan, S., Nie, B., Qi, H., Liu, F., Fan, T., & Chen, D. (2022). First-Principles Investigations on Structural Stability, Elastic Properties and Electronic Structure of Mg₃₂ (Al, Zn)₄₉ Phase and MgZn₂ Phase. *Crystals*, 12(5), 683.
- [108] Song, F. X., Zhang, X. M., Liu, S. D., Tan, Q., & Li, D. F. (2014). The effect of quench transfer time on microstructure and localized corrosion behavior of 7050-T 6 Al alloy. *Materials and Corrosion*, 65(10), 1007-1016.
- [109] Angappan, M., Sampath, V., Ashok, B., & Deepkumar, V. P. (2011). Retrogression and re-aging treatment on short transverse tensile properties of 7010 aluminium alloy extrusions. *Materials & Design*, 32(7), 4050-4053.
- [110] Robson, J. D. (2019). Analytical electron microscopy of grain boundary segregation: application to Al-Zn-Mg-Cu (7xxx) alloys. *Materials Characterization*, 154, 325-334.
- [111] Liu, C., Garner, A., Zhao, H., Prangnell, P. B., Gault, B., Raabe, D., & Shanthraj, P. (2021). CALPHAD-informed phase-field modeling of grain boundary microchemistry and precipitation in Al-Zn-Mg-Cu alloys. *Acta Materialia*, 214, 116966.
- [112] Qin, R. S., & Bhadeshia, H. K. (2010). Phase field method. *Materials science and technology*, 26(7), 803-811.
- [113] Bouhattate, Jamaa. Modeling texture evolution in polycrystalline materials using spherical harmonics. The Florida State University, 2006.
- [114] <https://sparkyswordscience.blogspot.com/2013/12/introduction-to-crystal-structure.html>, Accessed 23 August 2022.
- [115] Gerold V. Precipitation hardening. In: Nabarro, F.R.N. (Ed.), *Dislocations in Solids*. North-Holland, 1979, p. 222.
- [116] R. E. Smallman and A. H. W. Ngan. *Physical Metallurgy and Advanced Materials*. Elsevier, 2007.
- [117] Cheng, L. M., Poole, W. J., Embury, J. D., & Lloyd, D. J. (2003). The influence of precipitation on the work-hardening behavior of the aluminum alloys AA6111 and AA7030. *Metallurgical and materials transactions A*, 34(11), 2473-2481.

- [118] Li, Y., Shi, Z., & Lin, J. (2019). Experimental investigation and modelling of yield strength and work hardening behaviour of artificially aged Al-Cu-Li alloy. *Materials & Design*, 183, 108121.
- [119] Jiang, F., Huang, J., Tang, L., Wang, F., Xiao, Q., & Yin, Z. (2019). Effects of quench rate on mechanical properties and microstructures of high-strength 7046A aluminum alloy. *Jom*, 71(5), 1722-1730.
- [120] Godard, D., Archambault, P., Aeby-Gautier, E., & Lapasset, G. (2002). Precipitation sequences during quenching of the AA 7010 alloy. *Acta Materialia*, 50(9), 2319-2329.
- [121] Park, J. K., & Ardell, A. J. (1984). Effect of retrogression and reaging treatments on the microstructure of Al-7075-T651. *Metallurgical and Materials Transactions A*, 15(8), 1531-1543.
- [122] Liu, S., Li, Q., Lin, H., Sun, L., Long, T., Ye, L., & Deng, Y. (2017). Effect of quench-induced precipitation on microstructure and mechanical properties of 7085 aluminum alloy. *Materials & Design*, 132, 119-128.
- [123] Zhang, Y., Pelliccia, D., Milkereit, B., Kirby, N., Starink, M. J., & Rometsch, P. A. (2018). Analysis of age hardening precipitates of Al-Zn-Mg-Cu alloys in a wide range of quenching rates using small angle X-ray scattering. *Materials & Design*, 142, 259-267.
- [124] <https://www.press.bmwgroup.com/global/photo/detail/P90139475/the-mini-s-new-paint-being-baked-in-the-oven-at-plant-oxford-s-paintshop>, Accessed 18 December 2022.
- [125] Giampieri, A., Ling-Chin, J., Ma, Z., Smallbone, A., & Roskilly, A. P. (2020). A review of the current automotive manufacturing practice from an energy perspective. *Applied Energy*, 261, 114074.
- [126] Akafuah, N. K., Poozesh, S., Salaimeh, A., Patrick, G., Lawler, K., & Saito, K. (2016). Evolution of the automotive body coating process—A review. *Coatings*, 6(2), 24.
- [127] Balderach, D. C., Hamilton, J. A., Leung, E., Tejeda, M. C., Qiao, J., & Taleff, E. M. (2003). The paint-bake response of three Al-Mg-Zn alloys. *Materials Science and Engineering: A*, 339(1-2), 194-204

- [128] Min, J., Xie, F., Liu, Y., Hou, Z., Lu, J., & Lin, J. (2022). Experimental study on cold forming process of 7075 aluminum alloy in W temper. *CIRP Journal of Manufacturing Science and Technology*, 37, 11-18.
- [129] Li, H., Liu, X. T., & Wang, J. Y. (2019). Influence of Preaging Treatment on Bake-Hardening Response and Electrochemical Corrosion Behavior of High Strength Al-Zn-Mg-Cu-Zr Alloy. *Metals*, 9(8), 895.
- [130] Lee, Y. S., Koh, D. H., Kim, H. W., & Ahn, Y. S. (2018). Improved bake-hardening response of Al-Zn-Mg-Cu alloy through pre-aging treatment. *Scr. Mater*, 147, 45-49.
- [131] Dehghani, K., Nekahi, A., & Mirzaie, M. A. M. (2010). Optimizing the bake hardening behavior of Al7075 using response surface methodology. *Materials & Design*, 31(4), 1768-1775.
- [132] <https://www.pressmark.co.uk/tag/aluminum/>, Accessed 10 January 2023.
- [133] Yang, H. B., Li, M. N., Bu, H. Y., & Lu, X. (2020). Effects of alloying elements on the amounts of MgZn₂ and S-Al₂CuMg phase in 7075 aluminum alloy. *Journal of Micromechanics and Molecular Physics*, 5(02), 2050003.
- [134] D.R. Askeland, *The Science and Engineering of Materials*, 3rd edn. (Chapman and Hall, Boston, MA, 1996).
- [135] Li X.-M., & Starink, M. J. (2001). Effect of compositional variations on characteristics of coarse intermetallic particles in overaged 7000 aluminium alloys. *Materials science and technology*, 17(11), 1324-1328.
- [136] Zuo, J., Hou, L., Shu, X., Peng, W., Yin, A., & Zhang, J. (2020). Grain refinement assisted by deformation enhanced precipitates through thermomechanical treatment of AA7055 Al alloy. *Metals*, 10(5), 594.
- [137] Park, J. K., & Ardell, A. J. (1989). Correlation between microstructure and calorimetric behavior of aluminum alloy 7075 and Al-Zn-Mg alloys in various tempers. *Materials Science and Engineering: A*, 114, 197-203.
- [138] Liu, D., Xiong, B., Bian, F., Li, Z., Li, X., Zhang, Y., ... & Liu, H. (2013). Quantitative study of precipitates in an Al-Zn-Mg-Cu alloy aged with various typical tempers. *Materials Science and Engineering: A*, 588, 1-6.

- [139] Viana, F., Pinto, A. M. P., Santos, H. M. C., & Lopes, A. B. (1999). Retrogression and re-ageing of 7075 aluminium alloy: microstructural characterization. *Journal of Materials Processing Technology*, 92, 54-59.
- [140] Zou, Y., Cao, L., Wu, X., Wang, Y., Sun, X., Song, H., & Couper, M. J. (2020). Effect of ageing temperature on microstructure, mechanical property and corrosion behavior of aluminum alloy 7085. *Journal of Alloys and Compounds*, 823, 153792.
- [141] Dai, P., Luo, X., Yang, Y., Kou, Z., Huang, B., Wang, C., ... & Ru, J. (2018). Nano-scale precipitate evolution and mechanical properties of 7085 aluminum alloy during thermal exposure. *Materials Science and Engineering: A*, 729, 411-422.
- [142] Emani, S. V., Benedyk, J., Nash, P., & Chen, D. (2009). Double aging and thermomechanical heat treatment of AA7075 aluminum alloy extrusions. *Journal of materials science*, 44(23), 6384-6391.
- [143] Zhou, P., Song, Y., Lu, J., Hua, L., Wu, W., Sun, Q., & Su, J. (2022). Novel fast-aging process for Al–Zn–Mg–Cu alloy sheets and its micro-mechanisms. *Materials Science and Engineering: A*, 856, 143996.
- [144] Jegdić, B., Bobić, B., Pavlović, M. K., Alil, A. B., & Putić, S. S. (2015). Stress corrosion cracking resistance of aluminum alloy 7000 series after two-step aging. *Chemical Industry and Chemical Engineering Quarterly/CICEQ*, 21(2), 261-268.
- [145] Lumley, R. N., Polmear, I. J., & Morton, A. J. (2005). Development of mechanical properties during secondary aging in aluminium alloys. *Materials Science and Technology*, 21(9), 1025-1032.
- [146] Buha, J., Lumley, R. N., & Crosky, A. G. (2008). Secondary ageing in an aluminium alloy 7050. *Materials Science and Engineering: A*, 492(1-2), 1-10.
- [147] Rajan, K., Wallace, W., & Beddoes, J. C. (1982). Microstructural study of a high-strength stress-corrosion resistant 7075 aluminium alloy. *Journal of Materials Science*, 17(10), 2817-2824.
- [148] Talianker, M., & Cina, B. (1989). Retrogression and reaging and the role of dislocations in the stress corrosion of 7000-type aluminum alloys. *Metallurgical Transactions A*, 20(10), 2087-2092.

- [149] Thakur, A., Raman, R., & Malhotra, S. N. (2007). Hydrogen embrittlement studies of aged and retrogressed-reaged Al–Zn–Mg alloys. *Materials chemistry and physics*, 101(2-3), 441-447.
- [150] Jiang, D., Liu, Y., Liang, S., & Xie, W. (2016). The effects of non-isothermal aging on the strength and corrosion behavior of AlZnMgCu alloy. *Journal of Alloys and Compounds*, 681, 57-65.
- [151] International Alloy Designations and Chemical Composition Limits for Wrought Aluminum and Wrought Aluminum Alloys (Revised 2001).
- [152] Richard, D., & Adler, P. N. (1977). Calorimetric studies of 7000 series aluminum alloys: I. Matrix precipitate characterization of 7075. *Metallurgical Transactions A*, 8(7), 1177-1183.
- [153] Di Cola, E., Grillo, I., & Ristori, S. (2016). Small angle X-ray and neutron scattering: powerful tools for studying the structure of drug-loaded liposomes. *Pharmaceutics*, 8(2), 10.
- [154] Deschamps, A., & De Geuser, F. (2011). On the validity of simple precipitate size measurements by small-angle scattering in metallic systems. *Journal of Applied Crystallography*, 44(2), 343-352.
- [155] Liu, Y., Fang, D., Zhu, B., Wang, Y., Li, S., & Zhang, Y. (2021). Modeling of Isothermal Dissolution of Precipitates in a 6061 Aluminum Alloy Sheet during Solution Heat Treatment. *Metals*, 11(8), 1234.
- [156] Czerwinski, F. (2020). Thermal stability of aluminum alloys. *Materials*, 13(15), 3441.
- [157] Zhang, X., Guo, M., Zhang, J., & Zhuang, L. (2016). Dissolution of precipitates during solution treatment of Al-Mg-Si-Cu alloys. *Metallurgical and Materials Transactions B*, 47(1), 608-620.
- [158] Papazian, J. M. (1986). Differential scanning calorimetry evaluation of retrogressed and re-aged microstructures in aluminum alloy 7075. *Materials Science and Engineering*, 79(1), 97-104.
- [159] Chang, Y. L., Hung, F. Y., & Lui, T. S. (2017). Enhancing the tensile yield strength of A6082 aluminum alloy with rapid heat solutionizing. *Materials Science and Engineering: A*, 702, 438-445.

- [160] Papazian, J. M. (1981). Effect of Two-Stage Aging on Microstructure of 7075 Aluminum Alloys. GRUMMAN AEROSPACE CORP BETHPAGE NY RESEARCH DEPT.
- [161] Graf, G., Spoerk-Erdely, P., Staron, P., Stark, A., Martin, F. M., Clemens, H., & Klein, T. (2022). Quench rate sensitivity of age-hardenable Al-Zn-Mg-Cu alloys with respect to the Zn/Mg ratio: An in situ SAXS and HEXRD study. *Acta materialia*, 227, 117727.
- [162] Deschamps, A., De Geuser, F., Horita, Z., Lee, S., & Renou, G. (2014). Precipitation kinetics in a severely plastically deformed 7075 aluminium alloy. *Acta materialia*, 66, 105-117.
- [163] Dumont, D., Deschamps, A., Bréchet, Y., Sigli, C., & Ehrström, J. C. (2004). Characterisation of precipitation microstructures in aluminium alloys 7040 and 7050 and their relationship to mechanical behaviour. *Materials Science and Technology*, 20(5), 567-576.
- [164] Kirman, I. (1971). The relation between microstructure and toughness in 7075 aluminum alloy. *Metallurgical Transactions*, 2(7), 1761-1770.
- [165] Huang, L. P., Chen, K. H., Li, S., & Song, M. (2007). Influence of high-temperature pre-precipitation on local corrosion behaviors of Al-Zn-Mg alloy. *Scripta Materialia*, 56(4), 305-308.
- [166] Ou, B. L., Yang, J. G., & Wei, M. Y. (2007). Effect of homogenization and aging treatment on mechanical properties and stress-corrosion cracking of 7050 alloys. *Metallurgical and Materials Transactions A*, 38(8), 1760-1773.
- [167] LI, C., LIU, S., WANG, G., JIN, Y., & ZHANG, X. (2013). Effect of cooling rate on exfoliation corrosion of Al-Zn-Mg-Cu alloy thick plate. *Chinese Journal of Materials Research*, 27(3), 259-267.
- [168] Czerwinski, F. (2020). Thermal stability of aluminum alloys. *Materials*, 13(15), 3441.
- [169] Zhou, L., Chen, K., Chen, S., Ding, Y., & Fan, S. (2021). Correlation between stress corrosion cracking resistance and grain-boundary precipitates of a new generation high Zn-containing 7056 aluminum alloy by non-isothermal aging and re-aging heat treatment. *Journal of Alloys and Compounds*, 850, 156717.

- [170] Najjar, D., Magnin, T., & Warner, T. J. (1997). Influence of critical surface defects and localized competition between anodic dissolution and hydrogen effects during stress corrosion cracking of a 7050 aluminium alloy. *Materials Science and Engineering: A*, 238(2), 293-302.
- [171] H. Schmiedel, W. Gruhl, The influence of the Zn-, Mg- and Cu-concentrations at the grain boundaries on the stress corrosion susceptibility of AlZnMg alloys, *Zeitschrift Für Met* 74 (1983) 777–782 .
- [172] Song, R. G., Dietzel, W., Zhang, B. J., Liu, W. J., Tseng, M. K., & Atrous, A. (2004). Stress corrosion cracking and hydrogen embrittlement of an Al–Zn–Mg–Cu alloy. *Acta Materialia*, 52(16), 4727-4743.
- [173] Knight, S. P., Pohl, K., Holroyd, N. J. H., Birbilis, N., Rometsch, P. A., Muddle, B. C., ... & Lynch, S. P. (2015). Some effects of alloy composition on stress corrosion cracking in Al–Zn–Mg–Cu alloys. *Corrosion Science*, 98, 50-62.
- [174] Sun, Q., Hu, J., Li, J., Chen, K., Dong, P., Liao, X., & Yang, Y. (2017). Effect of tempers on electrochemical corrosion behavior of 7150 aluminum alloy plate in various corrosive media. *Int. J. Electrochem. Sci*, 12, 5363-5377.
- [175] Park, J. K. (1988). Influence of retrogression and reaging treatments on the strength and stress corrosion resistance of aluminium alloy 7075-T6. *Materials Science and Engineering: A*, 103(2), 223-231.
- [176] Kanno, M., Araki, I., & Cui, Q. (1994). Precipitation behaviour of 7000 alloys during retrogression and reaging treatment. *Materials Science and Technology*, 10(7), 599-603.
- [177] Chun, F. E. N. G., LIU, Z. Y., NING, A. L., LIU, Y. B., & ZENG, S. M. (2006). Retrogression and re-aging treatment of Al-9.99% Zn-1.72% Cu-2.5% Mg-0.13% Zr aluminum alloy. *Transactions of Nonferrous Metals Society of China*, 16(5), 1163-1170.
- [178] Ivanoff, T. A., Carter, J. T., Hector, L. G., & Taleff, E. M. (2019). Retrogression and reaging applied to warm forming of high-strength aluminum alloy AA7075-T6 sheet. *Metallurgical and Materials Transactions A*, 50(3), 1545-1561.

- [179] Islam, M. U., & Wallace, W. (1983). Retrogression and reaging response of 7475 aluminium alloy. *Metals Technology*, 10(1), 386-392.
- [180] Deschamps, A., De Geuser, F., Hutchinson, C. R., Lee, S. W., & Horita, Z. J. (2014). Dynamic interactions between precipitation and plastic deformation in Aluminium alloys. In *Materials Science Forum* (Vol. 794, pp. 1133-1140). Trans Tech Publications Ltd.
- [181] Lumley, R. N., Buha, J., Polmear, I. J., Morton, A. J., & Crosky, A. (2006). Secondary precipitation in aluminium alloys & its role in modern heat treatment. In *Materials science forum* (Vol. 519, pp. 283-290). Trans Tech Publications Ltd.
- [182] Fribourg, G., Bréchet, Y., Deschamps, A., & Simar, A. (2011). Microstructure-based modelling of isotropic and kinematic strain hardening in a precipitation-hardened aluminium alloy. *Acta Materialia*, 59(9), 3621-3635.
- [183] Meng, C., Long, H., & Zheng, Y. (1997). A study of the mechanism of hardness change of Al-Zn-Mg alloy during retrogression reaging treatments by small angle X-ray scattering (SAXS). *Metallurgical and Materials Transactions A*, 28, 2067-2071.
- [184] Liu, D., Xiong, B., Bian, F., Li, Z., Li, X., Zhang, Y., ... & Liu, H. (2014). In situ studies of microstructure evolution and properties of an Al-7.5 Zn-1.7 Mg-1.4 Cu-0.12 Zr alloy during retrogression and reaging. *Materials & Design* (1980-2015), 56, 1020-1024.
- [185] Lin, Y. C., Jiang, Y. Q., Zhang, J. L., & Chen, X. M. (2018). Influence of stress-aging processing on precipitates and mechanical properties of a 7075 aluminum alloy. *Advanced Engineering Materials*, 20(1), 1700583.
- [186] Danh, N. C., Rajan, K., & Wallace, W. (1983). A TEM study of microstructural changes during retrogression and reaging in 7075 aluminum. *Metallurgical Transactions A*, 14, 1843-1850